



**Politecnico
di Torino**

Collegio di Ingegneria Elettrica

Corso di Laurea Magistrale in Ingegneria Elettrica

Tesi di Laurea Magistrale

Dynamic Modelling of Virtual and Real Inertia Systems in Green Microgrids

Relatore

Dr. Andrea Mazza

Correlatori

Prof. Enrico Pons

Prof. Ettore Francesco Bompard

Prof. Alberto Tenconi

Candidato

Mattia Gangi

ID n. 246115

Luglio 2021

Contents

List of Figures	1
List of Tables	7
List of Symbols	8
List of Acronyms	12
1 Introduction	14
2 Characteristics of a Low-Inertia Power System	17
2.1 Inertia in a power system	17
2.2 Impact of low inertia on the power system frequency	19
2.3 Time scale of Power/Frequency control	20
2.4 Metrics and measures for Low-Inertia Power Systems	22
2.4.1 Synchronous Inertial Response Factor	22
2.4.2 EirGrid Metrics	22
2.4.3 Metric for inertia requirements analysis	23
3 State-of-the-art for Virtual Inertia implementations	24
3.1 Synchronization of CIGs in the power system	25
3.2 Inertia emulation control techniques	27
3.2.1 SG Model Based Emulation: Synchronverters	29
3.2.2 SG Model Based Emulation: VISMA and IEPE topologies	31
3.2.3 IM Based Emulation: inductverters	33
3.2.4 Swing Equation Based Emulation: Ise Lab’s topology	34
3.2.5 Swing Equation Based Emulation: Synchronous Power Controllers (SCP)	36
3.2.6 Frequency-Power Response Based Emulation: VSG/ VSYNCH’s Topology	38
3.2.7 Droop based approaches	40
3.3 Technologies for inertia enhancement	41
3.3.1 Batteries and Ultra-capacitors	41
3.3.2 Flywheel	42
3.3.3 Synchronous condenser	44
3.3.4 General Purpose Energy Storages	44
4 Power-hardware-in-the-loop applications in Low-Inertia Systems	48
4.1 Hardware-in-the-loop	48
4.2 Real-Time Simulation and Power-Hardware-in-the-loop	49
4.3 Stability in PHIL Simulation	50
4.3.1 Instability problems and error propagation	51
4.3.2 PHIL stability analysis	52
4.4 Interface methodologies	52
4.4.1 Ideal Transformer Method (ITM)	53
4.4.2 Transmission Line Method (TLM)	54

4.4.3	Partial Circuit Duplication (PCD)	55
4.4.4	Damping Impedance Method (DIM)	55
4.5	PHIL field applications in power systems	56
4.5.1	Megawatt-scale PHIL for tests of drive systems	57
4.5.2	Test of a 500 kW PV array inverter	60
4.5.3	Tests of a voltage controller for deployment in a low-inertia power system	62
4.5.4	Synthetic inertia control implementation in Distributed Energy Resources	63
5	Low-Inertia laboratory setup	65
6	Matlab/Simulink model of a micro hydro power plant	66
6.1	Aims of the modelling	66
6.2	Creation of the micro hydro plant model	68
6.2.1	Synchronous Generator Block (SG)	69
6.2.2	Hydraulic Turbine and Governor Block (HTG)	70
6.2.3	HTG speed governor model and tuning method	73
6.2.4	Effects of water starting time T_w and inertia on the power response of HTG	75
6.2.5	Matlab/Simulink model of the Hydroelectric Power Plant	76
6.3	HPP Model Simulation Tests	81
6.4	Model in OPAL-RT	84
7	Simulation of a microgrid with virtual inertia implementation	90
7.1	Implementation of a photovoltaic DC source in Matlab/Simulink	90
7.1.1	PV model with MPPT control	91
7.1.2	BESS model	93
7.1.3	PV array and battery model test	94
7.2	Virtual Synchronous Generator model implementation in Matlab/Simulink	96
7.2.1	Self-Synchronized Synchronverter: inverter without a synchronization unit	97
7.2.2	Matlab/Simulink Model of the Self-Synchronized Synchronverter	100
7.2.3	LCL Filter and Virtual Impedance	105
7.2.4	Synchronverter Model Simulation Tests	106
7.3	Full Microgrid Model (HPP and Synchronverter)	112
7.3.1	Microgrid Offline Tests (Simulink Environment)	114
7.3.2	Microgrid Real-Time Tests (OpalRT Environment)	121
8	Conclusions	128
	References	130

List of Figures

1	Traditional power system characterized by high inertia, provided by the rotating parts of Synchronous Generators. The main source of generation is provided by fossil fuel, nuclear and hydroelectric plants.	14
2	Low-inertia power system characterized by high RES penetration, that reduces inertia in respect to the installed generation power. The main source of generation is provided by fossil fuel, nuclear and hydroelectric plants.	15
3	A roadmap of global electrification with renewables up to 2050 (IRENA) [4].	15
4	References and tools.	16
5	Power responses after a contingency event: instantaneous inertia response is followed by Primary Control response, consisting in frequency containment reserves (FCR) and frequency dependent loads response (Rotating Loads) [8].	18
6	Impact of increasing RES penetration on the frequency profile after a contingency event [9].	18
7	a) Comparison of frequency response after a contingency event with high and low system inertia [5]; b) RoCoF standards for protection relays for countries with high RES penetration [4].	20
8	Time frame for inertia response and power/frequency controls application [2].	21
9	a) a positive/negative reserve of power is maintained for Primary Control Generators, around their reference working point P_0 , to actively participate to power regulation [6]. b) Evolution of frequency after a contingency event [10].	21
10	a) Operational metric 1 shows the % of RES penetration for which frequency deviations are acceptable. b) Operational metric 2 shows when the kinetic energy is not sufficient to safely contain a contingency event [3].	23
11	General representation of grid-connected converters: a) Grid-forming; b) Grid-feeding; [11].	24
12	General representation of grid-supporting converters: a) Voltage based; b) Current based; [11]	25
13	Time-frame frequency response following a contingency event. The introduction of Virtual Inertia in the system allows to contain RoCoF and frequency deviations in the first instants of the event [12].	25
14	Simplified layout of CIG connection to the AC-grid [13].	26
15	PLL block diagram [2], [11].	26
16	Virtual Inertia Emulation. The main RES typologies are: wind turbines, with physical inertia completely decoupled from the grid by an AC/DC converter; Energy Storage System (ESS) and Photovoltaic plants (PV), with null inertia contributions and interfaced trough DC/DC converters [12].	27
17	Energy storages and controllers implemented for: a) Synchronous Generators; b) Converter-interfaced Generators [2].	28
18	Synchronverter schematic: power references (P^*, Q^*) are set and the control is obtained by piloting the inverter with PWM , generated by frequency/voltage control loops [14].	29

19	VISMA schematic: current control is exploited by setting the mechanical torque and EMF [15].	31
20	Bidirectional active power settings with VISMA control [15].	32
21	Inductverter schematic [3], [16].	33
22	Ise lab's control schematic [18].	35
23	First order governor for input power computation [12].	36
24	SCP control schematic [19].	36
25	Electrical characteristic of SPC: a) SG model; b) Virtual admittance implementation; [19].	37
26	Start-up process for SCP Synchronization [19].	38
27	VSG/VSYNCH schematic [3].	38
28	Frequency and voltage droop controllers for microgrids [12], [21].	40
29	General topology for Energy Storage (batteries) and Supercapacitor hybrid grid-integration [22].	42
30	Electromechanical layout of a FESS [23].	42
31	Electrical layout of a FESS [23].	43
32	SC connected to a load bus [25].	44
33	PHES plant general layout [28].	45
34	CAES systems: a) SF-CAES architecture; b) NSF-CAES architecture [30].	45
35	Primary frequency modulation schematic for CAES [31].	46
36	Example of a HIL laboratory setup. The real time digital simulator RTDS is used to simulate a network and the HUT is connected via I/O ports and an amplification stage (RTDS Technologies, [32]).	48
37	Control-Hardware-in-the-loop (CHIL) schematics for HUT/RTS interface [33].	49
38	Power-Hardware-in-the-loop (PHIL) schematics for HUT/RTS interface [33].	49
39	a) Four-Quadrant amplifier operations for PHIL. b) Schematics for Voltage and Current Controlled Amplifiers with input impedance Z_i , output impedance Z_o and voltage/current gain K_v/K_i	50
40	Instability in PHIL is shown in the simulated voltage divider circuit [35].	51
41	PHIL generic block diagram [35].	52
42	Nyquist stability criterion. In a stable system the OL function must not encircle the point (-1,0), as shown by the second graph.	53
43	Voltage type ITM. The amplifier controls the HUT voltage with a current feedback [33], [36].	53
44	Linking inductor or capacitor in a TML connection [35].	54
45	TLM Thevenin Equivalent [33].	54
46	Voltage type PCD [33], [36].	55
47	Voltage type DIM [33], [36].	55
48	a) Computing capability and time steps requirements for different PHIL applications. b) Comparison of real-time simulation and non-real-time (offline) simulation [37].	56
49	5 MW facility layout for PHIL applications [41].	57
50	One line schematic of the PHIL simulation, interfacing the simulated power system with the 2,5 MW motor drive [41].	58

51	PHIL tests on the power system response: a) 2 MW resistive step load; b) inductive load 50 mH/s ramp; c) $\pm 10\%$ load torque oscillations @ 0,2 Hz; d) Measured bus voltage (ATG1). [41]	59
52	PHIL test setup of the 500 kV array inverter. [42]	60
53	a) Normalized PV power profiles of the simulated grid. b) Voltage and power response tracking of the inverter with moderate PV power profile. [42]	61
54	a) PHIL for testing an physical AVR control over a real-time simulated SC system. b) Frequency and RoCoF response without SC (black) and with SC control (red) [43].	62
55	Synthetic inertia control schematic for a DER with power system model PHIL implementation [44].	63
56	a) Power and frequency trajectories with the SI controller. b) Frequency response without SI (black), with ideal SI (red) and with SI controller and variable gain K. [44]	64
57	Global Real Time Simulation Lab setup at the Energy Center in Torino.	65
58	Marelli Synchronous Generator nameplate.	65
59	Representation of the laboratory setup of the Synchronous Machine with prime movers.	66
60	voltage-behind-transient-reactance simplified model.	67
61	Simplified schematic of an hydroelectric power plant [46].	68
62	Block diagram of the Hydroelectric Power Plant (HPP) model [47].	68
63	Synchronous Machine models (Simulink Library browser \rightarrow Simscape / Electrical / Specialized Power Systems / Fundamental Blocks / Machines).	69
64	IEEE standard 1110-2002 equivalent dq axis dynamic model. All parameters are viewed from the stator's point of view (l = leakage, m = magnetizing, f = field, k = damper) [45],[48].	70
65	Hydraulic Turbine and Governor (HTG) (Simulink Library Browser \rightarrow Simscape / Electrical / Specialized Power Systems / Fundamental Blocks / Machines).	70
66	IEEE Working Group non-linear model of the turbine with non-elastic water column [49].	71
67	Correlation between ideal gate opening and real gate opening [50]	72
68	Simulink HTG turbine non-linear model [53].	73
69	PID controller and servomotor model featured in the HTG Block [53].	73
70	Ziegler-Nichols tuning procedure: a) choice of critical gain and oscillation period; b) choice of PID gains [55].	74
71	Impact of water starting time T_W on the system response to load variations [54].	75
72	Impact of machine starting time T_M on the system response to load variations, assuming a constant value of T_W [54].	75
73	Matlab/Simulink model of the Hydroelectric Power Plant.	76
74	Parameters of the Synchronous Machine and the HTG blocks.	77
75	a) ISO Standard 8528-5 for generators in islanded microgrids [12]; b) Model test response to a $10\%P_n$ load step with $H = 0.1$ s and $T_W = 0.25$ s: Nadir = -11.5 Hz, RoCoF = 25 Hz/s.	78
76	Microgrid configuration for step tests: a 6 kW load is connected to the main AC line via a <i>Circuit Breaker Block</i> . Positive/negative load steps are performed by disconnecting/connecting the load with controlled commutations of the circuit breaker.	81

77	Test 1: negative 6 kW load step @ $t = 5$ s, with Ziegler-Nichols parameters and standard HTG frequency control.	81
78	Test 2: negative 6 kW load step @ $t = 5$ s and positive 6 kW load step @ $t = 25$ s, with corrected PID parameters and HTG primary frequency control.	82
79	Test 3: a) 2 kW multi-step test @ $t = 5/9/13$ s; b) negative 30 kW step test ($50\%P_n$) @ $t = 5$ s.	83
80	Test 4: a) three-phase fault test @ $t = 5$ s with fault clearing time of 0.1 s; b) positive 6 kW ramp test (0.4 kW/s).	84
81	HPP Model regrouped into two subsystems.	85
82	Console Subsystem SC: data are acquired from SM via the input OpComm block and breaker signals are sent back for frequency step tests.	85
83	Master Subsystem SM: the HPP + microgrid system is simulated and data are sent to SC.	86
84	OpWriteFile and OpTrigger parameters. The file size limit equation is indicated in the help tab of the function.	87
85	Solver parameters for fixed-time discrete simulation.	87
86	Offline Opal-RT Test: negative 6 kW load step @ $t = 5$ s and positive 6 kW load step @ $t = 30$ s.	88
87	Assignment of the Master Subsystem to the Opal-RT Target Node.	88
88	Online Opal-RT Step Test: negative 6 kW load step @ $t = 5$ s and positive 6 kW load step @ $t = 25$ s. The second step of the Simulink offline test is executed @ $t = 30$ s.	89
89	Online Opal-RT Ramp Test: positive 6 kW load ramp (0.4 kW/s) @ $t = 5$ s.	89
90	Matlab/Simulink model of the PV array with MPPT control.	91
91	Parameters of the PV Array with I-V and P-V characteristics @ $T = 25^\circ\text{C}$	91
92	a) Flowchart of P & O algorithm [61]. b) Simulink implementation of the P & O algorithm [62].	92
93	Matlab/Simulink model of the BESS system.	93
94	Control scheme of the BESS system [63].	93
95	PV array + Battery Simulink model connected to the DC bus with resistive load.	94
96	PV-Battery test with irradiation steps of [100, 300, 500, 800, 1000] W/m^2 and $V_{ref} = 650$ V.	94
97	PV-Battery test with constant irradiation (initial steps of $1000\text{W}/\text{m}^2$) and $V_{ref} = 650$ V.	95
98	General schematic of the VSG structure [64].	96
99	Comparison of control structures for grid-connected inverters. a) Voltage-controlled inverter; b) Compact control structure [5].	97
100	Per-phase model of a SG connected to an infinite bus [5].	98
101	Self-synchronizing Synchronverter schematic [5].	98
102	Self-Synchronized Synchronverter main layout in Simulink.	100
103	Self-Synchronized Synchronverter control schematic in Simulink, based on [5].	101
104	Virtual Synchronous Generator dynamic equations [14].	102

105	Control characteristics of the synchronverter: a) P-f characteristic in set mode (constant P) and droop mode; b) Q-V characteristic in set mode (constant Q) and droop mode [66].	103
106	LCL filter implementation in simulink	105
107	Layout for standalone tests of the Self-Synchronized Synchronverter.	106
108	Test 1: Synchronization process. The synchronization starts @ $t = 0.5$ s.	107
109	Test 2: synchronverter in PQ node configuration. Synchronization @ $t = 0.5$ s, connection to the grid @ $t = 1$ s, multiple 5 kW steps @ $t = 2, 3, 4$ s, 5 kvar step @ $t = 5$ s.	108
110	Harmonic distortion of current and voltage at the connection point with the grid. . .	109
111	FFT analysis and THD measurement of synchronverter's output voltage and current. . .	109
112	Test 3: synchronverter in PV node configuration. Synchronization @ $t = 0.5$ s, connection to the grid @ $t = 1$ s, voltage droop control enabled @ $t = 2$ s, 5 kW step @ $t = 3$ s, 10 kW step @ $t = 5$ s.	110
113	Test 4: synchronverter in PV node configuration. Synchronization @ $t = 0.5$ s, connection to the grid @ $t = 1$ s, 20 kW nominal active power step @ $t = 2$ s, voltage droop control enabled @ $t = 6$ s.	111
114	Test 5: synchronverter in PQ node configuration. Synchronization @ $t = 0.5$ s, connection to the grid @ $t = 1$ s, 10 kW active power ramp (3.3 kW/s) @ $t = 2$ s. . .	111
115	Full microgrid model layout in RTlab-Simulink (in the SM subsystem).	112
116	RTLab blocks for data saving and triggering in the SM subsystem.	113
117	Console Subsystem SC.	113
118	Test 1: voltage-current synchronization with the grid @ $t = 5$ s, grid connection @ $t = 5.2$ s.	115
119	Test 1: HPP-Synchronverter synchronization @ $t = 5$ s, grid connection @ $t = 5.2$ s. . .	115
120	Test 1: HPP-Synchronverter synchronization @ $t = 5$ s, grid connection @ $t = 5.2$ s, 20 kW synchronverter step + PV mode enabled @ $t = 8$ s.	116
121	Test 2: Fast Steady-State Load connection @ $t = 8$ s, for speeding up the simulation to HPP-Synchronverter's steady state conditions.	116
122	Test 2: starting for steady state a negative 6 kW is applied @ $t = 25$ s and a positive 6 kW is applied @ $t = 55$ s.	117
123	Test 2: state of charge, DC-link voltage and synchronverter voltage during a 6 kW steps.	117
124	Test 3: negative 9 kW step @ $t = 30$ s.	118
125	Test 3: State of charge and DC-link voltage during the negative 9 kW step.	118
126	Test 4: positive 9 kW ramp @ $t = 25$ s, 0.36 kW/s load change ends @ $t = 50$ s. . . .	119
127	Test 4: State of charge and DC-link voltage during the 9 kW ramp.	119
128	Test 5: three-phase fault @ $t = 25$ s, time of clearing of 0.1 s.	120
129	Test 5: State of charge, inverter current and photovoltaic power during the three-phase fault.	120
130	Elimination of the conflicting algebraic loop in the self-synchronized synchronverter model.	121

131	OpalRT Test $25\mu\text{s}$: Synchronization @ $t = 5$ s, grid connection @ $t = 5.2$ s, synchronverter 20 kW power step @ $t = 8$ s, negative 9 kW load step @ $t = 85$ s, positive 9 kW ramp (0.36 kW/s) @ $t = 135$ s.	121
132	OpalRT Test ($T_S = 2.5\mu\text{s}$): a) synchronization and grid connection with OpalRT; b) synchronization and grid connection with Simulink.	122
133	OpalRT Test ($T_S = 25\mu\text{s}$) : real-time synchronization and grid connection with OpalRT.	123
134	OpalRT Test ($T_S = 25\mu\text{s}$): a) harmonic distortion on i_s ; b) harmonic distortion on V_g .123	
135	OpalRT Test: a) PV mode power sharing with with $T_S = 2.5\mu\text{s}$; b) PV mode power sharing with with $T_S = 25\mu\text{s}$;	124
136	OpalRT Test: a) negative 9 kW step @ $t = 85$ s with $T_S = 2.5\mu\text{s}$; b) negative 9 kW step @ $t = 85$ s with $T_S = 25\mu\text{s}$;	125
137	OpalRT Test: a) positive 9 kW ramp @ $t = 135$ s with $T_S = 2.5\mu\text{s}$; b) positive 9 kW ramp @ $t = 135$ s with $T_S = 25\mu\text{s}$;	126
138	Monitoring of the computation time and step size in tests with $T_S = 25\mu\text{s}$	127

List of Tables

1	Classification of emulation control techniques for virtual inertia applications [3], [12].	28
2	Classification and quantification of inertia for different generation sources [56].	79
3	Computation of a feasible T_W value for the HTG model and turbine specific speed/head classification [58].	80
4	Computation of the HTG PID parameters.	80
5	Computation of the HTG PID parameters.	92
6	Operation modes of the self-synchronized synchronverter [5]	99
7	Parameters for the Self-Synchronized Synchronverter.	104
8	Parameters for the LCL filter and the virtual impedance.	105
9	PI line and transformer parameters used in the simulation.	106
10	Microgrid main blocks parameters.	114

List of Symbols

Symbol	Unit of Measure	Description
J	$Kg \cdot m^2$	Inertia
r	m	Radius
m	Kg	Mass
$\omega(\omega^*, \omega_0)$	rad/s	Rated angular frequency
W_{KE}	J	Kinetic energy
f	Hz	Frequency (general)
f_0	Hz	System reference frequency (50 Hz)
P_m	W	Mechanical power
P_e	W	Electrical power
T_a	s	Starting time constant of generators
S_B	VA	Nominal system power
H	s	Inertia constant
P_{SG}	W	Mechanical power share referred to synchronous generators
P_{NSG}	W	Mechanical power share referred to non-synchronous generators
P_{LD}	W	Electrical power share referred to load demand
P_J	W	Electrical power share referred to Joule losses
ΔP	W	Power variation
Δf	Hz	Frequency variation
df/dt	Hz/s	Rate of Change of Frequency (RoCoF)
f_{COI}	Hz	Center of Inertia
ω'	rad/s	Estimated angular frequency
$\Delta\omega'$	rad/s	Estimated angular frequency variation
ϵ	-	Closed loop error
V_{abc}	V	Three-phase voltage (abc axis)
V_{dq}	V	Voltage (dq axis)
C_{DC}	F	DC-link capacitor
V_{DC}	V	DC-link voltage
K_d	-	Damping factor
i_{ref}	A	Reference current
ω_r	rad/s	Induction machine rotor speed
ω_{slip}	rad/s	Induction machine slip speed
λ_{dqs}	$V \cdot s$	Induction machine stator flux
λ_r	$V \cdot s$	Induction machine rotor flux
R_r	Ω	Rotor resistance
L_m	H	Magnetization inductance
L_r	H	Rotor inductance
Δ_{SOC}	Hz	Frequency variation
K_{SOC}	-	Droop factor
m_p	$\frac{rad/s}{W}$	Active power droop factor
m_q	$\frac{rad/s}{Var}$	Reactive power droop factor

Symbol	Unit of Measure	Description
K_P	-	Proportional gain
K_I	-	Integral gain
K_D	-	Derivative gain
E_{FW}	J	Flywheel kinetic energy
R	-	Speed governor droop
v_1	V	Simulated voltage (PHIL)
v_2	V	Physical voltage (PHIL)
i_1	A	Simulated current (PHIL)
i_2	A	Physical current (PHIL)
v_s	V	Voltage source (PHIL)
z_s	Ω	Source impedance (PHIL)
z_L	Ω	Load impedance (PHIL)
G_{OL}	-	Open-loop function (PHIL)
T_{11-22}	Ω	Impedance matrix (PHIL)
T_{filter}	-	Filter transfer function (PHIL)
T_{Amp}	-	Power amplifier transfer function (PHIL)
T_d	s	Delay time (PHIL)
Z_{HUT}	Ω	HUT impedance (PHIL)
Z_{ROS}	Ω	ROS impedance (PHIL)
v_1	V	Simulated voltage (PHIL)
v_2	V	Physical voltage (PHIL)
Z_{lk}	Ω	Transmission line impedance (PHIL)
Z_{ab}	Ω	Linking impedance (PHIL)
Z_{damp}	Ω	Damping impedance (PHIL)

Hydraulic Turbine and Governor Parameters

Symbol	Unit of Measure	Description
$\bar{q}(Q)$	m^3/s	Hydraulic flow rate
$\bar{h}_0(h_0)$	$m(pu)$	Static head of water
$\bar{h}(h)$	$m(pu)$	Head of turbine admission
$\bar{h}_l(h_l)$	$m(pu)$	Friction head loss
g	m^2/s	Gravity acceleration
L	m	Penstock length
A	m^2	Penstock cross-section
T_W	s	Water starting time
T_M	s	Mechanical starting time
G	-	Penstock gate opening
A_t	-	Turbine gain
q_{nl}	m^3/s	No-load flow
D_T	-	Gate damping factor
g_{nl}	-	Gate no-load opening
g_{fl}	-	Gate full-load opening

Hydraulic Turbine and Governor Parameters		
Symbol	Unit of Measure	Description
K_{CR}	-	Critical proportional gain
P_{CR}	s	Critical oscillation period
ρ	Kg/m^3	Water density
H	m	Water net head
η_T	-	Turbine efficiency
n	rpm	Turbine speed
n_C	rpm	Specific turbine speed
d	m	Penstock diameter

DC Source Model Parameters		
Symbol	Unit of Measure	Description
P_{PV}	W	Photovoltaic power
V_{PV}	V	Photovoltaic array voltage
I_{PV}	A	Photovoltaic array current
$\Delta V(dv)$	V	Voltage variation
$P(k)$	W	Measured power
$P(k-1)$	W	Previous step measured power
$V(k)$	V	Measured voltage
$V(k-1)$	V	Previous step measured voltage
D	-	Duty cycle
f_{sw}	Hz	Converter switching frequency
L_{boost}	H	Boost converter inductance
V_{in}	V	Converter input voltage
V_{out}	V	Converter output voltage
I_{in}	A	Converter input current
I_{out}	A	Converter output current
ΔI	%	Current ripple
ΔV	%	Voltage ripple
$SOC\%$	%	Battery State of Charge
I_B	A	Battery current
V_{bus}	V	Point of Common Coupling (PCC) voltage
V_{ref}	V	PCC reference voltage
C_{bus}	F	PCC capacitor

Self-Synchronized Synchronverter Parameters		
Symbol	Unit of Measure	Description
T_S	s	Simulation discrete step time
θ	rad	VSG phase angle
θ_g	rad	Grid phase angle
δ	rad	Power angle
T_e	Nm	Electromechanical torque
P	W	Active power
Q	Var	Reactive power
e	V	Internal voltage
M_{fi}	$V \cdot s$	Synchronous generator excitation
θ	rad	Rotor position
$\dot{\theta}$	rad/s	Rotor speed
ω_{VI}	rad/s	Virtual generator angular speed
$i_{S,abc}$	A	Stator current (or virtual current during synchronization)
R_v	Ω	Virtual resistance
L_v	H	Virtual inductance
$1/s$	-	Integrator
D_P	$J \cdot s$	Active power droop coefficient
D_Q	A	Reactive power droop coefficient
R_S	Ω	Stator resistance (LCL filter)
L_S	H	Stator inductance (LCL filter)
R_g	Ω	Grid-side resistance (LCL filter)
L_g	H	Grid-side inductance (LCL filter)
C_f	F	Parallel capacitance (LCL filter)
V_g	V	Grid voltage
V_m	V	Measured grid current
τ_f	s	Frequency loop time constant
τ_v	s	Voltage loop time constant
K	-	Voltage loop gain
P_{vsg}	W	VSG active power
Q_{vsg}	Var	VSG reactive power
P^*	W	VSG active power reference
Q^*	Var	VSG reactive power reference
P_{meas}	W	VSG measured active power
THD	$\%$	Total Harmonic Distortion
$vsg - ref$	Hz	VSG internal frequency reference

List of Acronyms

The acronyms used in the text have been regrouped for type of topic in the following tables.

Power System Related Acronyms	Description
RES	Renewable Energy Resources
DC/AC	Direct Current/Alternate Current
COI	Center of Inertia
RoCoF	Rate of Change of Frequency
SG	Synchronous Generator
TSO	Transmission System Operator
DER	Distributed Energy Resources
DG	Distributed Generation
CIG	Converter Interfaced Generator
HPP	Hydroelectric Power Plant
WPP	Wind Power Plant
PV	Photovoltaic Source
PV node	Power-Voltage Controlled Generator
PQ node	Active-Reactive Power Controlled Generator
PCC	Point of Common Coupling

General Control Related Acronyms	Description
PLL	Phase Locked Loop
PD	Phase Detector
VCO	Voltage Controlled Oscillator
PWM	Pulse Width Modulation
EMF	Electromotive Force
MPPT	Maximum Power Point Tracking
SPM	Superficial Permanent Magnet machine
PMSM	Permanent magnet Synchronous Machine
VVS	Variable Voltage Source
D1-D2	Dynamometers
VSP	Variable Speed Drive
AVR	Automatic Voltage Regulator
PID	Proportional Integral Derivative controller
HTG	Hydraulic Turbine and Governor

Virtual Inertia Related Acronyms	Description
VSG	Virtual Synchronous Generator
SI	Synthetic Inertia
VISMA	Virtual Synchronous Machine
IEPE	Institute of Electrical Power Engineering
SCP	Synchronous Power Controller

Storage Systems Related Acronyms	Description
ESS	Energy Storage System
BESS	Battery Energy Storage System
FESS	Flywheel Energy Storage System
VSC	Voltage Source Converter
SC	Synchronous Condenser
PHES	Pumped Hydroelectric Energy Storage
CAES	Compressed Air Energy Storage
TLC	Thermostatic Regulated Loads

Real-time Simulation Acronyms	Description
PHIL	Power-hardware-in-the-loop
CHIL	Control Hardware-in-the-loop
RT(D)S	Real Time (Digital) Simulator
HUT/DUT	Hardware/Device Under Test
ROS	Rest of the System
EMT	ElectroMagnetic Transient
IA	Interface Algorithm
OL	Open Loop
A/D - D/A	Analog/Digital Interface
ITM	Ideal transformer Method
TLM	Trasmission Line Method
PCD	Partial Circuit Duplication
DIM	Damping Impedance Method
PC	Personal Computer
SM	Master Subsystem
SC	Console Subsystem
SS	Slave Subsystem

1 Introduction

In the last decades the application of *Renewable Energy Sources* (RES) in the power generation activities has substantially increased. Starting from the first large applications of hydroelectric generation at the beginning of the *20th* century [1], a progressive awareness of the limited availability of fossil fuels and of their negative impact on the environment led to a progressive investment in new renewable sources, as wind and solar energy. The large-scale diffusion of RES began to be effective in the 1980s [1], limited only by the technical and economic barriers of those times. Nowadays, with the advancing of technology in sustainability of costs, availability and reliability, the RES have reached an high level of penetration in the power system, in order to satisfy a raising global demand of power and more strict rules of environmental protection. The growth of the RES quote on the grid, alongside or in substitution of the traditional power plants (based on a turbine-generator coupling shown in *Fig.1*), introduced the new conception of *Low-inertia Power System*.

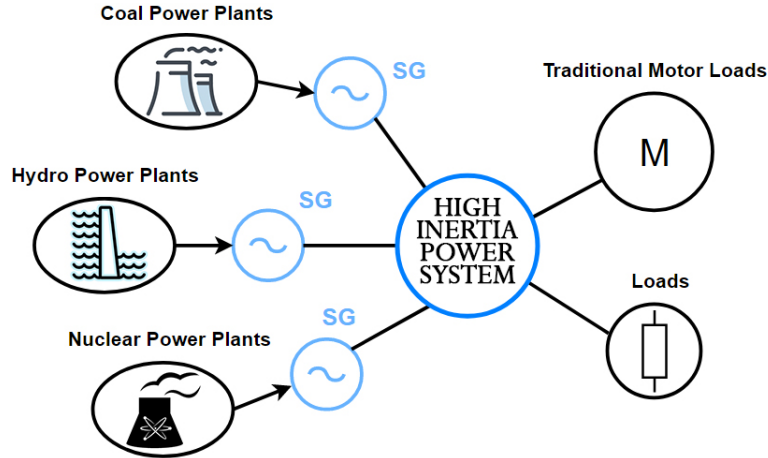


Fig. 1: Traditional power system characterized by high inertia, provided by the rotating parts of Synchronous Generators. The main source of generation is provided by fossil fuel, nuclear and hydroelectric plants.

A Low-inertia Power System is an electrical system of interconnected power generators in which the global inertia, inherently provided to the system via the rotating parts of synchronous generators, is reduced consistently introducing “static” RES generation [2].

Inertia is a useful mechanism to front supply/demand imbalances or contingency events, making available a reserve of kinetic energy that can be instantaneously converted into electrical power. Inertia guarantees to grid operators a time window to respond with an adequate action (with power/frequency controls) to maintain the system stability and align the mechanical power production of plants to the electrical power requested. However, RES are connected to the grid by means of power converters: this solution is necessary to adapt the frequencies of the produced energy to the reference value of the power system (theoretically known as Center Of Inertia).

The main inconvenient of power converters is the absence of an inertial response. A Low-inertia Power System is characterized by an high penetration of RES, that leads to a reduction of the global power system’s inertia, which in order increases the Rate of Change of Frequency (RoCoF) of the system while facing load unbalances [2], [3]. An example of low inertia power system layout is showed in *Fig.2*.

A greater deviation of the frequency in a short period of time is a threat to the frequency stability of the power system, as RoCoF protection relays might trip, isolating some generators and increasing the difference between supply and demand.

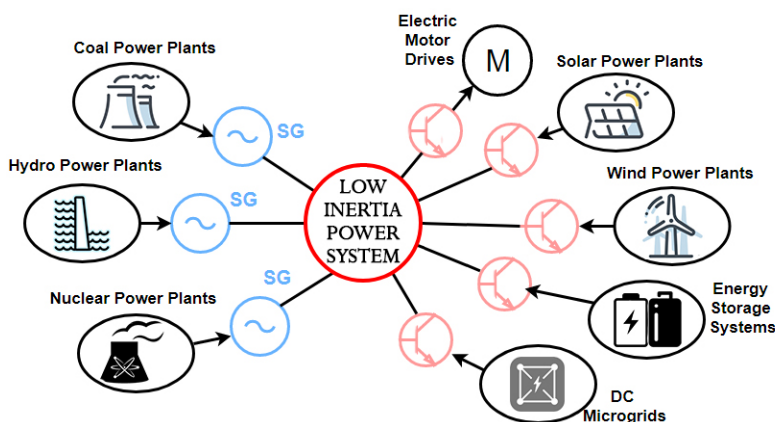


Fig. 2: Low-inertia power system characterized by high RES penetration, that reduces inertia in respect to the installed generation power. The main source of generation is provided by fossil fuel, nuclear and hydroelectric plants.

The arise of aforesaid problems requires new solutions to properly control the frequency stability of low-inertia power systems. The necessity of new ways to create additional inertia in the system is also important to make possible the global energy transformation, that will lead grids all over the world to an even greater penetration of RES. Major investments in low-carbon power sources, alongside increasing energy efficiency, are considered the main strategy to reach the target goal [4] of limiting the rise of global temperature below $2^{\circ}C$.

Estimations made by the *International Renewable Energy Agency (IRENA)* states that, on a roadmap up to 2050, the employment of electricity as main energy carrier will increase from actual 20 % up to 50 % of final consumption, as shown in *Fig.3*. Power systems will acquire more and more importance and, to face global climate changes and the reduction of CO_2 emissions, renewable sources will become the primary energy supply, covering the two-thirds of total production.

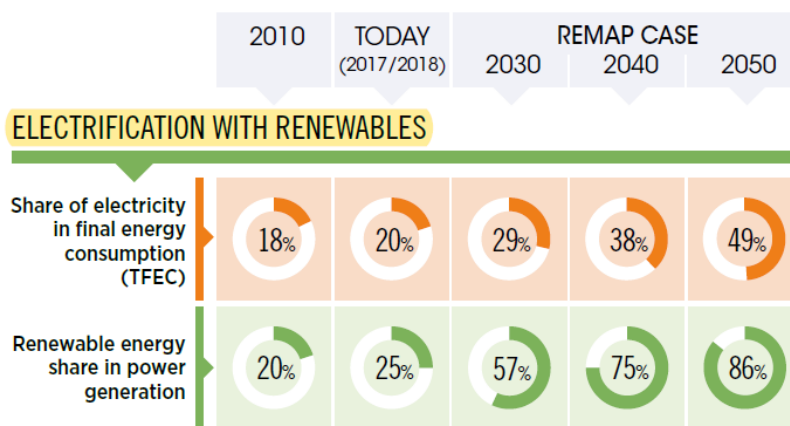


Fig. 3: A roadmap of global electrification with renewables up to 2050 (IRENA) [4].

The objective of this master thesis is to study the effects of low inertia conditions on power systems and to implement, in a simulated environment, the application of one of the many virtual inertia solutions proposed in the literature.

The first part of the work is focused on the description of low inertia power system behaviour, presenting the relevant equations and concepts that describe inertia and frequency on the grid (**section 2**). A wide panoramic of solutions to improve low inertia power systems is then presented in **section 3**, introducing the concept of virtual/synthetic inertia. Virtual inertia can be implemented in a system by controlling power converters to behave in an equivalent way to normal rotating generators on the grid, providing an inertial response to frequency variations. The work presents a literature research for both a set of virtual inertia emulation techniques (virtual synchronous machines) based on different machine models applied to power converters (**3.2**), and a set of storage technologies aimed at enhancing inertia accumulation in the system (**3.3**). The Power-Hardware-in-the-Loop (PHIL) concept is also introduced with all its characteristics and methodologies in **section 4**, to provide relevant informations about performing real-time emulations of parts of the grid with interconnected real components. Real-time simulations are used to perform studies on low inertia power systems and for developing and testing components for virtual inertia applications in a secure off-grid environment. Multiple examples from the literature are presented to provide an overview of PHIL applications in the field.



Fig. 4: References and tools.

The second part of the thesis work is focused on the development of a functioning model of a standalone microgrid, in order to represent a situation with inherent low inertia. A fully functional model of an hydroelectric power plant was made, based on the specifications of a real 60 kVA synchronous generator located at the *Energy Center* in Turin (**6.2**). The hydro plant model represents the behaviour of synchronous machine connected to an hydraulic turbine governor, that simulates the effects of the penstock on the mechanical power regulation of the plant. An additional renewable power source was added with a photovoltaic power plant and a storage battery, to introduce a power converter with inertial reserve in the microgrid (**7.1**). The model is used to study the frequency behaviour of the microgrid, with and without the presence of renewable resources, and implements a virtual synchronous generator algorithm to control the power converter as a synchronous generator (**7.2**). The virtual synchronous machine is based on the *Self-Synchronized Synchronverter* algorithm, presented in the literature [5]. The full model was developed first in the *MatLab/Simulink* environment and was successively implemented in *RT-Lab*, the reference platform of *Opal RT* for real-time simulation. The model is tested in both environments with the intent to create a fully functioning model suitable for future PHIL tests in the Energy Center laboratory, where parts of the model will be substituted by real hardware, such as the synchronous generator or the photovoltaic plant.

2 Characteristics of a Low-Inertia Power System

A Low-Inertia Power System is characterized by a different response to load shifts or contingency events in respect to a more traditional power system. This section addresses the most important parameters and measures applied to evaluate the functioning and stability of a power system.

2.1 Inertia in a power system

A traditional power system is fed by plants that use fossil fuels, nuclear energy or hydic resources. The typical layout is focused on setting into motion a turbine, which is connected to a synchronous generator (SG) to convert mechanical power into electric energy. Each SG connected to the grid provides a share of inertia J , which is related to the radius r [m] and the weight m [kg] of the rotating parts:

$$J = \int r^2 dm \quad [\text{Kg m}^2] \quad (1)$$

Inertia is directly related to the kinetic energy W_{KE} , which is a relevant way to store energy in the system (at speed ω), as on the grid the electric energy can only transit:

$$W_{KE} = \frac{1}{2} J \omega^2 \quad [\text{J}] \quad (2)$$

This fundamental SG feature allows to maintain the synchronism of the grid and, most importantly, is used alongside the power system operator's actions to prevent the grid from collapsing under load/generation unbalances. This function is made possible by the direct correlation between the variation of the average system frequency f and the inertia in the system, as shown in the *mechanical/swing equation* of the SG [6]:

$$\frac{d}{dt} \left(\frac{1}{2} J \omega^2 \right) = M \frac{df}{dt} = P_m - P_e \quad (3)$$

where the frequency variation is directly related to the difference between the mechanical power P_m and the electrical power P_e . M represents the total inertia of the synchronous machines, expressed as function of their total nominal power S_B , the system frequency reference f_0 and the starting time constant T_a , necessary to SGs to accelerate to their nominal speed:

$$M = \frac{T_a S_B}{f_0} \quad (4)$$

Another common metric to describe the system's inertia is the *Inertia Constant* H , defined as the amount of time in seconds in which the system can feed its nominal power S_B to loads using only the kinetic energy stored in SGs rotating parts:

$$H = \frac{1}{2} \left(\frac{J \omega^2 [\text{J}]}{S_B [\text{W}]} \right) = \frac{W_{KE}}{S_B} \quad [\text{s}] \quad (5)$$

The constant H is obtained as weighted sum of single SG kinetic energies referred to the global apparent power of the system. Typical values goes from 3 to 5 seconds.

The system kinetic energy is subjected to variation when the requested electric power P_e changes, assuming constant the mechanical power P_m generated by power plants. The variation is detected in the angular rotor speed ω , proportional to the frequency f through the constant 2π . An increment of electric load power correspond to a negative variation of speed, and therefore of frequency:

$$P_{e,L} > 0 \rightarrow \frac{df}{dt} < 0 \rightarrow P_{GEN} > 0 \quad (6)$$

The power supplied by generators is increased to pair the demand and, before a proper regulation by means of *Primary and Secondary Controls*, the inertia is temporarily employed to instantly feed the requested power and maintain the stability of the grid [7], as showed in *Fig.5*.

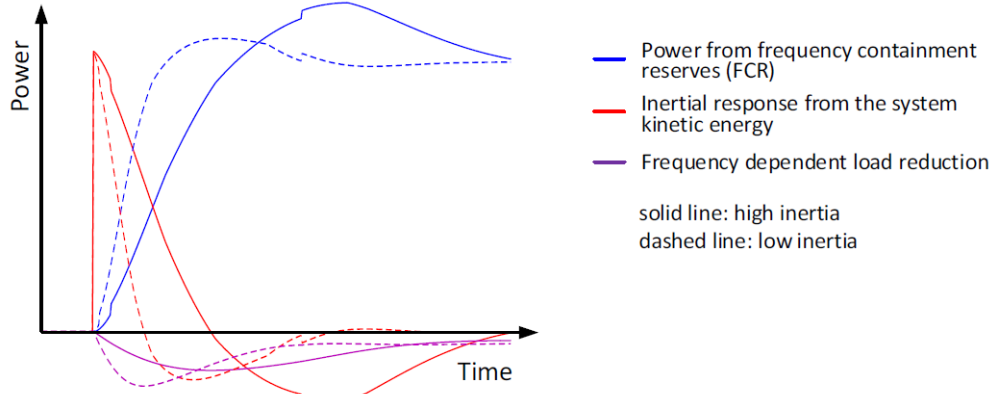


Fig. 5: Power responses after a contingency event: instantaneous inertia response is followed by Primary Control response, consisting in frequency containment reserves (FCR) and frequency dependent loads response (Rotating Loads) [8].

The introduction of RES in the power system can be described in the mechanical/swing equation [2] as

$$M \frac{df}{dt} = P_m - P_e = (P_{SG} + P_{NSG}) - (P_{LD} - P_J) \quad (7)$$

where the power generation is represented by both synchronous and non-synchronous generators (P_{SG} and P_{NSG}), while the electric power is the combination of load demand P_{LD} and power losses P_J . The non-synchronous quote P_{NSG} represents both converter-based generators, that can be used for voltage/frequency control, and other generators non suitable for control.

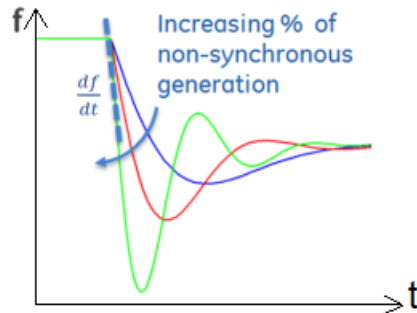


Fig. 6: Impact of increasing RES penetration on the frequency profile after a contingency event [9].

The main impact of RES in eq. (7) is on the inertia M , which is reduced if compared to a fully traditional system: the mechanical power quote is increased with non-synchronous generators, while inertia remains related only to the SGs quote. This occurrence leads to higher frequency fluctuations in the first instants while facing a power unbalance, as shown in *Fig.6*.

An hypothetical system operated only by means of non-synchronous generators would be than characterized by a *complete decoupling between frequency and the system power balance*, as the inertia would be approximately null:

$$M \approx 0 \rightarrow 0 = (P_{NSG}) - (P_{LD} - P_J) \quad (8)$$

In this case the power system can't autonomously respond to power variations and a proper control should be set to maintain the balance and stability in every instant. This behaviour would be currently unrealistic for large power system, where the RES penetration is far from *100%* and will require many years to increase to similar values. This scenario might happen for short instants in little systems working in island mode, or if the non-synchronous generation reaches an instantaneous penetration far superior to synchronous generation, as consequence of temporarily high production of energy by wind or solar power.

2.2 Impact of low inertia on the power system frequency

Frequency is the main signal used to regulate the power balance in a power system, as its fluctuations can be a threat for the power quality of the electrical service. The impact of low inertia in a power system is disclosed during contingency events, such as load shifts and faults on the grid. The reduced capacity of the power system to quickly compensate power variations with inertia leads to an increased *Rate of Change of Frequency (RoCoF)*: the frequency is subjected to higher deviations and stability problems may arise in the power system. The RoCoF is an indicator that represents how fast the frequency changes over time after a sudden unbalance between load and generation:

$$RoCoF = \frac{df}{dt} = \frac{(P_m - P_{e,L})f_0}{2S_B H} = \frac{\Delta P f_0}{2S_B H} \quad [\text{Hz/s}] \quad (9)$$

The relation is obtained from eq. (3), considering the kinetic energy as function of eq. (6). It can be observed that a small value of H , symptom of a low inertia, is translated in an higher RoCoF value and more rapid changes of frequency will occur in the same time span (*Fig.7-a*). The highest RoCoF value is detected right after the disconnection of a load or generator from a power system, when active frequency control is not yet available.

In order to maintain frequency in an adequate range of values (typically $\pm 0.5 \div 1$ Hz around the nominal value), RoCoF protection relays are used to prevent exceeding variations and disconnect from the grid local generators to avoid islanding or capability problems on SGs. A severe RoCoF is dangerous to the system, because it can lead to a substantial loss of generators (due to protection relay trips) before the Primary Control of frequency can intervene. RoCoF *ride-through requirements* have been modified in many grid codes over the years, to mitigate undesired disconnection and to favour RES penetration targets. The relaxation of RoCoF limits allowed to accept worst frequency deviations during power unbalances, while still maintaining generators connected to the grid (*Fig.7-b*).

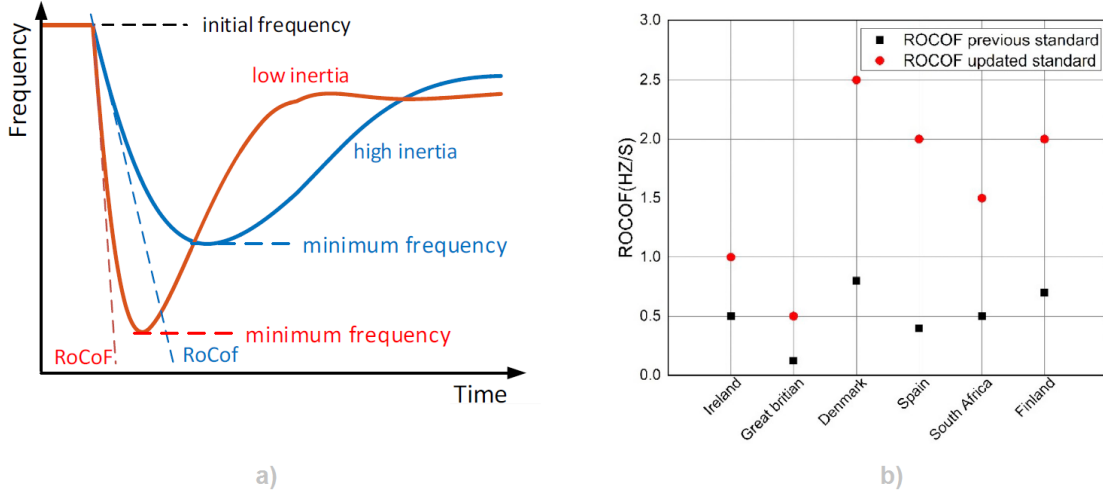


Fig. 7: a) Comparison of frequency response after a contingency event with high and low system inertia [5]; b) RoCoF standards for protection relays for countries with high RES penetration [4].

Frequency is normally considered as a single quantity, equally distributed in every point of the grid. This approximation is used to study frequency regulation, but in reality the signal differs for every generator. An average value, called *Center Of Inertia* (COI), is computed as weighted sum of frequencies in regard to the inertia quote of every N generator that participate to primary control:

$$f_{COI} = \frac{\sum_{k=1}^N M_K f_K}{\sum_{k=1}^N M_k} = \frac{\sum_{k=1}^N M_K f_K}{M_{TOT}} \quad [\text{Hz}] \quad (10)$$

The parameter is useful in simulations, but has not practical application, because it is not possible to know the measurement of every SG rotor speed. Grid operators typically measures frequency in specific relevant points of the power system, rather than estimate it using COI: this procedure is not representative of the average frequency and is tied to the closest generator's behaviour.

2.3 Time scale of Power/Frequency control

The stability of the power system is maintained by a series of actions taken by *Transmission System Operators* (TSOs) to restore the average frequency value in the allowed range (referred to the nominal value of 50-60 Hz) and align power production to power consumption. It is possible to define a time scale of frequency control, to establish the evolution of control after a contingency event.

The first contribution to balance the power fluctuation is given by the inertia response of synchronous machines, as shown in *Fig.8*. SGs reduce their speed and kinetic energy for a mean time of 5 s to compensate the load demand. The regulation of frequency and active power is then performed by a group of generators, in regard to their size, using a bandwidth of reserve of power (typically $\pm 1.5 \div 10\% P_{MAX}$) and a droop strategy (b_P). *Primary Control* adjusts the production level of P_m of both synchronous and non-synchronous generators (20 ÷ 30 s to a steady state of frequency). *Secondary Control* restores primary power reserves and returns the system to nominal average frequency (10 ÷ 15 min), correcting the residual frequency error left by Primary Control.

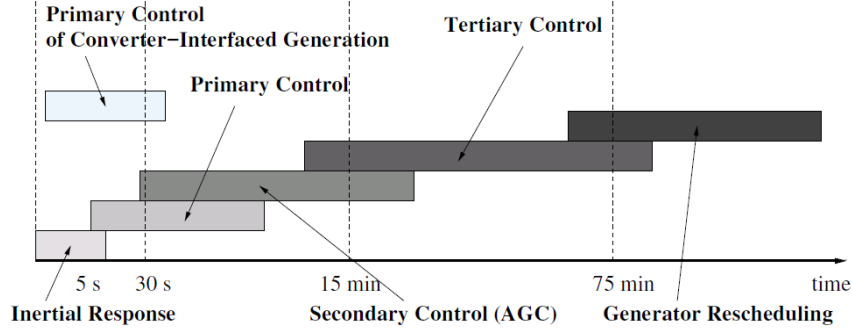


Fig. 8: Time frame for inertia response and power/frequency controls application [2].

Tertiary Control and generator rescheduling follows in the next hours. It is important to underline that inertia is fundamental to contain the dynamic behaviour of the system in the first instants. All the other levels of regulation are independent from inertia and can be performed if a sufficient reserve of power is available for the task (*Fig.9-a*).

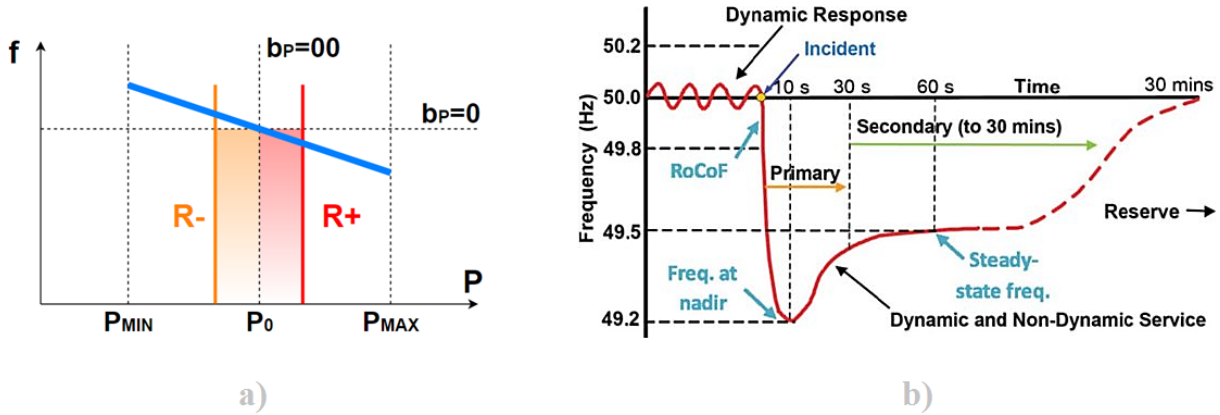


Fig. 9: a) a positive/negative reserve of power is maintained for Primary Control Generators, around their reference working point P_0 , to actively participate to power regulation [6]. b) Evolution of frequency after a contingency event [10].

In a traditional power system the high inertia is the only physical storage of energy available to compensate the power unbalance, before the relatively “slow” *Primary Frequency Control* can be performed by SGs. RES generators are different, because of their grid interface by means of power converters: in this case energy can be stored in equipped DC batteries. Batteries are not comparable to the inertia of the system in terms of energy stored, but allow a faster *Primary Control* using converters. The combination of SGs and RES generators partially compensate a low inertia status of the power system, with two main limitations:

- power converters lack a “natural” response to contingency, leaving the covering of the first instants of frequency deviation to regular SGs.
- the energy provided by converters to primary control is limited and an adequate reserve is not guaranteed, as most of RES generation is stochastic.

A system with low inertia is hence less secure and requires additional precautions, both for SGs and non-synchronous generators, to operate in stability conditions.

2.4 Metrics and measures for Low-Inertia Power Systems

An important matter to establish while operating a low-inertia power system is the *Critical RES Penetration Limit*, that represents the instantaneous RES limit above which frequency would exceed its normative limits in case of a contingency event. Such metric is hard to define, as the power system is dynamic and more than one value might be obtained in different times. Nonetheless it would be useful to quantify an adequate percentage of RES, introduced on the grid, to safely operate the system.

The RES generation has largely grown in the past decades, as many countries have set higher renewable targets and have invested into better exploitation of renewable resources. Independent grid operators have adopted different measures to deal with arising problems in system stability, creating standard metrics.

2.4.1 Synchronous Inertial Response Factor

The necessity of inertia response in power systems has led some operators to require an additional service, disposing some generators to improve the maximum inertia in the system. The *Synchronous Inertial Response Factor* (SIRF) is defined as the kinetic energy to the minimum active power output of SG units:

$$SIRF = \frac{W_K}{P_{min}} \quad (11)$$

The factor is used to determine the stability and strength of a system, with acceptable values included in a range from 15 to 45 s. If the inertia response service is available for the minimum overall power in the system it is possible to introduce more RES.

2.4.2 EirGrid Metrics

The Irish operator *EirGrid* has defined a couple of metrics to monitor the functioning of an islanded power system with increasing RES penetration. The first metric, labelled *Operational metric 1* (*Fig.10-a*), is the ratio of the non-synchronous inertia-less generation active power to the instantaneous load:

$$OP_{METRIC1} = \frac{P_{NSG}}{P_L} \quad (12)$$

The metric increases only when the RES power share in the system increases, allowing to quickly monitor how inertia and system stability in turn decrease: when the metric exceed a specific value (80%) the frequency deviation is outside of bandwidth limits and RoCoF protections are enabled to protect generators. The second metric, *Operational Metric 2* (*Fig.10-b*), is the ratio of the available kinetic energy to the largest maximum active power in feed (P_{LiF}):

$$OP_{METRIC2} = \frac{W_K}{P_{LiF}} \quad (13)$$

The metric shows frequency instability: if the value is too low the kinetic energy is not enough to face power losses and RoCoF protection are enabled.

The two metrics are useful tools to study and properly limit the level of RES penetration in the system, in order to preserve a certain quantity of inertia from traditional SGs.

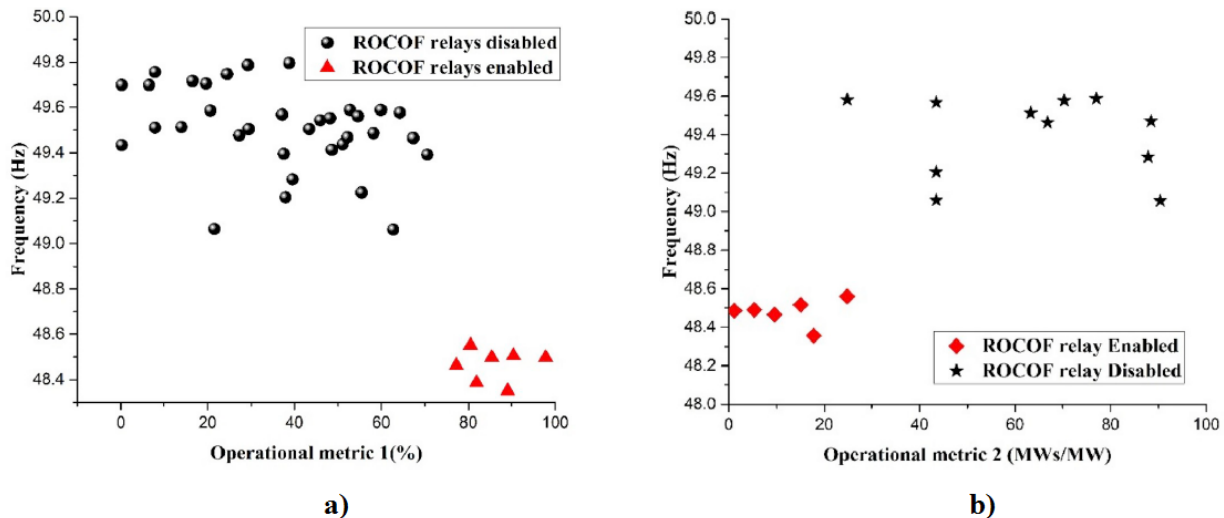


Fig. 10: a) Operational metric 1 shows the % of RES penetration for which frequency deviations are acceptable. b) Operational metric 2 shows when the kinetic energy is not sufficient to safely contain a contingency event [3].

2.4.3 Metric for inertia requirements analysis

The *Australian Market Operator* proposed two indicators to analyse the required inertia in the system, after increasing instability events due to RES.

- **Minimum threshold level of inertia:** amount of inertia necessary to operate an islanded grid in stable condition, with frequency deviation correctly limited after a contingency event.
- **Secure operating level of inertia:** amount of inertia available in the power system exceeding the minimum threshold level.

If an area of the power system is working at a secure operating level of inertia, part of the exceeding can be transferred to another area, reducing low-inertia related problems. The creation of synchronous storage systems, based on power plant in low load conditions or compressed air energy storages (CAES), can help to introduce an additional inertia reserve. Storage system technologies are discussed in more details in **section 3.3**.

3 State-of-the-art for Virtual Inertia implementations

As stated in previous chapters, RES hold nowadays a major share in power generation. The connection of these sources to the grid is made by means of power converters, which lead to the definition of RES as *Converter-Interfaced Generation* (CIG). CIG is not characterized by a natural dynamic response and interaction with the grid, which is typical of SGs, and requires a control approach to properly work in the power system. Three main approaches are commonly chosen [2], [11] for grid-connected converters.

- 1) The *Grid-feeding Mode* allows to use the CIG in synchronous state with the grid, by simply following the voltage and frequency imposed by other generators. In this configuration a power converter can provide a fixed amount of power without participating to power/frequency control. The unit can be represented as an ideal current source connected to the grid in parallel with an high impedance (*Fig.11-b*). The option is feasible only if there is a consistent share of traditional SGs generators in the power system.
- 2) The *Grid-forming Mode* is used to ‘form’ the power system by setting the power converter’s output voltage amplitude E^* and frequency ω^* in a specific point of the grid. The unit can be represented as an ideal AC voltage source with a low output impedance (*Fig.11-a*). In this case the objective is to simulate the functioning of a synchronous machine, both in inertia response and control mechanisms. This option is used to form the grid alongside SGs, and it’s a preferable solution in islanded micro-grids operations.

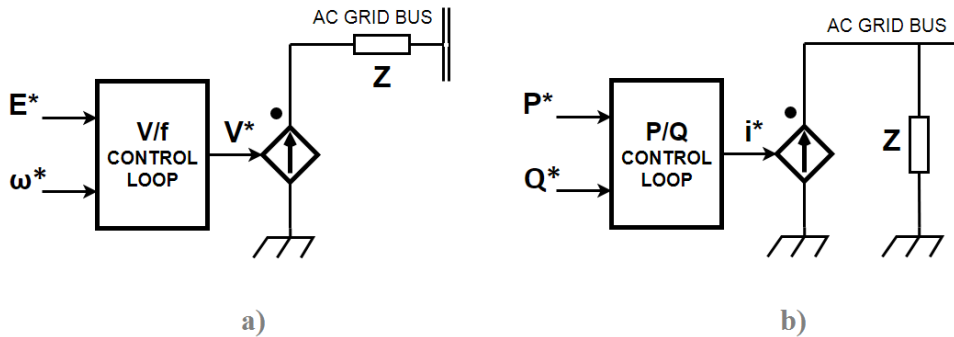


Fig. 11: General representation of grid-connected converters: a) Grid-forming; b) Grid-feeding; [11].

- 3) The *Grid-supporting Mode* is used as a compromise between the other two modes. The objective is to support the grid by feeding proper values of active and reactive power for grid voltage and frequency regulation. The unit can be represented both as an ideal voltage source (*Fig.12-a*) and as an ideal AC-controlled current source (*Fig.12-b*), depending on the control approach. The option is used to enhance the overall stability of a grid.

The grid-connected power converters are controlled in order to mimic the behaviour of synchronous machines from traditional power plants. The emulation of SGs is implemented to maintain or enhance the system stability, by both increasing the total inertia in the system and allowing more converter units to take part to power and frequency regulation. The various CIG control strategies developed in the literature for this specific purpose are addressed under the name of *Virtual Inertia* or *Synthetic Inertia*.

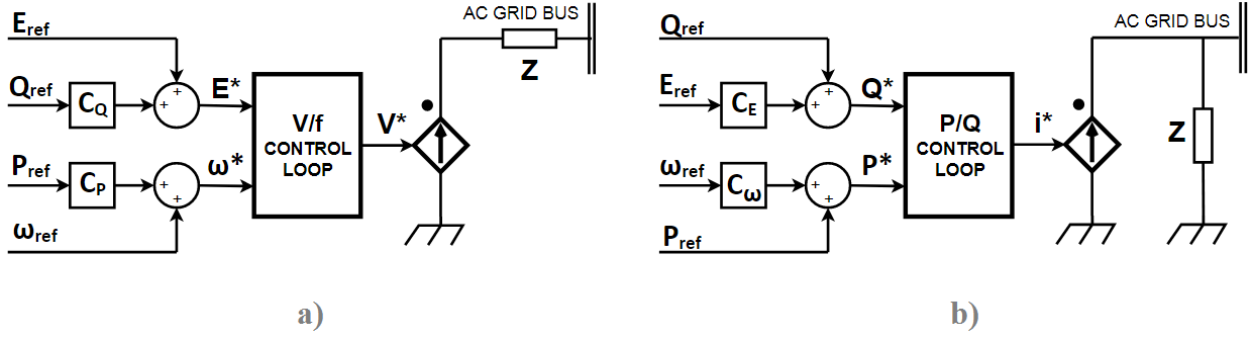


Fig. 12: General representation of grid-supporting converters: a) Voltage based; b) Current based; [11]

In large power systems the majority of CIGs are currently used in *Grid-following Mode*, which is a very efficient solution in terms of costs. The necessity to measure voltage and frequency reference values, set on the grid by other generators, is the main limitation of this strategy. A future low-inertia scenario implies that most of CIGs will be required to make a transition to *Grid-forming Mode* and *Grid-supporting Mode*, to provide synchronous reference and control to the power system and to increase RES penetration. In microgrids the RES penetration is already at high levels, making the system more sensitive to frequency instabilities compared to grid connected operations. Especially in islanded or isolated condition, the need of virtual inertia is of great importance to maintain an allowable range for RoCoF and frequency fluctuations (*Fig.13*).

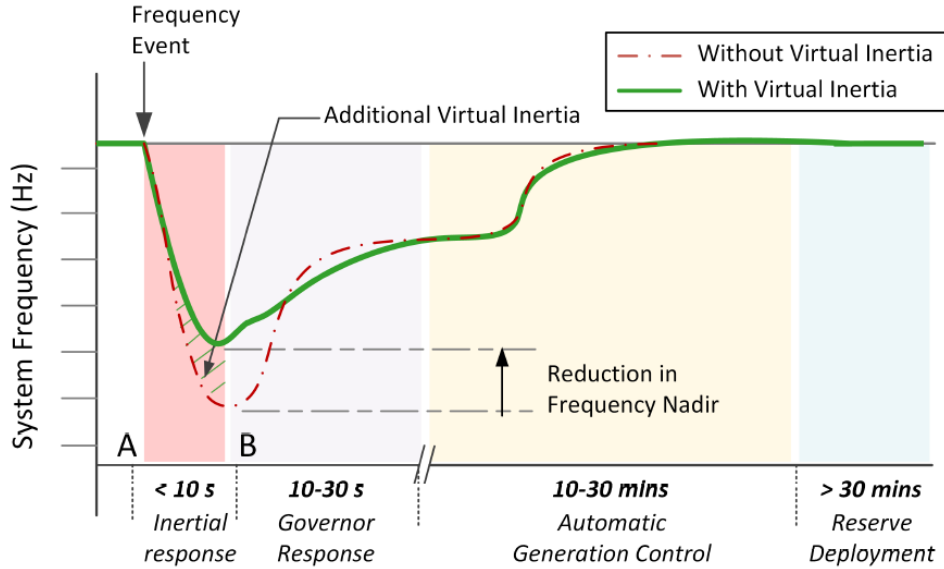


Fig. 13: Time-frame frequency response following a contingency event. The introduction of Virtual Inertia in the system allows to contain RoCoF and frequency deviations in the first instants of the event [12].

3.1 Synchronization of CIGs in the power system

The performances of CIGs are strongly dependent on their ability of synchronization and subsequent connection with the grid. A successful connection requires an accurate estimation of grid parameters, such as voltage amplitude, phase angle and frequency, that are unknown without using a proper synchronization unit.

Grid-connected converters require also an accurate monitoring of the grid, to perform the control of the constant active and reactive power injected in the point of connection (*Fig.14*), to actively participate to power/frequency regulation (in grid-forming and grid-supporting mode) and to determine the most suitable operation mode in case of sudden variation of grid parameters.

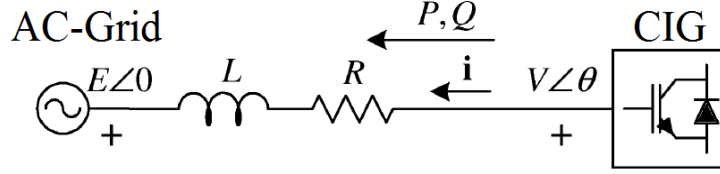


Fig. 14: Simplified layout of CIG connection to the AC-grid [13].

A widely adopted solution is the use of a *Phase Locked Loop* (PLL) as synchronization unit (*Fig.15*). The main function of the PLL is to estimate the grid's parameters and align the CIG voltage vector with the grid voltage vector [11]. When the two vectors are coincident it is possible to perform a smooth connection of the converter AC-side to the grid, without the risk of developing transients due to out-of-phase closings. The estimation of the grid's parameters is obtained with a *Phase Detector* (PD), by measuring the three-phase voltage V_{abc} in the point of connection with the grid. The voltage is converted in dq -axis frame using the estimated angular position θ' and the V_q component is computed. The error ϵ_q is obtained comparing the measured V_q with the esteemed \widehat{V}_q .

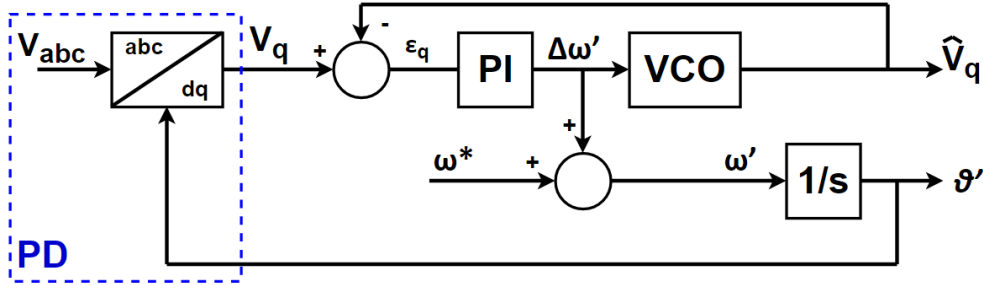


Fig. 15: PLL block diagram [2], [11].

The *PI* controller output is the bus frequency deviation $\Delta\omega'$, used to esteem the bus voltage \widehat{V}_q with a *Voltage Controlled Oscillator* (VCO). The VCO is typically a pure integrator, to avoid steady state errors and to impose the V_d component equal to zero. The estimated frequency ω' , required for synchronization, is obtained from the voltage control loop:

$$\omega' = \Delta\omega' + \omega^* \quad (14)$$

where ω^* is the grid rated frequency, used as feed-forward to improve the PLL's dynamic. The phase angle θ' is obtained by integrating ω' and is used to perform the abc/dq -axis transform. The PLL is a basic requirement for a grid-connected inverters, but presents an inherent harm to the synchronization stability because of the introduction of delays in the signal processing chain. If the unit delays is too large the whole CIG virtual SG dynamic behaviour could be affected, especially in weak grid where parameters are unbalanced or distorted.

3.2 Inertia emulation control techniques

The virtual inertia emulation is based on the combination of power converters, energy storages and an algorithm to represent CIGs as synchronous machines from the grid's point of view, as shown in *Fig.16*. The algorithm is commonly based on current/voltage feedbacks from the inverter output and implements an adequate control loop. The inertia emulation compensates the lack of kinetic energy in the system with short-term energy stored in DC-links capacitors or dedicated storage systems. The inertia constant can be written as [3]:

$$H_{VirtualInertia} = \frac{E_{DCstorage}}{S_B} = \frac{C_{DC}V_{DC}^2}{2S_B} \quad (15)$$

where C_{DC} is the bus capacitance and V_{DC} is the DC bus voltage. An inverter that emulates inertia by means of energy storages is addressed as *Virtual Synchronous Machine (VSG)*. A VSG must provide inertia for a short period of time ($< 10s$ as shown in *Fig.13*), to maintain the system's stability during the first instants after a contingency events.

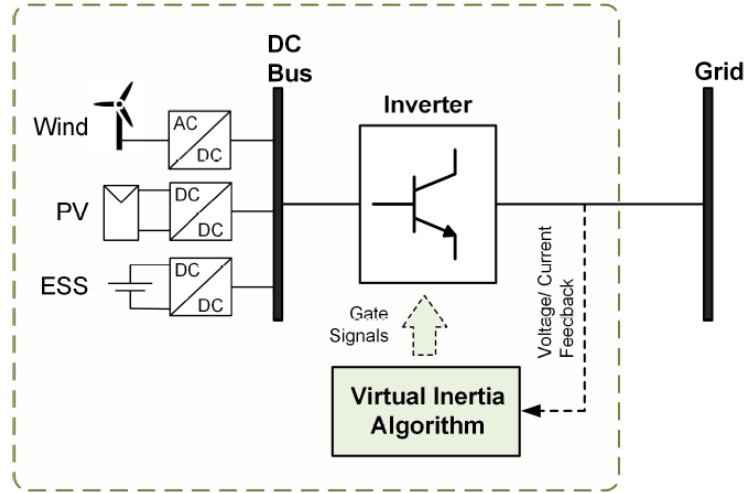


Fig. 16: Virtual Inertia Emulation. The main RES typologies are: wind turbines, with physical inertia completely decoupled from the grid by an AC/DC converter; Energy Storage System (ESS) and Photovoltaic plants (PV), with null inertia contributions and interfaced through DC/DC converters [12].

The inertia emulation can be realized by charging/discharging DC-link capacitors or using energy excesses from RES plants (accumulated by de-loading operations or storage devices). Emulated inertia presents some differences if compared to synchronous inertia:

- Emulated inertia employs dead bands: inverters are used only when frequency deviation is greater than a threshold value.
- The response time of virtual inertia depends from virtual parameters such as inertia J and drooping coefficient D_P and the control must be properly tuned to maintain stability.
- Power converters have strict current limits, to preserve components from thermal failure. During a post-contingency events current saturation is likely to occur, potentially excluding converters from virtual inertia control, in strong opposition to synchronous machines, that can be overloaded and can sustain a short-circuit current for brief period.

- The complexity of the control and the necessity to measure and process feedback parameters introduces time delays, limiting the otherwise fast response of inverters in the first instants of inertial response.

CIG limitations must be taken into account also for power/frequency regulation. A SG is deployed for Primary Control by controlling frequency and voltage respectively through mechanical power and field voltage (*Fig.17-a*). Otherwise, a power converter is controlled with *Pulse-Width Modulation* (PWM) in dq -axis frame: in this case the d -axis and q -axis are used to regulate the CIG AC voltage output, allowing primary voltage control, and the output current or DC voltage. To perform primary power/frequency control is necessary an additional regulation, that manages the CIG's DC energy storages for active power injection (*Fig.17-b*).

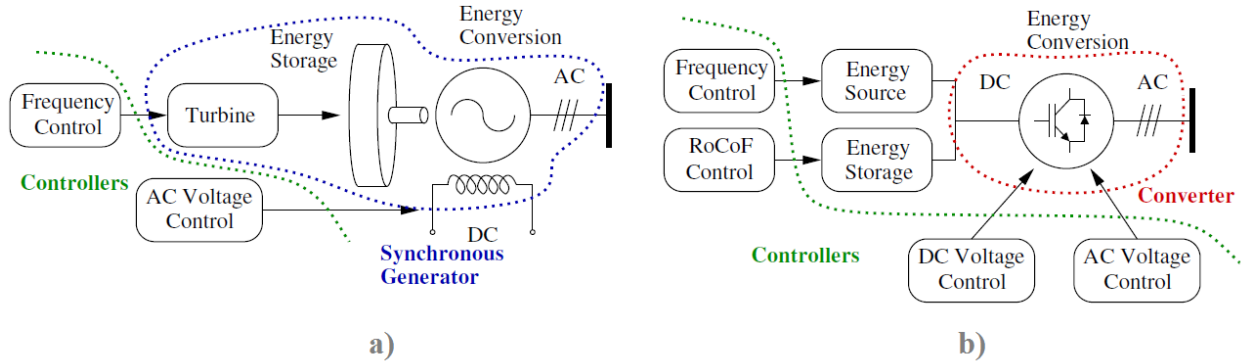


Fig. 17: Energy storages and controllers implemented for: a) Synchronous Generators; b) Converter-interfaced Generators [2].

Different inertia emulation techniques have been proposed in the literature, to widely cover different applications and levels of detail. Some typologies are based on detailed mathematical models (5^{th} or 7^{th} order models), to faithfully replicate the SG dynamics, while other approaches use the swing equation approximations (2^{th} order model) or frequency-power response algorithms. The main goal is to improve the inertia response of inverter-dominated power systems. An overview of the characteristics of the various techniques is presented in *Tab.1* and in the following sections.

Table 1: Classification of emulation control techniques for virtual inertia applications [3], [12].

VIRTUAL INERTIA EMULATION TECHNIQUES				
Synchronous Generator Model Based	Induction Machine Model Based	Swing Equation Based	Frequency-Power Response Based	Other
Virtual Synchronous Machines (VISMA)	Inductverters	Ise Lab's Topology	Virtual Synchronous Generators (VSG/VSYNC) Topology	Virtual Oscillator Control (VOC)
Institute of Electrical Power Engineering's Topology (IEPE)		Synchronous Power Controller (SCP)		Droop-Based Approach
Synchronverters				

The vector $i_{S,abc}$ represents the three-phase stator current and is obtained as feedback of the inverter current, alongside inverter voltage V_{abc} . The control is exploited as shown in *Fig.18*, and can be summarized in four fundamental blocks:

- **SG Dynamics Equations Block:** the SG differential equations (eq. (16) ÷ eq. (18)) are solved. T_e and Q are used as feedbacks for the voltage and frequency loops, while the generated voltage e is sent to the PWM block.
- **Frequency Drooping Loop Block:** the synchronverter's output active power is adjusted based on angular speed variations, simulating the frequency drooping mechanism of SGs with the swing equation in eq. (20). A reference mechanical torque T_m^* is generated from the reference active power P^* and confronted with T_e . An additional feedback T_m is added to simulate the frequency droop. The virtual inertia frequency ω_{VI} is obtained and confronted with the grid nominal frequency ω^* , in order to set a proper frequency control. ω_{VI} is integrated to obtain the phase of the signal θ , and both the information are sent to the *Dynamic Equation Block*.

$$\omega_{VI} = \frac{1}{J_S}(T_m - T_e - D_P \Delta\omega) \quad (20)$$

- **Voltage Drooping Loop Block:** the output reactive power is controlled by means of the machine excitation flux. A reference reactive power Q^* is set and confronted with generated Q . The difference between reference voltage amplitude V^* and measured voltage amplitude V_m is multiplied by a drooping voltage constant D_q and added to the reactive power error. An integrator $\frac{1}{k_S}$ is used to generate the excitation flux M_{fi_f} , sent to *SG Dynamic Equations Block*.
- **PWM Block:** outputs e and θ are used for pulse-width modulation, producing switching signals for the inverter.

The stability of operation requires an appropriate selection of inertia and drooping constants. The frequency and voltage drooping factors are defined as:

$$D_p = -\frac{\Delta T}{\Delta\omega} \quad D_q = -\frac{\Delta Q}{\Delta v} \quad (21)$$

The drooping constants introduce a built-in frequency-drooping control, that allows to automatically share the load variations with other SGs, grid-forming and grid-supporting inverters on the grid (with a load distribution weighted on the nominal power of every generator). The synchronverter topology is comparable to a PLL, making the system capable of maintaining synchronism with the grid during normal operation. The initial synchronization with the grid can be ensured by a second PLL, that might however introduce instability by adding more delays to the system, or by *self-synchronized* synchronverters. Another advantage of a synchronverter is the absence of the derivative term of frequency, not implemented by the SG model. Derivative terms often introduce noises in the system. The weaknesses of the synchronverter are the possible numerical instability, introduced by the necessity to resolve complex differential equations, and the voltage-source implementation in the grid: the structure has not an inherent protection against transients. The ability to work in grid-forming mode exposes a synchronverter to severe transient over-currents and external current protections are needed for safe operation.

3.2.2 SG Model Based Emulation: VISMA and IEPE topologies

The *Virtual Synchronous Machines* (VISMA) approach is based, as synchronverters, on the real-time execution of the SG full detailed mathematical model. The inverter, equipped with a battery storage, is controlled by measuring the grid voltage and computing the stator currents, then sent to the grid as fast outputs through a hysteresis regulator (Fig.19). Thus, the VISMA algorithm is implemented as a fast current-controlled voltage source for the grid's point of view.

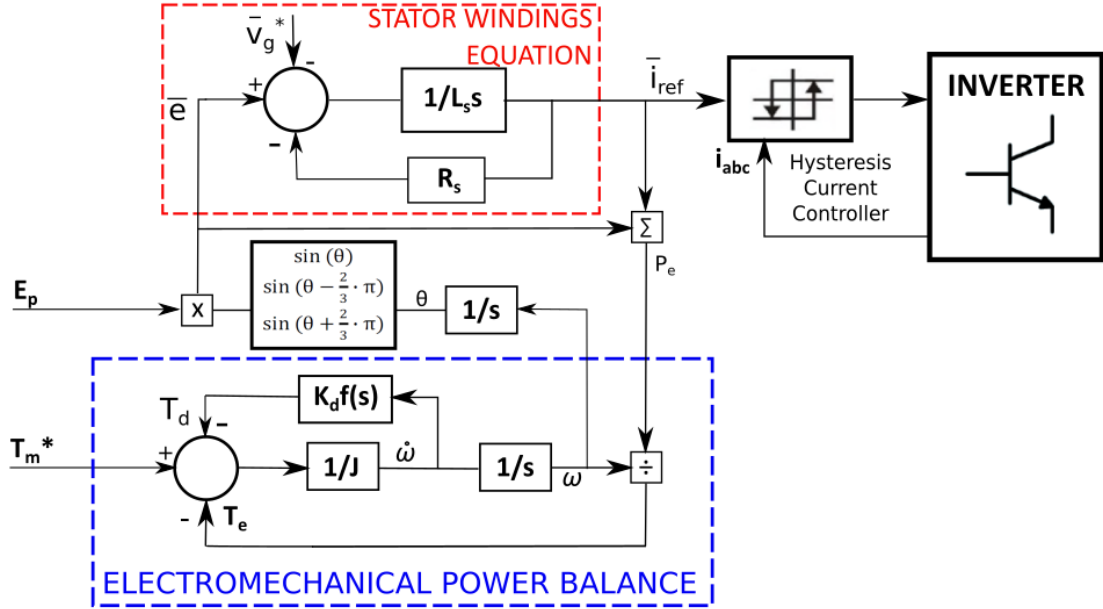


Fig. 19: VISMA schematic: current control is exploited by setting the mechanical torque and EMF [15].

The SG model is represented by the stator electrical equation eq. (22) and with a mechanical subsystem, that incorporates the damping effect of the field circuit [15]. For simplification purpose the electromechanical power balance equation is used (eq. (23)):

$$\vec{e} - \vec{v}_g = R_s \vec{i}_{ref} + L_s \frac{d\vec{i}_{ref}}{dt} \quad (22)$$

$$T_m - T_e = \frac{1}{J} \frac{d\omega}{dt} + k_d f(s) \frac{d\omega}{dt} \quad (23)$$

In eq. (23) J represents the moment of inertia, k_d is the damping factor and $f(s)$ is the phase compensation term that ensures that the virtual damping force counteracts any rotor oscillation in opposite phase. The simplification of the SG model removes the transient and sub-transient stator current components. The computation of the reference current is obtained by solving the electrical eq. (22) in Laplace domain:

$$\vec{i}_{ref}(s) = \frac{|\vec{e}(s) - \vec{v}_g(s)|}{R_s + L_s s} \quad (24)$$

where R_s and L_s are the stator windings resistance and inductance, \vec{e} is the three-phase electromotive force and \vec{v}_g is the three-phase voltage measured in the point of common coupling with the grid.

In eq. (24) a three-phase model is used to improve the control stability in presence of unsymmetrical load conditions and fast variations on the grid. Active power P can be regulated by means of the virtual mechanical torque T_m , while reactive power Q can be adjusted using the virtual field control voltage e . The control schematic can be summarized in three fundamental blocks:

- **Electromechanical Power Balance Block:** eq. (23) is solved to emulate the virtual inertia response of the SG. T_m^* is set and confronted with the requested electrical torque T_e , obtained by eq. (25). The angular frequency derivative is integrated twice to obtain angular frequency ω and angular position θ .

$$T_e = \frac{P_e}{\omega} = \frac{\vec{e} \cdot \vec{i}_{ref}}{\omega} \quad (25)$$

- **Stator Windings Equation Block:** the induced EMF is obtained by setting an adjustable amplitude E_p . Voltage \vec{e} is then confronted with the grid voltage on the point of common coupling to generate the reference current.

$$\vec{e} = \begin{bmatrix} e_1 \\ e_2 \\ e_3 \end{bmatrix} = E_p \begin{bmatrix} \sin\theta \\ \sin(\theta - \frac{2\pi}{3}) \\ \sin(\theta - \frac{4\pi}{3}) \end{bmatrix} \quad (26)$$

- **Hysteresis Current Controller Block:** the reference current obtained from eq. (24) is confronted with the current feedback i_{abc} measured on the inverter output. The fast application of the hysteresis controller allows to set an immediate flow of current and active power.

The VISMA topology can be used to control active power flows with positive and negative torque reference (*Fig.20*): a negative torque is used to support the grid by discharging the battery, while a positive torque enables a motor function and the surplus energy on the grid is absorbed and stored in the battery. In a similar way the reactive power is proportional to the virtual excitation ΔE_p and can be bidirectional on the grid, to exploit a voltage control. The transient and sub-transient dynamics can be implemented with a secondary parallel machine [15] by joining the two stator current signals: this solution allows to set the transient behavior independently from the main CIG.

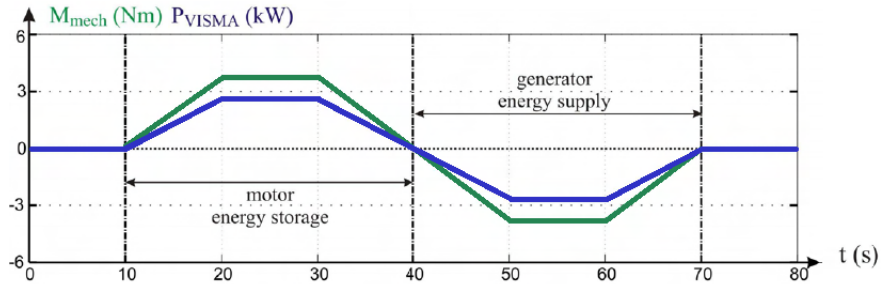


Fig. 20: Bidirectional active power settings with VISMA control [15].

A similar approach is used by the Institute of *Electrical Power Engineering* (IEPE) topology, which works as voltage source by measuring the CIG output current and generating voltage references for the inverter. IEPE's topology is better suited for islanded operations, while in grid-connected mode fast current transients might lead to instabilities during synchronization.

3.2.3 IM Based Emulation: inductverters

The *inductverter's* control is based on the inertial response of the *Induction Machine* (IM). The possibility of IMs to self-start, to track variations in the grid and to synchronize with them (without the need for grid frequency and voltage information) is used to create an effective inertia emulation. The inductverter's auto-synchronization feature is used to interface the inverter with the grid without introducing a PLL unit: the PLL-less operation is an important advantage if compared to SG based models, that require an additional non-linear controller for smooth synchronization. The structure is also used for active power and frequency regulation (*Fig.21*).

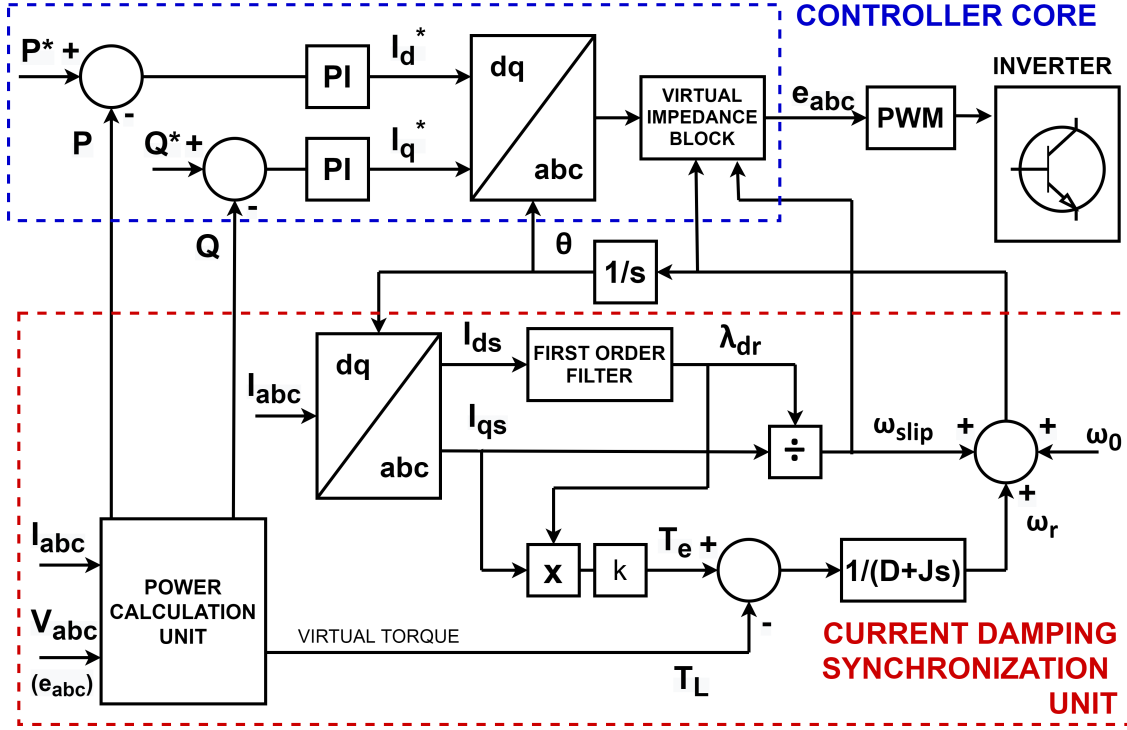


Fig. 21: Inductverter schematic [3], [16].

The inductverter's core algorithm is based on the IM equivalent model in dq frame [16]. A IM field-oriented control is implemented to overcome the problem of the unknown synchronous grid speed ω_s . The d -axis is aligned with the virtual rotor flux λ_r and the grid frequency is estimated as function of other parameters. The original IM model is simplified as follows:

$$T_e = \frac{3}{2} (\lambda_{ds} I_{qs} - \lambda_{qs} I_{ds}) = \frac{3}{2} \lambda_{ds} I_{qs} = \frac{3}{2} \frac{L_m}{L_r} \frac{\lambda_{dr}}{I_{qs}} \quad (27)$$

$$\omega_{slip} = \frac{L_m}{\tau_r} \cdot \frac{I_{qs}}{\lambda_{dr}} \quad (28)$$

$$\omega_r = \frac{1}{D + J_s} (T_e - T_m) \quad (29)$$

The virtual torque T_e and the active power regulation are proportional to the q -axis current. The slip frequency in eq. (28) is an adaptive term and can vary according to output power, grid frequency and impedance variations.

The mechanical dynamic of the virtual rotor is described by eq. (29), where ω_r is the dominant term of angular frequency. A virtual impedance is used to represent the voltage at the virtual IM terminals for a given current waveform, and the transfer function is written approximately as:

$$Z = \frac{V_s}{I_s} \approx \frac{(\text{slip}[(L_m + L_{lr})R_s + L_{ls}R_r + L_mR_r]s + R_sR_r)}{[(L_{lr} + L_m)\text{slip}]s + R_r} = \frac{s + z}{s + p} \quad (30)$$

The inductverter's schematic is composed by three main parts:

- **Current/power Dumping and Synchronization Unit Block:** the synchronization unit generates the reference estimated frequency, which is used to emulate the soft-start and auto-synchronization of IM. The procedure is similar to a PLL implementation, but without using grid's information. The angular reference for abc/dq transform is obtained as:

$$\theta = \int (\omega_r + \omega_{\text{slip}} + \omega_0) dt \quad (31)$$

where ω_0 represents the virtual rotor initial frequency, which emulates the connection of a rotating IM to the grid. If ω_0 is chosen similar to the synchronous frequency, transients and frequency variations after the connection can be substantially reduced.

- **Power Calculation Block:** the calculation of active and reactive power P and Q is performed by measured feedbacks of the inverter output current I_{abc} and the voltage at the point of connection with the grid v_{abc} . Alternatively is possible to use the reference voltage e_{abc} , generated for PWM control by the *Core Controller Block*.
- **Core Controller Block:** the inductverter control is built in hybrid dq/abc frame. Reference currents are generated in dq frame as function of active and reactive power errors, using PI controllers to force the error to zero. The reference I_{dq} is than transformed in abc frame, using the angle reference obtained by the synchronization unit, and is used to create vector voltage references by means of the adaptive virtual impedance.

The main advantage of the inductverter, other than the inherent auto-synchronization function, is that the controller can feed to the grid a constant amount of active and reactive power in front of parameter variations or faults in the grid. This function is not guaranteed by SG based models, where frequency deviations introduce a permanent offset of the output power. Frequency dynamics in the grid are enhanced by the introduction of virtual inertia. Operation is guaranteed in grid-connected mode and for de-loaded operation of *RES*.

3.2.4 Swing Equation Based Emulation: Ise Lab's topology

The virtual inertia emulation control developed by *Ise Lab* is based on the solution of the power-frequency swing equation, implemented in a digital controller to create a VSG. Similarly to SG model based techniques, the inverter output current I_g and the voltage at the point of common coupling V_g are used as feedbacks to compute the grid frequency ω_g and the output power P_{OUT} . Power and frequency measures are then used in the algorithm to pilot the PWM generator.

The swing equation model is based on the following equations [17]:

$$P_m - P_e = P_{in} - P_{out} = J\omega_{VI} \left(\frac{d\omega_{VI}}{dt} \right) + D_P \Delta\omega \quad (32)$$

$$\Delta\omega = \omega_{VI} - \omega_g \quad (33)$$

where P_{in} represents the input power (simulating the prime mover power P_m of a real SG), P_{out} is the inverter's output power, ω_{VI} and ω_g are the virtual and grid reference angular frequency, J is inertia and D_P is the damping factor. These parameters are also used to set the inertia time constant of the VSG unit:

$$\tau_f = \frac{J}{D_P} \quad (34)$$

The control's schematic (*Fig.22*) is composed by three main parts:

- **Power Governor Block:** the input power is computed based on the frequency deviations from the reference frequency ω^* by using a first order element (*Fig.23*), which introduces a power deviation from the reference power P_0 of the CIG unit. Delays are introduced by the governor, resulting in higher RoCoF and frequency nadir during contingency events.
- **VSG Control Block:** the swing eq. (32) is solved and the virtual angular frequency ω_{VI} is integrated to obtain the virtual mechanical phase angle θ_{VI} , used alongside the voltage reference to operate the PWM unit.
- **Q Droop Block:** a voltage droop mechanism is implemented. The reactive power reference Q^* is confronted with the measured reactive power Q in a control loop and a the reference voltage E^* is set for PWM operations.

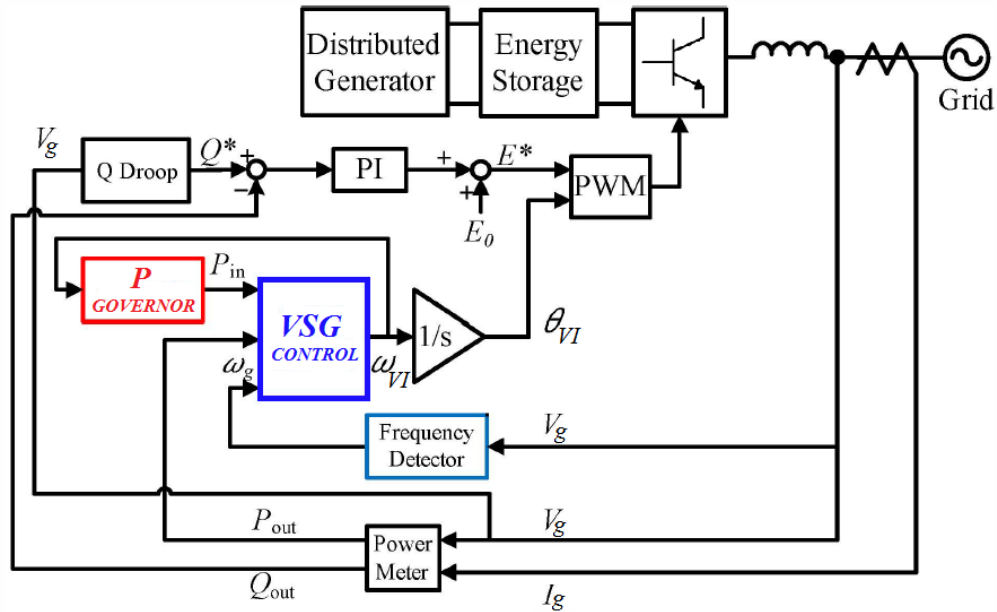


Fig. 22: Ise lab's control schematic [18].

The Ise lab's control approach does not require frequency derivative computations, that typically introduces noises in the system. The topology can be used to operate DG units in grid-forming mode, but numerical instability can occur if parameters J and D_p are not properly tuned. The moment of inertia J is determined by its proportionality to H : an high constant of inertia results in an higher time constant, which implies a slower response to instantaneous frequency deviations, but also a better overall containment of the latter.

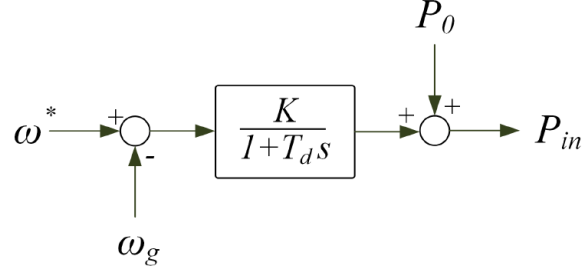


Fig. 23: First order governor for input power computation [12].

3.2.5 Swing Equation Based Emulation: Synchronous Power Controllers (SCP)

The SCP approach proposes a core algorithm similar to Ise Lab's topology. The main difference is in the control loop: instead of using a system based on voltage or current control, a nested structure is proposed. The control is implemented with an outer voltage loop and an inner current loop, interfaced by a virtual admittance (Fig.24).

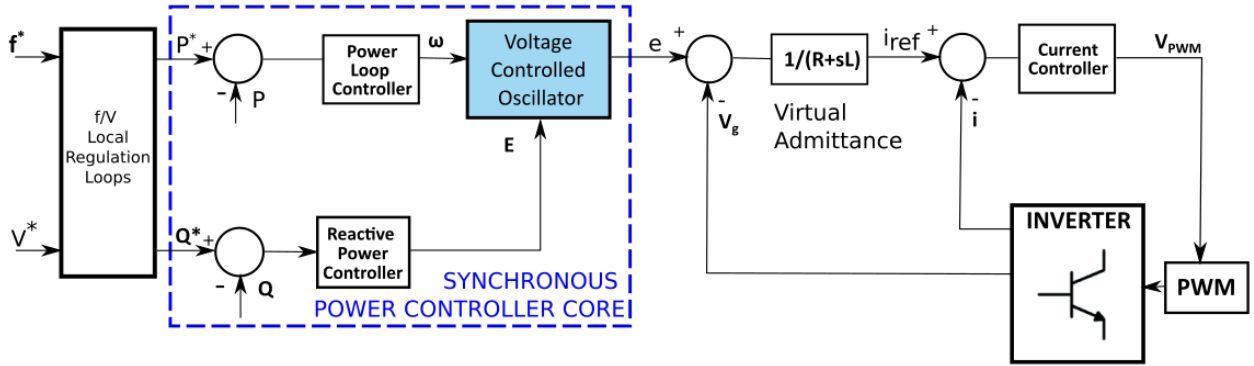


Fig. 24: SCP control schematic [19].

The SG model is represented as a voltage source by a simple electric characteristic, in which the reference current is generated considering the voltage drop between the electromotive force E and the grid voltage V_g in the point of connection (eq. (35)), as shown in (Fig.25). The voltage drop induces in every phase a current by means of a virtual admittance, where R and L are the resistance and inductance virtual parameters:

$$\Delta v = E - V_g \quad (35)$$

$$\frac{di}{dt} = \frac{1}{L}(\Delta v - Ri) \quad (36)$$

The virtual admittance reproduces the electrical virtual response of the SG and can be used to limit the current injection, in order to protect the inverter's electronic components and avoid any undesired disconnection by the protection system.

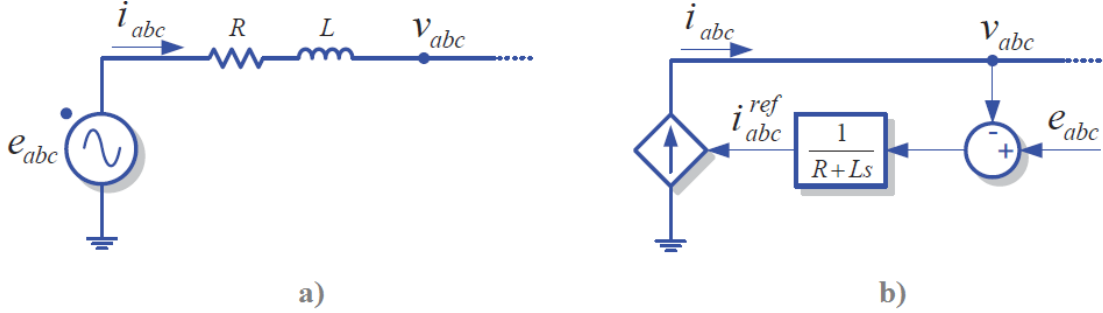


Fig. 25: Electrical characteristic of SPC: a) SG model; b) Virtual admittance implementation; [19]

The electromechanical characteristic of the SG is expressed by the swing equation and allows inertia emulation and synchronization with the grid:

$$P_{in} - P_{out} = P_m - P_e = 2H\omega \frac{d\omega}{dt} \text{ p.u.} \quad (37)$$

The swing equation is implemented in a *Power Loop Controller* (PLC) by means of a proportional-integral controller. The control can be summarized in three fundamental blocks:

- **SCP Core Block:** inertia emulation is performed by the active power control PLC, that implements the swing eq. (37). Reference power P^* and Q^* are compared with instantaneous power measurements P and Q , calculated using the inverter output voltage V_g and current i . The outcomes are the virtual angular speed ω and the electromotive force amplitude E , used by the *Voltage-Controlled Oscillator* unit (VCO) to define the three-phase voltage e_{abc} .
- **Nested Voltage/current Loops Block:** the electromotive force e_{abc} generated by the VCO is confronted with the measured voltage V_g to implement eq. (35). The reference current i_{abc}^{ref} is generated via the virtual admittance block and is sent to the inner current loop, that in turn generates voltage PWM references for the inverter.
- **f/V Local Regulation Loops Block:** the inverter can actively contribute to voltage and frequency regulation on the grid. The local references P^* and Q^* are set accordingly to frequency and voltage errors. To avoid continuous references fluctuations a filter with dead-bands is applied.

The main advantage of a nested control is the inherent over-current protection, which is not present in open loop solutions such as synchronverters, but also introduce major complexity in tuning the control system parameters. Being based on the simple swing equation, numerical instabilities are unlikely to occur. The SCP can operate in grid-connected or islanded micro-grid configuration. The virtual admittance emulation of the SG allows load sharing with other generators on the grid. The synchronization with the grid is necessary during the start-up of the SPC controller, in order to avoid excessive current references.

The synchronization condition is possible when the voltage drop Δv from eq. (35) is equal to zero: the condition is obtained by connecting the CIG to the grid with a PWM modulation that sets the reference current to zero. The SPC core is enabled with power references set to zero and e_{abc} is rapidly modified to match the grid voltage V_g , without any exchange of power. When a given power tolerance S_t is respected (in a given stabilization time T_a) the SCP control can become fully operative, enabling the grid's parameters reading and the local regulation (*Fig.26*).

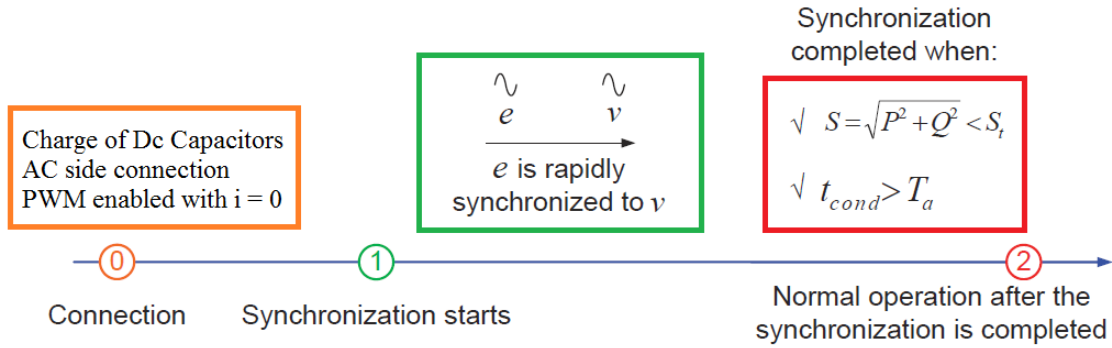


Fig. 26: Start-up process for SCP Synchronization [19].

3.2.6 Frequency-Power Response Based Emulation: VSG/ VSYNCH's Topology

The VSG inertial response emulation is mainly focused on the ability of SGs to respond to frequency changes. The dynamic of release and absorption of kinetic energy is used to transform the DG unit in a current-controlled voltage source, that can change its output power based on system frequency deviations during a contingency event. The main difference with more traditional droop controls is in the possibility for VSG to provide a dynamic frequency control, based on the measurement of the derivative of frequency (*Fig.27*).

The VGS topology is used by the European VSYNCH research group for inertia emulation.

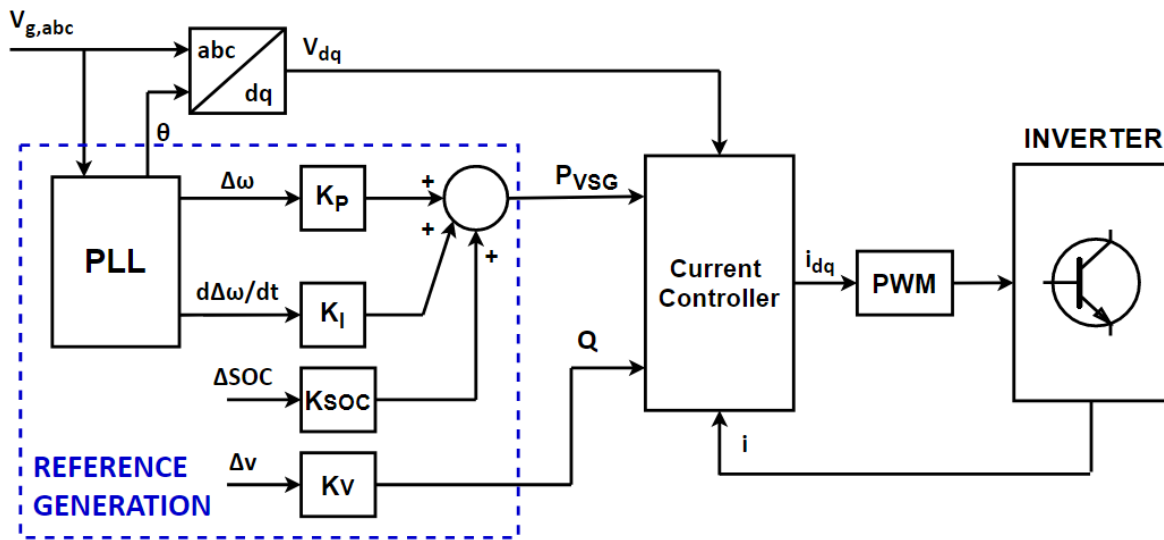


Fig. 27: VSG/VSYNCH schematic [3].

The VGS control is mainly based on a simple output power equation [12]:

$$P_{VSG,out} = K_J \frac{d\Delta\omega}{dt} + K_d \Delta\omega + K_{SOC} \Delta SOC \quad (38)$$

where $\Delta\omega$ is the angular frequency variation from reference ω^* , $\frac{d\Delta\omega}{dt}$ is the corresponding RoCoF and K_d and K_J are the damping and inertial constants. The damping constant K_d has the same function of a frequency droop, which is to return the frequency to a steady-state value and contain frequency oscillations. The inertial constant K_J provides a fast dynamic response to initial RoCoF in order to limit the derivative frequency term. The last term in eq. (38) is introduced only if a droop mechanism is active: K_{SOC} is the droop factor (3 - 5 %) while ΔSOC represents the frequency variation on the grid ($f - f^*$) [20]. The droop factor is set to zero if the grid frequency is not controlled by the injection of output power P_{VSG} .

The reference current is obtained as:

$$I_d^* = \frac{V_d P_{VSG,out} - V_q Q}{V_d^2 + V_q^2} \quad (39)$$

$$I_q^* = \frac{V_d Q - V_q P_{VSG,out}}{V_d^2 + V_q^2} \quad (40)$$

where V_d and V_q are the dq -components of the measured grid voltage $V_{g,abc}$. The equations are implemented in a dedicated current controller.

The control can be summarized in two fundamental blocks:

- **Reference Generation Block:** the reference output power P_{VGS} is generated from the measures of $\Delta\omega$ and $\frac{d\Delta\omega}{dt}$, acquired by means of a PLL. The reactive power reference Q is obtained with a droop controller according to the voltage variation Δv in the point of connection.
- **Current Controller Block:** the current references are generated in dq frames. Typically the VSYNCH's control is focused only on active power, thus I_q^* and the reactive power Q are set to zero. The reference currents are confronted with the grid current feedback and proper gate signals are sent to the PWM generator.

A VSG represents one of the simplest solutions to implement virtual inertia for CIG, given the absence of complex mathematical models of SGs. Equation (38) is in fact a first order model of the SG and the swing equation. The current-source implementation of the topology allows current control and provides inherent protection against over-currents. The main disadvantage is due to the introduction of the derivative term of frequency, that introduces instability in the power system if multiple units are operated with the same VSG approach.

Additional instability and steady-state errors can be introduced by the PLL measurements, especially in grids with enhanced harmonic distortion and voltage sags. The topology is used in grid-connected microgrid applications and wind systems, while in islanded mode is not feasible for grid-forming operations: the system can emulate inertia during frequency variations, but not during input power variations.

3.2.7 Droop based approaches

The wide majority of inertia emulation techniques is designed to reproduce or approximate the functioning of a SG unit connected to large power systems, where more units are generating and performing regulation (*Fig.28*). A frequency droop based approach is mainly developed for a different purpose, that is to operate a CIG in converter dominated microgrid system.

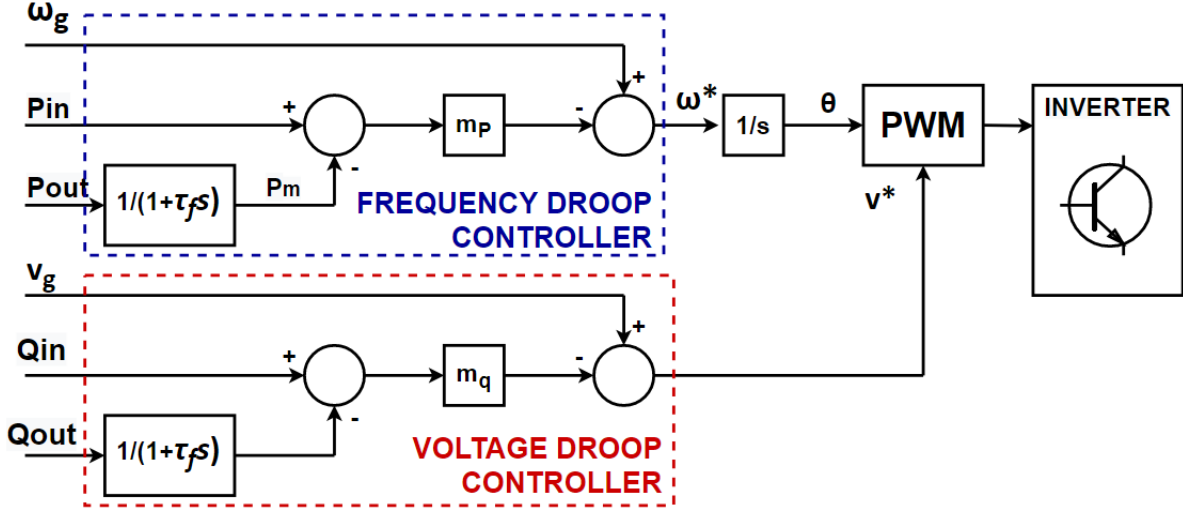


Fig. 28: Frequency and voltage droop controllers for microgrids [12], [21].

Under the assumption of a grid inductive impedance, frequency and voltage droop strategies are implemented with droop regulators for active and reactive power:

$$\omega_g = \omega^* - m_p(P_{out} - P_{in}) \quad (41)$$

$$v_g = v^* - m_q(Q_{out} - Q_{in}) \quad (42)$$

where v_g and ω_g are the local grid values, v^* and ω^* are the reference values, P_{in} and Q_{in} are the reference active and reactive power, P_{out} and Q_{out} are the measured power outputs of the DG unit and m_p and m_q are the active and reactive power drooping coefficients.

A low pass filter is usually applied to the measured power P_{out} and Q_{out} , so that the droop based control can approximate the behaviour of a virtual inertia system. The equivalence between the frequency-droop regulator and VSG methods based on the swing equation can be proved referring to eq. (41) and the low pass filter from *Fig.28*.

$$P_{out} = P_e = (1 + \tau_f s) \left[\frac{1}{m_p}(\omega_g - \omega^*) + P_{in} \right] \quad (43)$$

$$P_{in} - P_{out} = \frac{1}{m_p}(\omega_g - \omega^*) + \tau_f s \frac{1}{m_p} \omega^* \quad (44)$$

Equation (43) is rearranged in eq. (44), where is possible to underline that the filter is a mathematical delay that is equivalent of virtual inertia, while the droop gain is comparable to the damping effect:

$$K_I = \tau_f \frac{1}{m_p}; \quad K_D = \frac{1}{m_p}; \quad (45)$$

The equivalence with other VSG is particularly effective because of the low pass filter. Without the filtering the power-frequency droop would be equivalent to a VSG with no inertia, that would result in unstable operations. The possibility to properly tune K_I and K_D allows the emulation of specific synchronous machine. The main disadvantage of this approximated technique is the slow transient response and the imprecise power and load sharing during transients. The droop based approach is overall the simplest emulation strategy.

3.3 Technologies for inertia enhancement

The introduction of VSGs in low-inertia power systems has been an important contribution to support the grid and improve RES penetration. However, VSGs present some limitations in virtual inertia emulation, both by voltage and frequency range limits of equipped DC-links and by inadequate storage unit capabilities. Nonetheless, the inertia in a low-inertia power system can be enhanced introducing various independent *Energy Storage System* (ESS) technologies on the grid. Typical solutions are dedicated batteries, supercapacitors and flywheels, but more complex technologies are established or in development. The objective is to further improve frequency stability and decrease the RoCoF and frequency excursions.

3.3.1 Batteries and Ultra-capacitors

Batteries are electrical storage units operated in DC and a power converter is required to perform the grid connection. Inertia emulation by means of batteries can be obtained only with a proper dedicated control algorithm, in stand-alone ESSs or in CIGs as discussed in **section 3.2**. Not all batteries can participate to frequency regulation, as a fast response time is required: in this regard *electrochemical batteries* (lithium-ion and sodium sulphur) are one of the most extended technology used for grid-connected applications, having the best characteristics in energy density and dynamics. Other storage systems, such as hydrogen, synthetic natural gas and fuel cell technology are not adequate for frequency control and can only be implemented for services that manage medium-long term energy demands [3], [22].

A *Battery Energy Storage System* (BESS) is effective to increase stability in low-inertia power system and to replace the role of SG's inertia, especially in microgrid applications. However, the sudden large draw or absorption of energy during a contingency event can induce stress in the batteries and severely reduce their expected lifetime.

An optimal solution to overcome the problem is the introduction of an hybrid system composed by a lithium-ion battery and a supercapacitor (*Fig.29*). The system is connected to the grid via a bidirectional DC/AC power converter that can control the charging/discharging status of the batteries with an appropriate voltage-current profile.

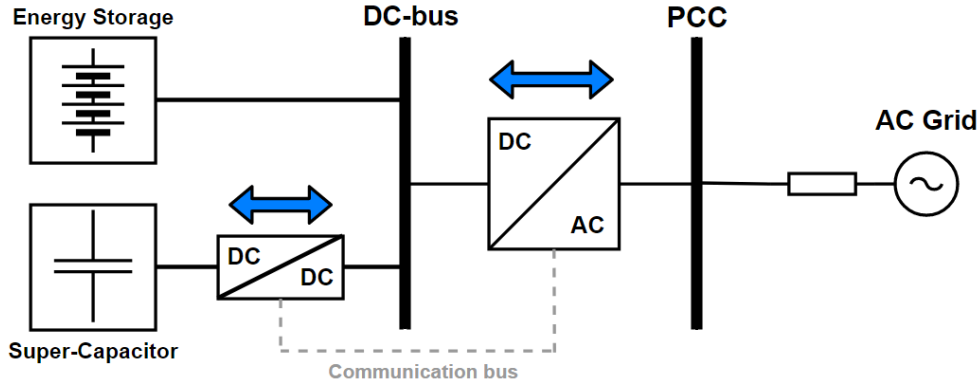


Fig. 29: General topology for Energy Storage (batteries) and Supercapacitor hybrid grid-integration [22].

Supercapacitors, or ultra-capacitors, can store or discharge large amount of energy in less time if compared to a normal battery. The high efficiency of the process is counterbalanced by a minor storing capability. The supercapacitor can be controlled by an additional DC/DC converter for fast power injection during high dynamic load shifts.

The mix of the two technologies allows to use the best features of both: the supercapacitor is used for sustaining fast power peaks and inertial response, preventing the battery from damages, while the battery provides a large amount of energy for primary frequency regulation, following large energy requirements with smoother transients. The algorithm monitors the *State of Charge* of the batteries and constraints are set to limit the converter currents and the voltage ratio at which the batteries work. The presence of batteries on the grid is also important to provide other ancillary services, such as voltage support, power quality and uninterrupted power supply.

3.3.2 Flywheel

A *Flywheel Energy Storage System* (FESS) is a simple technology based on the use of mechanical elements, such as rotating disks (*Fig.30*), to store kinetic energy. The energy can be absorbed or released in the grid as electric power by using the rotor of a motor/generator unit. The main purpose of a flywheel is to provide additional inertia and frequency support to the power system. The main characteristic of a FESS is a the high power density, that makes it suitable for short-term operations.

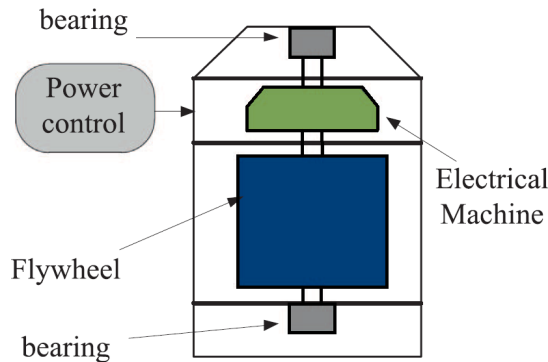


Fig. 30: Electromechanical layout of a FESS [23].

The flywheel is the main component of a FESS and is a rotating disk made of steel or composite-based materials. The kinetic energy stored is proportional to the moment of inertia J and the rotor angular speed eq. (46). The kinetic storage capability can be enhanced by increasing the flywheel speed or its inertia, by augmenting the disk radius or using high-density materials eq. (47):

$$E_{FW} = \frac{1}{2}J\omega^2 \quad (46)$$

$$J = \frac{1}{2}mr^2 \quad (47)$$

The flywheel is directly connected to an electrical machine, that is used to convert the kinetic energy in electric power and vice-versa by means of a dedicated control. Different machines can be used depending on the application: for low speed applications on the grid IM, SPM and PMSM machine are commonly used. Mechanical bearings are used for low speed, introducing high friction and losses, while magnetic bearings are used to reach high speed, allowing low friction and contactless operation.

The electrical layout of a FESS is shown in Fig.31. The flywheel-motor system is generally connected to two voltage source back-to-back converters (VSCs). The converter on the electric machine's side is used for speed and flux regulation to perform the power control of the FESS. The second converter is used for voltage regulation on the DC-link. The converter block is used to optimize the exchange of power between the grid and the flywheel.

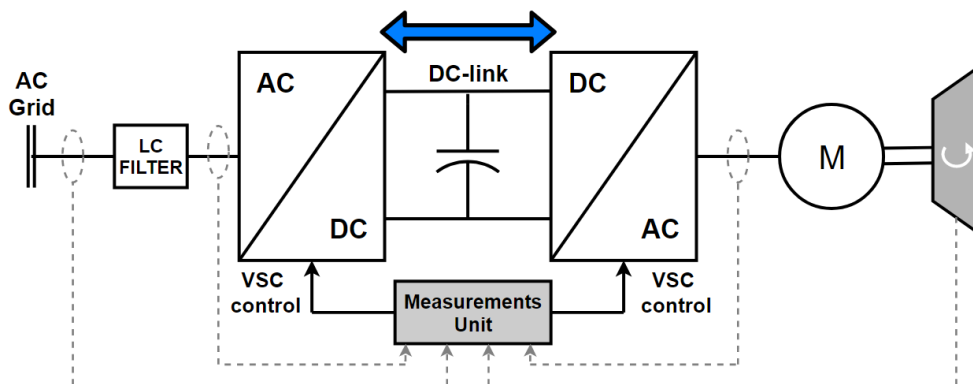


Fig. 31: Electrical layout of a FESS [23].

The FESS configuration is typically used in association with PV and wind plants, where sudden deficiencies in in power generation are more likely to occur. The fast time response, on the order of milliseconds, is the perfect match to provide large power quantities for a short period of time, underlining a fast ramping capability. The FESS can also sustain hundreds of thousands of charge-discharge cycles, far better than batteries from BESSs.

Other advantages introduced by using FESS are the long lifetime, the absence of pollution and the high system efficiency. Periodic maintenance is unnecessary if mechanical friction is avoided by using magnetic bearings. The flywheel is connected to the grid via power converters, which implies the inertia is emulated. There are no geographical restrictions for installation and grid voltage support is available. The main limitation is due to the limited storage capacity, if compared to other technologies.

3.3.3 Synchronous condenser

A *synchronous condenser* (SC) is a conventional inertia enhancement technology consisting in a freely-spinning synchronous generator connected to the grid with no load or prime movers (*Fig.32*). The SC is used as a reactive compensation device to control the network voltage by absorbing or supplying reactive power. The VAR control (both inductive or capacitive) is obtained by regulating the excitation current of the machine, to maintain voltage stability and an adequate power factor. Typically the active power control is set to zero.

The SC is a synchronous machine and has an inherent inertia, that can be seen as a kinetic energy storage from the power system's point-of-view. Typical values of H are on the scale of $1 \div 1.5$ s, which is lower than normal SGs because the absence of a prime mover is translated into a minor rotating mass [25]. The inertia is used to increase the stability of close generators and the SC can improve inertia response and primary regulation by acting as an active power source [26].

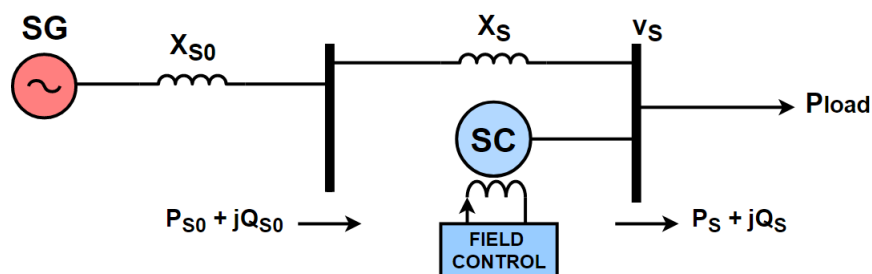


Fig. 32: SC connected to a load bus [25].

The frequency on the bus is regulated during disturbances by releasing the rotational energy during SGs trips (to prevent the frequency decrease), or absorbing additional energy when the load suddenly decreases causing power unbalances (to prevent the frequency increase). A secondary advantage of SCs is the contribution to the overall short-circuit capacity in the power system, that allows a better system protection and enhances the possibility of introduce RES and power converter operations on the grid.

The main limitations of this technology are the operating costs, the high cooling requirements and the slow response to fast load changes, that affect the efficiency of the control during the first instants of a contingency event. There are no particular constraints for installation, however is important to study the best location on the grid to install a SC due to its high costs.

3.3.4 General Purpose Energy Storages

Additional technologies are available to perform storage functions on the grid, even if not directly related to virtual inertia implementation.

Pumped Hydroelectric Energy Storages (PHES) are a well-established technology based on conventional hydro power plants. A storage function is obtained by moving water from a lower to an upper reservoir, accumulating potential energy. The energy is released and converted into electric power under frequency disturbances to provide inertia support to the grid, while any energy surplus on the network is used to pump the water back into the reservoir (*Fig.33*).

The main advantage of PHES is to be both a storage unit and a hydroelectric power plant. The unit can be used for frequency regulation and for grid feeding during peak demands. The typical inertia constant for PHES is of $2 \div 4$ s, given the fast utilization of the accumulated water.

The almost instantaneous ability to produce electric energy is important to grant black start capability, even if the time response is not as fast as other sources (supercapacitors or inertia of rotating parts). Another important feature is the storage capability, that can go up to hundreds of GWh and is far greater than a DC-battery [27]. The storage is also long-term and the lifetime of a plant is of many decades depending on the scheduled maintenance.

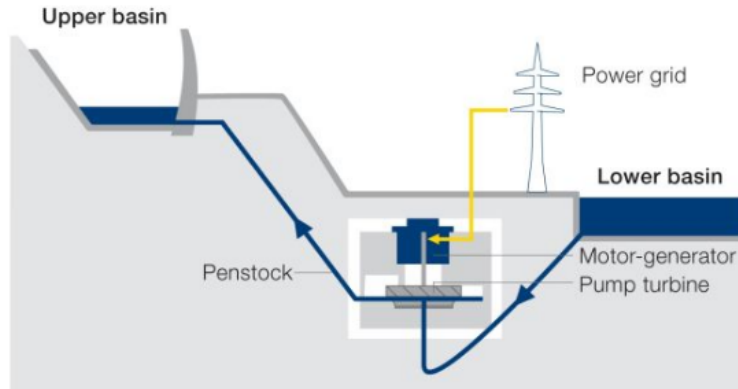


Fig. 33: PHEs plant general layout [28]

Additional flexibility can be added to the grid by implementing *Variable Speed PHEs*, that can perform frequency control both in generation mode and in pump mode with fast power injections, even under the rated power condition [29]. The main disadvantage of PHEs is the geographical constraint. PHEs plants are mostly associated to river operations, where water is easily controlled in open loop basins. Off-river PHEs can also be built by creating a closed-loop water system with two reservoirs at different latitude connected by pipes and tunnels. In both cases is necessary to carefully locate the position of the site in order to satisfy the structural requirements.

Another possibility is represented by *Compressed Air Energy Storages (CAES)*, an in-development gas-turbine technology based on the accumulation of potential energy by pressurizing ambient air in dedicated reservoirs. The pressurization is made using the exceeding electric energy from off-peaks of RES plants and the storages are located in underground facilities such as caverns, mines or gas chambers.

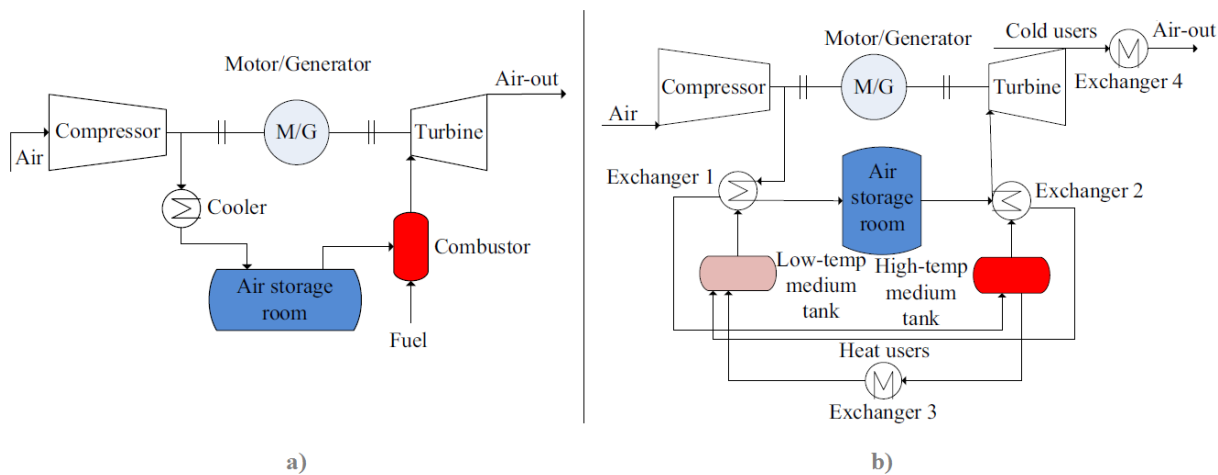


Fig. 34: CAES systems: a) SF-CAES architecture; b) NSF-CAES architecture [30].

The stored energy can be released by channelling the air through turbines to produce electric energy for the power system during a load shifting. The CAES architectures can be classified in *Supplementary Fired CAES* (SF-CAES) and *Non Supplementary Fired CAES* (NSF-CAES).

In SF-CAES the ambient air is compressed and stored in a dedicated storage room (*Fig.34-a*). When power is requested by the grid a fuel combustion is needed to heat the air for the turbine expansion, implying a dependence from fossil fuel and consequential environment pollution.

Referring to a NSF-CAES systems (*Fig.34-b*), the ambient air is compressed and cooled in a multi stage compressor and is stored in an air storage room. The NSF-CAES collects the heat obtained from the air compression process and accumulate it in an high-temperature tank. The compressed air is then heated with a thermal exchanger (*Exchanger 2*) and sent in the turbine. The system can be used simultaneously to produce electricity, to heat users (*Exchanger 3*) and to cool users (*Exchanger 4*): the multiple energy utilizations leads to high system efficiencies. A CAES system can also be controlled by opening and regulating valves. The generator is driven from stationary to rated speed condition, with an adequate air inflow in the turbine, and is connected to the grid. The output active power regulation is then controlled based on the dispatching instruction from the grid. The primary frequency modulation can be realized as shown in *Fig.35*.

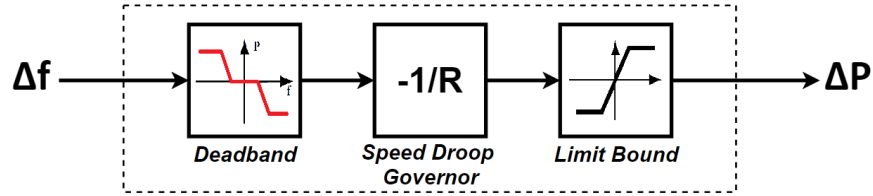


Fig. 35: Primary frequency modulation schematic for CAES [31].

The CAES has typically a large insensitive dead-band (up to ± 0.1 Hz), as the unit is used for frequency modulation and peak load regulation. A speed governor droop R is set to determine if the unit is working or not, based on the frequency variation Δf . The droop values are set as $3\% \div 4\%$, given then strong variation ability of CAESs to go from static to full load operation in few minute. The provided output power variation is:

$$\Delta P = -\frac{\Delta f}{f_{rated}} \frac{P_{rated}}{R} \quad (48)$$

A limit bound is applied on the output to limit the maximum load adjustment of the unit. The upper limit for frequency regulation can be set to the maximum capacity of the CAES. Typical values of H are on the scale of $3 \div 4$ s, and are almost comparable with traditional power plants such as gas turbine and thermal power units ($4 \div 5$ s).

The CAES technology is promising for large scale storage of power on the grid. The advantages of compressed air are the large storage capacity and a very low pollution impact on the environment (for NSF-CAES). The ability to perform primary regulation is used to provide frequency and voltage support to the grid as an ancillary service. The added inertia contribution allows for further RES penetration in the power system. The main limitation is the possible geographical constraint, as a CAES plants might require a specific underground locations with proper geological formation depending on the storage solutions adopted.

One last possibility to obtain a storage function within the grid, without the use of dedicated structures, is the implementation of the *demand-side management* in power systems. The management of power system is typically performed by controlling the generation accordingly to the load demand variations. Knowing that the frequency deviations are caused by discrepancies between generation and demand it's possible to implement *self-regulated loads* on the grid. Self-regulated loads, such as refrigerators and air-condition systems, are equipped with dedicated relays to measure RoCoF and the frequency deviations. This category of loads are classified as *Thermostatic Controlled Loads* (TLCs) and can be used to manage power unbalances from the consumer point of view, by accordingly switch them on and off to reduce the frequency deviations. The alteration of the normal cycle of TLCs has not a negative impact on the controlled temperature [3]. The demand-side management can be employed to maintain the stability on the power system and to partially resolve the problem of low-inertia systems, by implementing an inertia contribution from the load side of the network. The main disadvantage of this management strategy is the requirement of a communication network to handle all the regulated loads. The initial costs of implementation is high, as it requires a system redesign, and an eventual collapse of the communication system might lead to the trip of the entire grid.

4 Power-hardware-in-the-loop applications in Low-Inertia Systems

The low-inertia is a characteristic that is present in various degrees and extensions in power systems, depending on the level of RES penetration and the structure of a grid/microgrid. The studies on the phenomenon and the different solutions proposed in **section 3** and the literature are in constant development, requiring an experimental application and validation of the technologies before the physical implementation in the power system. A way to perform such studies and tests in laboratories, without the need for a grid connection, is by using an Hardware-in-the-Loop system.

4.1 Hardware-in-the-loop

The *Hardware-in-the-Loop* (HIL) is a method that allows to simulate a physical system by replicating it in real time. The main purpose of this methodology is to study prototypes or new technologies that are planned to be integrated in the real energy system. The analysis can be performed on protections devices, control algorithms and power electronic devices, without a direct connection to the main system. The direct connection can be avoided for two different reasons:

- Deploying a physical device on the grid without a proper knowledge of its functioning might be harmful for the grid stability or for the device itself. The simulation allows to test devices for virtually all possible faults and operating conditions in the safety of a controlled environment.
- In an early stage of study the prototype might not be physically built, but is only represented by a mathematical model or a simulation.

In both cases the HIL method is useful to replicate in simulation the real-world conditions of the power system or the device under study. The typical laboratory setting is made of the real device, called *Hardware/Device under Test* (HUT/DUT), virtually connected to the grid, that is replaced by a mathematical model named *Rest of the System* (ROS). As the simulation runs in real time, HUTs can be physically interfaced to the simulated network in a closed loop. The device's performances are verified in laboratory by performing tests under normal and extreme conditions, such as faults and contingency events.

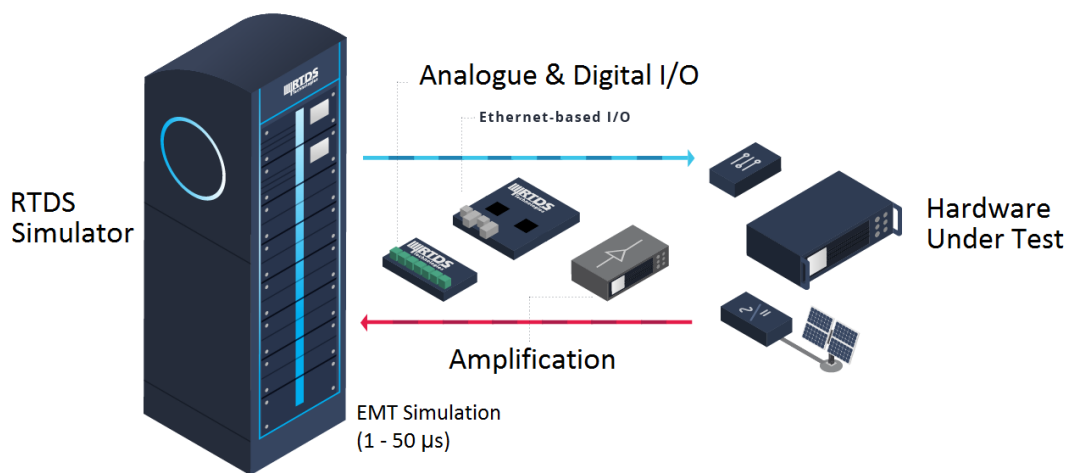


Fig. 36: Example of a HIL laboratory setup. The real time digital simulator RTDS is used to simulate a network and the HUT is connected via I/O ports and an amplification stage (RTDS Technologies, [32]).

4.2 Real-Time Simulation and Power-Hardware-in-the-loop

A *Digital Real-Time Simulation* (DRTS) is used to fully represent the real electric power system with a model and aims to reproduce the output voltage/current waveforms of the system with the desired accuracy, in order to correctly simulate its behaviour. The HIL is a subcategory of DRTS, as it is used to study the dynamic behaviours of a real prototyped hardware in a simulated network, and the response of the latter given an input from the HUT.

The analysis is focused specifically on *electromagnetic transients* (EMT), so the process requires a simulation that can respect the times set by the real-world phenomena ($1 \div 100 \mu\text{s}$). The *Real-Time Simulation* (RTS) is obtained by means of a dedicated computer, which is a simulation platform that can execute fast computations with a time step comparable to the real-world time-line.

The RTS is essential to guarantee the synchronization of the HUT with the ROS and the accuracy and stability of the overall system. The benefit of real-time operations is the possibility to study the interaction between the grid and the HUT in great detail and over a wide range of frequency bandwidth, maintaining low costs for tests and allowing great flexibility if the HUT and the simulated network are changed over time.

The HIL method can be divided in two main typologies:

- **CHIL** : *Control Hardware-in-the-Loop*
- **PHIL** : *Power Hardware-in-the-Loop*

The CHIL is used to interface a physical controller board or a protection relay to the RTS. The signals of the control device under test are exchanged with the RTS via low voltage analog-digital converters (*A/D*). The RTS can send voltage/current outputs back using a digital-analog (*D/A*) converter and eventually a two-quadrant amplifier, to adapt the RTS's signals to the HUT.

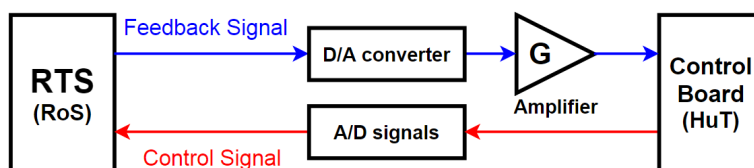


Fig. 37: Control-Hardware-in-the-loop (CHIL) schematics for HUT/RTS interface [33].

The PHIL is used when the HUT is a source device (*e.g.* SG, batteries, RES) or a load device (*e.g.* asynchronous motors). The production or consumption of energy of the HUTs requires a bidirectional power exchange with the simulated network. The connection of the HUT with the ROS is then not direct, but is obtained by means of a power interface.

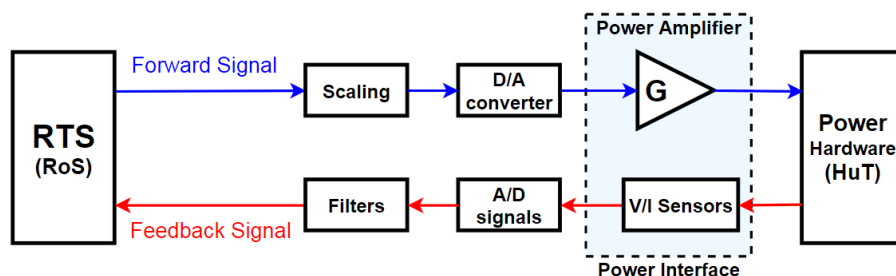


Fig. 38: Power-Hardware-in-the-loop (PHIL) schematics for HUT/RTS interface [33].

The power interface consists in an amplification stage and a set of sensors. The amplifier is a key element in the power interface, being used as a sink or as a source to respectively absorb or generate power. The bidirectional power exchange requires to implement a four-quadrant amplifier, in order to handle both active and reactive power in both directions (*Fig.39-a*).

Voltage/current signals can be extracted from the RTS to control the amplifier output in order to correctly feed the HUT. Commonly HIL uses *Voltage Controlled Amplifiers* or *Current Controlled Amplifiers* (*Fig.39-b*), that have a limited operating capability but are compensated by a larger bandwidth and a fast time response [33]. *Switched Mode Amplifier* can also be used to control either the current or the voltage injected in the HUT, introducing higher time delays and reducing accuracy [34]. The amplifier should have a frequency bandwidth sufficient to effectively boost the frequencies of interest with minimum harmonic distortion.

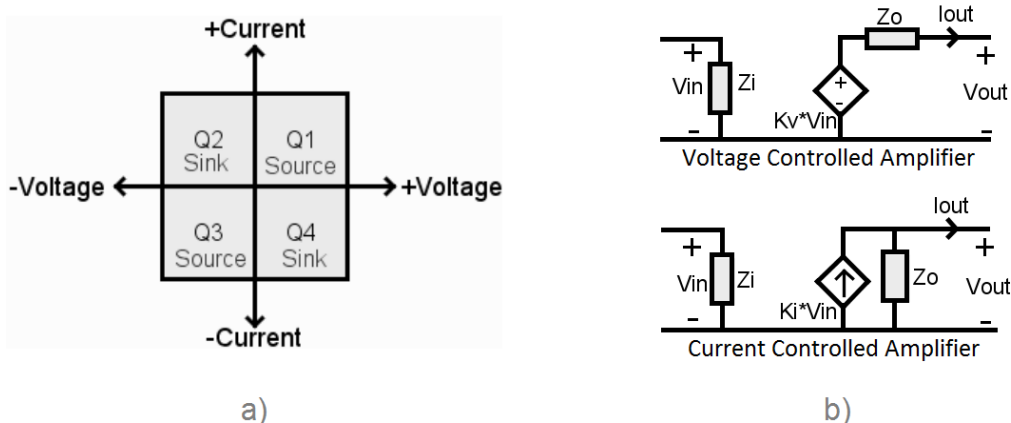


Fig. 39: a) Four-Quadrant amplifier operations for PHIL. b) Schematics for Voltage and Current Controlled Amplifiers with input impedance Z_i , output impedance Z_o and voltage/current gain K_v/K_i .

The low voltage levels of the RTS signals ($\pm 10 V / \pm 5 mA$) are scaled up to the operating voltage/currents of the power hardware. V/I sensors are used to send feedbacks to the RTS and to close the simulation loop. It's important to consider that A/D converters, amplifiers and V/I transducers can introduce noises in the system.

The signals are filtered to reduce the impact of noise on the PHIL simulation and to avoid error amplifications in the power interface. The filtering, on the other hand, introduces in the system additional delay and a signal attenuation depending on the cut-off frequency and must be carefully implemented to preserve a balance between the improved stability and the accuracy of the PHIL simulation.

4.3 Stability in PHIL Simulation

The system stability is an important aspect that can negatively affect PHIL simulations. The presence of closed-loop instability might lead to the production of inaccurate simulation results and, in particular conditions, even to irreversible damages on the devices under tests and the laboratory equipment. Non-ideal behaviours are introduced by both the amplification stage and the sensors response, resulting in time delays, harmonic injection and limited bandwidth.

The power interface can be therefore considered as a *disjunction* between the ROS and the HUT, and its quality depends on the 'transparency' of the connection.

The ideal power interface, which is the equivalent of the connection between the HUT and the real network, is considered to have unity gain, infinite frequency bandwidth and zero delays [34]. The ideal condition is not feasible as the three parameters are hardly coincident with their reference values. A stability analysis is then required to study the overall HIL system and to properly set the accuracy and the safety of the simulation.

4.3.1 Instability problems and error propagation

The propagation of errors in the PHIL closed-loop is due to the fact that the real-time simulation is normally performed in the discrete domain. The continuous feedback signals that are sent from the HUT to the real-time simulator are translated into samples in a discrete time-line. A generic physical electric system can be represented as shown in *Fig.40*.

The system has the function of a voltage divider and is always stable in a real application [35]. If the voltage source V_s and the source impedance Z_s are simulated, a voltage amplifier must be used to translate the simulated voltage V_1 into the physical voltage V_2 imposed on the load. In the same way the real current i_2 is measured and sent as feedback in the simulation, where is modelled as a virtual current source i_1 .

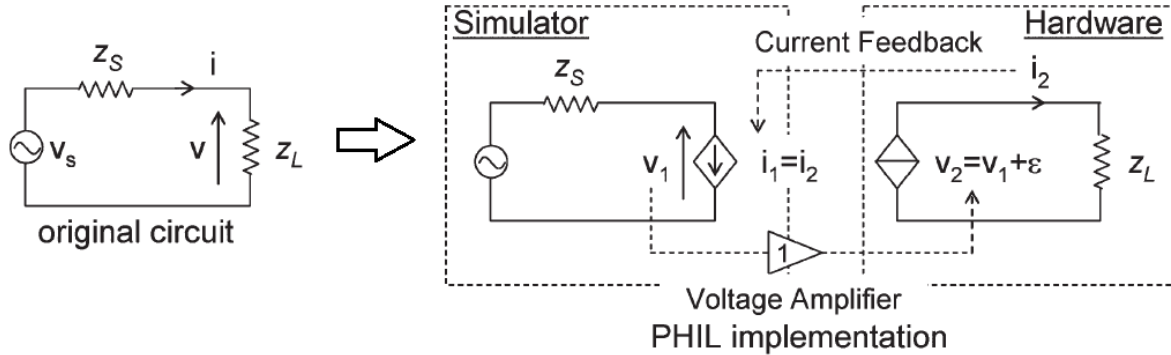


Fig. 40: Instability in PHIL is shown in the simulated voltage divider circuit [35].

The voltage amplifier is the primary cause for the introduction of errors. In the generic instant t_k the amplification of v_2 might propagate an error as follows:

$$v_2 = v_1 + \Delta v_2(t_k) = v_1 + \varepsilon \quad (49)$$

$$i_2 = \frac{v_2}{z_L} \rightarrow \Delta i_2(t_k) = \frac{\varepsilon}{z_L} \quad (50)$$

When the current i_2 is fed back to the simulation an ulterior error is introduced in the simulated voltage:

$$v_1 = v_s - z_s * i_1 = v_s - z_s * i_2 + \Delta i_2 \rightarrow \Delta v_1(t_{k+1}) = -\frac{z_s}{z_L} \varepsilon \quad (51)$$

For every successive time step the error is amplified by the magnitude of the impedance ratio: if the value is greater than 1 the error keeps to increase until the hardware limit is reached. The system results unstable.

4.3.2 PHIL stability analysis

The stability of the PHIL system is checked by confronting the open-loop transfer function of the overall system with the *Nyquist stability criterion*: the OL function must not encircle the point $(-1, 0)$ on the complex plane. In the example in *Fig.40* the transfer function is obtained from the generic PHIL block diagram in *Fig.41*, assuming T_{11} and T_{21} equal to zero:

$$G_{OL}(s) = T_{12}T_{Amp}T_{22}T_{Filter} \quad (52)$$

The block diagram can be customized based on the characteristics of the HUT, the interface and the simulated power system.

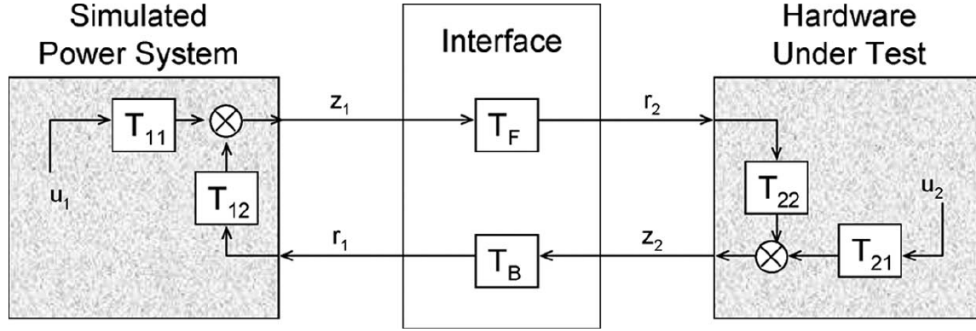


Fig. 41: PHIL generic block diagram [35].

In the diagram in *Fig.41* u represents internal stimuli, z and r represent the voltage/current signals exchanged between the two subsystems and T is representative of the impedance matrix. For the study it's important to define the transfer function of the power amplifier and the filters:

$$T_{Filter} = e^{-sT_s} \quad T_{Amp} = e^{-sT_d} \cdot T_{Filter} \quad (53)$$

where T_s and T_d are the delay introduced by the filter and the amplifier. The amplifier transfer function is obtained considering the time delay introduced by the output filter of the RTS DC/AC converter. A unity gain is considered assuming that the amplifier operates in its working bandwidth range, thus the only non-ideal behaviour is introduced by the control delay.

4.4 Interface methodologies

The stability in a PHIL system is necessary to obtain accurate simulation results and to preserve the physical components from damages. The stability problems can be solved or reduced by using an *Interface Algorithm* (IA). The IA is entitled to set the type of signal transmitted (typically voltage or current) to the RTS, the way signals are processed (*e.g.* filtering, noise reduction, bandwidth) and when the signals are transmitted during the simulation time-step. The topology of the control algorithm is chosen to be either in voltage or current, depending on the amplifier built in the power interface: a voltage control is used to pilot the voltage output of the amplifier, a current control to pilot the current output.

The introduction of the IA in the simulation loop might as well introduce instability. The stability and accuracy analysis is performed to study the whole power interface system (delay, noise, bandwidth, gain).

The stability region for safe operation is obtained depending on the topology of the interface and the value of impedances of the connection, accordingly with the Nyquist criterion. Different IA solutions are proposed in the literature and are briefly introduced below.

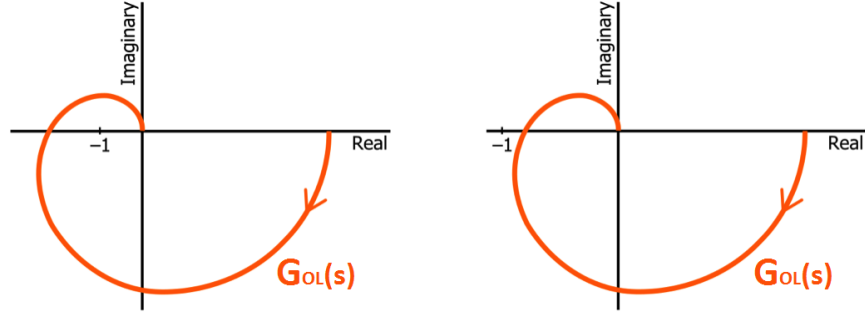


Fig. 42: Nyquist stability criterion. In a stable system the OL function must not encircle the point $(-1,0)$, as shown by the second graph.

4.4.1 Ideal Transformer Method (ITM)

The ITM method is the most common IA, given its simple implementation with high accuracy and low computation requirements. The ITM can be realized with voltage/current amplifier control and current/voltage sensor feedback (*Fig.43*). The ROS and the HUT are represented with a *thevenin equivalent*, where their equivalent impedances are respectively Z_{ROS} and Z_{HUT} . The open-loop transfer function for ITM is determined for both voltage and current type. Referring to the *V-type*:

$$G_{OL(V-type)}^{ITM}(s) = -\frac{Z_{HUT}}{Z_{ROS}} e^{-s(T_d+2T_s)} \quad (54)$$

The system stability is dependent by the value of the impedance ratio and by the total delay introduced by the power interface [36]. The stability is obtained by respecting the following criteria:

$$\left| \frac{Z_{ROS}}{Z_{HUT}} \right|_{V-type} \leq 1 \quad \left| \frac{Z_{HUT}}{Z_{ROS}} \right|_{I-type} \leq 1 \quad (55)$$

A way to improve stability in a ITM interface is by means of a low-pass filter on the feedback circuit, with the consequence of reducing the overall accuracy. Another possibility is given by the shift of a portion of virtual Z_{ROS} to the HUT side. The insertion of a new portion of physical impedance might however increasing the costs, especially for large PHIL systems (MW-level systems).

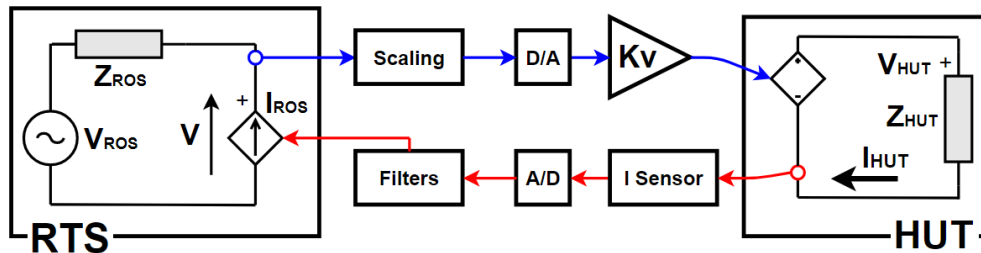


Fig. 43: Voltage type ITM. The amplifier controls the HUT voltage with a current feedback [33], [36].

4.4.2 Transmission Line Method (TLM)

The TLM method is obtained by implementing a linking inductor or capacitor to interface the RTS with the HUT (Fig.44). The reactive element is used to represent a transmission line and can be described by a thevenin equivalent. The impedance can be expressed in inductive or capacitive terms as [35]:

$$Z_{lk} = \frac{L}{\Delta T_d}; \quad Z_{lk} = \frac{\Delta T_d}{C}; \quad (56)$$



Fig. 44: Linking inductor or capacitor in a TML connection [35]

The term ΔT_d is the travel time transmission line, that in the PHIL simulation is translated into the total time delay. The time delays introduced by A/D conversion units, amplifier, sensors and filters are taken into account while selecting the minimum length of the transmission line interface, in order to ensure the system stability.

$$\Delta T_d = l\sqrt{LC} > t_{A/D} + t_{D/A} + t_{amp} + t_{filt} + t_{sensors} + \Delta T_{time-step} \quad (57)$$

The open-loop transfer function is written as:

$$G_{OL}^{TLM}(s) = \frac{1 - \left(\frac{Z_{ROS} - Z_{lk}}{Z_{ROS} + Z_{lk}} \right) e^{-2s\Delta T_d} Z_{ROS}}{1 + \left(\frac{Z_{ROS} - Z_{lk}}{Z_{ROS} + Z_{lk}} \right) e^{-2s\Delta T_d} Z_{lk}} e^{s(\Delta T_d + 2T_s)} \quad (58)$$

The TLM method is highly stable. The main limitations are the reduced accuracy, due to power loss in the linking impedance, and the major complexity in the PHIL implementation. The wiring and the sizing of the linking impedance must be changed every time the circuit configuration changes, reducing the overall flexibility of the system in different situations. Additional errors are introduced in the PHIL simulation if using a fixed total time delay, as the real total time delay varies with the test conditions and the frequency of the simulation.

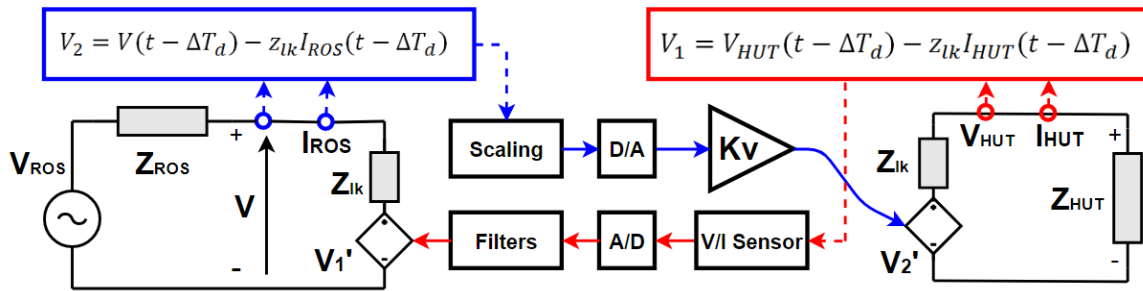


Fig. 45: TLM Thevenin Equivalent [33].

4.4.3 Partial Circuit Duplication (PCD)

The PCD method requires a linking impedance Z_{ab} both in the simulated system and in the HUT (Fig.46), similarly to the TLM [33]. Large values of the linking impedance improves the stability of the interface, solving the stability issues of the ITM method. The open loop transfer function of the PCD method is given by:

$$G_{OL}^{PCD}(s) = \left(\frac{Z_{ROS}Z_{HUT}}{(Z_{ROS} + Z_{ab})(Z_{HUT} + Z_{ab})} \right) e^{-s\Delta T_d} \cdot T_{Amp}(s)T_{filt}(s) \quad (59)$$

The complexity of the circuit is increased by the introduction of the linking impedance. The Z_{ab} is also required to have an higher value than Z_{ROS} and Z_{HUT} , and as consequence it introduces major inaccuracies due to increased power losses. The method is nonetheless promising for large-scale systems and circuits.

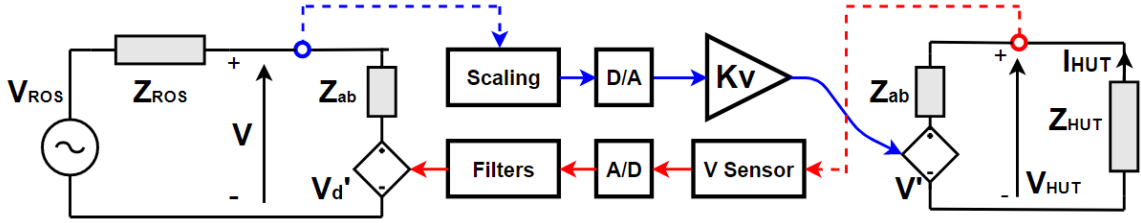


Fig. 46: Voltage type PCD [33], [36].

4.4.4 Damping Impedance Method (DIM)

The DIM method is a generalization of the ITM and PCD methods. The linking impedance Z_{ab} is generally neglected, if the value is small, and a damping impedance Z_{damp} is inserted in the simulated circuit (Fig.47). The DIM is characterized by an higher accuracy, and also a higher region of stability, if compared to the ITM. The stability of the system increases and reach its maximum when the value of the damping impedance is equal to the impedance of the HUT: in this case the magnitude of the transfer function goes to zero and the system is completely stable.

$$G_{OL}^{DIM}(s) = \left(\frac{Z_{ROS}(Z_{HUT} - Z_{damp})}{(Z_{ROS} + Z_{ab} + Z_{damp})(Z_{HUT} + Z_{ab})} \right) e^{-s\Delta T_d} \cdot T_{A/f}(s) \quad (60)$$

The exact value of the HUT impedance is not always known exactly, but can be esteemed.

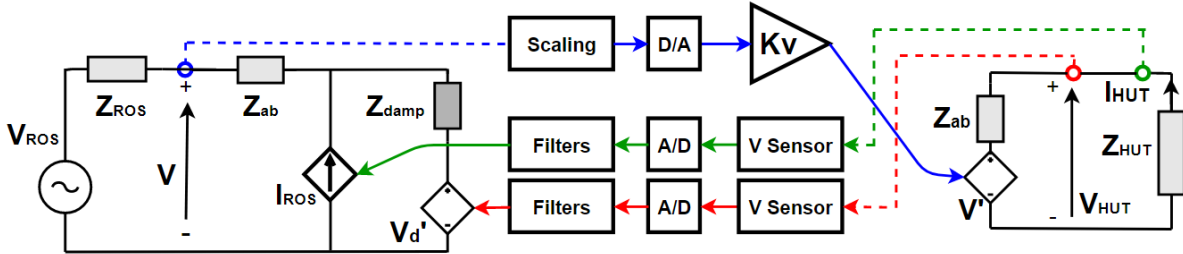


Fig. 47: Voltage type DIM [33], [36].

4.5 PHIL field applications in power systems

The application of fully digital RT simulations in power systems, made possible by the computers evolution by the end of the 1990s, was initially focused on a wide range of *transmission systems applications*, such as:

- protection systems tests;
- implementation and improvement of protection/defence strategies against voltage collapses and frequency instability;
- improvements on the implementation of electronic devices for voltage support;
- test and integration of large HVDC transmission links in the grid;
- assessment of the impact of large integration of RES generation on the grid.

The use of a RTS modeling for the transmission systems is useful to perform a partition of the network model into smaller sections. The advantage is to allow to multiple processors to perform a parallel computation of the nodal voltages. The network sections are made in reference to the propagation delay of the travelling waves: typically, to solve a 50/60 Hz power system grid-scale model, a RTS requires generally $50 \div 100 \mu s$ time-step to obtain an adequate resolution (*Fig.48-a*). The computing capability of the simulator depends by the number of nodes/buses in the simulated system and the time-step required. The system model is split when the propagation time exceeds the time-step of the simulation, in order to avoid an overrun in the execution of every time step (*Fig.48-b*).

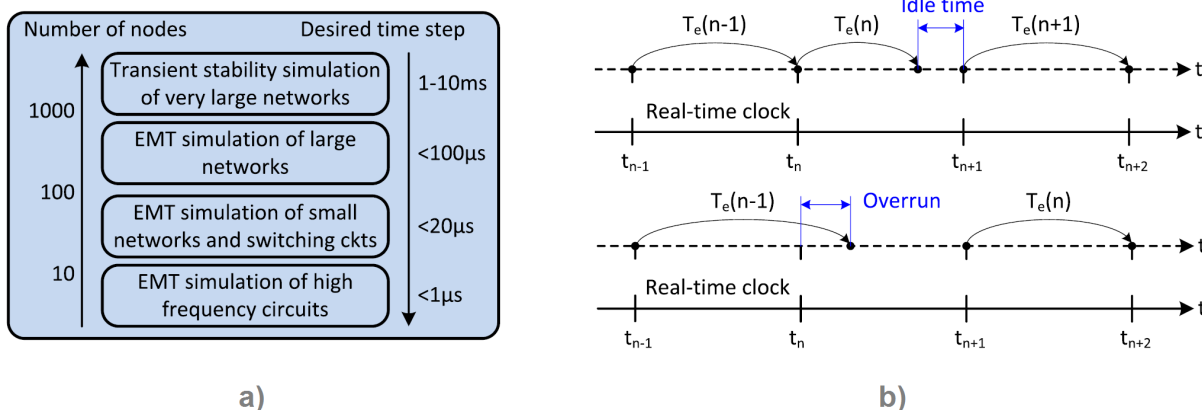


Fig. 48: a) Computing capability and time steps requirements for different PHIL applications. b) Comparison of real-time simulation and non-real-time (offline) simulation [37].

The RTS has more recently been applied to *distribution systems applications* with the main purpose of developing smart grids and micro-grids studies. Distribution systems are characterized by short length feeder lines and by the presence of high-frequency power electronic converters. The propagation delays are way shorter, if compared to transmission lines, and the execution of EMT simulation becomes more challenging (with typical time-steps of $1 \div 10 \mu s$), as the system can't be partitioned for parallel processing without the risk of creating loops [38]. For most cases, when the fast transient behaviour of the network is not of interest, a more simple *phasor RTS* can be used to analyse large-scale distribution systems [39].

The PHIL method is becoming particularly popular because of the derisking of power systems, power electronics and other electrical devices before the the actual implementation in working systems. Some of the main field applications in distribution systems are:

- voltage regulation with distributed generation (DG) in smart grids;
- PHIL simulation of power control and voltage capability of CIG units connected to the grid;
- real-time operation and control of micro-grids;
- control applications to enable synthetic inertia response of DG sources.

Applications in realistic systems are explored to study the response of components in a microgrid or in a low-inertia environment. In general, for power systems applications, PHIL is implemented for flexible tests and data collection in more advanced phases of device development, before performing field tests for the final integration with the grid [38]. Various examples of PHIL applications in the study and management of low inertia power systems are proposed.

4.5.1 Megawatt-scale PHIL for tests of drive systems

The implementation of PHIL for tests and validations of high power applications is particularly challenging, given the fact that high-precision amplifiers for interfacing HUTs with the RTS are typically not available for high power capabilities. Despite the cost of specifically designed systems, the PHIL simulation is particularly advantageous in various stages of motor drive development, by testing single components and sorting out eventual defects in their manufacturing. Motors can also be tested in extreme scenarios or in applications they were not initially projected for, maintaining low risks and costs.

Specific facilities can be built to perform high-scale PHIL tests. An example is discussed in [41], where a 5 MW facility was built to conduct PHIL simulations at megawatt levels (*Fig.49*). The utility system supplies two *variable speed motor drives* (VSDs) via a power amplifier.

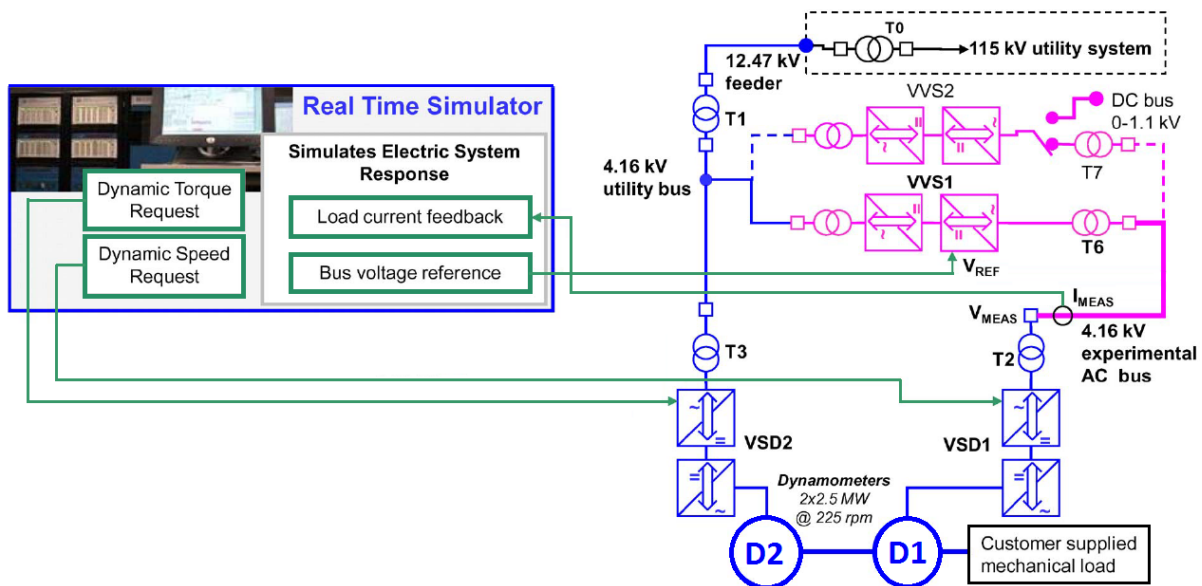


Fig. 49: 5 MW facility layout for PHIL applications [41].

The power amplifier, used to perform the physical interface, is a 5 MW double *Variable Voltage Source* (VVS1 and VVS2). Each VVS is made of two bidirectional converters with active front-end stage connected to the utility supply via the 4.16 kV transformer T_1 . The amplifier structure can be used in *normal mode* to control the voltage output magnitude up to the line-to-line voltage, or in *bypass mode* to use the instantaneous voltage waveform of the simulator as input for PWM in the second section of the converter. The *Variable Speed Drives* (VSD1 and VSD2) are connected to two 2.5 MW dynamometers (D1 and D2) with single shaft, normally used to counteract customer supplied mechanical loads.

The RTDS is used to simulate the response of an electric system. Voltage references can be sent to control the VVS's output and a current feedback is retrieved from the HUT at the measure point on the experimental AC bus. Both motor drives VSD1 and VSD2 can accept torque or speed reference from the simulator and allow a four-quadrant operation of the dynamometer shaft.

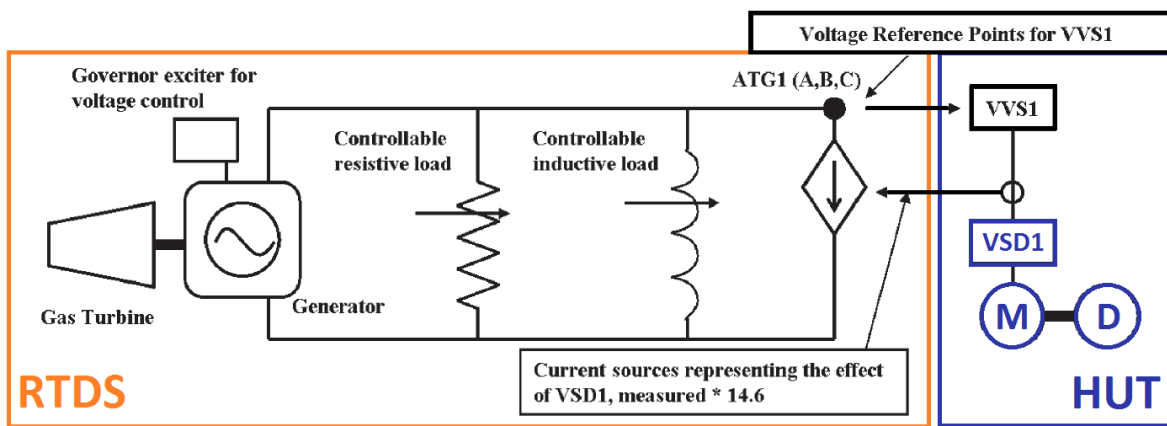


Fig. 50: One line schematic of the PHIL simulation, interfacing the simulated power system with the 2,5 MW motor drive [41].

A PHIL study performed at the facility was aimed at integrating a commercial motor drive of 2,5 MW rated power with a simulated power system, to evaluate the impact on the system performances. The RTDS was used to model the power system (*Fig.50*). A detailed 4 MW - 5 MVA gas turbine generator (comprehensive of an high-order synchronous machine model, a prime mover and a governor) was implemented using simulator libraries. Additional resistive and inductive controllable loads were added.

The simulated network is interfaced to the HUT, where the motor is controlled by the motor drive VSD1 and is connected to a single 2.5 MW dynamometer D_1 . The power interface is performed using the VVS1, linked to the simulated system at node ATG1, where the bus reference voltage is extracted to control the power amplifier. The VVS1 feedback currents are received by the simulation using a current source to represent the effects of the physical drive. The currents are measured on the 4,16 kV side of the transformer T_2 , implying the use of an ideal transformer interface (ITM Interface Algorithm) for the PHIL simulation. As discussed in **section 4.4.1**, the ITM interface is simple, but affected by possible instability: a first-order low-pass filter was introduced between the current measurements and the references applied to the current sources.

Experimental PHIL cases have been performed to test the system stability while working with the motor drive. The VSD2 drive was operated with utility bus feeding to apply a load torque to the HUT via the dynamometer M_2 .

Tests were carried out with 75 % of the dynamometers nominal speed. The gas turbine generator response was studied for various situations with resistive load steps (*Fig.51-a*), inductive load ramps (*Fig.51-b*) and load torque oscillations (*Fig.51-c*).

The generator reacted to load changes of tests *a*) and *b*) by adapting the output active and reactive power. Minor voltage sags and frequency changes were observed during the load shifting before reaching a new steady state. All the variations of the simulated bus voltage were reproduced in the real world, and fed to the VSD1, using the VVS1.

In case *c*) the load torque was obtained by controlling D_2 to superimpose oscillations on the average value. The motor drive VSD1 was then controlled in speed mode to compensate the oscillating load: as expected the voltage output was flat and the generator's output active power reflected the frequency oscillation.

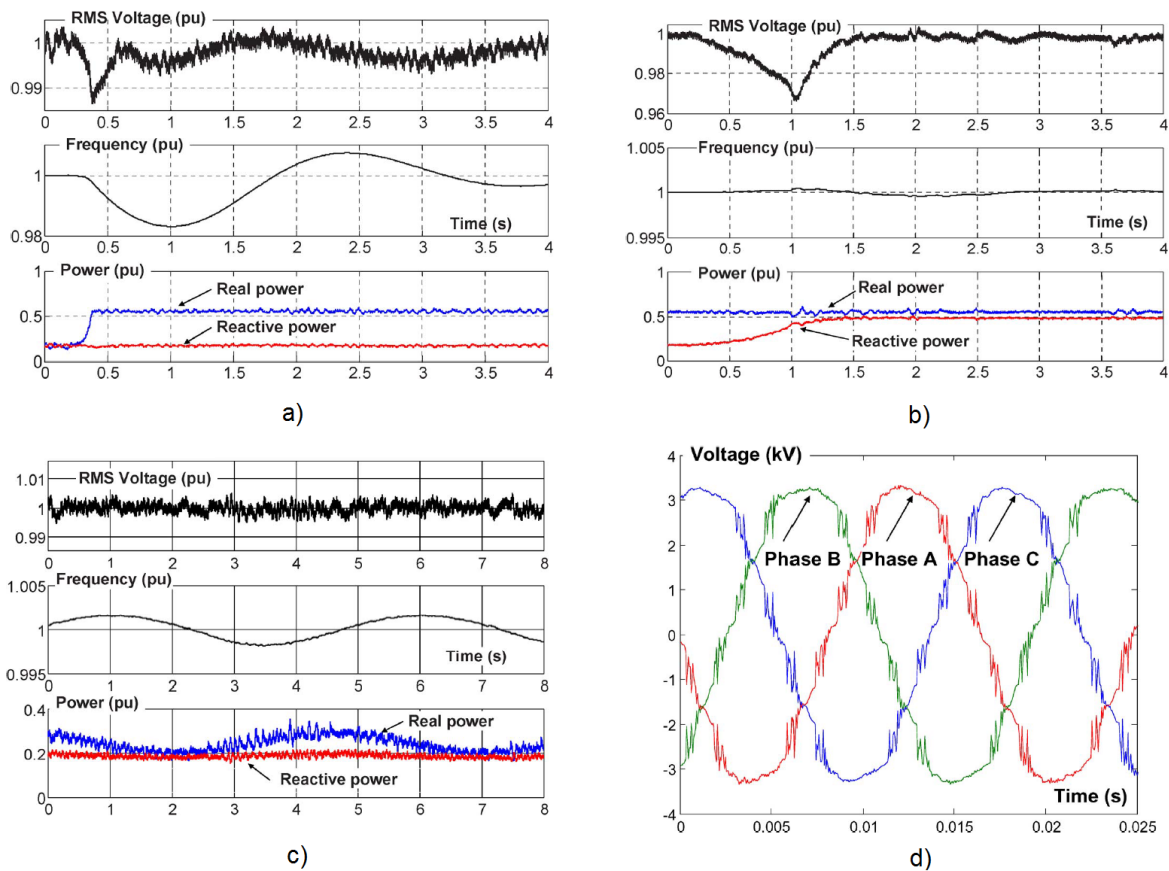


Fig. 51: PHIL tests on the power system response: a) 2 MW resistive step load; b) inductive load 50 mH/s ramp; c) $\pm 10\%$ load torque oscillations @ 0,2 Hz; d) Measured bus voltage (ATG1). [41]

The effectiveness of the experimentation proves that is possible to perform PHIL simulation at megawatt level. The existence of dedicated facilities is useful to study and validate models of high power drive systems and to test MW motors in any relevant electric system condition.

4.5.2 Test of a 500 kW PV array inverter

The increasing diffusion of DG technologies for microgrid and renewable applications require the implementation of power converters for interfacing different sources with the grid. Inverters for *photovoltaic applications* (PV) are normally tested in laboratory environment for specific reference conditions. However, to evaluate the performances of large-scale inverters (kW/MW levels) before installation, an approach that can simulate the real field conditions is preferable to evaluate the inverter behaviours in the grid.

Authors in [42] studied the dynamic behaviours of a solar PV inverter with variable voltage, variable frequency and fault conditions. Reactive power control and the impacts on the system were analysed to collect data and further develop models to assess the potential impact of DG technologies on the grid. The PHIL was introduced to connect the real inverter (*HUT*) with the model of a distribution system, simulated in real time by the RTDS (*Fig.52*). The inverter was tested in the facility described in *Fig.49*, where the power amplification is performed by a 5 MW VVS.

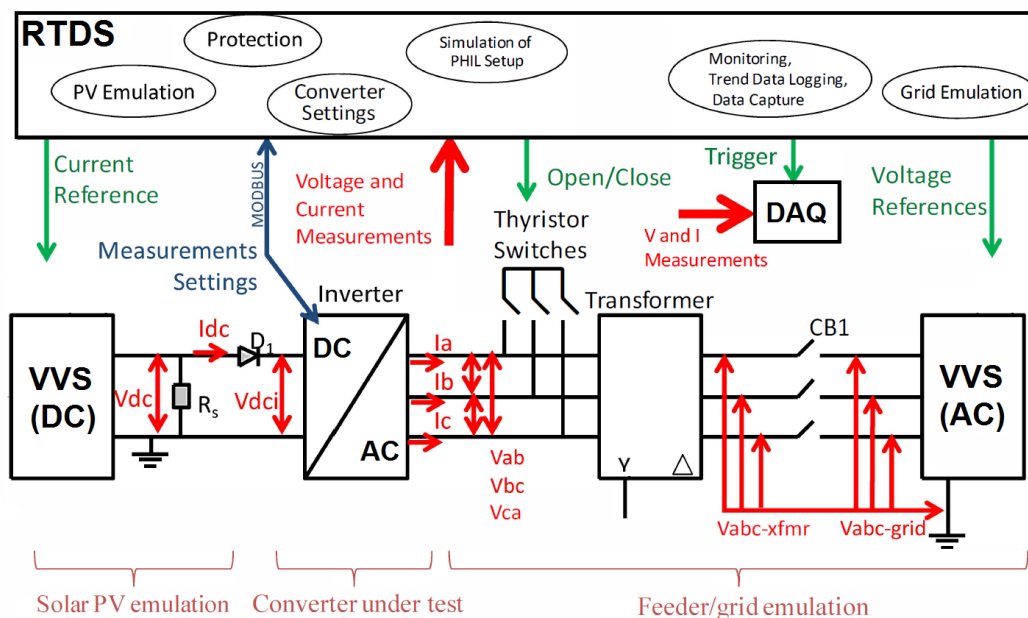


Fig. 52: PHIL test setup of the 500 kW array inverter. [42]

The inverter under test was connected on the DC side to a VVS_{DC} , operated in current mode to simulate the PV array. The emulation followed a simple voltage-current characteristic in maximum power point tracker (MPPT) mode, to dynamically control the inverter output power. The connection is made of a parallel bank load R_S and a protection diode D_1 , that imposes unidirectional current flow. On the AC side the inverter was connected to the power amplifier VVS_{AC} via a step up 480 V/4.16 kV transformer. Thyristor switches were used to apply various fault types (single-phase, three-phase, line-to-line) to the inverter, and a circuit breaker $CB1$ was used to simulate abrupt disconnections from the grid for analyse islanding behaviours.

Various current and voltage measurements were performed and sent to the RTDS for monitoring, control and data recording. The simulator provides reference current for the VVS_{DC} PV emulator, reference voltage for the VVS_{AC} and on/off signals for the thyristor switches. An additional *MODBUS* link channel was used to control the inverter to set the power factor or the reactive power contribution in the grid.

Tests were mainly focused on the interfacing of the inverter with the grid. During tests the reference voltage was applied in the physical point of common coupling PCC and the reactive power supplied by the inverter was injected in the PCC towards the simulated network. A first series of tests was conducted with open-loop PHIL, without confronting the VVS_{AC} reference voltage with a feedback. The main objective was to evaluate the current limiting and transient behaviours of the inverter for various levels of power:

- over-voltage deviations were applied to evaluate the time needed to induce a trip in the inverter protections, both in balanced and unbalanced conditions;
- under-voltage deviations were applied to evaluate the voltage threshold under which the inverter would go offline from the grid;
- frequency deviations ($\pm 0.8 Hz$) were applied to evaluate the trip time during disturbances;
- the circuit breaker $CB1$ was opened to study the inverter response in detecting the island condition and shut down, as well as analyse it's transient conditions and impact on the grid.

A second series of test was performed in closed-loop PHIL to explore the reactive power control capability of the inverter and the interactions with a simulated distribution grid with a large share of PV generators. The irradiance profile of PV generators was varied at the PCC referring to three different real load profiles based on real data collections (*Fig.53-a*). Authors observed that the impact of the inverter on the grid bus voltages was negligible, while voltage fluctuations at the PCC where more significant. Nonetheless, the inverter measured voltage V_m was able to follow the simulated PCC voltage V_{sim} and the reference voltage of the VVS_{AC} . Measured active/reactive power P_{act} and Q_{act} were fed back to the simulation, that successfully reproduced the real power injection. The inverter operated with constant power factor absorbing reactive power. In *Fig.53-b* operation with the moderate PV profile is shown. Scaled PHIL tests were also performed by scaling the $500 kW$ inverter up to $2 MW$, applying a factor of 4 the injected currents and the rating of the power amplifier. Scaling tests allowed to study more scenarios for the scaled inverter.

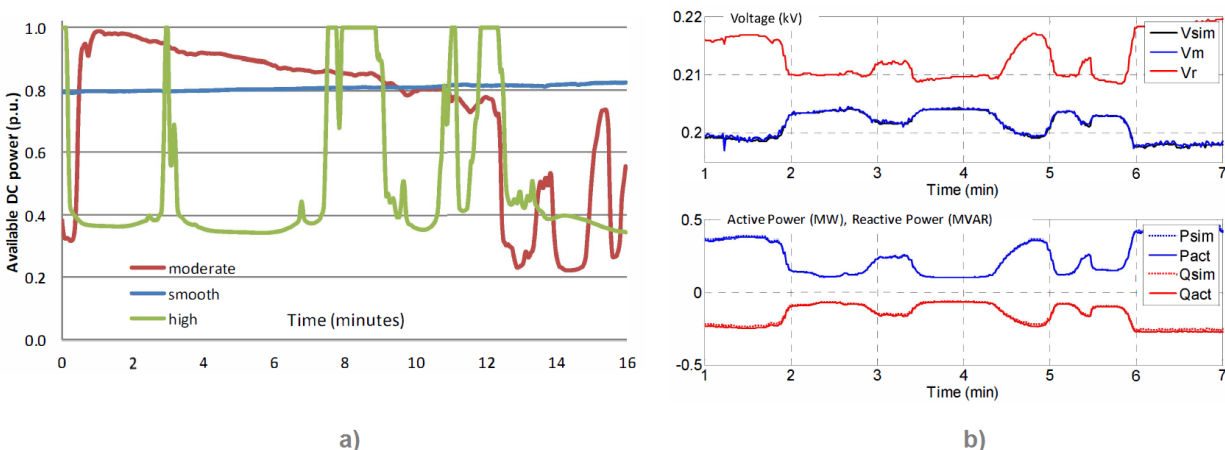


Fig. 53: a) Normalized PV power profiles of the simulated grid. b) Voltage and power response tracking of the inverter with moderate PV power profile. [42]

4.5.3 Tests of a voltage controller for deployment in a low-inertia power system

The necessity to enhance the frequency stability in a low-inertia power system requires the implementation of storages and devices that actively participate to frequency control. Authors in [43] have analysed different enhancement strategies using a combination of synchronous condensers (SCs) and the synthetic inertia of wind power plants (WPPs) in the Western Danish System, using a simplified simulation to represent a future RES-based version of the grid.

The participation of WPPs to frequency control has been addressed by TSOs grid codes, that allow onshore and offshore plants above a specific *MW* threshold to mimic the inertial behaviour response of traditional plants. The inertia response of WPPs is however too slow to react to severe frequency events. The presence of SCs, normally installed at specific bus locations to maintain voltage stability and perform reactive power compensation, provides additional inherent inertia to the system via their rotating parts and adds more time for primary control to react to disturbances.

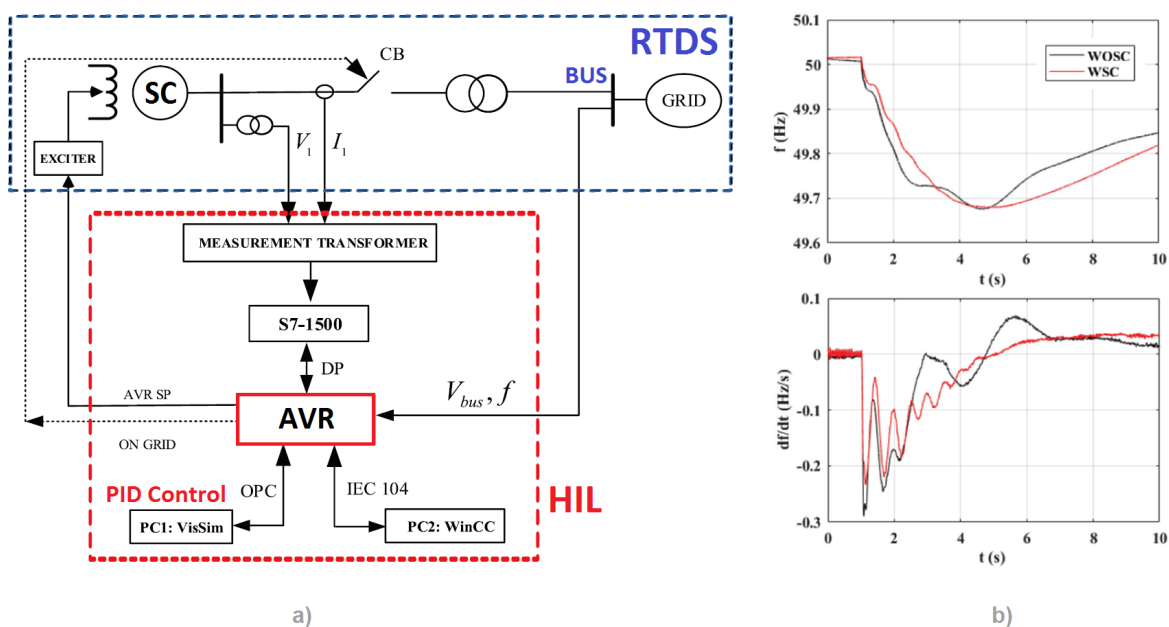


Fig. 54: a) PHIL for testing an physical AVR control over a real-time simulated SC system. b) Frequency and RoCoF response without SC (black) and with SC control (red) [43].

The whole power system (comprehensive of lines, plants, SCs and connections to neighbour systems) has been represented in RTDS. While performing stability studies, the authors have also tested a real *Automatic Voltage Regulator* (AVR) with the HIL method, connecting the physical device to the biggest simulated SC in the power system.

The HIL topology is shown in *Fig.54-a*: the RTDS sends to the AVR the measured currents and voltage from the SC's terminals and the measured frequency and voltage from the grid bus. The *AVR Set Points* are sent back to the simulation to control the field excitation and the connection status of the SC. A PID controller is implemented by an external PC1, while a constant monitor system is used on PC2 to study the SC behaviours for long real-time periods. The AVR tests are performed and allowed at the same time to observe the frequency behaviours of the system. The presence of SCs on the power system makes the frequency profile smoother and reduces the RoCoF (*Fig.54-b*), as electric energy is instantaneously supplied in front of any disturbance.

4.5.4 Synthetic inertia control implementation in Distributed Energy Resources

The wide diffusion of DG and *Distributed Energy Resources* (DERs) on the grid requires to improve the power system's inertia response by means of dedicated devices, such as VSGs and storage systems. The literature has also proposed the possibility to obtain *distributed synthetic inertia*, by means of DG resources and even by controlling DER units like local storages and domestic thermal loads. A practical application of a low-cost controller for synthetic inertia enhancement has been proposed in [44].

The controller is used to autonomously measure frequency and RoCoF from the power system, with the objective of implementing a virtual inertia control law that allows to manage the remote controlled DER. The unit must be equipped with a fast communication channel in order to receive the control signals. The DER power converter needs to be enabled fast enough to respond to frequency events in the time span of few milliseconds or cycles, implying that delays must be reduced as much as possible. The adopted solution is to move the RoCoF evaluation and the control at end-user level, where a *Fast Frequency Measurement* is adopted by the authors.

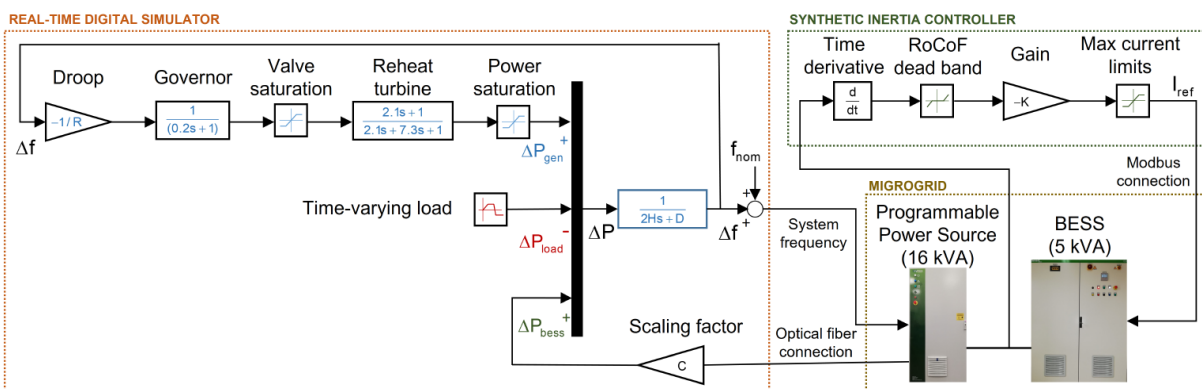


Fig. 55: Synthetic inertia control schematic for a DER with power system model PHIL implementation [44].

The PHIL methodology has been introduced to test the efficiency of the controller. The digital real-time simulator has been used to simulate the electromechanical response of an equivalent power system. As shown in Fig.55, the simulated power system generates frequency excursions with a fluctuating time-varying load. The frequency stability is maintained by implementing the primary frequency regulation algorithm, that represents the response of the synchronous generation. The power system's frequency is calculated in real-time and is imposed to the physical devices connected to the simulator.

An additional physical contribution to power control is given by the real DER, a 5 kV BESS system interfaced to the RTDS via an optical fibre connection. The BESS is controlled in grid-forming mode using a programmable power source. The *synthetic inertia controller* measures RoCoF and creates a proportional current reference I_{ref} to control the BESS system. A RoCoF deadband is typically implemented to avoid excessive BESS activity, that might negatively affect the battery lifespan, and I_{ref} is limited to the maximum charge/discharge power sustainable by the battery.

The authors run various tests to compare the system response without *Synthetic Inertia* (SI), with an ideal SI control (frequency "measurements" calculated by the RTDS) and with the standard SI control (frequency measurements and control performed by the low-cost controller).

The tests have been performed using a common reference, a steady-state system perturbed at $t = 0$ by a positive load step change equal to $+0.1 pu$, and then reversed back to normal after $35 s$ with a second load step of $-0.1 pu$. The primary frequency regulation was modelled with droop and governor parameters typical of a thermo-electric plant, while the inertia constant H has been reduced to simulate a low-inertia system. Secondary regulation was not modelled as the only interest is to simulate the ability of creating synthetic inertia with the BESS system in the first instants of the frequency event.

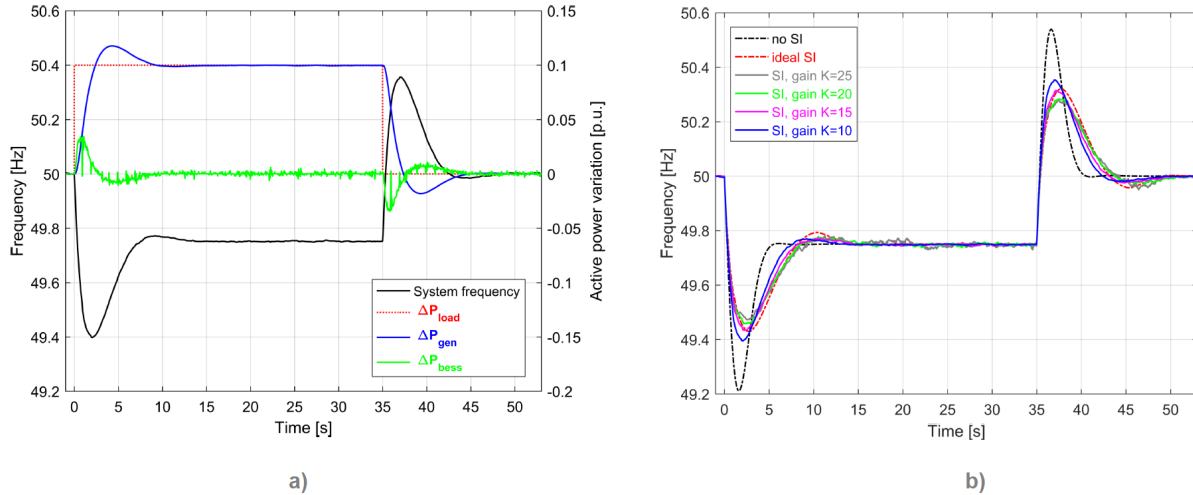


Fig. 56: a) Power and frequency trajectories with the SI controller. b) Frequency response without SI (black), with ideal SI (red) and with SI controller and variable gain K . [44]

The trajectories of frequency and active power while using the low-cost controller are shown in *Fig.56-a*. The BESS frequency response is obtained within the first few seconds after the frequency event. The errors on the RoCoF estimation are generally not negligible, so a smoothing low-pass filter was applied to the measured frequency, in order to preserve the accuracy of the BESS control. The filter introduces delays and as consequence the time response of the battery is slightly delayed if compared to the ideal case.

Overall the controller allows to effectively reduce the frequency nadir (*Fig.56-b*), obtaining smaller overshoots at the cost of an increased settling time. The controller has a different response based on the chosen gain value K : generally high gains help to reduce more the frequency nadir, but frequency fluctuations are increased by the amplification of RoCoF errors. Fluctuations corresponds to faster charge/discharge cycles of the battery, which are preferably avoided by choosing lower gain values or by setting a deadband (*Fig.55*).

The SI controller is in conclusion fast and accurate enough to perform a stable response and to reduce the frequency excursion during the transients, maintaining a low cost and allowing an autonomous frequency measurement from the local voltage bus.

5 Low-Inertia laboratory setup

The dynamic modelling work presented in the following sections is focused on realizing a model that can study the effects of virtual inertia on the grid without having a real microgrid at disposal. The model was built by referring to a real synchronous machine, in the optics of eventually perform PHIL studies with an hybrid physical-simulated system and real-time simulation. Real-time preparations and simulations were made possible by accessing the *Global Real Time Simulation Lab*, the real-time dedicated laboratory of the *Politecnico di Torino*. The laboratory is located at the *Energy Center* in Torino and is equipped by a main real-time simulator (OPAL RT5600), used for simulating big power grids, and by support real-time simulators (OPAL RT5700 and RTDS Novacor Chassis). Real-time simulators are sided by four power amplifiers, used for interfacing the simulated part with the real hardware on different power levels, and by two HBM measurement systems. The lab is connected with other international laboratories for multi-site simulations.



Fig. 57: Global Real Time Simulation Lab setup at the Energy Center in Torino.

The laboratory presents an initial hardware setup composed by a Marelli 60 kVA synchronous generator connected to a prime mover consisting in DC motor and a induction machine. During the development of the thesis the laboratory was still in the assembling phase and no PHIL test could be made. It has been decided then to create both the microgrid and the synchronous generator in a simulative environment, in order to prepare a full software model that can eventually be used for hardware tests in future works.



Fig. 58: Marelli Synchronous Generator nameplate.

6 Matlab/Simulink model of a micro hydro power plant

The in-depth study of the behaviours of low-inertia power systems and components can be performed in laboratory, by creating a PHIL workspace of both physical and virtual components. The possibility to use a physical synchronous generator can be useful to observe a realistic dynamic response in a simulated grid/microgrid context. However, in the initial step of development of the laboratory most of the physical components are not yet ready to fully operate in combination with the Real-Time Simulator.

A first step to prepare the PHIL environment for future tests with real hardware is then to create a model that includes a synchronous machine, for a full simulative study of low-inertia grids. The laboratory setup features a Marelli 60 kVA Synchronous Generator connected through its shaft and an electromagnetic joint to a prime mover (DC motor/Asynchronous motor), that will be used to simulate a turbine with a proper dedicated control (*Fig.59*). The objective is to create a model that can represent a power plant connected to the grid. Given the small size of the generator it has been decided to set up a micro hydroelectric power plant model ($P_{\mu Hydro} < 100 kW$) to study the behaviour of the synchronous machine into a small microgrid.

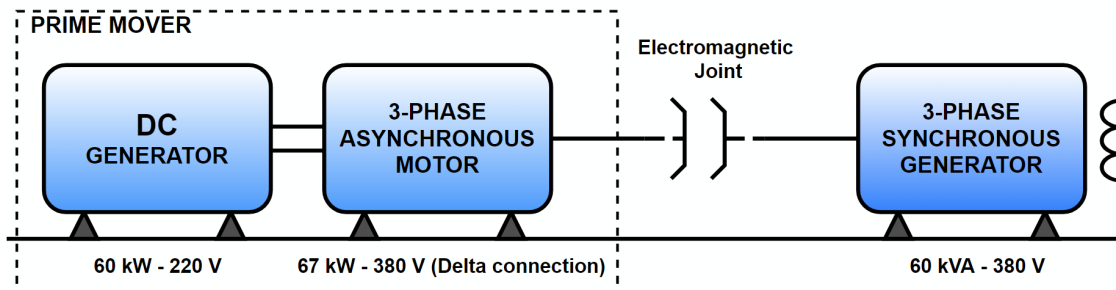


Fig. 59: Representation of the laboratory setup of the Synchronous Machine with prime movers.

The model has been developed using the *Matlab/Simulink* environment. The various components of the hydro plants are simulated using dedicated blocks of the *Simscape Specialized Power System* library. The *Simulink/Simscape* environment is suitable for Real-Time Simulation and PHIL applications, and models can be transferred to other simulations platforms using the C-code generation feature of Simscape. The following sections describe the aims and the building of the model, alongside its validation with tests on Simulink and on the RTDS hardware.

6.1 Aims of the modelling

The representation of synchronous generators in the stability analysis of a system depends on multiple factors, including the availability of data, the type of rotor structure, the computational capacity of the simulator and most importantly the purpose of the study. The area of study of low-inertia microgrids with PHIL is mainly focused on the *Post-Disturbances Analysis*, where the simulation of system evolution following major events (such as disturbances and blackout) is used to study how different components of the grid are affecting the grid.

Generally a detailed model representation of SGs, including the dynamics of field circuit and excitation systems, is preferred over simplified models. The choice is mainly related to the category of stability study and on the time domain of the simulation, that typically covers a time range going from tens of seconds up to few minutes (first instants + primary/secondary f/P regulation).

The categories of stability studies can be summarized as follows [45]:

- a) **Generator stability analysis:** the studies are focused on generators, in a time window in which control systems does not intervene and generation step losses can occur. A first approach is made for *large-disturbance rotor-angle stability analysis*, with a system under severe fault conditions. The transient response of SGs is significantly affected by the dynamics of the rotor circuit and dampers, that are necessarily modelled to accurately assess transient stability. *Small-disturbance rotor-angle stability analysis* is performed to study of the ability of the system to maintain synchronous operation when subjected to small perturbations. The models used should accurately take into account of damper-circuit effects, field circuit dynamics and the excitation control. *Voltage stability studies* can be made to check the ability of the power system to maintain steady voltages at all buses if subjected to disturbances. In this case SG models are focused on representing voltage controls and reactive power capability and do not require a detailed representation of rotor dampers parameters.
- b) **Frequency stability problems:** the power system performances are analysed after a severe system upset with a large discrepancy between generation and load. The focus is on the whole system behaviour and on the regulation function of generators controllers. The model is required to represent the generator response under large variations of voltage and frequency, taking into account the actions of prime movers, excitation systems and protections. A proper representation of the turbine/speed governor control and rotor dynamics is necessary.

The use of standard simplified models, that mainly neglects the effects of damper circuits from the full mathematical models of SGs, is useful to reduce the complexity and the computational efforts, reducing the time of simulation and allowing for large integration steps. The loss of precision can be accepted if the category of the study allows it. A further simplification is the classical “*voltage-behind-transient-reactance*” model, largely employed in early power systems studies. In this case the generator is represented by a simple voltage source E and a synchronous reactance X proportional to the field current supplied (and eventually the stator resistance R), as shown in *Fig.60*. This simplified model is mainly used for representing (remote) machines in large power system or to act as equivalent classical generator incorporating a group of coherent generators for dynamic-equivalencing techniques.

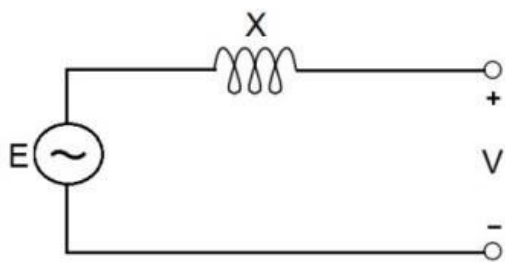


Fig. 60: voltage-behind-transient-reactance simplified model.

The purpose of the developed hydro plant model is to analyse a microgrid, and in general a system with limited quantities of hardware/components connected. The analysis of the low-inertia problem will be focused mainly on frequency stability, with particular attention to the small-disturbances transient response of an independent synchronous generator. The choice of the model complexity is then more oriented toward a full-detailed generator model rather than a simplified one.

6.2 Creation of the micro hydro plant model

The characterization of an *Hydroelectric Power Plant* (HPP) for simulation purpose is obtained by representing all its fundamental components in Matlab/Simulink. The layout of a HPP features a reservoir (a dam or a water basin), connected to a turbine by means of a simple penstock. The penstock is used to convert the potential energy stored in the water at a certain head H into kinetic energy. The kinetic energy obtained by the falling water at the end of the penstock is channelled on the blades of the turbine and converted into mechanical energy. The turbine acts as a prime mover and is connected to the generator to produce electric energy, fed to the grid (*Fig.61*).

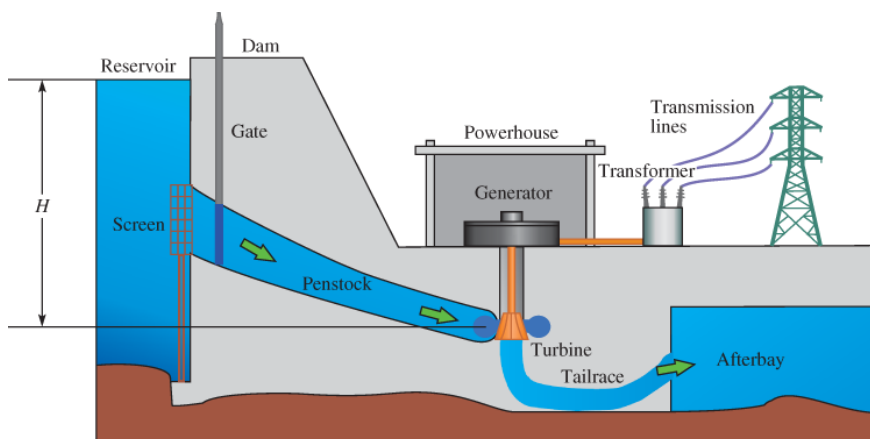


Fig. 61: Simplified schematic of an hydroelectric power plant [46].

The model must be able to accurately describe the behaviour of the water through the penstock [47] and the mechanical regulation of the prime mover, both needed to control the SG's electric power production. A turbine speed governing system (*Fig.62*) is implemented to adjust the generator speed by comparing feedbacks signal of the SG's measured frequency and output power with their relative references. The governor action is set to control the gate opening of the plant and to correct the output mechanical power. The objective is to ensure power generation at the synchronous frequency f_0 .

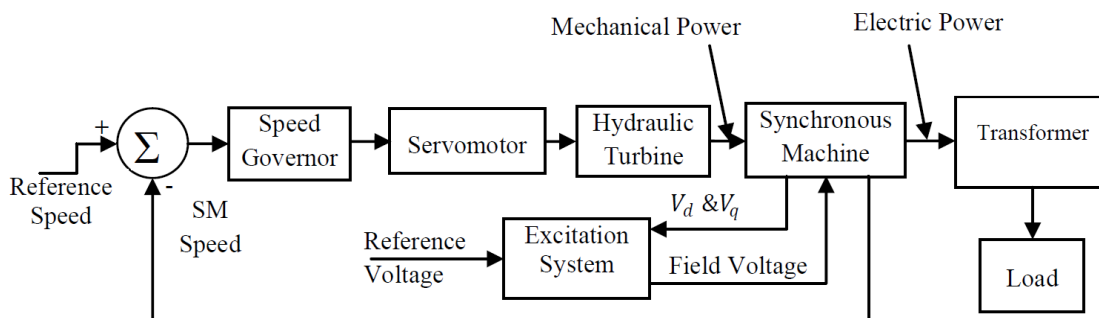


Fig. 62: Block diagram of the Hydroelectric Power Plant (HPP) model [47].

The hydroelectric plant can be thought to be composed of two main blocks, one being the *Synchronous Generator Block* and the other the *Hydraulic Turbine + Governor Block*. An additional *Excitation Block* might be needed to feed the required field voltage V_f to the machine, depending on the type SG model used.

6.2.1 Synchronous Generator Block (SG)

The *Simscape Specialized Power Systems* library presents two models for the simulation of three-phase synchronous generators: the *Simplified Synchronous Machine* model and the *Synchronous Machine* model, both showed in *Fig.63*. The models represent the electrical and mechanical behaviours of the machine, with a different degree of complexity for what concerns the electric characteristics. It is possible to choose between the standard SI units and pu units, based on the representation of available data and simulation necessities.

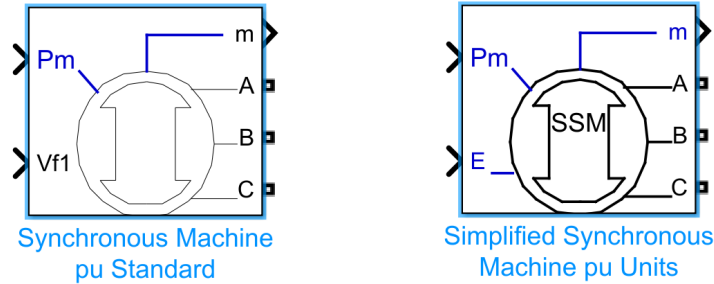


Fig. 63: Synchronous Machine models (Simulink Library browser → Simscape / Electrical / Specialized Power Systems / Fundamental Blocks / Machines).

The machine's mechanical system is equivalent for both models, and is represented by equations (61) and (62):

$$\Delta\omega(t) = \frac{1}{2H} \int_0^t [(T_m - T_e) - K_d\Delta\omega(t)]dt \quad (61)$$

$$\omega(t) = \Delta\omega(t) + \omega_0 \quad (62)$$

where the speed variation $\Delta\omega(t)$ is computed with respect to the speed of operation ω_0 ($1 pu$) and using the constant of inertia H . The output value is the mechanical rotor speed $\omega(t)$. The Kd damping coefficient is used to simulate the effect of the damper windings of the synchronous machine. The electrical system, instead, is different for the two blocks:

- The *Simplified Synchronous Machine* model consists, for each phase, of a voltage source in series with a RL internal impedance, with the inductance value $L > 0$ (*source-behind-synchronous-impedance* model of *Fig.60*). The model neglects the damping and the effects of all the self/magnetizing inductances of the armature and field circuits. The damping windings effect is approximated using the damping factor Kd .
- The *Synchronous Machine* model features a six-order representation that takes into account the dynamics of the stator, field, and damper windings. The rotor dq axis frame equivalent circuit is shown in *Fig.64*. The dynamic model for stability analysis normally considers identical the mutual inductances between the armature, damper, and field on direct-axis windings. However, for field current studies, a corrective term is introduced to represent the difference between field-damper and field-armature mutual inductances on d-axis. The term is called Canay inductance and corresponds to the leakage flux Φ_C between the two windings.

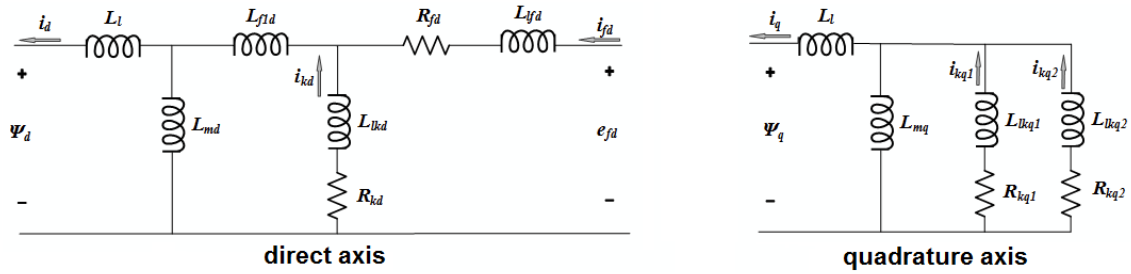


Fig. 64: IEEE standard 1110-2002 equivalent dq axis dynamic model. All parameters are viewed from the stator's point of view (l = leakage, m = magnetizing, f = field, k = damper) [45],[48].

The models can be implemented in a power system to perform stability studies by means of the *Load Flow Utility* of the Simulink Powergui. The generator's initial conditions are automatically set while performing the load flow computation before the start of a simulation. A dedicated *Load Flow Tab* is used to choose the generator type (PV, PQ, Slack) and its initial active/reactive power generation and limits for each case. Both blocks have two inputs. The first input is the mechanical power P_m , fed by an external signal (e.g., by a prime mover), used to determine the machine's rotor speed by means of the internal inertia J (or H) and the difference between the relative mechanical torque T_m and the internal electromechanical torque T_e . The second input is the field voltage V_f , which is fed by an excitation system to provide the adequate value to control the generator. In the *Simplified Synchronous Machine* the field voltage is replaced by the internal voltage E , represented by the voltage source in *Fig.60*, and can be automatically set by using the *Load Flow Utility*.

6.2.2 Hydraulic Turbine and Governor Block (HTG)

The hydraulic prime mover is represented by the *HTG Block*, which is comprehensive of a non-linear hydraulic turbine model, a PID governor and a servomotor. The block compares the rotor speed w_e and output electric power $P_{e,0}$ (w_e and $Pe0$ in *Fig.65*) of the generator with the reference values w_{ref} and P_{ref} . The power error $P_{ref} - P_{e,0}$ is processed through a permanent droop and is added to the speed error. The output of the PID governor is used to control the servomotor, that regulates the gate opening of the penstock and subsequently the mechanical output P_m of the hydraulic turbine.

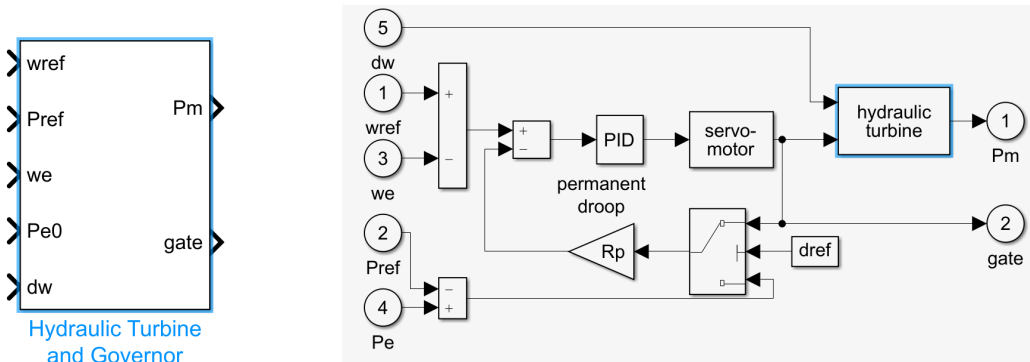


Fig. 65: Hydraulic Turbine and Governor (HTG) (Simulink Library Browser → Simscape / Electrical / Specialized Power Systems / Fundamental Blocks / Machines).

The performances of the hydraulic turbine are mainly influenced by the characteristics of the water column, that includes water inertia, water compressibility and the penstock pipe wall elasticity. The water inertia is directly related to the lag between the gate opening and the changes of the turbine output. The elasticity describes the travelling waves of pressure and flow that can lead to the ‘water hammer effect’ along the pipeline. The HTG non-linear model (*Fig.66*) is referred to a simple turbine under the hypothesis of non-elastic water column, incompressible water and no surge tanks [49]. Non-linear models are necessary in different situations, especially when the turbine is subjected to large speed/power variations, a typical case for isolated power stations.

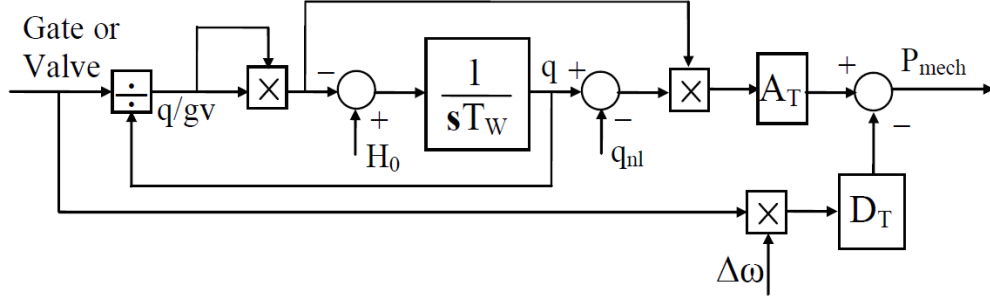


Fig. 66: IEEE Working Group non-linear model of the turbine with non-elastic water column [49].

Assuming a conduit of length L and cross-section A , the change of flow in the penstock is:

$$\frac{d\bar{q}}{dt} = (\bar{h}_0 - \bar{h} - \bar{h}_l)g \frac{A}{L} \quad (63)$$

where \bar{q} is the turbine flow rate, g is the gravity acceleration, \bar{h}_0 is the static head of the water column, \bar{h} is the head of the turbine admission and \bar{h}_l is the head loss due to friction. The equation can be expressed in per unit (full scale over-lined values are divided by \bar{h}_0) introducing the water time constant or water starting time T_W , as shown in equations (64) and (65).

$$\frac{dq}{dt} = \frac{(1 - h - h_l)}{T_W} \quad (64)$$

$$T_W = \frac{L \cdot q_{base}}{A \cdot h_{base}g} \quad [s] \quad (65)$$

The base quantities are arbitrary and the usual choice is to set q_{base} equal to the turbine flow rate at fully open gate ($G = 1$) and h_{base} equal to the static head. By omitting the head loss h_l , the per unit flow rate of the turbine is function of the gate position G and the head h :

$$q = G\sqrt{h} \quad (66)$$

Hence, by using equation (66) it is possible to define the turbine mechanical power P_m

$$P_m = A_t h (q - q_{nl}) - D_T G \Delta \omega \quad (67)$$

expressed considering the inefficiencies of the turbine by subtracting the no-load flow term q_{nl} from the total flow q . A_t is the turbine gain, a proportional factor that converts the gate opening to per unit turbine power on the power base S_B of the generator [49].

A supplementary term of speed deviation, characterized by a damping factor D_T due to the gate opening, can be subtracted. The Simulink HTG model presents some differences from the reference non-linear model, as shown in *Fig. 68*. The gain A_t is not used to scale the turbine/governor to the generator base, but instead to convert the *real gate position* g to the *ideal gate position* G . The different approach is given by the fact that the real gate position g generated by the servomotor is referred to the range from fully close to fully open gate position $[0 \div 1]$. The turbine is instead operated in a range going from no load to full load gate position $[g_{nl} \div g_{fl}]$.

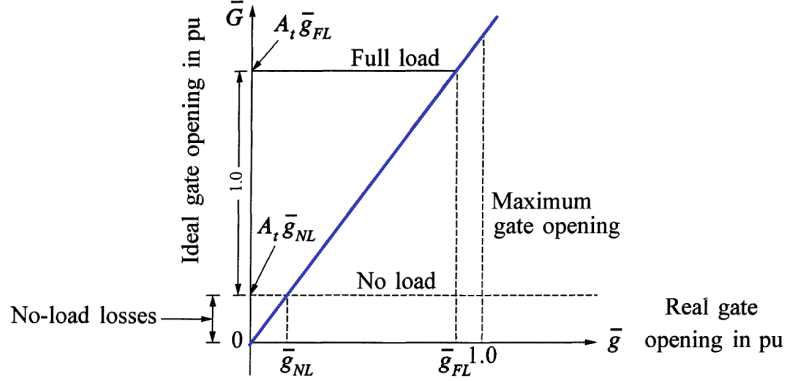


Fig. 67: Correlation between ideal gate opening and real gate opening [50]

The position G allows to inherently take into account the offset of the no-load flow q_{nl} , which is no more considered in (67). The relation between ideal gate opening and real gate opening is:

$$G = A_t g \quad (68)$$

By expressing the gate openings in per unit, the G full range from no load to full load is imposed equal to 1 and the turbine gain can be written as:

$$(1 - 0) = A_t (g_{fl} - g_{nl}) \rightarrow A_t = \frac{1}{g_{fl} - g_{nl}} = \frac{1}{g_{max} - g_{min}} \quad (69)$$

This correction allows to control the turbine only in its working range. Normally a different turbine gain, also called A_t in the literature [49] and showed in *Fig. 66*, is used for adapting the model output to S_B when the turbine rating is known. The gain is expressed as

$$A_t = \frac{\text{Turbine MW rating}}{(\text{Generator MVA rating})h(q - q_{nl})} \quad (70)$$

but the Simulink HTG model neglects it. This imply that by using the gain from equation (69) the mechanical output P_m is automatically scaled to the generator S_B and the model can be easily adapted for different systems, without the necessity to know the turbine parameters in detail. A second difference from the original model in *Fig. 66* is the choice to implement a modified non-linear model where the damping factor D_T is replaced by a water pressure coefficient β . The coefficient is introduced by combining the hydraulic models of different transient-stability programs PSS/E and ST600 [51], [52]) and is used to characterize the response of different turbines (Francis or Kaplan) to speed deviations. For sake of simplicity simplicity the parameter is set to zero: hence, the model does not consider the turbine construction type.

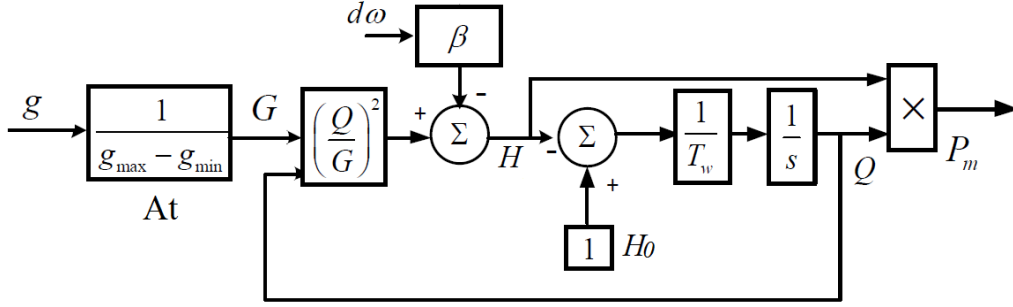


Fig. 68: Simulink HTG turbine non-linear model [53].

6.2.3 HTG speed governor model and tuning method

The speed governor of the *HTG Block* is summarized in a PID controller and a servomotor actuator, shown in *Fig.69*. The governing system is used to perform primary power/frequency regulation, ensuring the adequate control of power and frequency upon load variations. The primary speed control loop consists in comparing the speed set point input ω_{ref} with the rotor speed ω . The error is fed to the PID regulator and is used to control the gate position with the servomotor. A permanent droop gain R_P is inserted to ensure an equal load share among parallel units, to avoid that different generators compete in trying to control the system frequency independently. The value is set to 5%, meaning that a speed deviation of 5% causes a change of 100% in the power output if the generator is supplying an isolated load. The droop can be used with the power deviation or with the gate position signal g , as shown in *Fig.65*.

The servomotor is represented by a first-order model with gain K_a and time constant T_a . The position signal produced by the PID controller is fed to the servomotor block and the real gate position g is obtained by integrating its speed output.

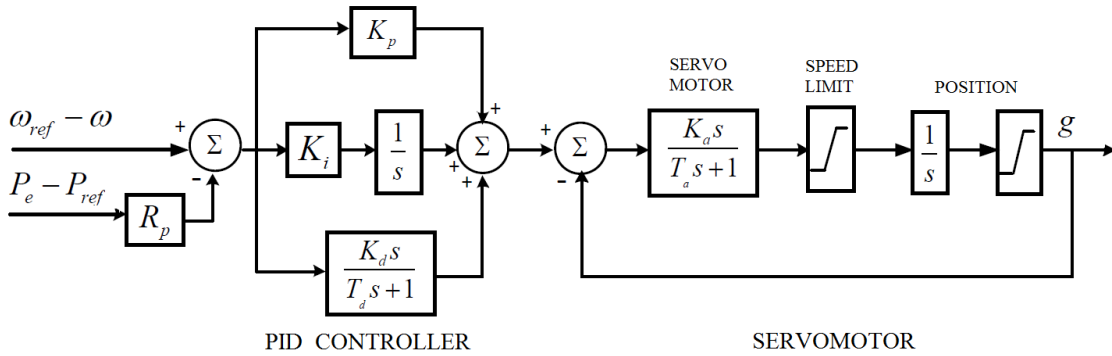


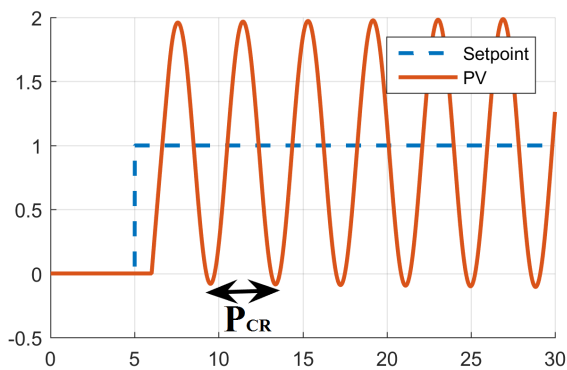
Fig. 69: PID controller and servomotor model featured in the HTG Block [53].

Hydraulic turbines are characterized by an initial opposite power response to changes of the gate position, due to the water inertia effect T_W . The first instants are generally handled by an additional *transient droop*, included in most of the literature to perform high regulation (low gain) during fast deviations in frequency. The HTG governor model neglects the additional transient droop, hence the permanent droop is effective only for slow changes and, in steady state, the governor performs a normal low regulation (high gain).

Therefore, the main problem in the frequency regulation of hydroelectric plants is given by the conflicting requirements of the governor response between stable operation of a system in islanding condition and load variations under synchronous conditions: the PID parameters used to ensure a fast power response to step load changes may cause frequency instability when the HPP has to manage the frequency independently [54]. The PID controller provides a triple action to control the system. The proportional action K_P is used to improve the speed of response and steady-state error by using the instantaneous value of the control error. The limited performance of K_P is improved by the integral action K_I , that allows to achieve a zero-steady error introducing oscillations in the system. The derivative action K_D is beneficial if used in isolated operations [50], especially to manage large water starting time ($T_W \geq 3\text{ s}$), but can introduce instability in interconnected systems. The predictive action of the rate of change of the error is used to further reduce the overshoot and quickly damp the system to the set-point value. The PID controller is described by:

$$C(s) = K_P \left(1 + \frac{1}{T_i s} + T_d s\right) = K_P + \frac{K_I}{s} + K_D s \quad (71)$$

The tuning of the PID parameters is based on the Ziegler-Nichols method [55], to establish a starting point upon which additional fine-tuning is done if required. The Ziegler-Nichols method is used to select the controller parameters K_P , T_i and T_d by forcing the simulated system into oscillation (*Fig. 70-a*). The first step is to set the integral and derivative gains equal to 0. The proportional gain K_P is increased starting from 0 until the closed-loop system begins to oscillate around the set-point. The critical proportional gain K_{CR} and the oscillation period P_{CR} of the signal are registered and used to determine the values of the three gains K_P , K_I , K_D (*Fig. 70-b*).



a)

Controller	K_p	T_i	T_d
P	$0.5K_{cr}$		
PI	$0.45K_{cr}$	$P_{cr}/1.2$	
PID	$0.6K_{cr}$	$0.5P_{cr}$	$0.125P_{cr}$

b)

Fig. 70: Ziegler-Nichols tuning procedure: a) choice of critical gain and oscillation period; b) choice of PID gains [55].

The Ziegler-Nichols method is aimed for a prominent gain and overshoot tuning. Further tuning is needed for minimizing the overshoot, and oscillations can be reduced by incrementing the values of T_i and T_d . The latter time constant is preferably set on small values, to avoid instability.

It is important to note that the initial K_P , K_I and K_D parameters obtained with the method are probably not feasible for the small HPP, as generally the proportional gain is too high and even small power oscillation might endanger the stability of the isolated grid. The adopted solution is aimed at reducing the gain values until acceptable responses are obtained.

6.2.4 Effects of water starting time T_W and inertia on the power response of HTG

The opening/closing of the penstock's gate has the effect of delaying the flow of water in the turbine. This effect is described in equation (65) by the water starting time T_W , a fundamental fixed parameter that depends on the layout of the penstock. If T_W is increased, the delayed flow has a more prominent effect on the turbine and contributes to enhance the oscillations of mechanical power, and consequently of the generator speed. It can be observed in *Fig.71* that a greater value of T_W results in greater speed deviations and frequency nadir.

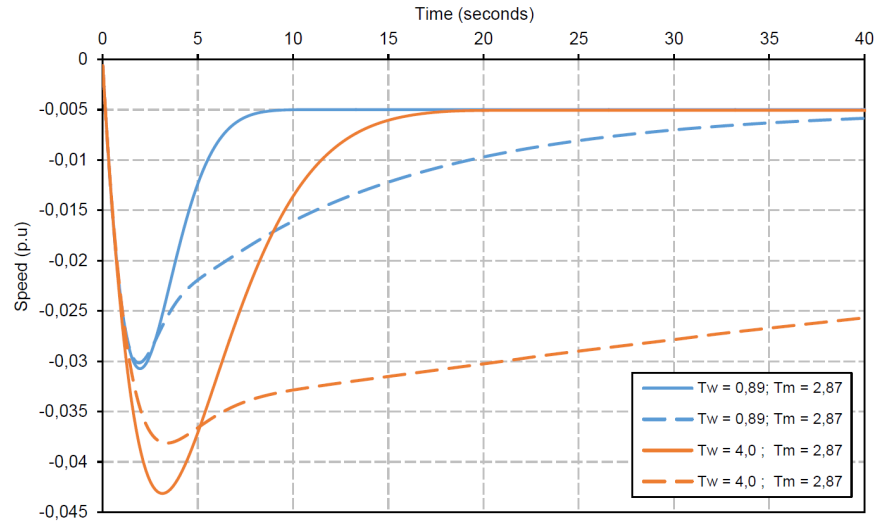


Fig. 71: Impact of water starting time T_W on the system response to load variations [54].

The effect of T_W can be partially mitigated by increasing the *machine starting time* T_M , which is proportional to the moment of inertia and mass of the generator. It can be observed that, by incrementing T_M , the maximum frequency deviation can be substantially reduced, at the cost of slowing down the response time to reach the steady state (*Fig.72*).

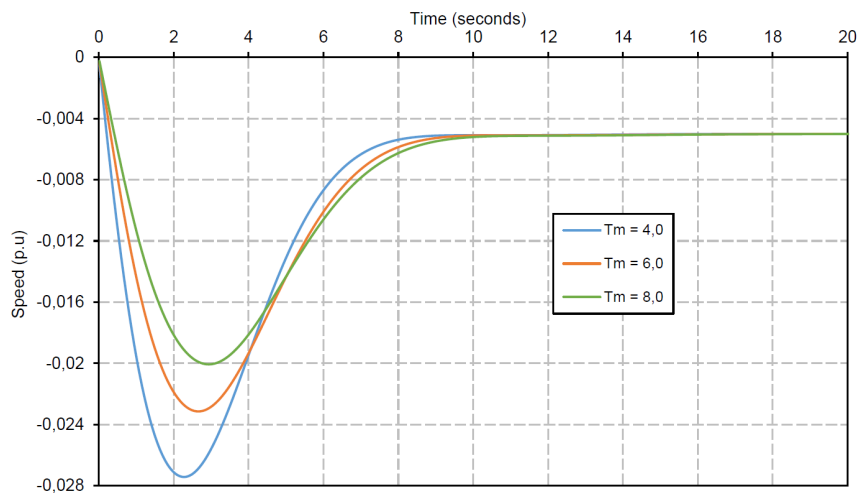


Fig. 72: Impact of machine starting time T_M on the system response to load variations, assuming a constant value of T_W [54].

This leads to the conclusion that, with a constant T_W value (dependent on the construction site of the plant), the generator rating S_B can directly affect the stability of the grid (*Fig.72*). A small generator will likely introduce major frequency deviation given the reduced amount of available inertia, while a machine with the size of tens of MVA will allow a more contained response to load deviation. The effects of the water starting time and inertia have been hence considered in the selection of realistic parameters for the characterization of the HPP model.

6.2.5 Matlab/Simulink model of the Hydroelectric Power Plant

The HPP is built in Matlab/Simulink by connecting the *Generator Block* and the *HTG Block* to an isolated grid (*Fig.73*). The HTG power output P_m and the *Excitation System Block* output V_f are connected to the generator. The generator phases A, B, C are connected to a grid composed of few loads, used to evaluate the response of the HPP to load variations. Different parameters (rotor speed w_e , output power $P_{e,0}$, voltages V_{dq} , currents i_{abc} , speed deviation $\Delta\omega$) are extracted from the generator to create control feedback loops and for monitoring purposes. The main objective is to evaluate the response of the generator to system perturbations, that are simulated by inserting/removing loads.

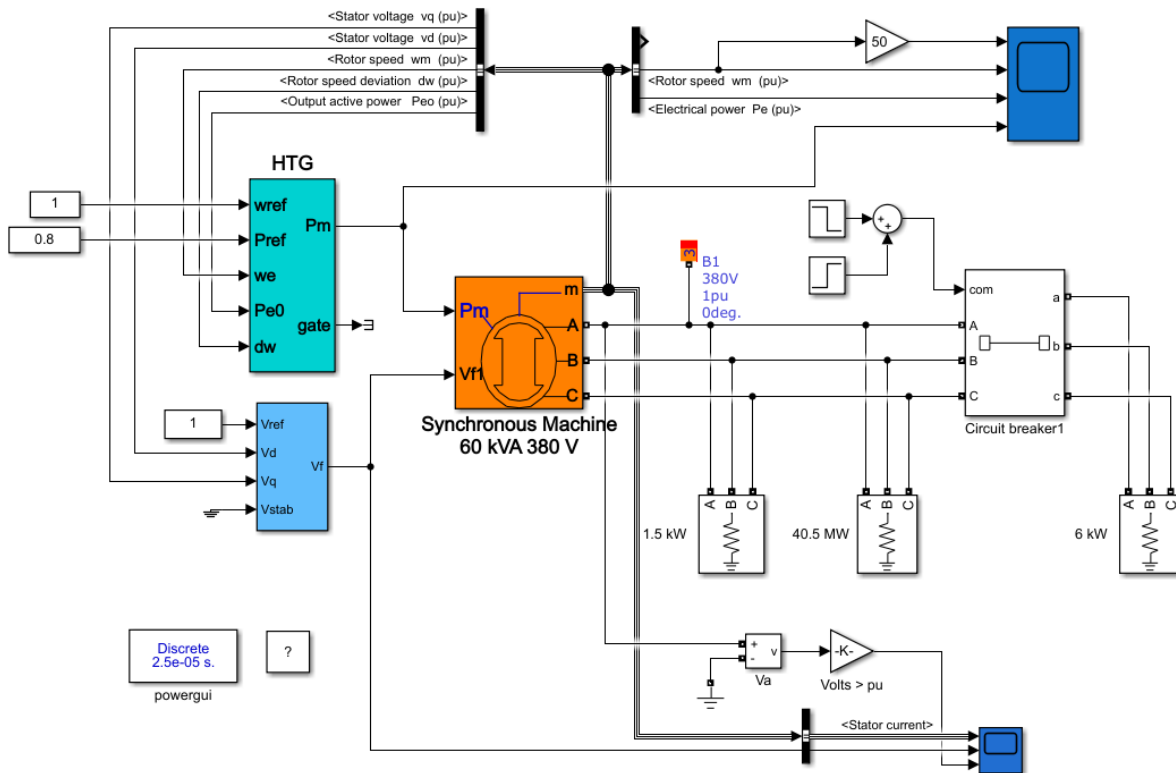


Fig. 73: Matlab/Simulink model of the Hydroelectric Power Plant.

The analysis is focused on response to small step variations and aims to prove that the HPP model is capable of controlling the generator speed and it ensures the system stability during and after events that affects the frequency. The simulation is set to 'Discrete' in the *Simulink Powergui*, in order to match the requirements of the Real-Time RTDS when exporting the model in *OPAL-RT*.

The models of the synchronous generator have limitations if put in discrete systems. To ensure a stable simulation and avoid numerical oscillations, the insertion of a small parasitic resistive load is required at the machine terminals. The minimum resistive load value is proportional to the sample time-step of the discrete simulation and to the nominal power of the machine (e.g. a step of $25 \mu s$ requires a minimum load of $2.5\%P_n$) [48].

The generator is the only power source in the system and therefore is set as a Slack/Swing unit to provide voltage and angle reference to the grid. The initialization of the machine can be performed by both the *Load Flow Tab* of the *Generator Block* and the *Machine Initialization Tool* of the Powergui. The entire model is initialized by performing the load flow computation, that sets the initial steady state of the system and the power reference P_{ref} of the HTG Block. The speed reference w_{ref} is set to $1 pu$ to ensure synchronous system operation at $50 Hz$.

The block parameters of the generator and the HTG are shown in *Fig. 74*. Given the limited information of real/measured values, and the absence of a real hydroelectric plant to work with, the parameters were chosen using a series of hypothesis with the objective to provide realistic and reasonable numbers in the description of the system. The adopted procedure is described below.

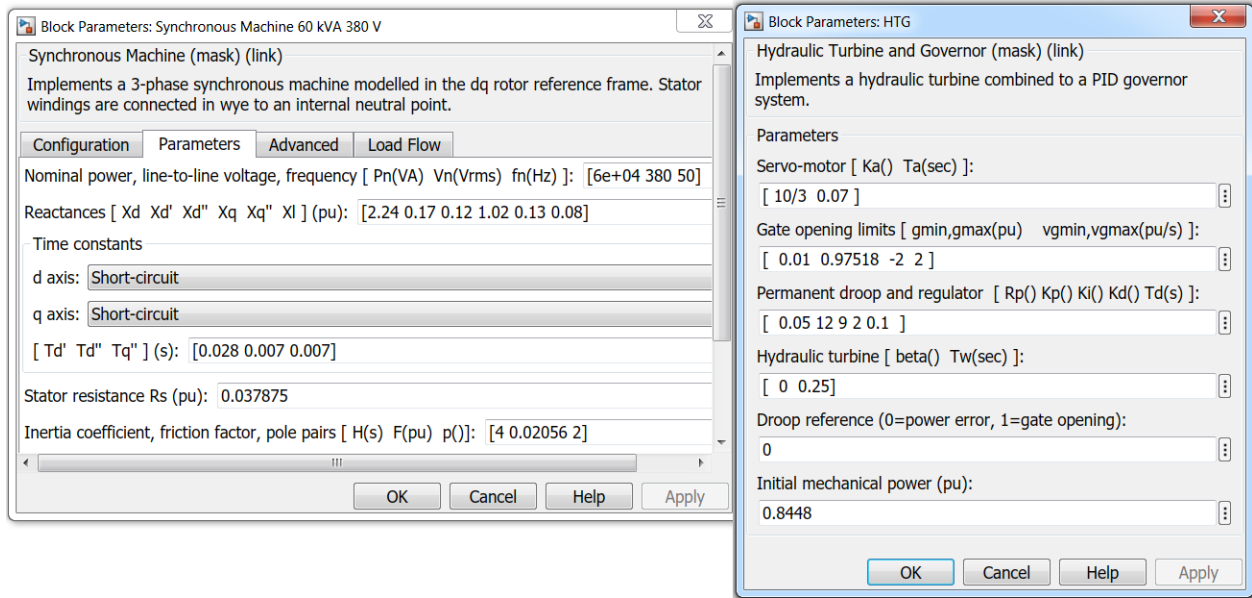


Fig. 74: Parameters of the Synchronous Machine and the HTG blocks.

1) Synchronous Machine Block - electrical parameters

The only available parameters for modeling the SG are the data displayed on the real machine nameplate (*Fig. 58*), given the impossibility to perform laboratory testing on the Marelli machines group during the model development. Starting from the basic data ($P_n = 60 \text{ kVA}$, $V_n = 380 \text{ V}$, $pp = 2$, salient poles machine) a preset model of $60 \text{ kVA} / 400 \text{ V} / 1500 \text{ rpm}$ was chosen from the various options in the *Synchronous Machine Block*. The reactances and resistance parameters are considered indicatively of the same magnitude of the Marelli machine ones. The preset nominal voltage was slightly adjusted to 380 V to impose the correct reference on the simulated microgrid.

2) Synchronous Machine Block - inertia constant H

The inertia constant H is a fundamental value, that determines how well the machine reacts to load variation in the first instants. The Marelli generator is a small machine and consequently its inertia contribution to simulated microgrids is limited. The inertia value is currently unknown, but could be estimated with a speed/acceleration laboratory test in future works. Rough estimation using equation (1) are hardly possible, as the rotor mass m and its dimensions are not known. The equipped preset model features an inertia constant of $H_{preset} = 0.1$ s. An early test shows that such low value is not feasible to control the frequency of an entire microgrid, as the frequency nadir and RoCoF go way past the normative standard limits for microgrid systems (*Fig.75-a*).

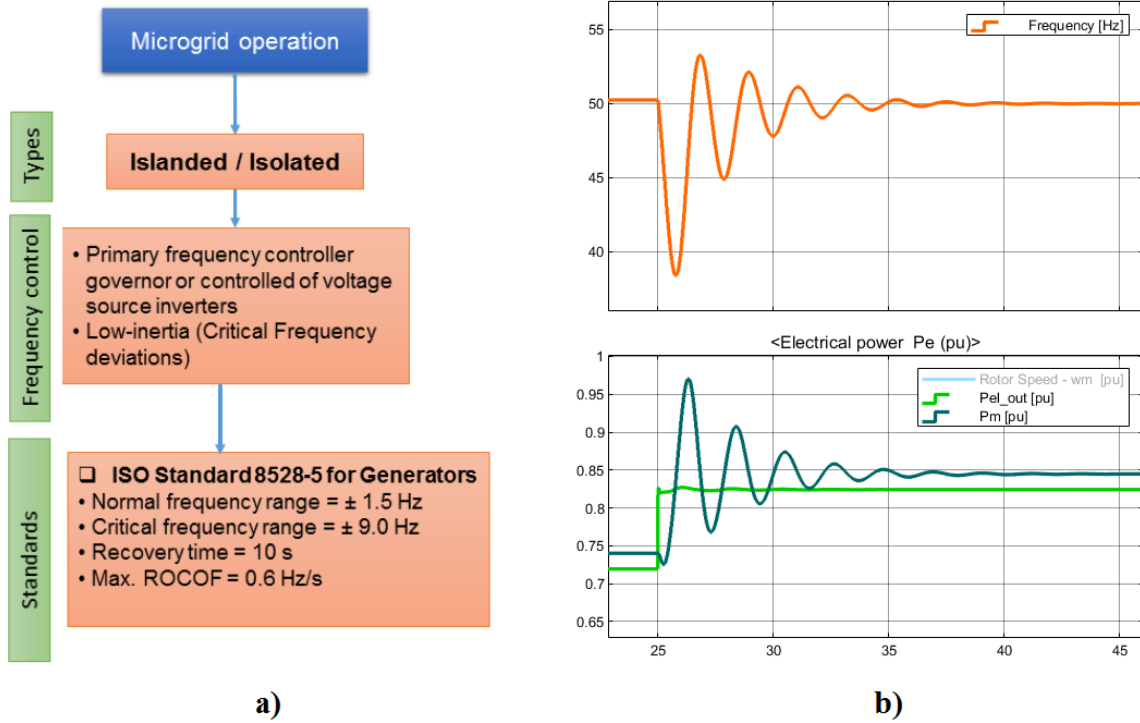


Fig. 75: a) ISO Standard 8528-5 for generators in islaned microgrids [12]; b) Model test response to a 10% P_n load step with $H = 0.1$ s and $T_W = 0.25$ s: Nadir = -11.5 Hz, RoCoF = 25 Hz/s.

The increased level of frequency fluctuations in *Fig.75-b* is considered unacceptable for the PHIL study of components in the microgrid. Assuming that the real inertia constant of the Marelli generator has a value close to H_{preset} , it has been decided to apply reverse engineering to the problem: knowing that the maximum RoCoF is set to 0.6 Hz/s, and assuming a 10% P_n load step ΔP , the required value of H is obtained from (9):

$$H = \frac{\Delta P \cdot f_0}{2 \cdot S_B \cdot RoCoF} = \frac{6 \text{ kW} \cdot 50 \text{ Hz}}{2 \cdot 60 \text{ kW} \cdot 0.6 \text{ Hz/s}} \cong 4 \quad [\text{s}] \quad (72)$$

The inertia constant is set equal to 4 s in the *Synchronous Machine Block*. This value is included in the range of small hydro plants, as shown in *Tab.2*. It must be considered that the inertia constant H is comprehensive of the inertia of the SG's rotor and the prime mover, thus the value can be variable in a consistent range depending on both the size and the construction type of the turbine

Table 2: Classification and quantification of inertia for different generation sources [56].

Energy Source Type	Generator Type	Inertia Constant H [s]
Conventional Power Plants (gas, oil, nuclear)	SG	$2 \div 9$ s
Hydropower	SG	$2 \div 6$ s
Wind Power	IG	± 5 s
Diesel Engines (ICM)	SG, IG	$1 \div 3$ s
Microturbines	SG, IG	$1 \div 4.5$ s
Small Hydropower	SG	$1 \div 4.5$ s
Solar Power	-	-
Concentrated Solar Power	SG	$2 \div 9$ s

and generator. In hydro plants the water wheel typically stores $4 \div 15\%$ of the total kinetic energy [56]. For the PHIL implementation of the real Marelli generator and prime mover (as substitution of the HPP model) in the simulated microgrid, after a more detailed measure of the inertia, a possible solution is to fit a flywheel on the generator shaft: the flywheel will be used to increase the rotating mass and the global inertia to obtain performances equivalent to the simulated HPP.

3) HTG Block - water starting time T_w

The water starting time is a parameter representative of the hydraulic structure of the plant and is computed using equation (65). The equation is dependent on the layout of the penstock (L , A), the water net head H and the water flow q_n . A hypothetical layout has been made to determine these unknown parameters with a reasonable approach. The starting data are the rated power of the Marelli generator ($P_n = 60$ kW with $\cos\varphi = 1$, $n = 1500$ rpm) and the use of a Pelton turbine (typical working heads of $15 \div 1800$ m). The net head was chosen to be equal to 120 m. The nominal mechanical power of the turbine P_m was set equal to P_n . When both P_m and H are known it is possible to determine the water flow required for producing the nominal power by using the power equation of the hydraulic turbine, shown in equation (73):

$$P_m = \rho \cdot g \cdot H \cdot Q \cdot \eta_T \quad \rightarrow \quad Q = \frac{P_m}{\rho \cdot g \cdot H \cdot \eta_T} \quad [\text{m}^3/\text{s}] \quad (73)$$

where ρ is the density of water (1000 kg/m³) and H is already unbundled of the head losses. The Pelton turbine efficiency η_T is typically high ($0.84 \div 0.92$). It is possible to compute the specific speed n_C to establish the turbine type required by the plant:

$$n_C = n \cdot \frac{\sqrt{P_m(\text{kW})}}{H^{1.25}} \quad (74)$$

The obtained value confirms the choice of the Pelton turbine for the plant, as shown in *Tab.3*.

The length L of the penstock is obtained with the hypothesis of an inclined pipeline with a degree of $\alpha = 60^\circ$, considering $L = \frac{H}{\sin\alpha}$. The cross section of the penstock can be obtained by using empirical equation for determining the inner diameter of the pipe.

With the empirical Ludin-Bundschu equation [57] for heads greater than 100 m and a round pipe, the cross section A is obtained as:

$$H > 100 \text{ m} \rightarrow d = \sqrt[7]{\frac{5.2 \cdot Q^3}{H}} \quad (75)$$

$$A = \frac{\pi d^2}{4} \quad (76)$$

The numerical application of equations (73) - (76) and (65) is shown in *Tab.3*. The obtained water starting time $T_W = 0.25 \text{ s}$ is lower than standard hydro plants (generally $T_W > 1 \text{ s}$) and is more representative of small plants, where limited pipe length and head reduce the time required for effectively adjust the water flow at the turbine head.

Table 3: Computation of a feasible T_W value for the HTG model and turbine specific speed/head classification [58].

Starting Data		Computed Values		Turbine Technology		
pp	2	Q_{base}	0.058 [m^3/s]	nc	Turbine Type	H
P_n	60 [kW]		58 [l/s]	[rpm]		[m]
n	1500 [rpm]	n_C	31,2 [rpm]	10 ÷ 70	Pelton 1 ÷ 4 jets	2000 ÷ 15
P_m	60 [kW]	L	139.5 [m]	70 ÷ 100	Slow Francis	400 ÷ 240
η_T	0.88	d (H>100m)	0.19 [m]	100 ÷ 200	Normal Francis	240 ÷ 90
H_{base}	120 [m]	A	0.028 [m^2]	200 ÷ 450	Fast Francis	90 ÷ 30
α	60°	T_W	0.25 [s]	400 ÷ 1000	Kaplan	30 ÷ 5

4) HTG Block - PID and servomotor parameters

The PID parameters were initially set using the Ziegler-Nichols tuning method described in **section 6.2.3**. The HPP model was brought in oscillation increasing K_P . K_{cr} and P_{cr} were measured and used to compute the first set of gains. Additional fine tuning on K_P, K_I, K_D and T_D was performed to decrease frequency oscillation, while still ensuring an adequate time of response. The results are showed in *Tab.4*.

Table 4: Computation of the HTG PID parameters.

HTG PID	Kcr	Pcr [s]	Kp	Ti [s]	Ki	Td [s]	Kd
Z-N Parameters	25	2,2	15	1,1	13,636	0,275	4,125
Final Parameters	-	-	12	-	6.25	0.1	2

The servomotor gain K_a and time constant T_a were not changed, while the gate opening speed limits $V_{g,min}$ and $V_{g,max}$ were increased from the original $\pm 0.1 \text{ pu/s}$ to $\pm 2 \text{ pu/s}$. The correction was made under the assumption that in a small penstock ($d = 19 \text{ cm}$) the gate has small dimensions and the servomotor can perform a faster opening/closing.

6.3 HPP Model Simulation Tests

The HPP simulations are performed assuming a load step/ramp change in the system. The objective is to observe how effective is the speed governor in controlling the frequency and the mechanical power output of the turbine. The tests are performed assuming that the generator is initially generating 80% of its nominal power. The step change is commonly imposed as $\pm 10\%$ of the unit's power capacity [54]. A 6 kW load (equal to $10\%P_n$) was implemented in the microgrid via a circuit breaker to simulate the step, as shown in *Fig. 76*.

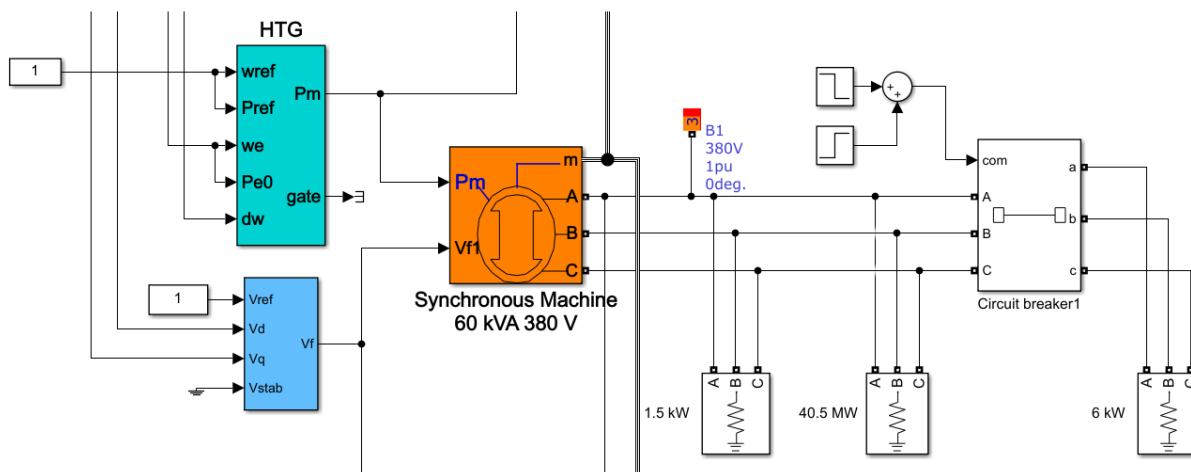


Fig. 76: Microgrid configuration for step tests: a 6 kW load is connected to the main AC line via a *Circuit Breaker Block*. Positive/negative load steps are performed by disconnecting/connecting the load with controlled commutations of the circuit breaker.

A first step test was performed using the calculated Ziegler-Nichols PID parameters of *Tab.4* and the standard model presented in *Fig.73*, as shown in *Fig.77*. A negative load step occurs at $t = 5$ seconds, highlighting a positive frequency deviation and a reduction of 10% in the output power.

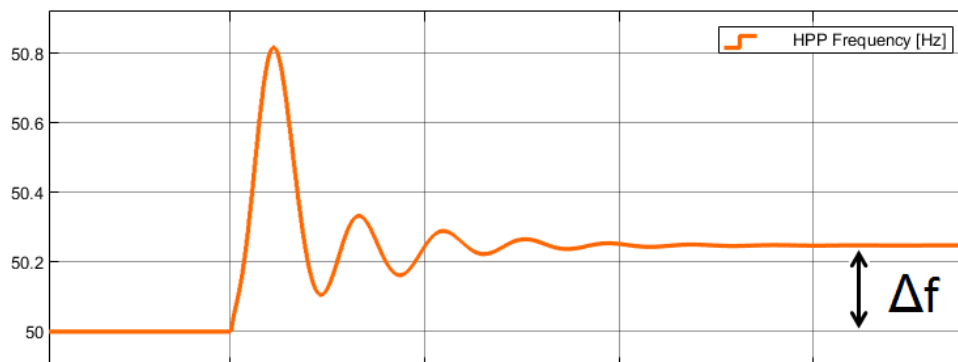


Fig. 77: Test 1: negative 6 kW load step @ $t = 5$ s, with Ziegler-Nichols parameters and standard HTG frequency control.

The simulation presents two frequency issues. The first issue is that the frequency regulation performed by the HTG Block is not restoring the frequency to $f_0 = 50$ Hz after the step event. The residual error of $\Delta f = +0.25$ Hz sets the system in a *quasi-steady state* and must be eliminated. This is necessary to avoid that potential subsequent steps sum their effects (leading to even greater

frequency deviations) and to be compliant with the normative range of normal islanded operation (*Fig.75-a*). The solution was found through the correction of the standard control of the HTG Block of *Fig.73*. The block normally implement a droop control R_P that considers the difference between electric power P_{e0} and the reference P_{ref} (*Fig.65*). This implies that the unit is performing primary power control. Ensuring the reference power is important when the unit is connected in a wide system, where primary regulation is performed by multiple units and remaining frequency errors are managed by the secondary regulation. However, in the studied microgrid, the objective of the single HPP is to ensure a constant 50 Hz frequency while adapting the power generation to the loads connected. To this purpose, the power input of the HTG Block where disconnected and substituted by the the reference speed w_{ref} and real generator speed w_e , as shown in *Fig.76*. The droop control is now working with the PID governor as primary frequency control and ensures the reference f_0 in steady state. The second issue is due to the Ziegler-Nichols parameters, that introduce an oscillating response in the frequency regulation. The problem was resolved by manually changing the parameters: K_P was slightly reduced to decrease the speed of convergence; K_I and K_D were reduced down to half their initial value to eliminated the excessive oscillations. The new values, shown in the second line of *Tab.4*, allows a much smoother frequency control. The effect of the final parameters can be observed in (*Fig.78*).

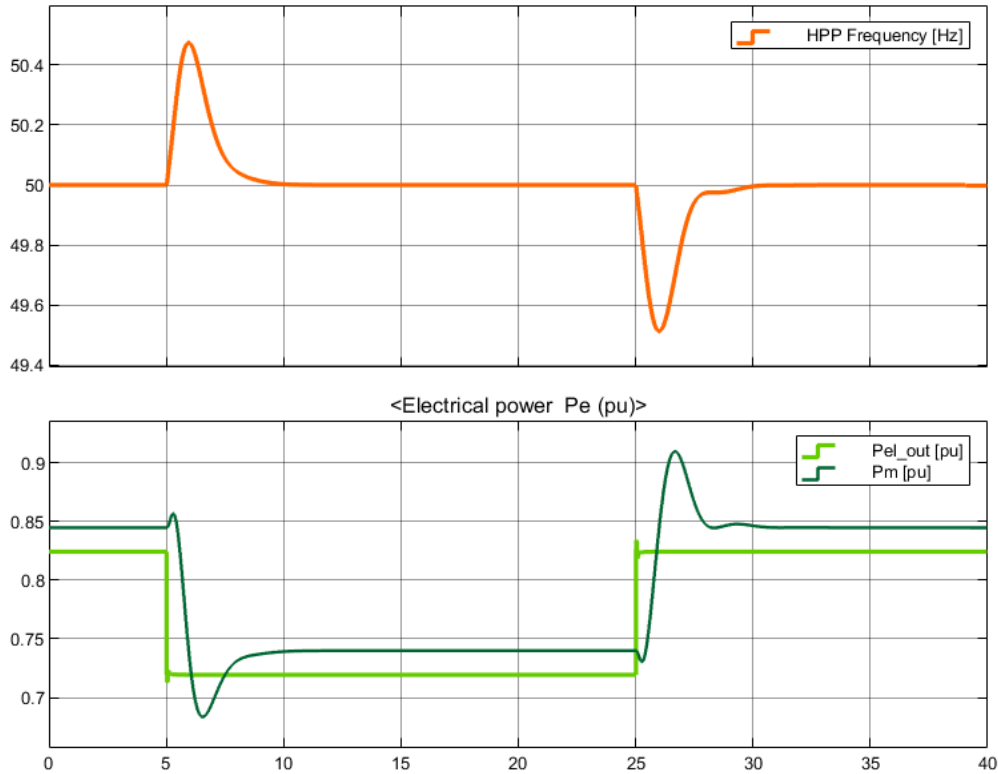


Fig. 78: Test 2: negative 6 kW load step @ $t = 5$ s and positive 6 kW load step @ $t = 25$ s, with corrected PID parameters and HTG primary frequency control.

A second test was performed by introducing a negative step at $t_1 = 5$ seconds and an opposite positive step at $t_2 = 25$ seconds. The frequency response of the HPP is improved by previous adjustments, presenting a smooth control, frequency deviations in the ± 1.5 Hz range and a recovery time under 10 seconds. The frequency is successfully re-aligned to the 50 Hz steady state.

The generator reacts to load steps with an instantaneous variation of the generated electrical power P_{el} . The P_m presents an initial opposite deviation to power changes, a behaviour typical of the hydraulic turbine gate control. The steady state offset between P_{el} and P_m takes into account the losses in the conversion form mechanical to electrical power.

The frequency control is maintaining good performances also for different load step conditions:

- in *Fig.79-a* a multiple 2 kW load step test was performed, showing how the control can regulate frequency during fast load variations.
- in *Fig.79-b* a substantial 30 kW load was detached from the grid, resulting in a prominent drop of the SG power. The control effectively controlled the turbine mechanical power and returned the frequency to steady state. With the current PID settings the control is not able to maintain the standard ± 1.5 Hz range of normal operation indicated in *Fig.75-a*.

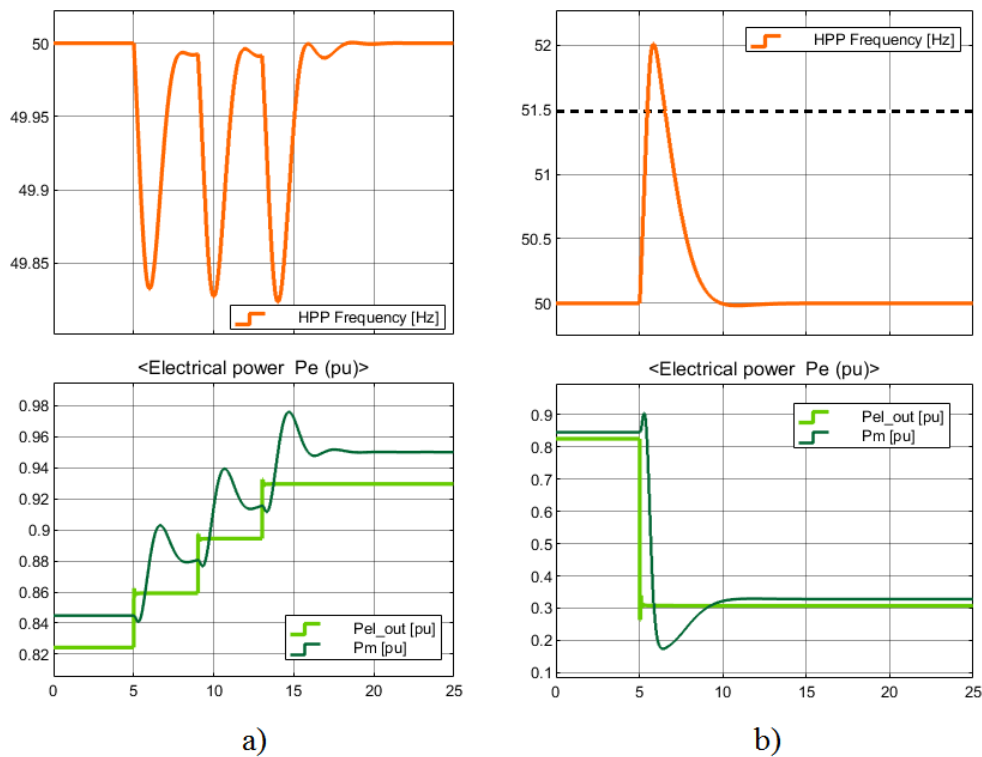


Fig. 79: Test 3: a) 2 kW multi-step test @ $t = 5/9/13$ s; b) negative 30 kW step test ($50\%P_n$) @ $t = 5$ s.

A fault test was performed to observe the system's behaviour. A three-phase short-circuit was applied with a dedicated Simulink block at the end of the microgrid's three-phase line. It can be observed in *Fig.80-a* that the generator sustains the fault transient for 0.1 s before the fault is cleared. The frequency deviation presents some fast oscillation due to the fault, and it is overall successfully contained and brought back to null value.

A final test was performed to observe the system's behaviours with ramp signals. A $10\%P_n$ ramp was applied. The control regulates the turbine P_m to correctly follow the active power ramp P_e , as shown in *Fig.80-b*. As expected from the swing equation (7), the frequency deviation df/dt decreases to a constant value for the duration of the ramp because of the constant difference between the increasing P_e and P_m . When the ramp is completed, the frequency is correctly returned to f_0 .

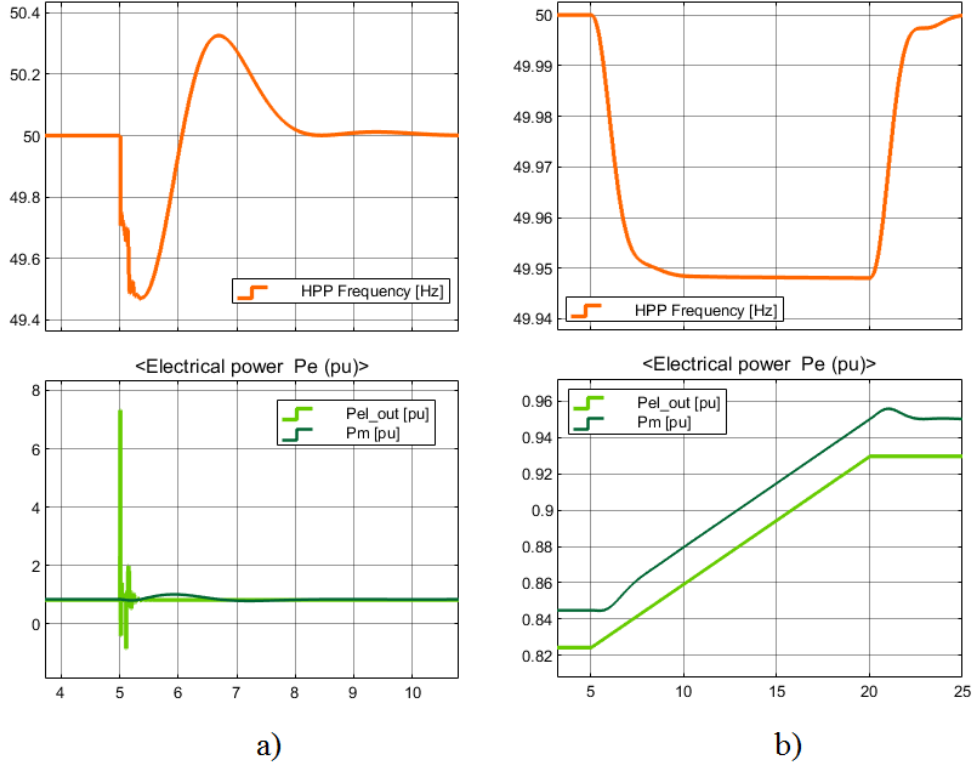


Fig. 80: Test 4: a) three-phase fault test @ $t = 5$ s with fault clearing time of 0.1 s; b) positive 6 kW ramp test (0.4 kW/s).

The HTG Block features a nonlinear model, which is sensitive to the size of the perturbation and the initial conditions. The PID governor parameters calculated in *Tab.4* have demonstrate to be optimum parameters to study variations in the $10\%P_n$ range, with the plant at nearly full generation capacity. If tests are performed in different conditions the choice of PID parameters should likely change, as confirmed by the frequency response in *Fig.79-b*.

6.4 Model in OPAL-RT

The HPP model has been verified in the Simulink environment. The successive step is to implement the model in the Real-Time (RT) environment for future PHIL studies. The RT platform chosen was *RT-LAB*, by *OPAL-RT* machines. The advantage of RT-Lab is the possibility to implement the real-time simulation of both custom models and models imported directly from MATLAB/Simulink and other environments.

The RT-Lab software is executed on a *Command Station*, a computer that undertake the role of user interface and development platform (the access to the Command Station, located at the Energy Center in Turin, was made with a remote desktop application). Once the model is developed, the code is sent to the *Target Node* (OPAL-RT), where real-time simulation is executed. The communication between *Command Station* and *Target Node* is ensured by a Ethernet connection. For PHIL applications, the communication with real hardware is established via I/O ports and the data are recorded and collected on local hard driver at high speed.

The HPP model was imported in RT-Lab from Simulink environment. The real-time simulator requires to regroup the various blocks of the model into two subsystems:

- **Master Subsystem (SM):** subsystem responsible for real-time computation, signal synchronization and I/O communication.
- **Console Subsystem (SC):** subsystem that enables the user to interact with the simulation during execution, comprehensive of all blocks related to data acquiring and data display.

Additional *Slave Subsystems* (SS) can be added to perform distributed computations on different target nodes on the OPAL-RT's hardware. Such subsystems are used only if required and are referred to the singular SM of the model. The HPP model was here divided in the two main subsystems, as shown in *Fig.81*.

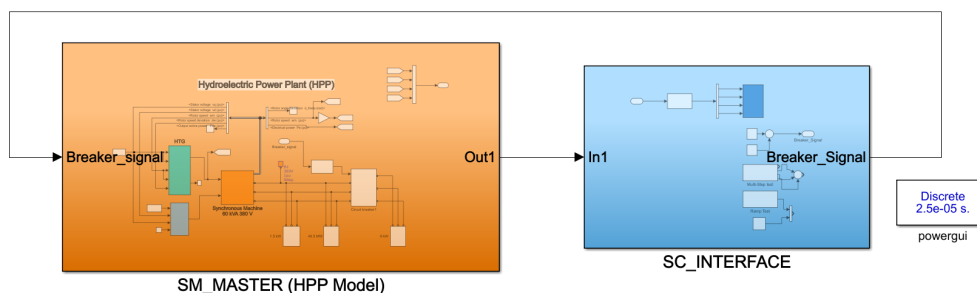


Fig. 81: HPP Model regrouped into two subsystems.

The subsystems require some additional blocks to enable and save informations carried by the input ports. Every input in SM and SC requires to be processed by the *OpComm* block before any operation is done on the signals they are associated with. In particular:

- in **SM** the a first OpComm block is used to receive signals from other potential real-time subsystems (SS), while a second OpComm block is used to receive commands from the SC subsystem.
- in **SC** one or more OpComm blocks are inserted to receive one or more signals from real-time subsystems (*SM*, *SS*).

In the current model, one OpComm block is used in SC to handle the input data of the HPP plant (w , f , P_e , P_m). The SC output, controllable by the user, is used to set the on/off status of the breakers of the test load ($P = 6$ kW), as shown in *Fig.82*.

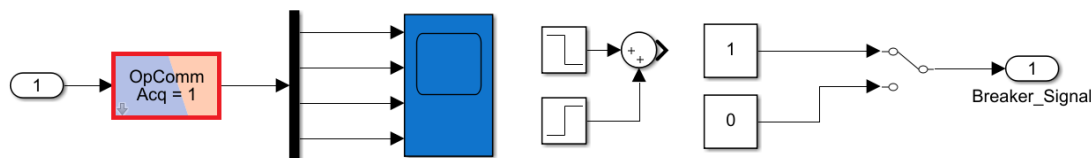


Fig. 82: Console Subsystem SC: data are acquired from SM via the input OpComm block and breaker signals are sent back for frequency step tests.

It is important to underline that the breaker signal, that can be generated both by step blocks or by the user's manual action on a switch, is not synchronized with the real-time simulation: while the SM subsystem is running in real time, the console SC is executed on the Command Station, receiving

and sending informations with a delay due to both the speed of ethernet communication and the speed of the host computer. This results in delayed breaker commands and, most importantly, in an inaccurate waveform generation by the scopes, that receives fragmented informations and are feasible only for general monitoring of the simulation.

The SM implements only one OpComm block, as in this specific case no slave subsystem was created. The master subsystem is comprehensive of the HPP and the microgrid. The OpComm block is used to handle the breaker signals sent by SC, as shown in *Fig.83*. In alternative, to maintain synchronization between the master subsystem and the signal breaker, the OpComm block can be left unconnected and step blocks with specific step time can be used in the SM.

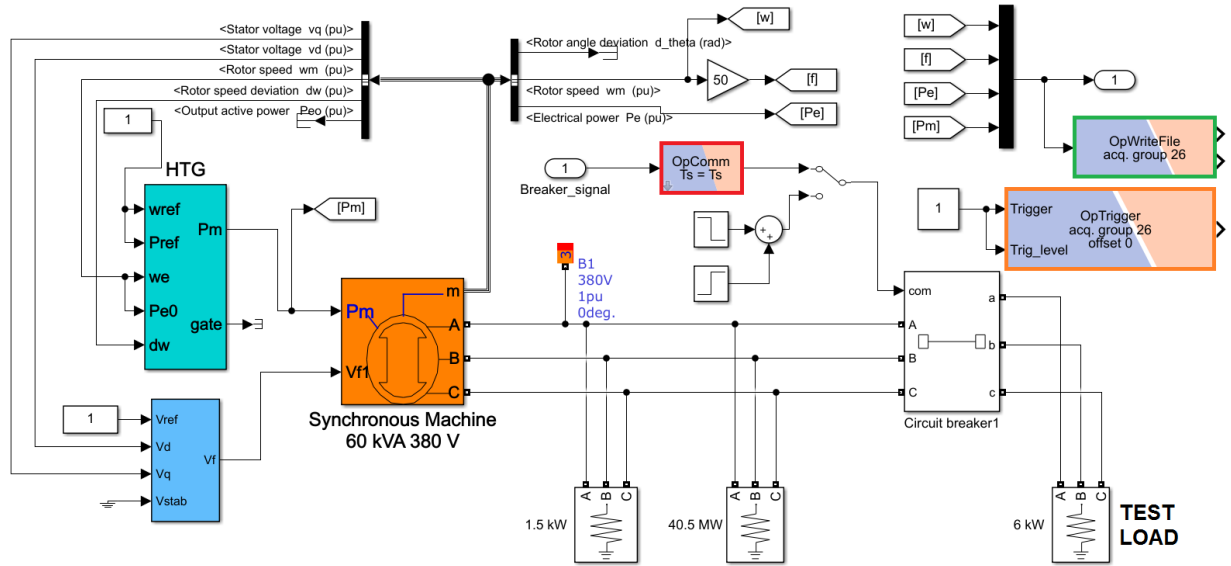


Fig. 83: Master Subsystem SM: the HPP + microgrid system is simulated and data are sent to SC.

The acquisition of the real time data is obtained by adding two additional blocks to the SM subsystem:

- **OpWriteFile Block:** the block extracts the output data of the SM subsystem and writes them in a *.mat* file as a matrix with $(n + 1)$ lines, containing the time and all the n output variables.
- **OpTrigger Block:** the block is entitled to enable the acquisition process of the OpWriteFile block, in continuous mode or in specific time frames.

The *OpWriteFile* block allows to set a decimation factor to select how many samples are used in the writing process. In the current simulation the factor is equal to 1, meaning that all the samples are written with a time step equal to $T_s = 25\mu s$. The variables can be named and saved in the *.mat* file, that is automatically generated in the SM model folder during the execution of the code. The file size must be specified based on the simulation parameters and the time window to be recorded, in order to allow the correct writing of all the data. The settings used are shown in *Fig.84*. The writing process is for real-time execution, but can also acquire data for offline simulations in Simulink by enabling the *Write in Simulink mode*.

The *OpTrigger* block must be set to the same *Aquisition Group* of the related *OpWriteFile* block

(channel 26 was chosen). The block is set to $TriggerSignal \geq TriggerLevel$: with both inputs equal to 1 the continuous mode is enabled and data are acquired for the whole duration of the simulation (or until the .mat is fully written).

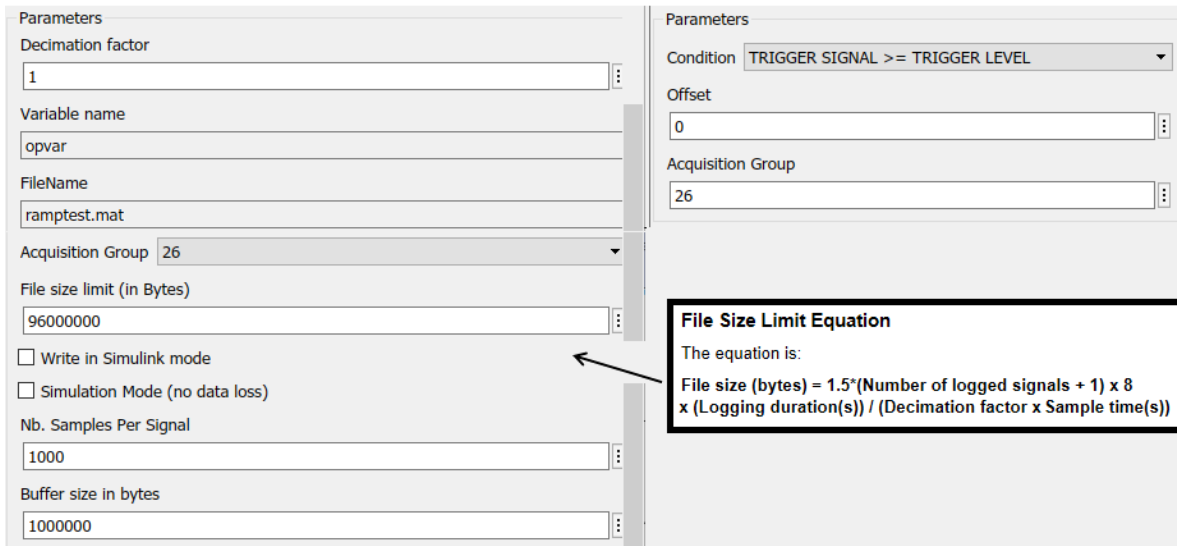


Fig. 84: OpWriteFile and OpTrigger parameters. The file size limit equation is indicated in the help tab of the function.

The model is due to be executed in real-time. Before running any simulation on the Opal-RT platform is important to prepare the model for discrete fixed-step operation: real-time simulations are performed with solvers that operate at regular time intervals from start to end. The parameters were properly set on Simulink, both in the *Configuration Parameter* tab and the *Powergui*. The fixed-step fundamental sample time used is $T_S = 25 \mu s$, the same used for tests in **section 6.3**. The chosen time is in the range of typical electrical applications and serves well the dynamics of the simulated model. T_S is also bounded by the type of *real-time simulation mode*: as no real hardware is considered in this test, the model is set under *Execution Properties* as *Software Synchronized* and requires the use of a time step $T_S \geq 20 \mu s$.

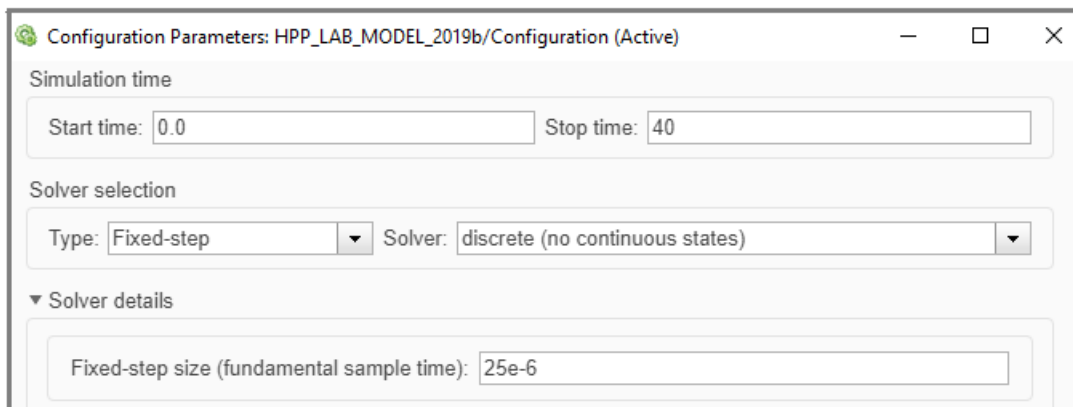


Fig. 85: Solver parameters for fixed-time discrete simulation.

The model was tested offline on the *Command Station* using Simulink, to ensure that the model was working properly before transferring to the real-time simulator. A step test similar to the one of *Fig.78* was performed, presenting an analogous behaviour for what concerns frequency nadirs and power fluctuations. The final result is acceptable, as the frequency and power waveforms are showing their time evolution without losing relevant informations (*Fig.86*).

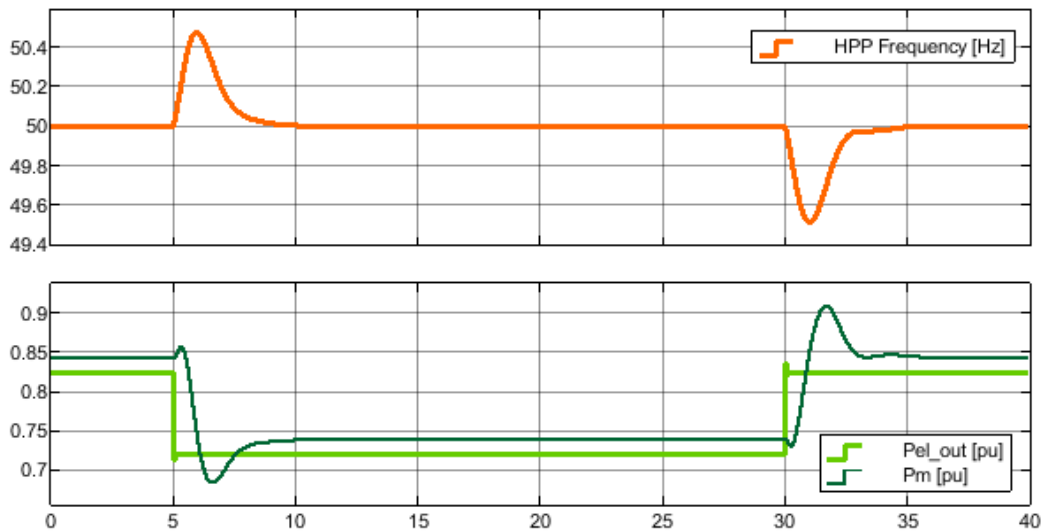


Fig. 86: Offline Opal-RT Test: negative 6 kW load step @ $t = 5 s$ and positive 6 kW load step @ $t = 30 s$.

Once the simulink model is verified offline it is possible to proceed towards real-time simulation. The model is built in RT-lab, where the compiler translates the simulink block-type code into C-type code taking into account the splitting of the final code into the SM and SC subsystems. The code is also prepared for transferring to the *Target Node*. The master SM is assigned to one of the physical nodes of the Opal-RT, which is entitled to run the real time simulation of that part of the model. After the node is assigned the model can be loaded and executed online. The XHP mode in *Fig.87* can be omitted when no real hardware is connected to the real time simulator.

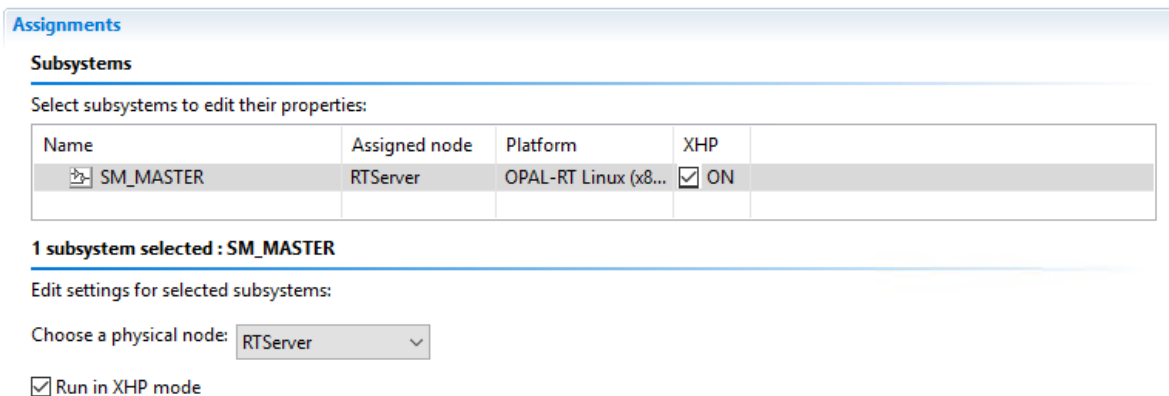


Fig. 87: Assignment of the Master Subsystem to the Opal-RT Target Node.

The model was performed online for a step test and for a ramp test, to confirm the results already obtained in Simulink.

Both tests have been performed first in offline mode, in order to compare the waveforms. Results are shown in *Fig.88* and *Fig.89*.

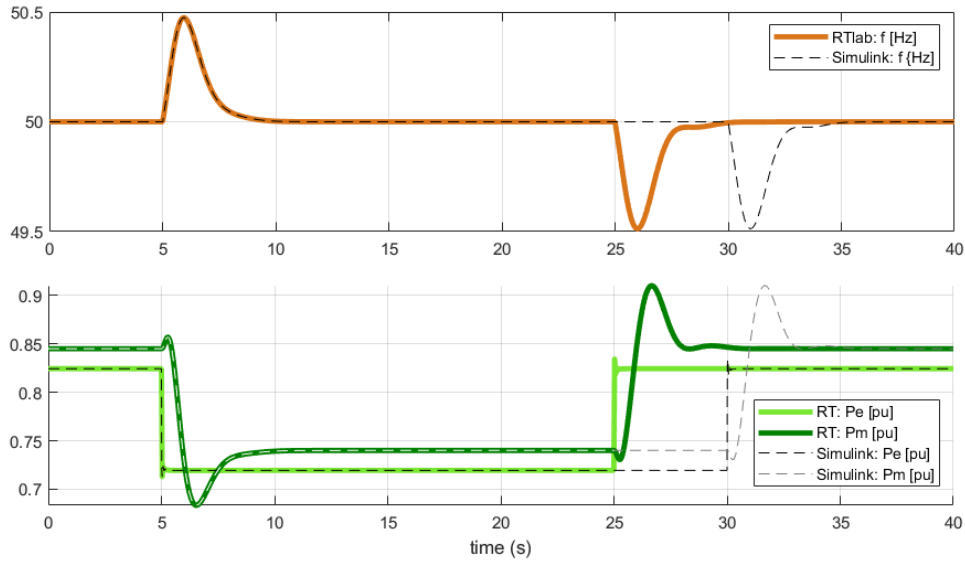


Fig. 88: Online Opal-RT Step Test: negative 6 kW load step @ $t = 5$ s and positive 6 kW load step @ $t = 25$ s. The second step of the Simulink offline test is executed @ $t = 30$ s.

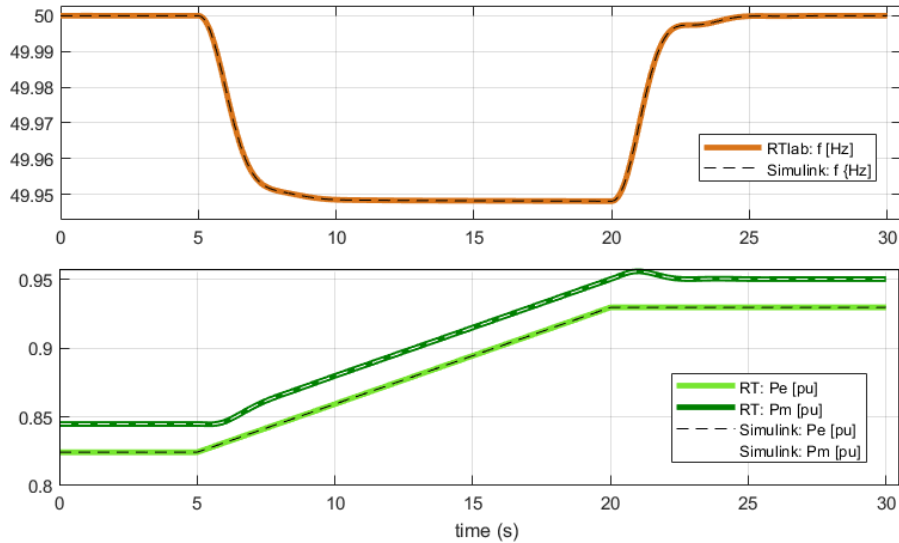


Fig. 89: Online Opal-RT Ramp Test: positive 6 kW load ramp (0.4 kW/s) @ $t = 5$ s.

The OpalRT execution is perfectly equivalent to the Simulink simulations, indicated with dashed lines in the charts. The frequency deviations are contained within normative limits and the HPP regulation successfully aligns the mechanical power to the electrical power requested by loads. The results validates the HPP model for future PHIL tests.

7 Simulation of a microgrid with virtual inertia implementation

Microgrids, in both islanded and grid-connected modes, can be mainly represented as semi-independent groups of *distributed generators* (DGs) and local loads. In many cases a microgrid is studied specifically to supply small off-grid communities with a wide use of renewable energy resources, such as photovoltaic (PV) and wind, that can represent a consistent share of the installed generation. A microgrid can be likely characterized by a small inertia constant H , which is typical for a low-inertia power system. The frequency stability of the low-inertia system, being it just the microgrid or the whole system to whom is connected, can be improved with a variety of different solutions (described in **section 3.2** and **section 3.3**) that can introduce virtual inertia as a valid support to the grid.

The aim of this second part of modelling is to introduce in the developed model a renewable source, in parallel with the conventional SG of the hydro plant. The new source is a PV array, which is simulated in *Simulink-OpalRT* environment and can as well be connected to the microgrid as a real hardware in future PHIL studies. The nominal power of the PV array was chosen to be 20.5 kW, approximatively 1/3 of the HPP nominal power ($P_n = 60$ kW). The total inertia constant of the microgrid can be calculated as:

$$H_{tot} = \frac{\sum_{i=1}^n H_i \cdot S_i}{S_{tot}} = \frac{S_{HPP} \cdot H_{HPP} + S_{PV} \cdot H_{PV}}{S_{HPP} + S_{PV}} \quad [\text{s}] \quad (77)$$

Considering that a PV array is normally connected to the grid via a converter with no inherent inertia support ($H_{PV} = 0$ s), by using equation (77) the global inertia is reduced from the original *HPP*'s value of 4 s calculated in (72) to 3 s. The reduced inertia can no longer provide a frequency response compliant to the microgrid quality standards presented in *Fig. 75-a*.

The objective of the simulation is to observe the microgrid frequency behaviours in a hybrid traditional-renewable scenario. A battery will be integrated with the PV array to constitute an energy storage for frequency regulation. The DC/AC inverter of the *PV+Battery* system will be controlled with a dedicated algorithm to provide virtual inertia to the microgrid. The expected results aim to show an improvement in the overall frequency response of the HPP and PV plants, in order to return the system to the situation described by tests in **section 6.3** and **section 6.4**.

7.1 Implementation of a photovoltaic DC source in Matlab/Simulink

The virtual inertia is implemented in the model by creating a *Virtual Synchronous Generator* (VSG), which transforms the behaviours of the PV array and battery in a virtual SG capable of providing synthetic inertia support to the grid. The DC source is composed by two main blocks:

- The PV array model with a *Maximum Power Point Tracker* (MPPT) control.
- The battery model with voltage-current control.

The PV-battery DC source will be connected to a capacitive DC-link to ensure a constant voltage V_{DC} for the DC/AC inverter, in order to simulate a prime mover and allowing the VSG to regulate its output power. The two blocks are described in the following **section 7.1.1** - **section 7.1.3**.

7.1.1 PV model with MPPT control

The PV array is simulated by using the *PV Array Block* from the *Simscape Specialized Power Systems* library. The block provides as output the DC voltage V_{PV} and current I_{PV} given by the solar irradiation and temperature inputs. The model implements an MPPT algorithm based on the *Perturb and Observe* (P & O) technique. The MPPT control creates the PWM signals for a DC/DC boost converter, that connects the PV array to the *DC Point of Common Coupling* (PCC) with the battery. The PV layout is described in *Fig.90*.

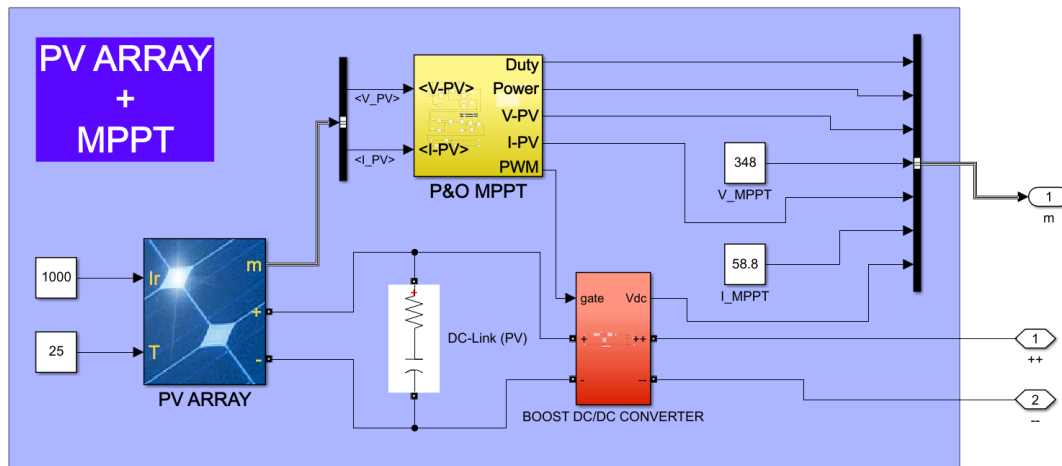


Fig. 90: Matlab/Simulink model of the PV array with MPPT control.

The PV configuration was made in the *PV Array Block* in *Fig.91*. A 8-parallel strings array with 12-series connected modules per each string was chosen to obtain a total nominal power $P_{PV} \cong 20.5$ kW. The *I-V* and *P-V* curves shows the MPPT points for various irradiation values at the reference temperature of 25°C . For the nominal irradiation of 1000 W/m^2 the MPPT point produces the nominal power with $V_{PV} = 348$ V and $I_{PV} = 58.8$ A.

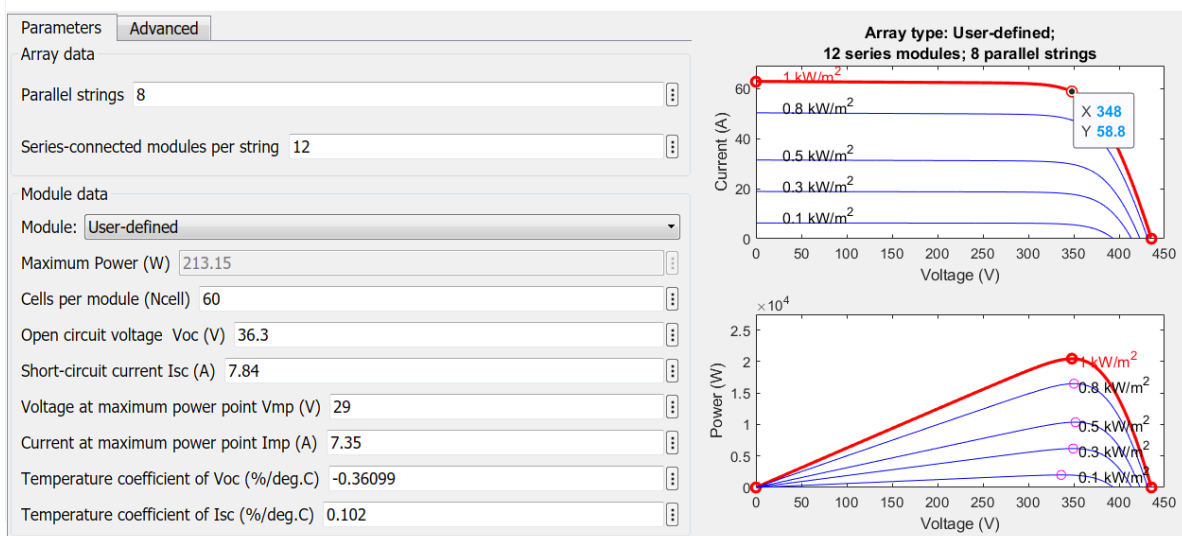


Fig. 91: Parameters of the PV Array with I-V and P-V characteristics @ $T = 25^{\circ}\text{C}$.

The MPPT control is based on the P & O algorithm, which is used to control the PV output power towards convergence at the maximum power point for a given solar irradiation. The algorithm is summarized in *Fig.92-a*. The current and voltage are measured to compute the power produced by the array. The measured $P(k)$ and $V(k)$ are compared with their precedent values $P(k-1)$ and $V(k-1)$: if ΔP and ΔV are both positive or negative, the PV voltage is increased of a fixed value, whereas if they present different signs the voltage is decreased. The final outcome is the output power oscillating around the maximum power point value.

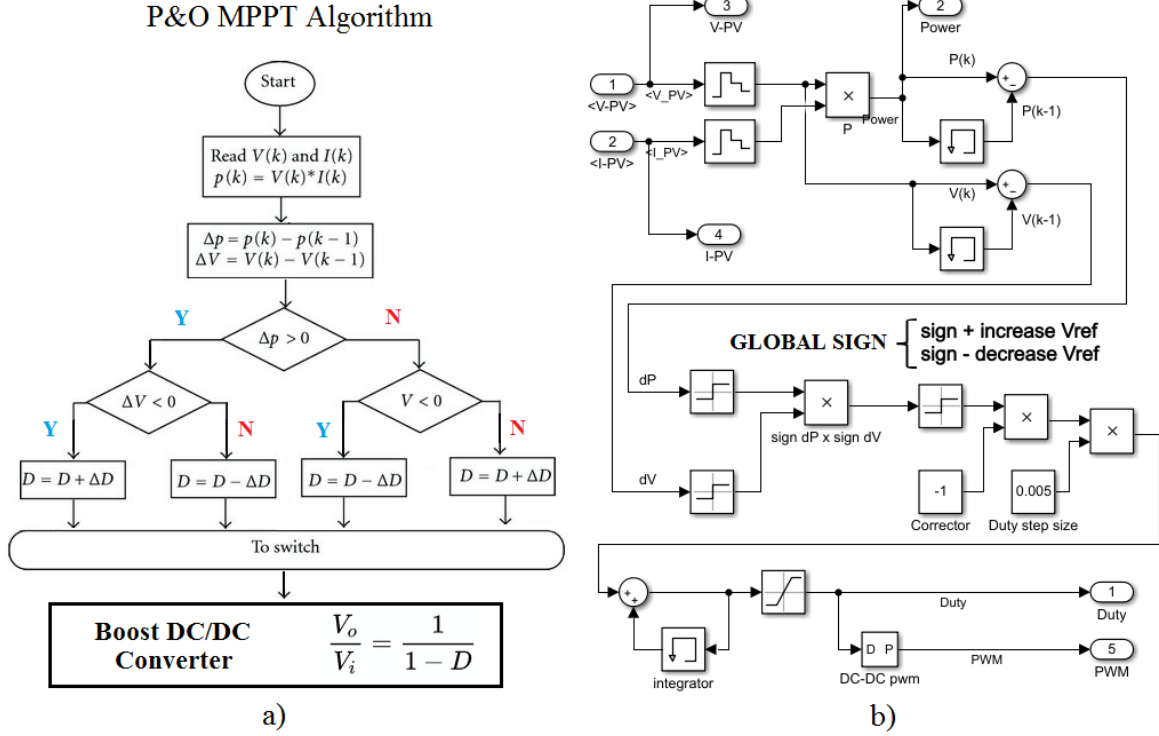


Fig. 92: a) Flowchart of P & O algorithm [61]. b) Simulink implementation of the P & O algorithm [62].

The Simulink implementation of the algorithm is made by using *Memory Blocks* to store the previous values of voltage, power and duty cycle. The variations dP and dV are multiplied by each other to obtain the global sign. Increasing the output voltage with a boost converter requires to decrease the duty cycle D , and vice versa: the global sign is inverted to perform the right duty cycle increment/decrement (*Fig.92-b*). The boost converter is projected for an input voltage of 300-350 V, the range of the MPPT voltages of the PV array observed in *Fig.91*. The value of the internal inductance is shown in *Tab.5* and is calculated in equation (78).

$$L_{BOOST} = \frac{V_{in} \cdot (V_{out} - V_{in})}{f_{sw} \cdot \Delta I \cdot I_{out} \cdot V_{out}} \quad [H] \quad (78)$$

Table 5: Computation of the HTG PID parameters.

P	f_{sw}	V_{in}	V_{out}	ΔI	ΔV	I_{in}	I_{out}	L_{BOOST}
20.5 kW	5 kHz	300 V	650 V	5%	1%	58.6 A	31.5 A	20.5 mH

7.1.2 BESS model

The battery is simulated by means of the *Battery Block* of the *Simscape SPS* library. The battery was chosen to be Lithium-Ion, the most common choice for virtual inertia applications [3]. The initial *State Of Charge* was set to 50 %, as the battery is normally operated in charge and discharge mode and must provide virtual inertia support and grid support when required. To this purpose, a bidirectional DC/DC converter was implemented to allow power flows in both directions (*Fig.93*).

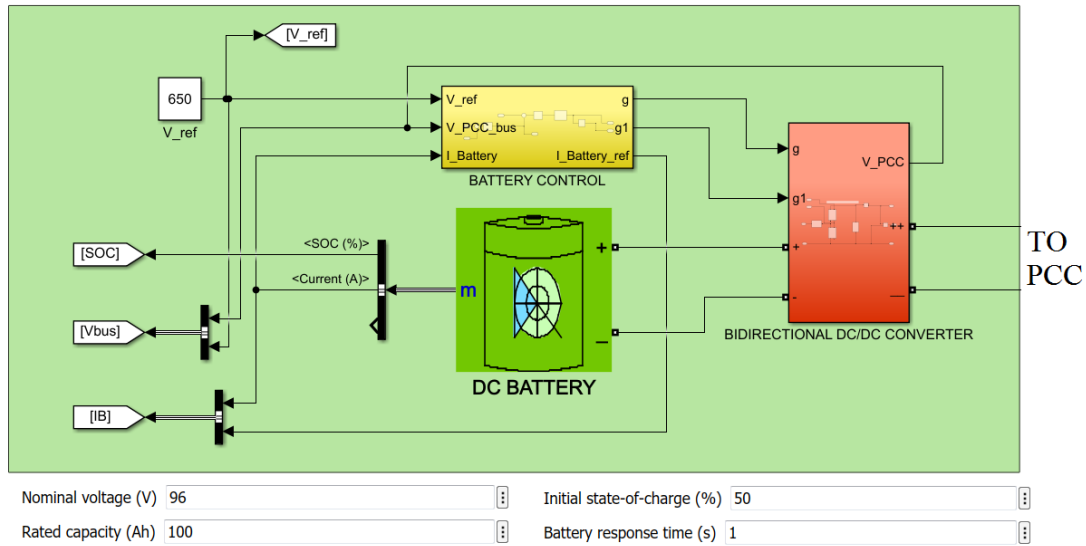


Fig. 93: Matlab/Simulink model of the BESS system.

The battery controller operates alongside the MPPT control to maintain a constant voltage on the DC-link in the point of common coupling PCC, as shown in *Fig.94*. The reference DC voltage V_{ref} is compared with the measured V_{PCC} and the error is given to a PI controller, in order to generate a reference current $I_{B,ref}$. The *SOC* % of the battery can be set by acting only on the battery current I_B : a positive value controls the discharge mode, while a negative value is used for enabling the charging mode. The current loop is made by using a second PI controller and generates the duty cycle that controls the converter gates with PWM.

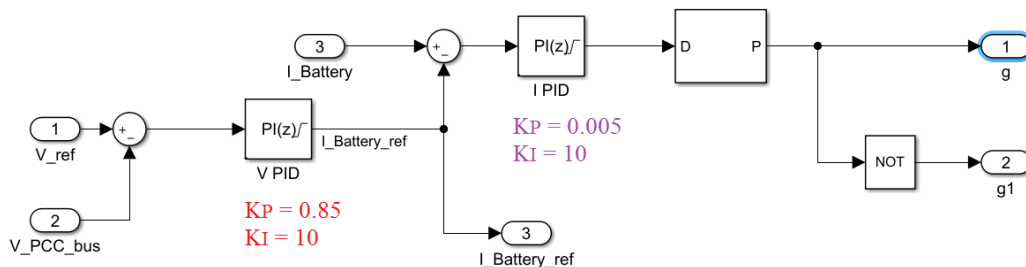


Fig. 94: Control scheme of the BESS system [63].

The bidirectional converter is a buck-boost configuration, that allows the bidirectional current flow by using two power transistors. The input inductance value was set as $L = 0.5$ mH and the output capacitor to $C = 1000$ μ F. The DC PCC bus, where both the PV array and the battery are connected together, is the boost converter's output capacitor $C_{bus} = 630$ μ F.

7.1.3 PV array and battery model test

The PV array model and the battery model were tested in a standalone DC configuration (*Fig.95*) before developing the VSG algorithm and connecting the virtual generator to the AC microgrid. The expected outcome of the test is to observe a system able to track the maximum power point with variable solar irradiation, while maintaining a constant voltage value on the DC bus and ensuring a charge/discharge mechanism based on the power production and load consumption.

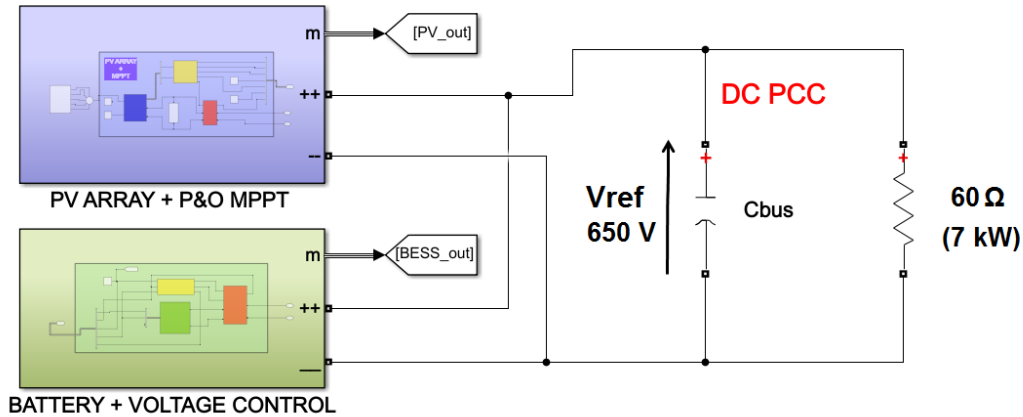


Fig. 95: PV array + Battery Simulink model connected to the DC bus with resistive load.

A first test was carried out by applying multiple irradiation steps [$100 \div 1000 \text{ W/m}^2$] starting from zero (null irradiation), as shown in *Fig.96*. The power P_{PV} and current I_{PV} outputs are proportional to the irradiation and coincide with the MPPT points on the P - V and I - V characteristics shown in *Fig.91*. The PV voltage V_{PV} is constant around the 348 V value (MPP for 1000 W/m^2), as expected when irradiation is not null.

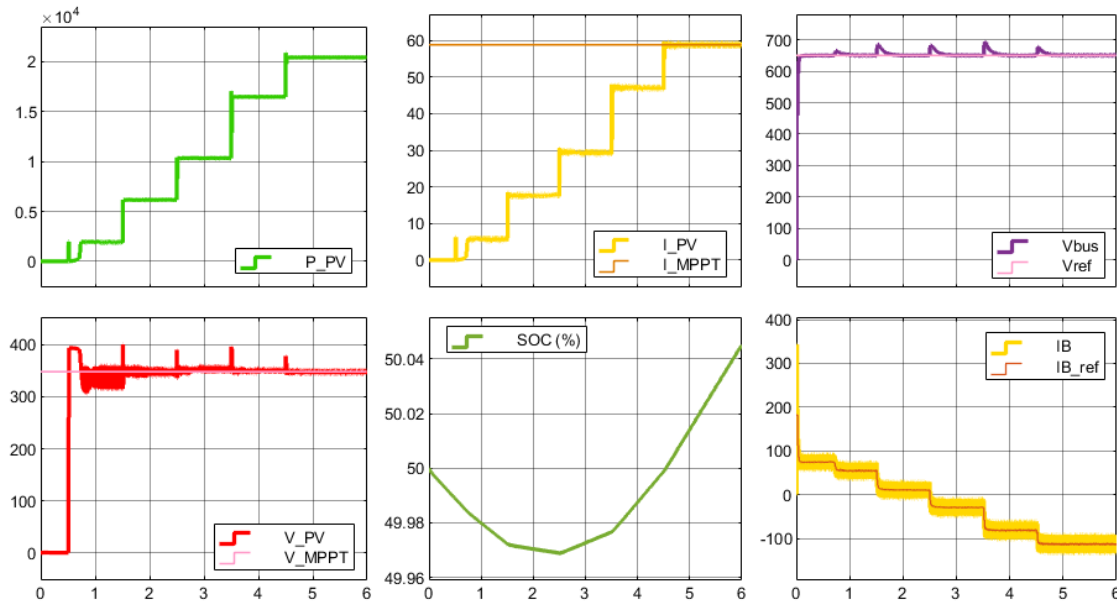


Fig. 96: PV-Battery test with irradiation steps of [$100, 300, 500, 800, 1000$] W/m^2 and $V_{ref} = 650 \text{ V}$.

Assuming to connect a test resistive load of $60\ \Omega$ (7 kW), the voltage control initially discharges the battery and the SOC% decreases from the 50% starting point to supply the load. As soon as the irradiation is equal to $500\ W/m^2$ (@ $t = 2.5\ s$), the PV power production reaches $P_{PV} = 10\ kW$, becoming adequate to fully supply the 7 kW load and charge the battery. The battery control is effective, as the bus voltage V_{bus} follows the imposed 650 V reference with temporary variations during irradiation steps. The battery current I_B follows the reference $I_{B,ref}$, positive during discharging and negative during charging. The MPPT control is overall stable and accurately follows the references. An initial PV voltage overshoot can occur due to the MPPT duty cycle initialization, as observed @ $t = 0.5\ s$. The initialization of the duty cycle can influence the way the simulation starts: in general the initialization is $D = 0.01$, the lower PWM limit. This value is a starting point more suitable for generic continuous variations, but can lead to a slower response in the starting of the simulation. The control requires some seconds to stabilize around the first point of maximum power before a correct execution. The ripples of voltage and current waveforms can be reduced by properly setting the duty step size of the MPPT algorithm.

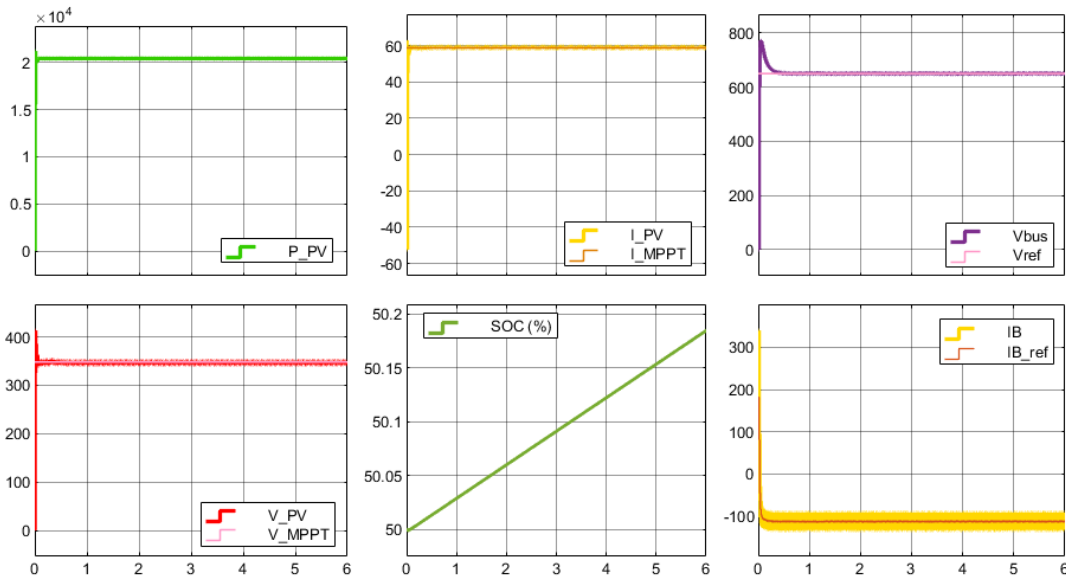


Fig. 97: PV-Battery test with constant irradiation (initial steps of $1000\ W/m^2$) and $V_{ref} = 650\ V$.

A second test, showed in *Fig.97*, was performed with a constant irradiation at standard conditions of $T = 25^\circ C$ and $1000\ W/m^2$. The settings are used as working point for simulations in the following sections. The duty cycle was here initialized to $D = 0.5$; this central value is used specifically to obtain a faster response as the simulation starts with a $1000\ W/m^2$ irradiation step, that otherwise would lead to severe voltage-current transients. Starting from a central point is helpful for large steps, but would be less responsive for slow variations or low irradiation values. At the beginning of the test the PV array quickly reaches and stabilizes around the MPP and the battery is controlled in charging mode.

7.2 Virtual Synchronous Generator model implementation in Matlab/Simulink

The VSG is implemented in *Simulink* as a DC/AC three-phase inverter connected to the grid and controlled by a specific algorithm, that simulates the behaviour of a synchronous machine (*Fig.98*). The connection is made by mean of a LCL filter, in order to reduce the switching voltage harmonics and improve the output currents. The filter can also be an LC filter made by using series R_s, L_s (representing the VSG's stator windings) and a parallel bank of capacitors C_f . The series R_g, L_g representing the grid parameters at the PCC can complete the LCL structure. The general structure of a VSG is represented by a *Power Block*, comprehensive of the inverter, the filter and the circuit breaker towards the grid, and the *Control Block*, that incorporates the control algorithm, the PWM modulation and the measurement blocks.

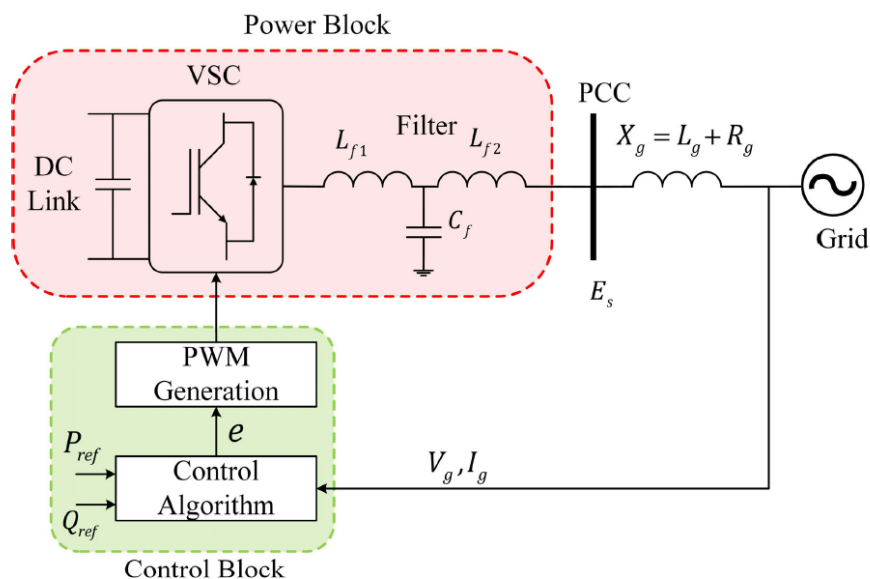


Fig. 98: General schematic of the VSG structure [64].

Not all the virtual inertia control techniques presented in **section 3.2** are suitable for operating in an independent microgrid and often require a strong AC grid connection to properly perform. Among them, *SG-Model-Based* and *Swing-Equation-Based* algorithms (such as *Synchronverter*, *VISMA* and *SPC*) can be implemented both in grid-connected mode or islanded mode, due to their improved frequency stability and the ability to work in grid-forming mode independently. In this thesis the *Synchronverter* algorithm has been modelled in Simulink, because of its control functions (for voltage, frequency, active and reactive power) and the ability to self-synchronize with the grid without the introduction of a PLL. The DC/AC inverter is voltage-controlled, a feature that in power grids is preferred to current-controlled inverters for its ability to taking part in V/f regulations and avoiding current injections during grid faults. The synchronverter is also completely equivalent to a real SG, as it implements all the characteristic dynamic equations of real machines and provides equivalent outputs. All the parameters, such as inertia, mutual inductance, excitation field inductance and stator windings impedances, can be introduced and freely chosen with the possibility of neglecting unwanted behaviours (magnetic saturation and eddy currents). The only physical difference in the layout is the mechanical power exchange, no longer made with a prime mover and replaced by a DC-link.

7.2.1 Self-Synchronized Synchronverter: inverter without a synchronization unit

The *Self-Synchronized Synchronverter* is an enhanced version of the original Synchronverter algorithm described in *Fig.18* and [14], that represents a reduced 2nd order model of a SG machine starting from the full mathematical 5th order model. The approximation can be considered almost identical in the low frequency region, hence a good approximation of the full model [65].

The main improvement is obtained by removing the dedicated PLL synchronization unit, that typically introduces delays and possible instability in the system, and by integrating the synchronization function directly in the power controller, as shown in *Fig.99*. The compact structure implements synchronization and V/f regulation in a single integrated controller.

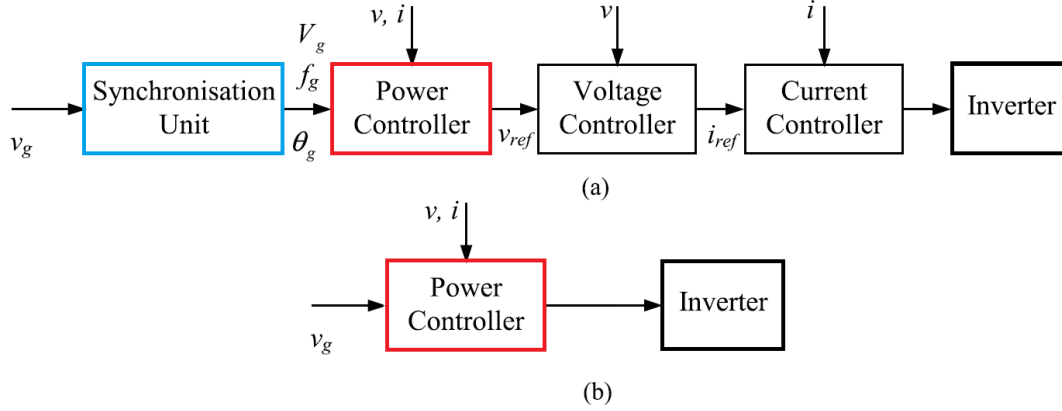


Fig. 99: Comparison of control structures for grid-connected inverters. a) Voltage-controlled inverter; b) Compact control structure [5].

The core algorithm of the self-synchronized synchronverter is the same as the one in *Fig.18*, implementing the SG equations eq. (16), eq. (17), eq. (18) and the virtual frequency/position eq. (20). Two channels are set: the first channel controls the active power and frequency, while the second channel can control the reactive power or the output voltage.

For a stable and safe grid connection, the synchronverter is required to synchronize with the grid voltage V_g in amplitude and phase, in order to avoid large current transients during connection and to deliver the desired power when required. The idea to perform a self synchronization is effectively applied by analysing the per-phase model of a SG connected to an infinite bus (*Fig.100*). The generation of active and reactive power is defined as follows:

$$P = \frac{3V_g E}{2X_S} \sin(\theta - \theta_g) \quad (79)$$

$$Q = \frac{3V_g}{2X_S} E [\cos(\theta - \theta_g) - V_g] \quad (80)$$

where V_g is the grid voltage, E is the SG internal voltage (controlled by the excitation term $M_f i_f$ in the synchronverter) and $\theta - \theta_g$ is the phase difference between the grid and the virtual generator, also called power angle δ . It results clear from the equations that P and Q values can be controlled by the voltages and the respective phases during normal grid-tied operations, to inject or absorb power in the grid depending on the generator type (PV or PQ).

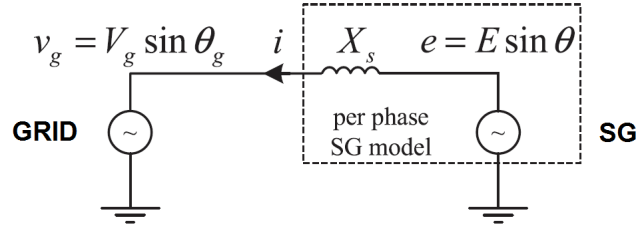


Fig. 100: Per-phase model of a SG connected to an infinite bus [5].

In particular P can be controlled by increasing the mechanical torque T_m , and consequently δ up to the synchronized stability limit of $\pi/2$, while Q is controlled by regulating E via the excitation system. The synchronization condition between the VSG and grid is obtained when:

$$E = V_g; \quad \theta = \theta_g; \quad (81)$$

This particular case can be achieved by controlling P and Q to zero during the synchronization process, and is possible because of the virtual representation of the SG (the $P = Q = 0$ condition is not a normal operation for a real synchronous generator).

The original synchronverter algorithm is partially modified to accommodate the synchronization process. The main changes are reported in red in Fig.101.

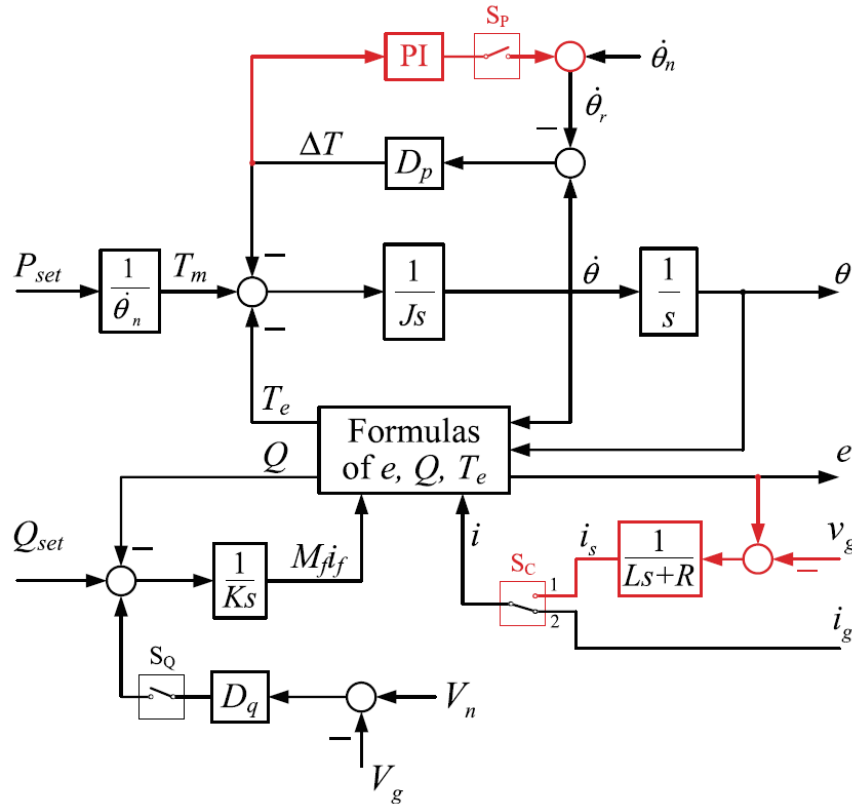


Fig. 101: Self-synchronizing Synchronverter schematic [5].

The first schematic modification is made by introducing a virtual current i_S , obtained by applying the voltage difference $e - V_g$ on a virtual impedance $R_V + jX_V$. The virtual current is used in the model instead of the real current only during synchronization.

The second modification is a PI controller in the frequency droop channel, that forces ΔT to zero, granting a perfect active power control and eventually correcting the frequency reference $\dot{\theta}_r$ if the grid is working on values different from the nominal $\dot{\theta}_n = 50 \text{ Hz}$. The operation of the synchronverter is subdivided in a set of modes, that can be enabled by controlling three switches S_P , S_C , S_Q as summarized in *Tab.8*.

Table 6: Operation modes of the self-synchronized synchronverter [5]

Mode	Switch S_C	Switch S_P	Switch S_Q
N/A	1	ON	ON
Self-Synchronization	1	ON	OFF
N/A	1	OFF	ON
N/A	1	OFF	OFF
P-Mode/ Q_D -Mode	2	ON	ON
P-Mode/Q-Mode	2	ON	OFF
P_D -Mode/ Q_D -Mode	2	OFF	ON
P_D -Mode/Q-Mode	2	OFF	OFF

1) The **Self-Synchronization Mode** is performed when S_C is set to 1, with S_P ON to enable the PI controller. In this mode, by setting $P^*=0$ and $Q^*=0$ the condition of eq. (81) is satisfied and the grid connection can be exploited. However, as long as the circuit breaker remains open during the synchronization, no real current i_g can be really exchanged between grid and inverter and the power regulation would be impossible. The measured i_g is then temporary replaced by the virtual current i_s (commuting S_C), that is used as feedback in the dynamic equations to calculate e , Q , and T_e and simulates the power regulation. In the model the virtual current is computed as:

$$i_S = \frac{1}{R_v + sL_v}(e - V_g) \quad (82)$$

When the internal voltage e is equal to V_g in amplitude and phase, the current i_S is equal to zero because of the ideally null voltage difference, and the circuit breaker can be closed for the safe physical connection with the grid.

2) The **N/A Modes** are not actual control strategies. If S_C is in position 1 (but not in self-synchronization mode) all the other operations are not allowed, as different S_Q/S_P combinations would not be feasible to correctly drive the powers P and Q to null value. These combinations should be avoided while performing the synchronverter control algorithm.

3) The **Grid-Connected Modes** (P and Q modes) are all available after the circuit breaker is closed and the switch S_C is thrown to position 2. In this position S_C redirects the measured i_g as PCC feedback in the algorithm. The synchronverter is enabled for power injection in the grid and can be used for voltage and frequency regulation, depending on the necessities of the grid:

- **P – Mode (S_P ON):** the PI controller is active and controls ΔT to 0. The electromechanical torque T_e is controlled to be equal to $T_m = \frac{P^*}{\omega_n}$ and the virtual frequency is controlled to be:

$$\dot{\theta} = \dot{\theta}_r = \dot{\theta}_n + \Delta\dot{\theta} \quad (83)$$

In P-mode the power angle δ stabilizes on a fixed value and as result $P = P^*$.

- **P_D – Mode (S_P OFF):** the PI controller is removed from the upper loop and the channel works in *frequency droop mode*, meaning that the droop coefficient $D_P = \frac{-\Delta T}{\Delta\dot{\theta}}$ uses the frequency deviation $\Delta\dot{\theta}$ from the nominal frequency to recover the synchronverter frequency:

$$\dot{\theta} = \dot{\theta}_n + \Delta\dot{\theta} \quad (84)$$

In this case the output power can be deviated from the reference: $P \neq P^*$.

- **Q – Mode (S_Q OFF):** the voltage droop control of the lower channel is disabled and the excitation $M_f i_f$ is generated from the tracking error between Q and Q^* . In steady state the synchronverter perfectly tracks $Q = Q^*$, regardless of the difference of V_g and V_n .
- **Q_D – Mode (S_Q ON):** the *voltage droop function* is enabled and the voltage error $\Delta V = V_n - V_g$ is taken into account for the calculation of $M_f i_f$. The droop coefficient $D_Q = \frac{-\Delta Q}{\Delta V}$ is used to minimize the voltage difference and the reactive power is deviated from its reference: $Q \neq Q^*$.

7.2.2 Matlab/Simulink Model of the Self-Synchronized Synchronverter

The Self-Synchronized Synchronverter is mainly composed by an IGBT three-phase inverter (*Universal Bridge Block*) and the *Controller Block*. The controller inputs/outputs can be enabled with a switch to start the synchronization at the desired time during simulations, as shown in *Fig.102*.

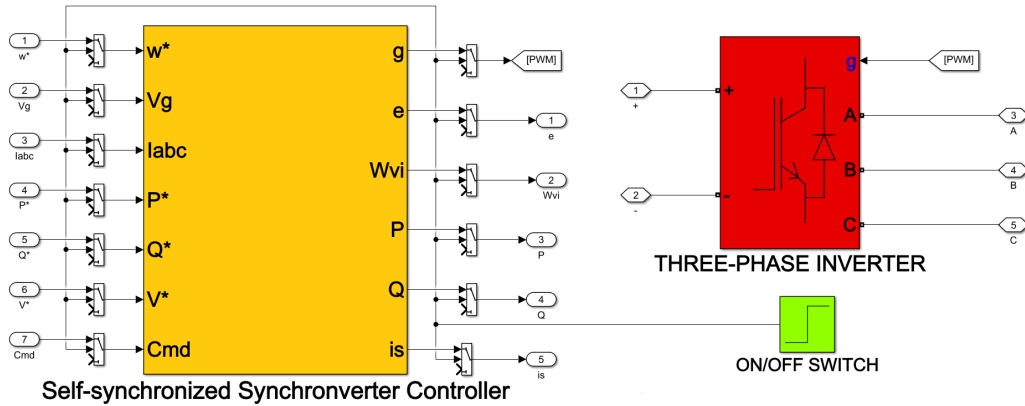


Fig. 102: Self-Synchronized Synchronverter main layout in Simulink.

As shown in *Fig.103*, the frequency loop is used to determine the synchronverter virtual frequency w_{VI} and the relative position θ , while the voltage loop sets the value of the field excitation M_{fi_f} . The initial condition for the excitation value was set in the integrator to be equal to eq. (86):

$$M_{fi_f} = |e|/\omega_n \quad (86)$$

with $|e|$ equal to the voltage grid amplitude to facilitate the synchronization process. The values obtained from the two loops are sent alongside the measured I_{abc} into the *SG Equation Block* of *Fig.104*, where all the output values are computed using the dynamic equations of the SG virtual machine.

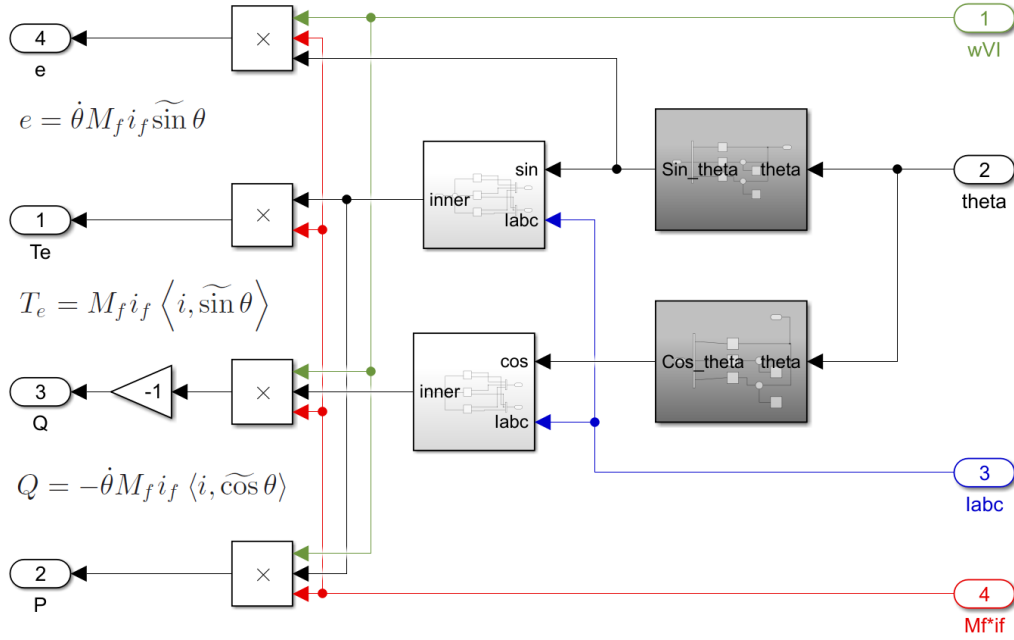


Fig. 104: Virtual Synchronous Generator dynamic equations [14]

The outputs are e , which represents the back electromagnetic force EMF obtained from the rotation of the imaginary rotor, the electromagnetic torque T_e and the generated active and reactive power P and Q . The powers have been obtained by using the measured current and the internal voltage e , considering the conventional definition in dq coordinates [5]:

$$P = \langle i_{abc}, e \rangle = \dot{\theta} M_{fi_f} \langle i, \sin\theta \rangle \quad (87)$$

$$Q = \langle i_{abc}, e_q \rangle = \dot{\theta} M_{fi_f} \langle i, \sin(\theta - \pi/2) \rangle = -\dot{\theta} M_{fi_f} \langle i, \cos\theta \rangle \quad (88)$$

The two equations have been used as feedbacks for regulating the active and reactive power generated by the virtual SG and are filtered with a low pass filter LPF for scope readings.

The internal voltage e is sent to a *PWM Block* to generate the inverter pulses and reproduce the same voltage on the synchronverters terminals. The PWM modulation is performed using the natural sampling technique with a switching frequency $f_{SW} = 10$ kHz, to avoid possible resonance with the LCL filter.

The Self-Synchronized Synchronverter presents four parameters that require a proper tuning to achieve a good control: J and D_P in the frequency loop, K and D_Q in the voltage loop. The chosen values are presented in *Tab.7*.

1) Active Power/Frequency Loop Parameters

The synchronverter's frequency typically follows the grid frequency and the algorithm can be set to share load variations with other generators on the grid (in P_D -Mode), meaning that the power is reduced for frequencies above nominal and increased for frequencies below nominal. The droop coefficient D_P ensures that the synchronverter can share power regulation with other generators when the grid frequency changes of $\Delta\omega$. The coefficient is calculated as [66]:

$$D_P = -\frac{\Delta T}{\Delta\omega} \simeq -\frac{\Delta P}{\Delta\omega * \omega_n} \quad [\text{Js}] \quad (89)$$

where ΔP represents the rated power of the virtual generator (a value of $P_n = 20$ kW was chosen based on the PV plant size) and $\Delta\omega$ the frequency variation. For the simulation D_P was chosen to double the power in front of 0.5% frequency variations. The inertia J is strictly proportional to the droop coefficient via a time constant τ_f , that defines the dynamic response of the frequency loop:

$$\tau_f = \frac{J}{D_P} \quad [\text{s}] \quad (90)$$

The time constant was chosen in order to obtain an inertia constant that can represent a real generator (generally $H = 1 \div 12$ s), even if smaller values can be set to increase the time response of the virtual generator. The τ_f and J values have been chosen to obtain an inertia constant of approximately 2 seconds, which is comparable to the hydro plant inertia constant ($H_{HPP} = 4$ s) and can help appreciate the benefits of an additional generator on the simulated microgrid. The power-frequency characteristics for P -Mode and P_D -Mode are shown in *Fig.105-a*.

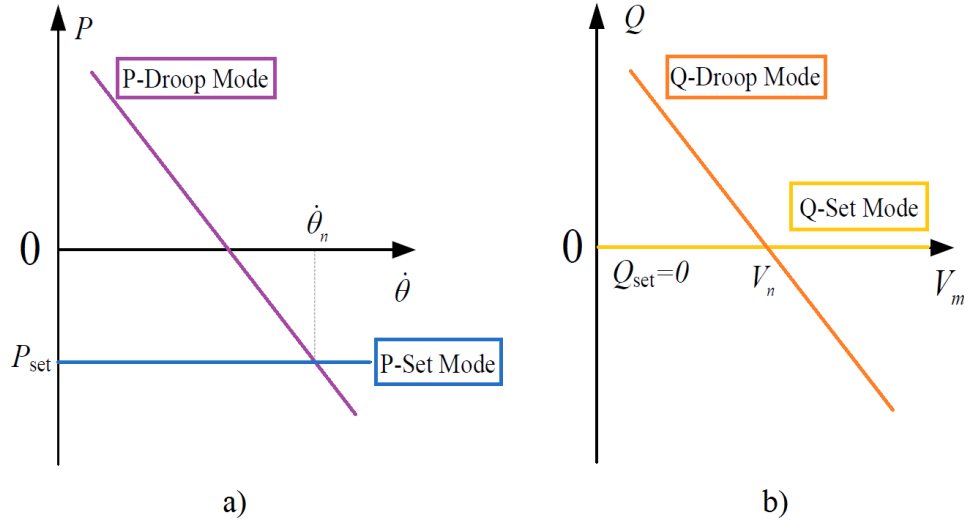


Fig. 105: Control characteristics of the synchronverter: a) P-f characteristic in set mode (constant P) and droop mode; b) Q-V characteristic in set mode (constant Q) and droop mode [66].

A large virtual inertia value requires an energy storage to simulate the mechanical energy accumu-

lated by the virtual rotor: in the simulation the short-term storage is represented by the photovoltaic plant, while the battery acts as long-term storage during power frequency regulation. The storages are decoupled by the synchronverter with the DC-link, where the voltage is kept constant by the battery control. The drooping coefficient and the inertia also present a second set of values D_{PS} and J_S , that are reduced approximately of one order of magnitude to speed up the self-synchronization process. These values are switched to normal values once the grid synchronization and connection is concluded, as shown in *Fig.103* (Switch $J\text{-init}$).

2) Reactive Power/Voltage Loop Parameters

The main purpose of the voltage loop is to control e and Q using the rotor flux with a simple integrator, with minimum changes on the controlled P . Most of the generators on the grid work in power-voltage mode PV , meaning they help stabilizing the voltage by generating or absorbing reactive power. For this purpose a reactive droop coefficient is defined:

$$D_Q = -\frac{\Delta Q}{\Delta V} \quad [\text{A}] \quad (91)$$

where ΔQ is the variation of reactive power corresponding to a voltage variation ΔV . In the simulation chosen D_Q makes the reactive power changes of its 100% for a 5% voltage variation. The parameter K is chosen to define the dynamics of the synchronization process. Small K values can introduce oscillations in the system, while a greater values slow down the synchronization process, but improve its stability. The coefficient is obtained from D_Q by imposing the time constant τ_v :

$$\tau_v = \frac{K}{\omega D_Q} \simeq \frac{K}{\omega_n D_Q} \quad [\text{s}] \quad (92)$$

The time constant is generally much greater than τ_f to ensure that $M_f i_f$ remains constant for the dynamics of the frequency loop. In the simulation the two time constants have instead the same order of magnitude, because of the high value of inertia chosen (typically synchronverters work with small inertia values). A greater τ_v would impose a value of K way too high, that would lead to the impossibility of synchronize properly with the grid.

During synchronization the droop control is not active and a smaller value K_S is used to speed up the process. After the connection to the grid the normal K is enabled with S_Q , when the droop mode is activated. The power-voltage characteristics for $Q\text{-Mode}$ and $Q_D\text{-Mode}$ are shown in *Fig.105-b*.

Table 7: Parameters for the Self-Synchronized Synchronverter.

Electric Parameters		Frequency Loop Parameters		Voltage Loop Parameters	
V_{DC}	650 V	τ_f	0.02 s	τ_v	0.05 s
V_n	$\sqrt{2} * 219.4$ V	D_P	40.55 J·s	D_Q	1290 A
f_n	50 Hz	J	0.81 Kg·m ²	K	20000
P_n	20 kW	D_{PS}	5.1 J·s	D_{QS}	—
$M_f i_f$	0.987 V·s	J_S	0.1015 Kg·m ²	K_S	2000

7.2.3 LCL Filter and Virtual Impedance

The LCL filter is used mainly to reduce the higher harmonic content generated by the inverter's switching. The parameters are chosen to contain the current and voltage ripple under reasonable values. Typically current ripple is 5% and the voltage drop is under 10% of nominal value. Initial values for inductive and capacitive parameters were determined starting from parameters used [65], by scaling the nominal transferred power from the original P_1 to the synchronverter's $P_2 = 20$ kW while maintaining the switching frequency and ripple constraints:

$$L_{S2} = L_{S1} \frac{P_1}{P_2}, \quad C_2 = C_1 \frac{P_2}{P_1}, \quad L_{g2} = L_{g1} \frac{P_1}{P_2} \quad (93)$$

The initial values presented prevalent harmonic content on the inverter's output voltage. The harmonic issue was solved by doubling inductance values and choosing a greater capacitor. The virtual impedance, used to create the virtual current described in equation (82), was set by choosing a virtual resistor twice the size of the stator resistor R_S and the virtual inductor slightly smaller than L_S .

Table 8: Parameters for the LCL filter and the virtual impedance.

LCL Filter Initial Parameters		LCL Filter Parameters		Virtual Impedance	
P_1	5 kW	R_S	0.3 Ω	R_v	0.6 Ω
L_{S2}	1.1 mH	L_S	2.2 mH	L_v	2 mH
P_2	20 kW	R_g	0.3 Ω	$Z_V(s)$	1/(0.002s + 0.6)
L_{g2}	0.55 mH	L_g	1.1 mH	$Z_V(z)$	0.0012/(z - 0.9)
C_2	40 μ F	C	280 μ F	-	-

The LCL filter was implemented in Simulink by using *Three-phase Series RLC branch Blocks*, which allow to set the branch type and set R , L and C parameters as model variables (*Fig.106*). The filter is connected directly to the output voltage of the *Universal Bridge Block*. The virtual impedance was transformed from Laplace domain to discrete domain by using the Matlab command *c2d*. The new transfer function is calculated for the set discrete sampling time T_S .

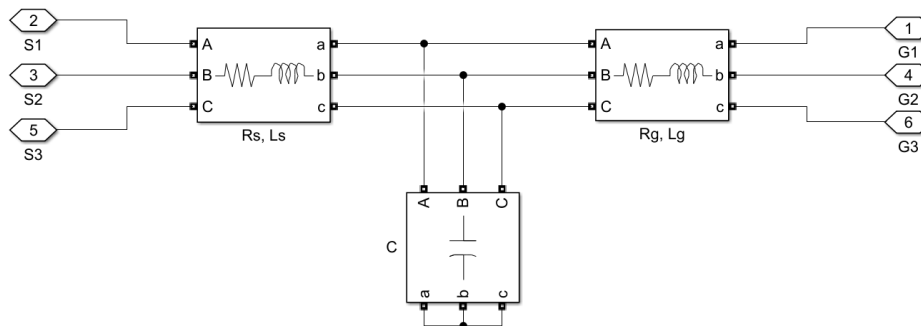


Fig. 106: LCL filter implementation in simulink

7.2.4 Synchronverter Model Simulation Tests

The Self-Synchronized Synchronverter model was tested firstly in a standalone configuration in Simulink (*Fig.107*), independently from the simulated HPP plant and microgrid. The synchronverter is supplied by the PV plant and battery DC source with the interposition of a DC-link with two $630 \mu\text{F}$ condensers with middle grounded connection, to allow the inverter to produce positive and negative voltages. The synchronverter's power output is cascade connected to the LCL filter followed by the grid-connection breaker, a $0.38/20 \text{ kV}$ step-up transformer, a 2 km medium voltage *PI Section* line and an infinite 20 kV bus, represented by a *Three-Phase Voltage Source*. *V-I* measures are performed before and after the LCL filter and after the breaker, where the grid voltage V_g is detected at 380 V level to perform the synchronization with the grid. The parameters in the PI section line are typical values for MV cables and define resistances, inductances and capacitances per km for both the positive and zero sequences ($r_1, r_0, l_1, l_0, c_1, c_0$). The transformer parameters were computed for a 630 kVA transformer using data from catalogues. The data are shown in *Tab.9*.

Table 9: PI line and transformer parameters used in the simulation.

PI Line parameters	$r_1 = 0.453 \Omega/\text{Km}, r_0 = 0.601 \Omega/\text{Km}, l_1 = 1.292 \text{ H}/\text{Km}$ $l_0 = 4.835 \text{ H}/\text{Km}, c_1 = 9.02 \text{ nF}/\text{Km}, c_0 = 4.41 \text{ nF}/\text{Km}$
Transformer parameters	$V = 0.38/20 \text{ kV}, P_n = 630 \text{ kVA}, R' = 1.3\text{m}\Omega, x' = 4.91\text{m}\Omega$ $R'' = 3.6\Omega, X'' = 13.6\Omega, R_m = 123\Omega, X_m = 14.2\Omega$

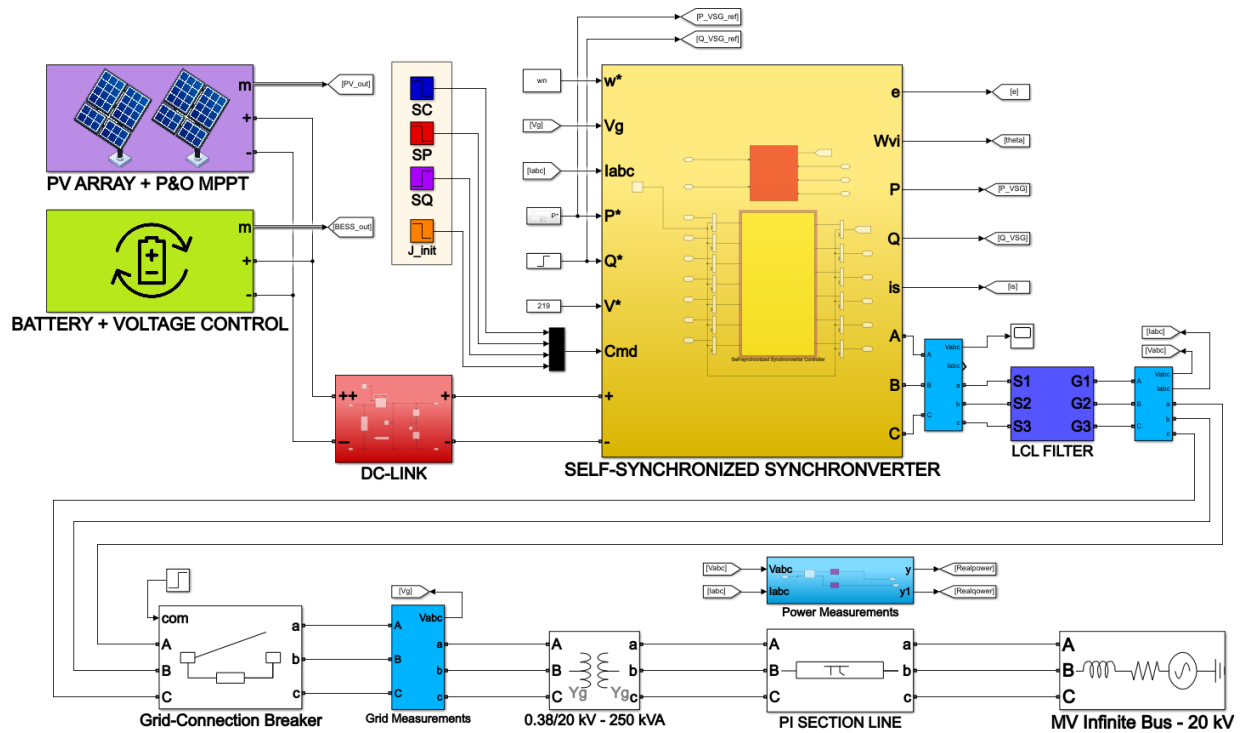


Fig. 107: Layout for standalone tests of the Self-Synchronized Synchronverter.

The tests of the synchronverter model are focused on verifying its ability to self-synchronize with the grid and to observe how it responds to power control. Since the synchronverter can be used as grid-forming generator, tests have been made to exploit the model both as PQ node and PV node on the ideal grid. A first test was made specifically to observe the synchronization process. Results are shown in *Fig.108*. The synchronverter controller was started at $t = 0.5$ seconds (simulation time) and the synchronization with the grid voltage was completed in around 0.15 seconds. It can be observed for phase a that the internal voltage e starts from null value and evolves to match the grid voltage V_g both in amplitude and phase. The virtual current i_S is correctly driven to zero by the controller, as the voltage difference $e - V_g$ also get to null value, while the two voltages converge to the same waveform. It can be noted that the active and reactive power have a transient, even if they are virtual values computed with i_S , but the controller efficiently drive both values to zero as required by the synchronization process ($P^*=0, Q^*=0$). The synchronverter frequency stabilized at 50 Hz, matching the grid frequency.

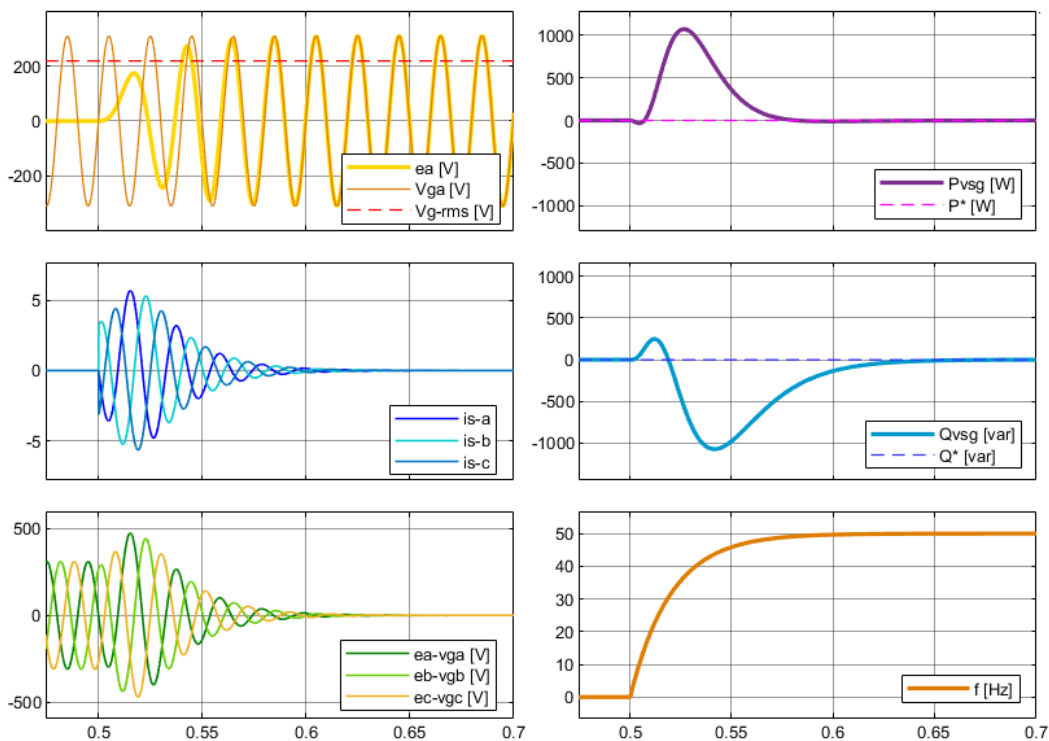


Fig. 108: Test 1: Synchronization process. The synchronization starts @ $t = 0.5$ s.

The second test was performed with the synchronverter in PQ mode (S_P ON, S_Q OFF), meaning no droop control is enabled. Results are shown in *Fig.109*. Synchronization starts at $t = 0.5$ s, after the DC voltage V_{DC} is brought to reference by the battery control. After the initial synchronization, the circuit breaker is closed at $t = 1$ s and S_C is switched to the measured current position. The connection to the grid presents a current transient, that is also reflected on the active and reactive power: this is due to the fact that the synchronization is made between e and V_g , but the LCL filter introduces a voltage drop. The graphic shows that the voltage $V_{LCL-rms}$ is lower than the actual $e-rms$ before the connection. When the breaker is closed the grid imposes that $V_{LCL} \equiv V_g$, causing the transient. The control resolves the transient in few cycles and maintains the $P^*=0, Q^*=0$ condition.

At $t = 2$ s, a set of three 5 kW steps was applied to control the active power P . The controller correctly followed the reference power steps with the internally computed P_{VSG} , which is used as feedback for the frequency loop. The current $i_S = i_g$ increased every step, as expected for power injections in the grid. The internal voltage e remained constant during the power variation, as active power is controlled by varying the power angle δ as seen in eq. (79). The reactive power was correctly regulated to be 0. At $t = 5$ s a 5 kvar step was applied. The reactive power control correctly followed the reference. Active power and current remained constant on their reference value. The voltage e increased to allow the reactive power variation, as described in eq. (80). The measured active power is labelled P_{meas} in Fig.109 and is used to check how the power is injected in the grid. The value follows the active power steps, but presents Joule losses as more active power is generated. The losses are due to the impedances of the LCL filter and partially to the harmonic content in the current.

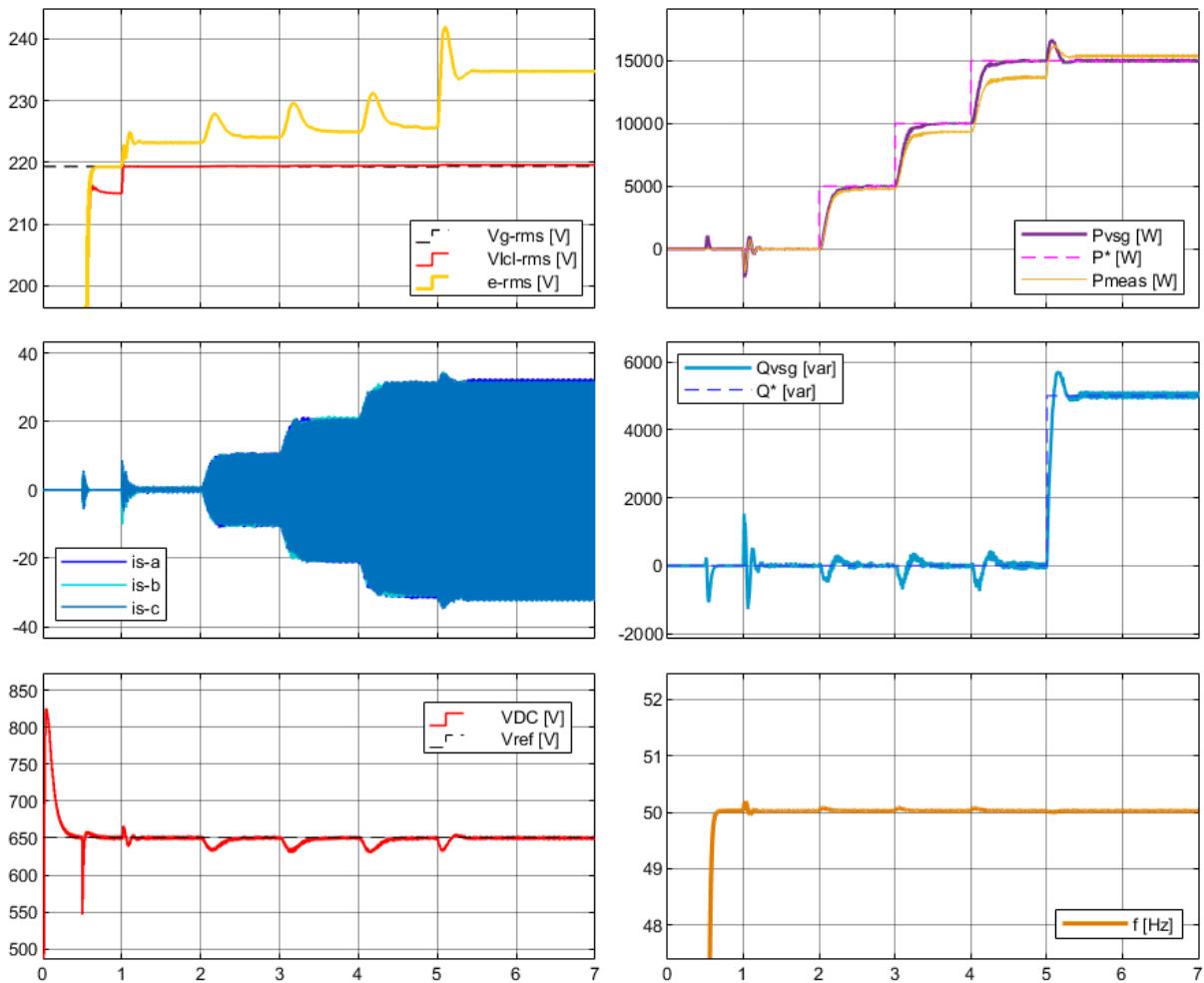


Fig. 109: Test 2: synchronverter in PQ node configuration. Synchronization @ $t = 0.5$ s, connection to the grid @ $t = 1$ s, multiple 5 kW steps @ $t = 2, 3, 4$ s, 5 kvar step @ $t = 5$ s.

The controller is overall performing a smooth control, introducing minor oscillations in the output powers during step variations. The frequency and the DC-link voltage V_{DC} presented small deviations from reference during the power steps, but were correctly regulated. The active and reactive

powers P_{VSG} and Q_{VSG} were filtered to cut out higher harmonic content, as both the measured current and the inverter voltage are not perfectly sinusoidal.

The power flow towards the grid is generally not directly measured, but can be determined starting from voltage and current measures. In *Simulink* is possible to perform power measures using the *Power (3ph Instantaneous) Block*. The main problem of the block is that reactive power measure is not accurate for systems that are not balanced and harmonic-free. The output of the synchronverter presents harmonic content especially on the current i_S , as shown in *Fig.110*, making reactive power measures not reliable (in a non-sinusoidal system the concepts of non-active power and deformed power are introduced). The active power definition is still valid and is computed as the integral of the instantaneous power on the period T , as shown in eq. (94).

$$P = \frac{1}{T} \int_T p(t) dt = P_0 + \sum_{h=1}^{\infty} Ph = V_a \cdot I_a + V_b \cdot I_b + V_c \cdot I_c \quad (94)$$

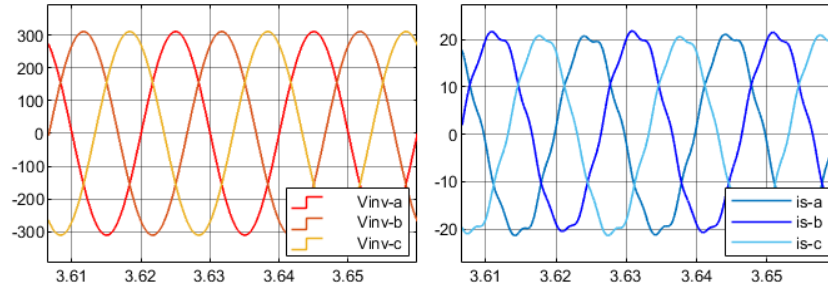


Fig. 110: Harmonic distortion of current and voltage at the connection point with the grid.

The harmonic content of voltage-current waveforms was measured by performing a *Fast Fourier Transform* analysis using the dedicated *Powergui* tool in *Simulink*. The analysis was executed on both voltage and current waveforms in steady state conditions with $P = 10$ kW. The analysis window was chosen to be 10 cycles of the fundamental frequency (50 Hz), in order to have a resolution bandwidth of $\Delta f = 5$ Hz. Results are showed in *Fig.111*.

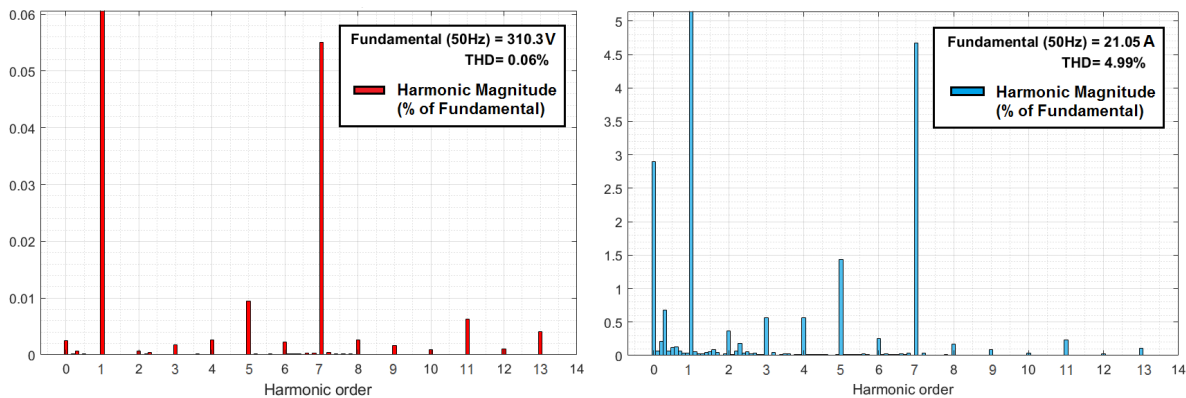


Fig. 111: FFT analysis and THD measurement of synchronverter's output voltage and current.

The harmonic magnitude for various frequencies is displayed as percentage of the fundamental value. The waveforms present harmonic content up to the 13th order. The voltage waveform has

a THD = 0.06 %, meaning that the total harmonic distortion is not impacting on the grid and can be considered negligible. The voltage can be then considered sinusoidal with good approximation. The current waveform, on the other end, presents a THD = 4.99 %, with predominant harmonic components on the 7th and 5th order and on the DC component (0th order). As long as the THD is less than 10 % the distortion is considered within normal boundaries for power quality [67], but the system remains non-sinusoidal.

The third test was performed with the synchronverter in PV mode (S_P ON, S_Q ON), meaning the voltage droop control is enabled. Results are shown in *Fig.112*. Synchronization starts at $t = 0.5$ s and the circuit breaker is closed at $t = 1$ s. The voltage droop control is enabled at $t = 1.5$ s. The synchronverter is set to regulate the node voltage to $V^* = 220$ V and the reactive power changes accordingly to the required value. A 5 kW active power step is applied at $t = 3$ s and a second 10 kW step is applied at $t = 5$ s. The active power is correctly regulated to follow the reference P^* . The reactive power Q_{VSG} and the internal voltage e are maintained to the values set by the voltage controller, and present overshoots during the step regulation of active power. The synchronverter controller demonstrated of being able to follow different power step sizes and managed transients in under 1 s, without any strong oscillations and overall limited overshoots.

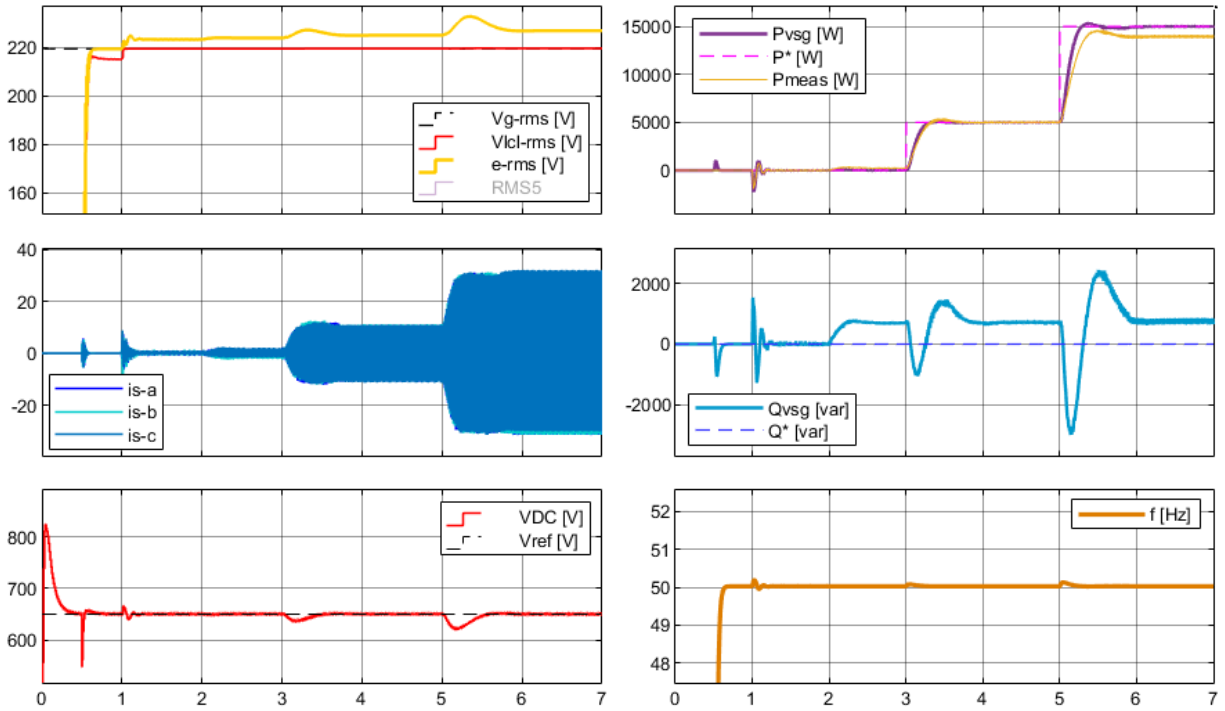


Fig. 112: Test 3: synchronverter in PV node configuration. Synchronization @ $t = 0.5$ s, connection to the grid @ $t = 1$ s, voltage droop control enabled @ $t = 2$ s, 5 kW step @ $t = 3$ s, 10 kW step @ $t = 5$ s.

The fourth test is an extension of the third test and shows in *Fig.113* how the synchronverter controller performs a nominal 20 kW step. The results shows analogous behaviours for all the variables, confirming what have been said for the third test. The fifth test was performed to observe the controller response for active power ramps. Results are presented in *Fig.114*. After the synchronization and grid connection a 10 kW load ramp (3.3 kW/s) was applied to the system. The synchronverter active power P_{VSG} correctly followed the reference. The reactive power is controlled

to be null. The current injected in the grid increased as a ramp to match the power generation request. The frequency remained reasonably constant, as it is set by the infinite bus at the point of connection with the grid. The DC-link voltage V_{DC} presented a negligible reduction during the ramp and was maintained constant by the battery control.

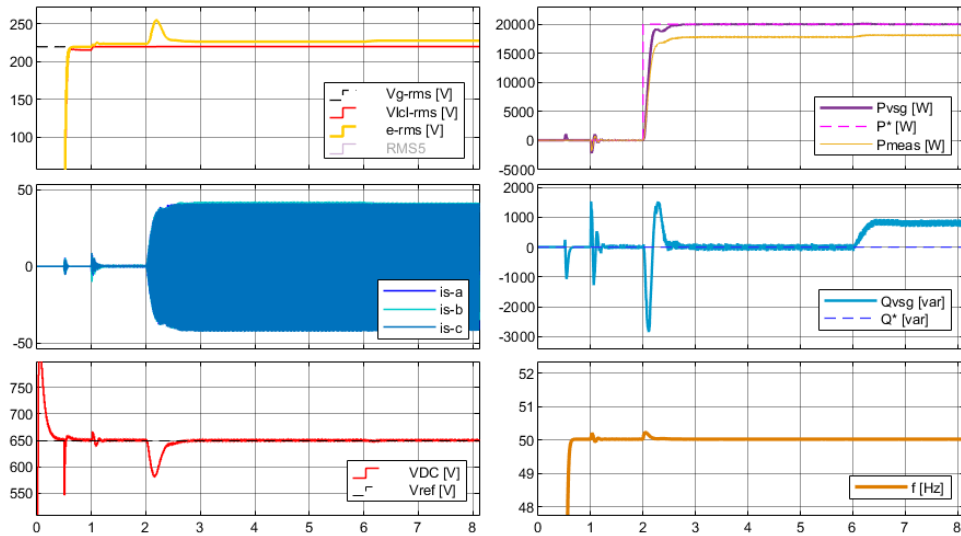


Fig. 113: Test 4: synchronverter in PV node configuration. Synchronization @ $t = 0.5$ s, connection to the grid @ $t = 1$ s, 20 kW nominal active power step @ $t = 2$ s, voltage droop control enabled @ $t = 6$ s.

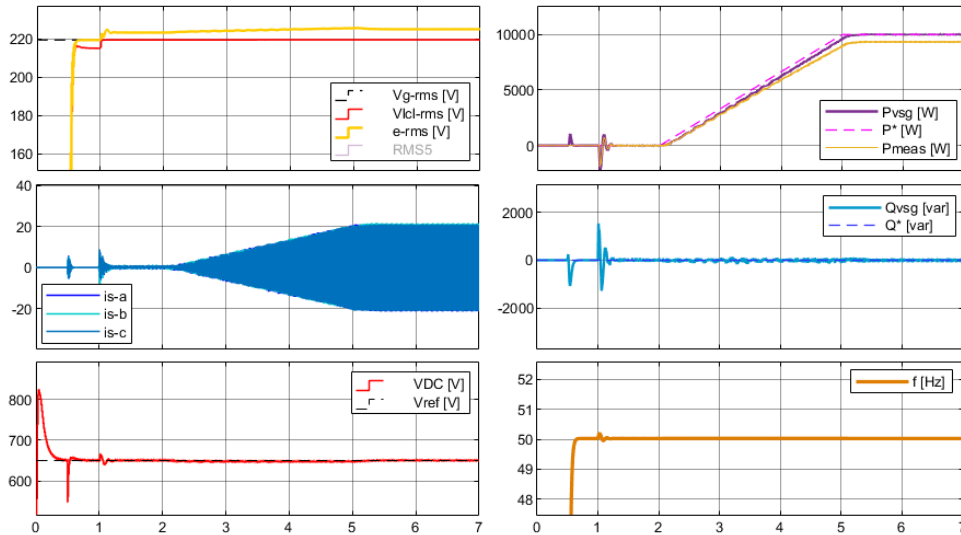


Fig. 114: Test 5: synchronverter in PQ node configuration. Synchronization @ $t = 0.5$ s, connection to the grid @ $t = 1$ s, 10 kW active power ramp (3.3 kW/s) @ $t = 2$ s.

The implementation of the *Self-Synchronized Synchronverter* model in Simulink proved to be overall stable with the chosen set of parameters. The LCL filter tuning successfully shaped the inverter's output voltage and maintained the current harmonic distortion within acceptable limits.

7.3 Full Microgrid Model (HPP and Synchronverter)

The full microgrid model is obtained by connecting the HPP model, the *Self-Synchronized Synchronverter* model and the DC source model to a small independent group of loads, as shown in Fig.115. The model was arranged in Simulink via the RTLab software, in order to use the same file for both offline and online real-time tests. The main layout presents the HPP plant connected to the microgrid with a short 150 m LV line. The DC source (photovoltaic + battery) is supplying the synchronverter via a DC-link. The synchronverter is connected at the end of the LV line via a grid-connection breaker. The microgrid is composed by two main inductive loads (10 kW and 20.25 kW) and different smaller loads for simulating different situations for tests (steps, ramps). The microgrid parameters for all its main parts are summarized in Tab.10.

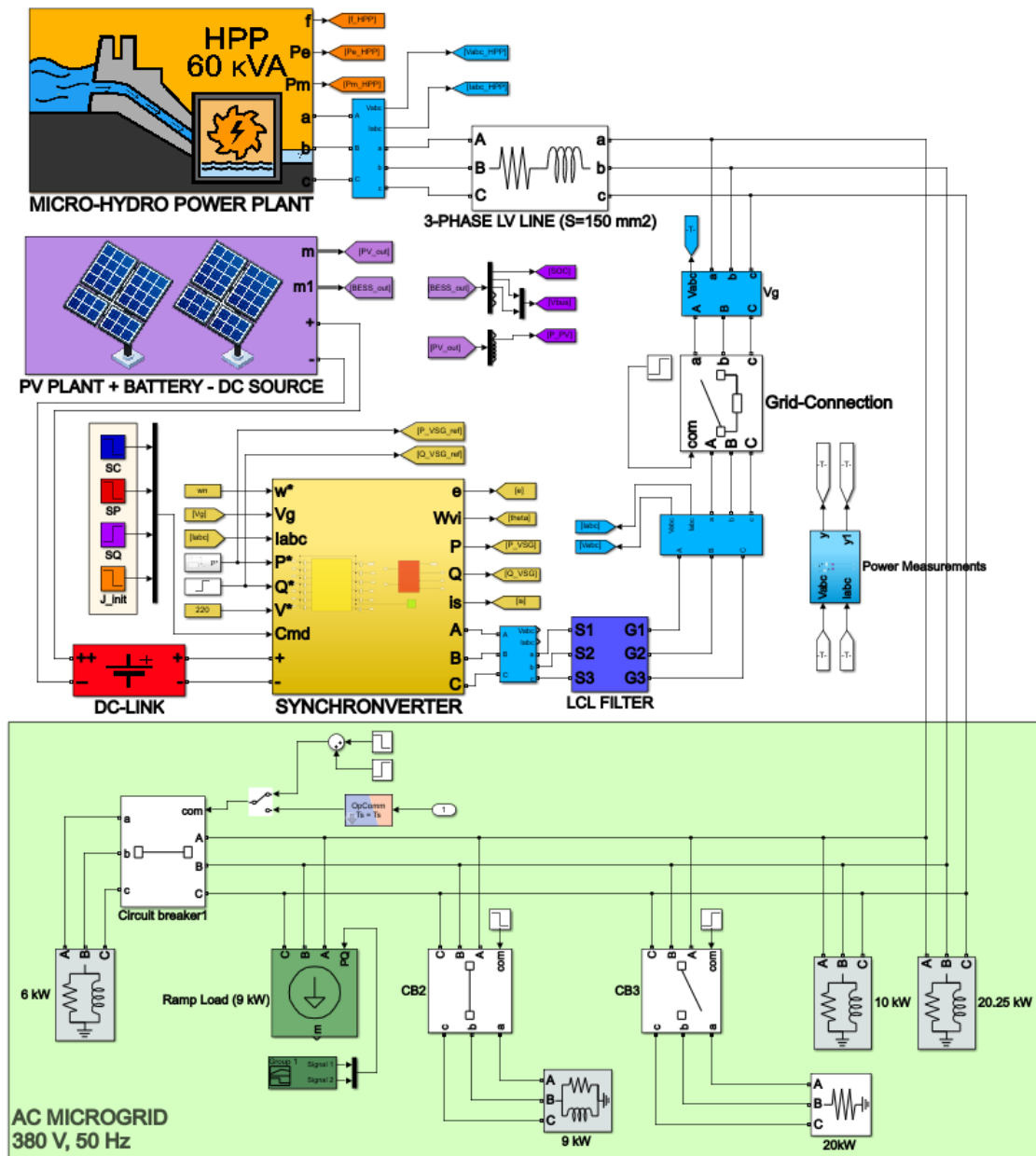


Fig. 115: Full microgrid model layout in RTlab-Simulink (in the SM subsystem).

The model is divided in the *Master Subsystem SM* and the *Interface Subsystem SC*, as discussed in **section 6.4**. The SM-MASTER block is comprehensive of the full microgrid model of *Fig.115* and a series of *OpTrigger* and *OpWriteFile* blocks for saving simulation data and communicating with the SC subsystem (*Fig.116*). The whole model in the SM-MASTER block is executed on the main target node of the OpalRT real-time simulator.

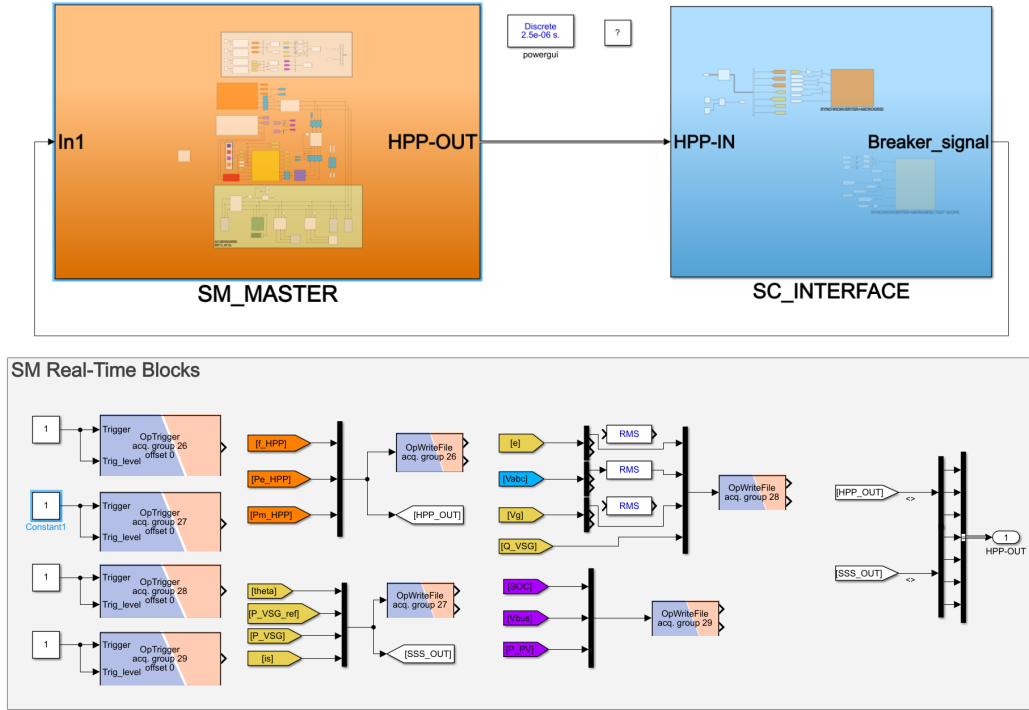


Fig. 116: RTLab blocks for data saving and triggering in the SM subsystem.

The SC-INTERFACE block is comprehensive of an *OpComm Block*, that processes the signal output of the *SM* block, and a scope for non-real time monitoring (*Fig.117*). Additional switches can be implemented for controlling the real-time simulation without a proper synchronization (due to delays in the communication between the console and the target node). For real-time tests this function was substituted by fixed breaker commands directly in the SM subsystem.

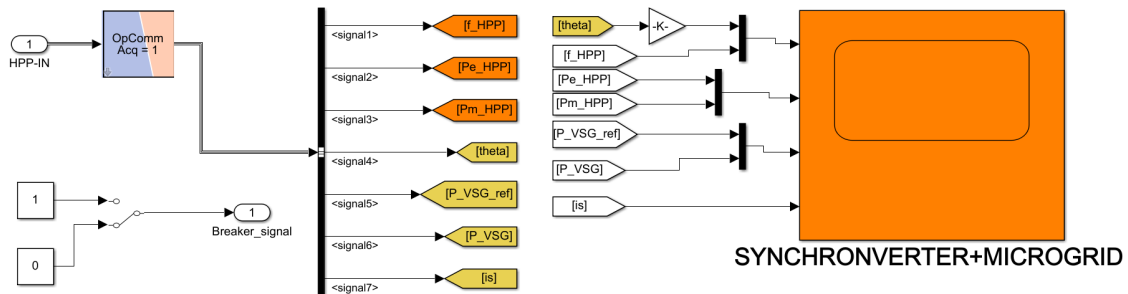


Fig. 117: Console Subsystem SC.

The microgrid simulations are performed assuming a load step/ramp change in the system. The objective is to observe how effective is the HPP in controlling the microgrid frequency alongside the synchronverter and how the added virtual inertia impacts on frequency variation during a

contingency event. A further aim is also to observe how the HPP and the synchronverter share power regulation according to their droop controls and set-points. The tests are all performed assuming that the HPP is initially generating 80% of its nominal power. The synchronverter is connected to the microgrid after the voltage synchronization and tests are started once the connection has reached its steady state.

Table 10: Microgrid main blocks parameters.

HPP: Micro-Hydro Power Plant	
Synchronous Generator	380 V - 60 kVA - 50 Hz - $H = 4$ s
Hydraulic Turbine	$T_w = 0.25$ s - $R_P = 5\%$
VSG: Self-Synchronized Synchronverter	
Power Block	650 Vdc - 380 V - 20 kW
Control Block	$H = 2$ s - $D_P = 0.5\%$ - $D_Q = 5\%$
DC Source	
Photovoltaic Plant	20.5 kW - 300/650 Vdc
Battery	96 Vdc - 100 Ah - SOC 50 %
Microgrid Parameters	
LV Three-phase Line	150 mm^2 - 150 m - $0.076\ \Omega/Km$ - $0.0057\ \Omega/Km$
Load 1	20.25 kW - 9.81 kvar - $\cos\varphi 0.9$
Load 2	10 kW - 5 kvar - $\cos\varphi 0.9$
Test Load 1	6 kW - 2 kvar - $\cos\varphi 0.95$
Test Load 2	9 kW - 3 kvar - $\cos\varphi 0.95$
Dynamic Load	9 kW - 0.36 kW/s ramp
Fast-Steady-State Load	20 kW

7.3.1 Microgrid Offline Tests (Simulink Environment)

The microgrid tests were initially performed offline in Simulink to verify the overall correct operation of the model. For this stage of simulation the console block SC was not necessary, as the model was executed completely on the host PC. Simulation data were acquired using the *OpWriteData* blocks with the *Write in Simulink Mode* enabled and they were further elaborated afterwards in Matlab. All the simulations were performed in discrete time with a time step $T_s = 2.5\ \mu\text{s}$. The data acquisition was made with a decimation factor of 10, meaning that the sample time for acquisitions was $T_s^* = 25\ \mu\text{s}$ (one sample stored every 10 samples). The decimation allowed to reduce the size of data matrix and the speed of data storing without losing relevant information in the final display of waveforms. A first test was performed to observe the synchronverter connection to the grid and its functioning in PV mode. The simulation results for the initial synchronization are shown in *Fig.118*, indicating the VSG voltage and current at the point of connection with the

microgrid. The synchronization with the grid started at $t = 5$ s and was successfully completed in 0.1 s, with the internal e aligned in amplitude and phase with the microgrid voltage V_g . The grid connection was performed at $t = 5.2$ s and presented a transient with peaks of 20 A on the synchronverter side. The current is due to the voltage difference upon the LCL filter.

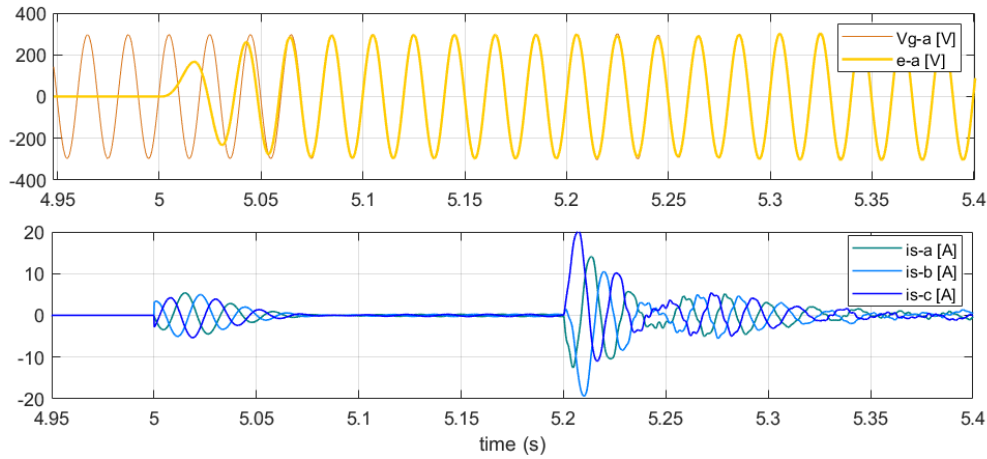


Fig. 118: Test 1: voltage-current synchronization with the grid @ $t = 5$ s, grid connection @ $t = 5.2$ s.

In Fig. 119 is shown the evolution of the powers in the microgrid during the connection process. The HPP plant temporarily balanced the VSG negative 5 kW power peak with a positive active power variation, while the frequency remained reasonably stable at 50 Hz. The transient was resolved within 2 seconds with small oscillations. The HPP frequency correctly tracked the nominal 50 Hz, while the internal synchronverter frequency reference $vsg-ref$ presents a 0.025 Hz offset due to the controller settings.

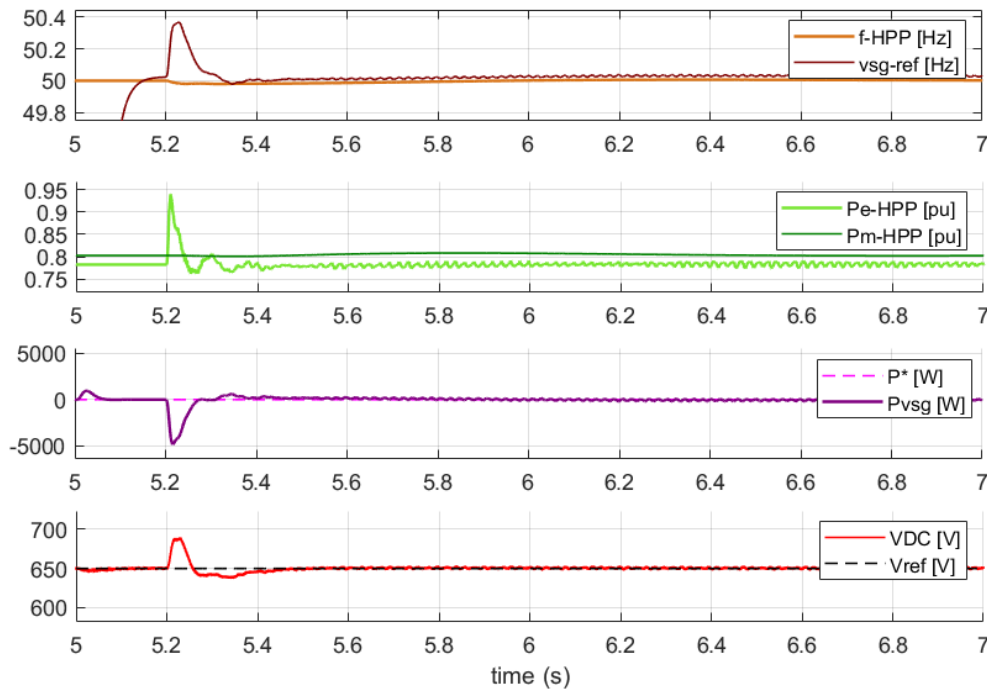


Fig. 119: Test 1: HPP-Synchronverter synchronization @ $t = 5$ s, grid connection @ $t = 5.2$ s.

The synchronverter was switched to PV mode (S_P OFF, S_Q ON) at $t = 8$ s and was controlled to provide 20 kW to the microgrid. Simulation results are shown in *Fig.120*. The power step initially presented oscillations due to the voltage drooping control, that increased the internal voltage e to set the reference V^* . The initial microgrid frequency nadir was of 50.4 Hz. The synchronverter successfully aligned the active power P_{vsg} to the step reference P^* in around 70 seconds. The slow rise was due to the HPP drooping control, that adapted its output power P_e to the synchronverter's 20 kW step (33 % of $P_{HPP,n}$) by reducing the power production from 0.78 pu (46.8 kW) to 0.42 pu (25.2 kW). The frequency successfully returned to 50 Hz.

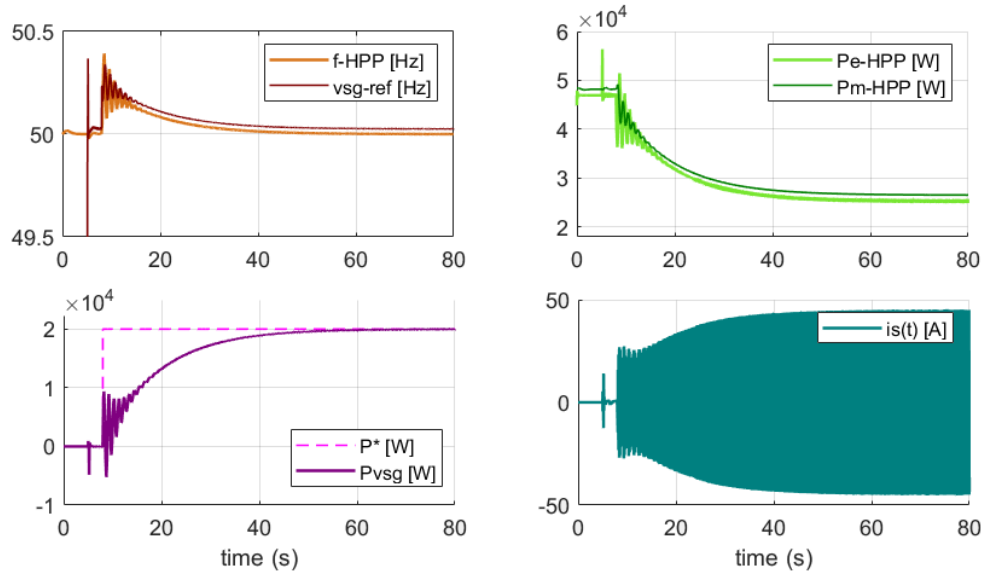


Fig. 120: Test 1: HPP-Synchronverter synchronization @ $t = 5$ s, grid connection @ $t = 5.2$ s, 20 kW synchronverter step + PV mode enabled @ $t = 8$ s.

The second test was performed to observe the effects of 6 kW steps (10 % of $P_{HPP,n}$) on the microgrid, in comparison to tests performed in **section 6.3** and **section 6.4**. The model was rapidly brought to generate the 20 kW nominal power with the synchronverter by connecting the 20 kW *Fast Steady-State Load* at $t = 8$ s, as shown in *Fig.121*. This action avoids the intervention of the slow droop regulation of the HPP plant and speeds up the simulation (steady state is reached at $t = 25$ s instead of previous $t = 80$ s). The HPP power was slightly reduced from 46.8 kW (0.78 pu) to 45 kW (0.75 pu). The synchronverter active power P_{vsg} could not exactly track the reference as S_P was OFF, removing the perfect active power control loop in favour of the drooping control.

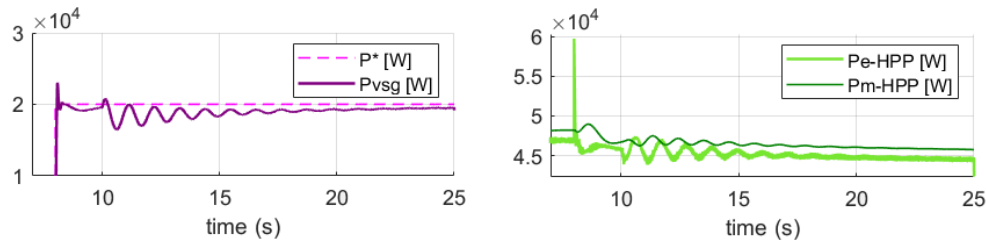


Fig. 121: Test 2: Fast Steady-State Load connection @ $t = 8$ s, for speeding up the simulation to HPP-Synchronverter's steady state conditions.

The 6 kW *Test Load 1* was disconnected from the microgrid at $t = 25$ s and successively reconnected

at $t = 55$ s, as shown in *Fig.122*. The synchronverter controller maintained the 20 kW reference and the HPP droop control adapted the P_e -HPP output power (reducing and increasing production of $10\% \equiv 6$ kW). The frequency was contained in the range $[49.9 \div 50.1$ Hz] and presented more oscillation if confronted with the independent HPP control observed in *Fig.78*. The frequency nadir was nonetheless reduced from initial 0.5 Hz to 0.1 Hz, confirming the positive influence of the additional virtual inertia introduced by the synchronverter. The power-frequency regulations were performed within 30 seconds, the typical time for primary control based on the response of turbine governors.

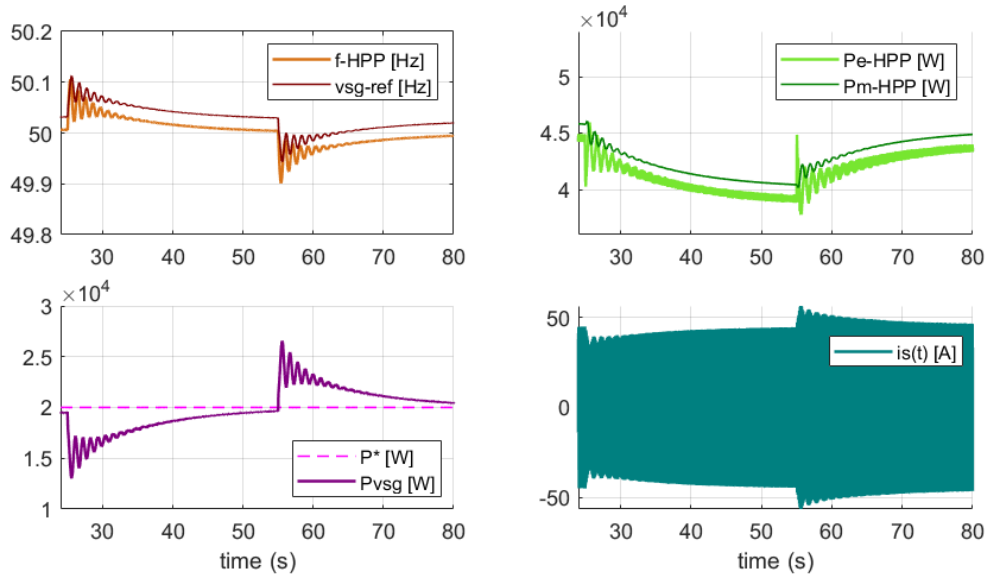


Fig. 122: Test 2: starting for steady state a negative 6 kW is applied @ $t = 25$ s and a positive 6 kW is applied @ $t = 55$ s.

During the load variations, the inverter voltages presented small oscillations (*Fig.123*). The DC-link was correctly controlled to its reference value and the internal voltage e remained constant at the value imposed by the droop voltage control. The battery supported the grid during the load reconnection at $t = 55$ s. The SOC started to decrease during the second transient, which temporarily required to the synchronverter a power peak of 26 kW for the initial inertial response of generators.

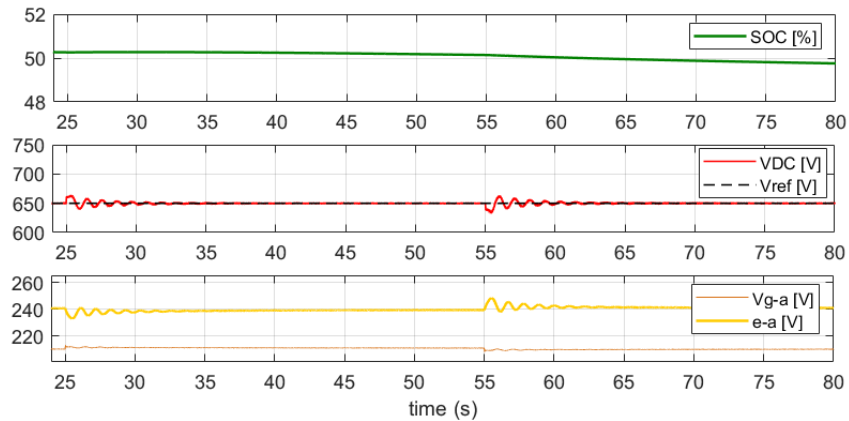


Fig. 123: Test 2: state of charge, DC-link voltage and synchronverter voltage during a 6 kW steps.

The third test was performed to observe the effects of 9 kW steps (around 10% of the total microgrid power $P = P_{vsg,n} + P_{HPP,n} = 80$ kW). Results are presented in *Fig.124*. The model was brought to steady state in the same way described for *Test 2*. The 9 kW *Test Load 2*, representing a group of three houses, was disconnected from the grid at $t = 30$ s. The inertial response of the synchronverter managed to reduce instantaneously the required active power of 9 kW and the controller managed to set again the P_{vsg} value to the 20 kW set point. The HPP plant reduced its output power with the drooping control in around 50 s, starting from 0.76 pu (45.6 kW) to 0.63 pu (37.5 kW). The microgrid frequency was correctly regulated to 50 Hz and presented a nadir of 0.15 Hz, confirming an improved frequency behaviour, with the same test condition, with respect to what shown in *Fig.78*.

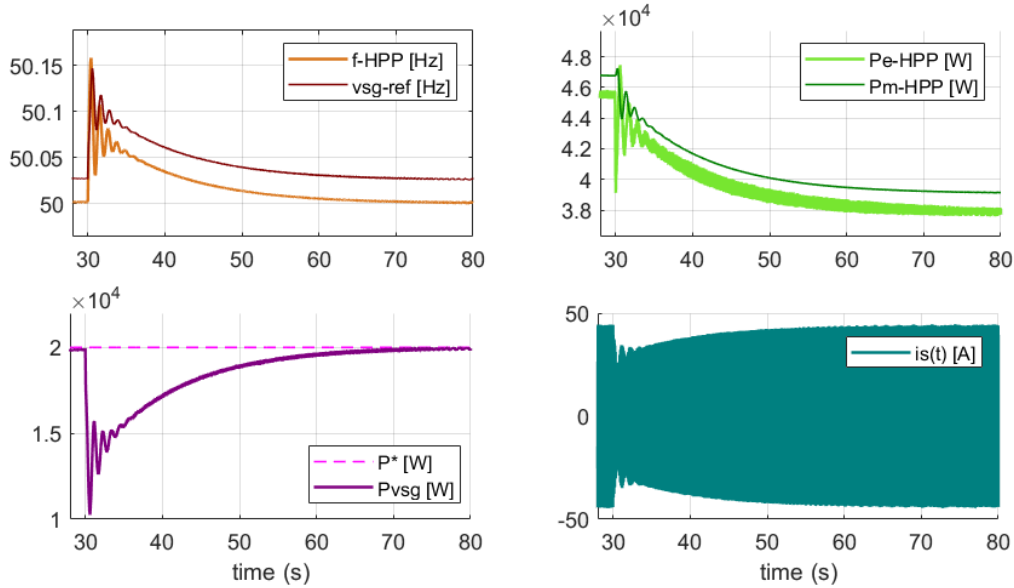


Fig. 124: Test 3: negative 9 kW step @ $t = 30$ s.

The synchronverter frequency reference $vsg-ref$ presented again a small tracking error with a 0.025 Hz offset due to the drooping control. The synchronverter controls at the same time the 20 kW step and the frequency, but the active power is always slightly inferior to the reference P^* leading to a frequency internal reference slightly above the nominal 50 Hz. The DC-link voltage was maintained constant around the reference value (*Fig.125*). The battery started to recharge at $t = 30$ s to store part of the negative active power on the synchronverter side.

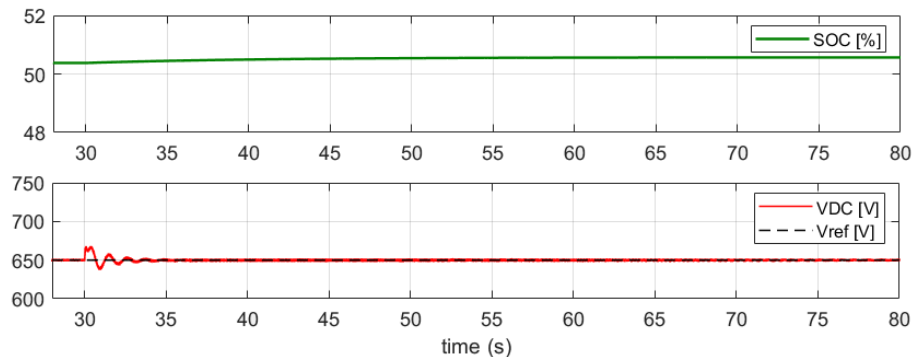


Fig. 125: Test 3: State of charge and DC-link voltage during the negative 9 kW step.

The fourth test was aimed at observing the response of the system to a ramp equal to 10% of the total nominal power. Results are shown in *Fig.126*. The *Three-phase Dynamic Load Block* was used to simulate an active power ramp load, starting from 0 up to 9 kW. A positive ramp was applied at $t = 25$ s and was completed at $t = 50$ s, with a speed of 0.36 kW/s.

When the active power load started to increase, the frequency decreased. As consequence the synchronverter provided the required active power with its faster response, due to a lower constant of inertia. The HPP plant adjusted its power at a slower pace, starting from 0.76 pu (45.6 kW) and sharing power-frequency regulation with the synchronverter. When the ramp ended at $t = 50$ s, the P_{vsg} started to decrease from 23.3 kW and was brought back to the 20 kW set point. The HPP plant adapted its P_e leading it to 0.91 pu (54.6 kW), taking charge of the whole 9 kW load variation by the end of the simulation. The frequency was correctly regulated to 50 Hz with a small negative nadir of -0.04 Hz induced by the ramp.

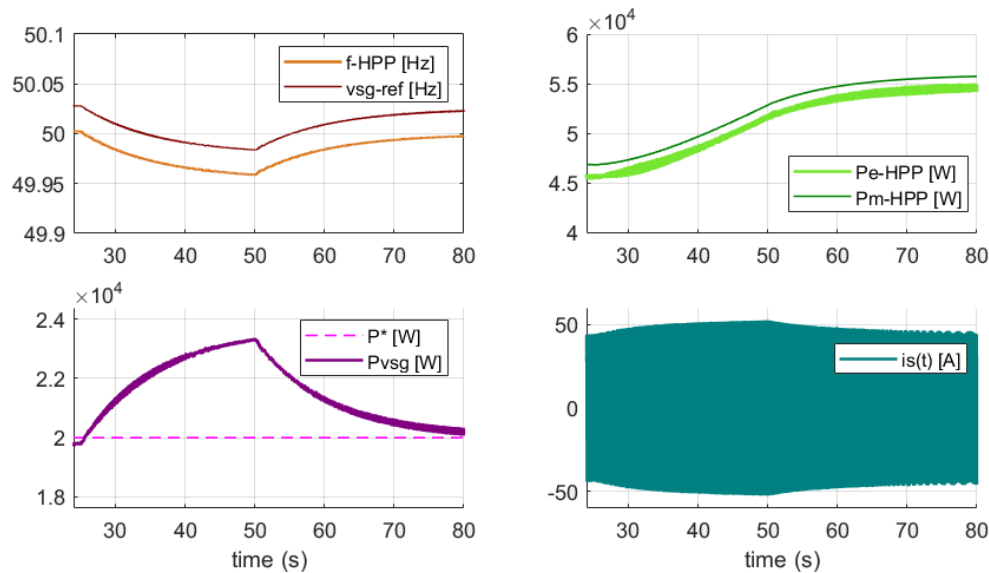


Fig. 126: Test 4: positive 9 kW ramp @ $t = 25$ s, 0.36 kW/s load change ends @ $t = 50$ s.

The DC-link voltage was not perturbed by the ramp, and the battery supported the grid by providing additional power to the synchronverter during the load shift (*Fig.127*). The time for resolving the frequency transient is around 40 s after the end of the ramp, confirming a time range lower than a minute for primary regulation in the microgrid.

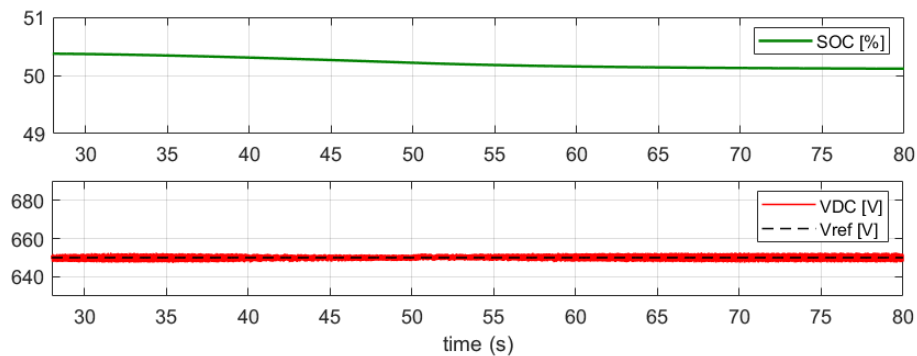


Fig. 127: Test 4: State of charge and DC-link voltage during the 9 kW ramp.

A fifth test was performed to analyse the system response to a three-phase fault on the microgrid using the dedicated Simulink block. Results are shown in *Fig.128*. The fault started at $t = 25$ s and was cleared in 0.1 s and the results are compared with previous test in *Fig.80-a*. Both the HPP frequency and the synchronverter frequency presented oscillations with nadirs in the range $[49.6 \div 50.25]$ Hz, similarly to the previous test. The fault impact on the HPP's generator resulted less intense, reducing from 7 pu (420 kW) to 4 pu (240 kW), and the power was correctly maintained to the reference value after clearing the fault. The synchronverter presented a power peak of 50 kW, around two times larger than its nominal power. The transient was resolved in few seconds and the active power was correctly tracked to the reference value.

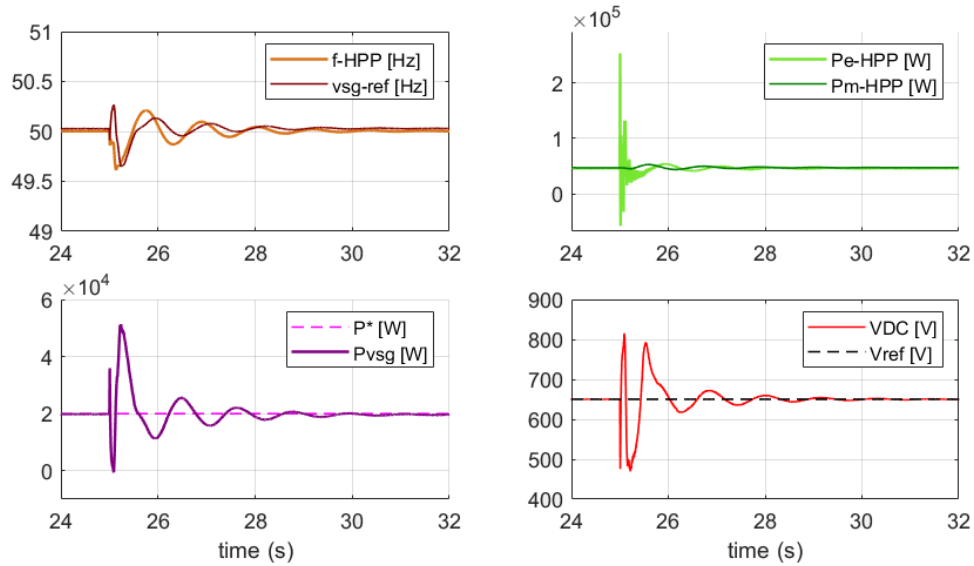


Fig. 128: Test 5: three-phase fault @ $t = 25$ s, time of clearing of 0.1 s.

The fault impacted on the synchronverter's inverter, presenting voltage oscillations on the DC-link. The oscillation propagated in the photovoltaic plant while the battery's state of charge was not affected. The inverter current reached a peak of 210 A during the fault (*Fig.129*). The transient on the inverter was recovered by the synchronverter controller, as no over-current protection was implemented in the model. In a field application the current protection would result in the disconnection of the inverter from the grid, in order to protect the equipment from internal fault.

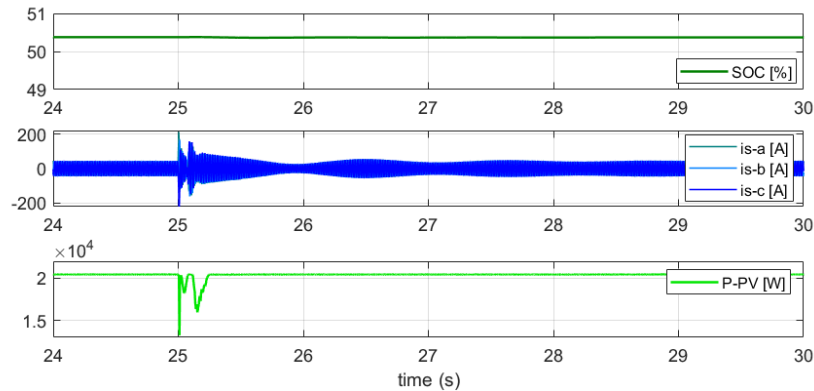


Fig. 129: Test 5: State of charge, inverter current and photovoltaic power during the three-phase fault.

7.3.2 Microgrid Real-Time Tests (OpalRT Environment)

The full microgrid model was successfully imported in the *RT-LAB* software. The online simulations have been executed by enabling both the *SM* master block and the *SC* console block. The simulation data channelled through the *OpWriteFile* blocks were set for simulation mode recording. The model has been successfully executed with discrete time steps of $T_S = 2.5 \mu\text{s}$ and $T_S = 25 \mu\text{s}$. Greater time steps resulted into malfunctioning in the battery control, as parameters were tuned to work specifically with lower time steps. A modification in the model was necessary to correctly compile, build and load the model on the *OpalRT* target node (*Fig.130*). The real-time simulator is not allowed to simulate algebraic loops and was stopped by the presence of the *PI* controller in the power-frequency channel of the self-synchronized synchronverter model (*Fig.101*). The *PI* controller is mainly added for performing a perfect active power tracking, which is not used during simulations with the droop control enabled, but is required for the initial synchronization. The loop was commented out to proceed with real-time tests, but the synchronization was still possible with the chosen settings, as discussed below.

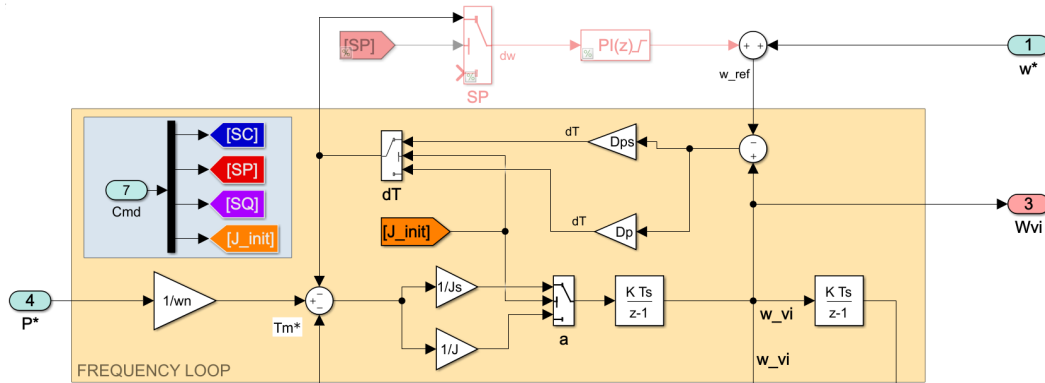


Fig. 130: Elimination of the conflicting algebraic loop in the self-synchronized synchronverter model.

The objective of the tests is to validate the full model of the microgrid in real-time simulations and observe analogous behaviours of *Simulink* tests. Results are presented in *Fig.131* and further below.

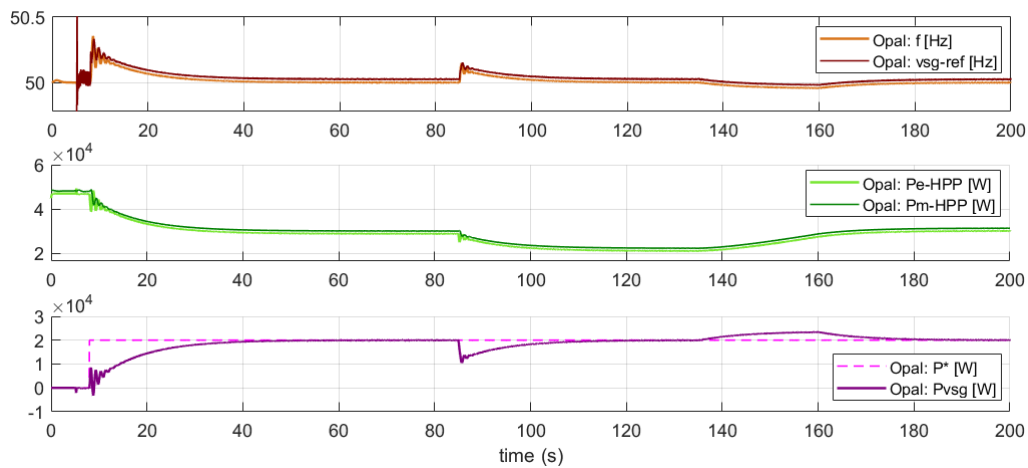


Fig. 131: OpalRT Test $25 \mu\text{s}$: Synchronization @ $t = 5$ s, grid connection @ $t = 5.2$ s, synchronverter 20 kW power step @ $t = 8$ s, negative 9 kW load step @ $t = 85$ s, positive 9 kW ramp (0.36 kW/s) @ $t = 135$ s.

The simulations exploit the initial synchronization, the connection of the synchronverter to the grid, a step test and a ramp test. The synchronverter's synchronization and connection to the grid is shown in *Fig.132* for a time step of $T_S = 2.5 \mu s$. The synchronization started at $t = 5$ s and was successfully completed. The grid connection was performed at $t = 5.2$ s and the system quickly resolved the connection's transient. The results of (*Fig.132-a*) are compared to the Simulink data (*Fig.132-b*), presenting an identical behaviour for all the variables.

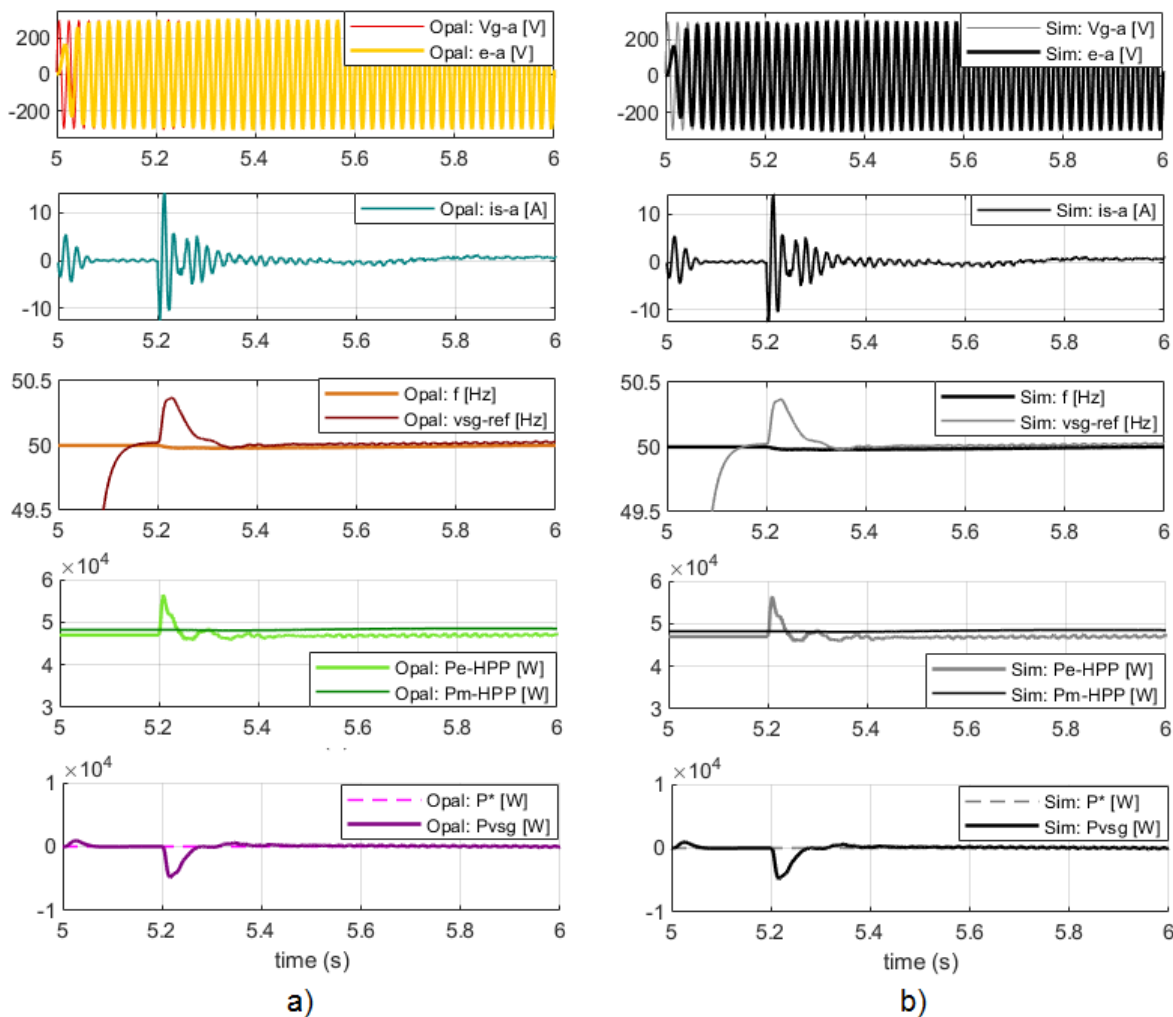


Fig. 132: OpalRT Test ($T_S = 2.5 \mu s$): a) synchronization and grid connection with OpalRT; b) synchronization and grid connection with Simulink.

It can be observed that the removal of the PI controller and the switch S_P did not influence the synchronization process and the active power correctly tracked the null reference P^* . This is due to the fact that the synchronverter is controlled with a frequency reference of 50 Hz and is connected to a grid already working at nominal 50 Hz: the PI block adjustments are needed only if the grid frequency differs with respects to the synchronverter reference. The synchronverter connection to the grid presented a system frequency nadir of -0.02 Hz, while the internal reference $vsg-ref$ adapted to the grid with a nadir of 0.35 Hz. The current on the PCC presented a 14 A peak and correctly decreased around null value, confirming the behaviour seen in offline tests.

The real-time simulation with a time step of $T_S = 25 \mu s$ presented similar behaviours for power

and frequency, but diverged for what concerns current and voltage harmonics. The synchronization process was overall smooth, while the connection presented an higher current peak and an increased harmonic content on the microgrid voltage V_g , resulting in a larger current residual while the synchronverter power is driven to zero. Results are shown in *Fig.133*. The real-time simulation presented a reduced transient on the HPP power during connection, while the synchronverter presented a negative power peak of 1 kW with a corresponding negative current peak of 50 A. The transient dynamic was slower if compared to the $2.5\mu\text{s}$ simulation, but provided the same system frequency behaviour. The synchronverter internal reference v_{sg-ref} presented small oscillations, but correctly tracked the system frequency. Oscillations are introduced by the harmonic content on the measured i_S , that is used in the synchronverter core algorithm to generate internal P , Q , e and impacts on the frequency and voltage loops. The grid voltage V_g increased in amplitude because of the harmonic content, but was correctly followed by the synchronverter internal voltage e .

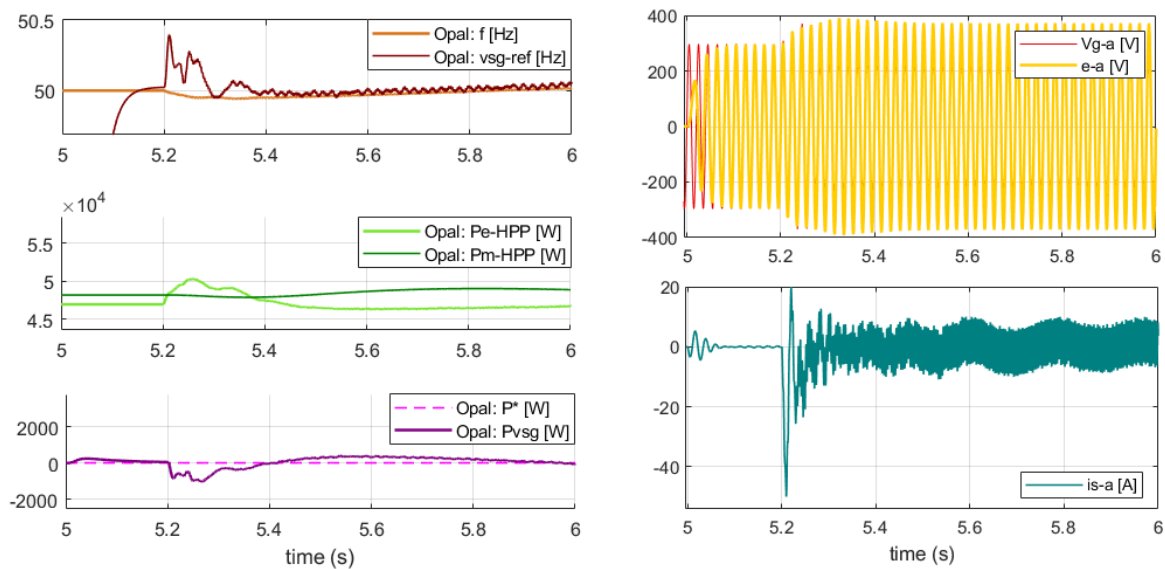


Fig. 133: OpalRT Test ($T_S = 25\mu\text{s}$) : real-time synchronization and grid connection with OpalRT.

The increased harmonic content is due to the synergy between the LCL filter parameters and the synchronverter parameters (as shown in *Fig.134*), that were specifically chosen with a $2.5\mu\text{s}$ time step. The time step was later increased of one order of magnitude (up to $25\mu\text{s}$), while the internal synchronverter time constants τ_f and τ_v remained the same to preserve the virtual generator size (J) and drooping responses (D_P , D_Q , K).

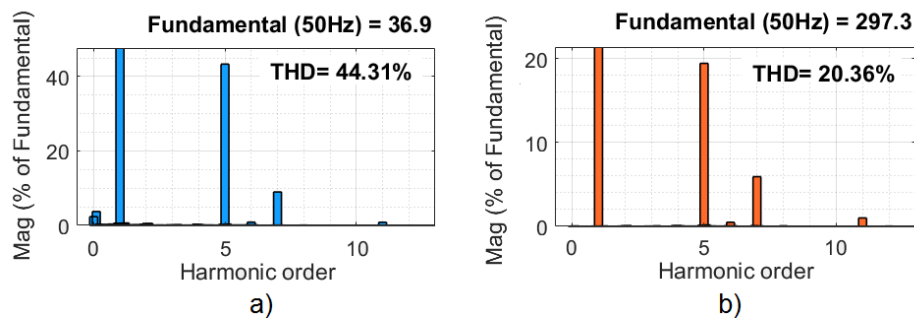


Fig. 134: OpalRT Test ($T_S = 25\mu\text{s}$): a) harmonic distortion on i_s ; b) harmonic distortion on V_g .

The LPF filters used for displaying the output powers and the measured current were adapted to reduce harmonics without introducing instability, but the feedback current i_S presented more noise if compared to $2.5\mu s$ simulations and introduced additional distortion in the synchronverter controller. The harmonic content is reduced during the PV mode operation of the synchronverter, but it is still more relevant than in tests with $T_S = 2.5\mu s$. A FFT was performed at $t = 60$ s for 10 cycles and presented a current THD of 44% and a voltage THD of 20%. A different tuning of the LCL filter could be beneficial to improve the response of the real-time model in terms of V/I waveform quality, as it would impact directly on the PCC.

The PV mode was enabled at $t = 8$ s and a 20 kW step reference was set for the synchronverter contribution to the grid. The simulations presented similar behaviours for both the $2.5\mu s$ time step (*Fig.135-a*) and the $25\mu s$ time step (*Fig.135-b*). The system frequency was contained under 50.4 Hz in both tests and the steady state was achieved in 60 seconds. The synchronverter active power correctly tracked the reference P^* and the HPP reduced its output power P_e from the initial 47 kW, adapting to the synchronverter's injection. In the $25\mu s$ test, the HPP power reduced less than 20 kW, but steady state was achieved nonetheless with a final value of 28kW.

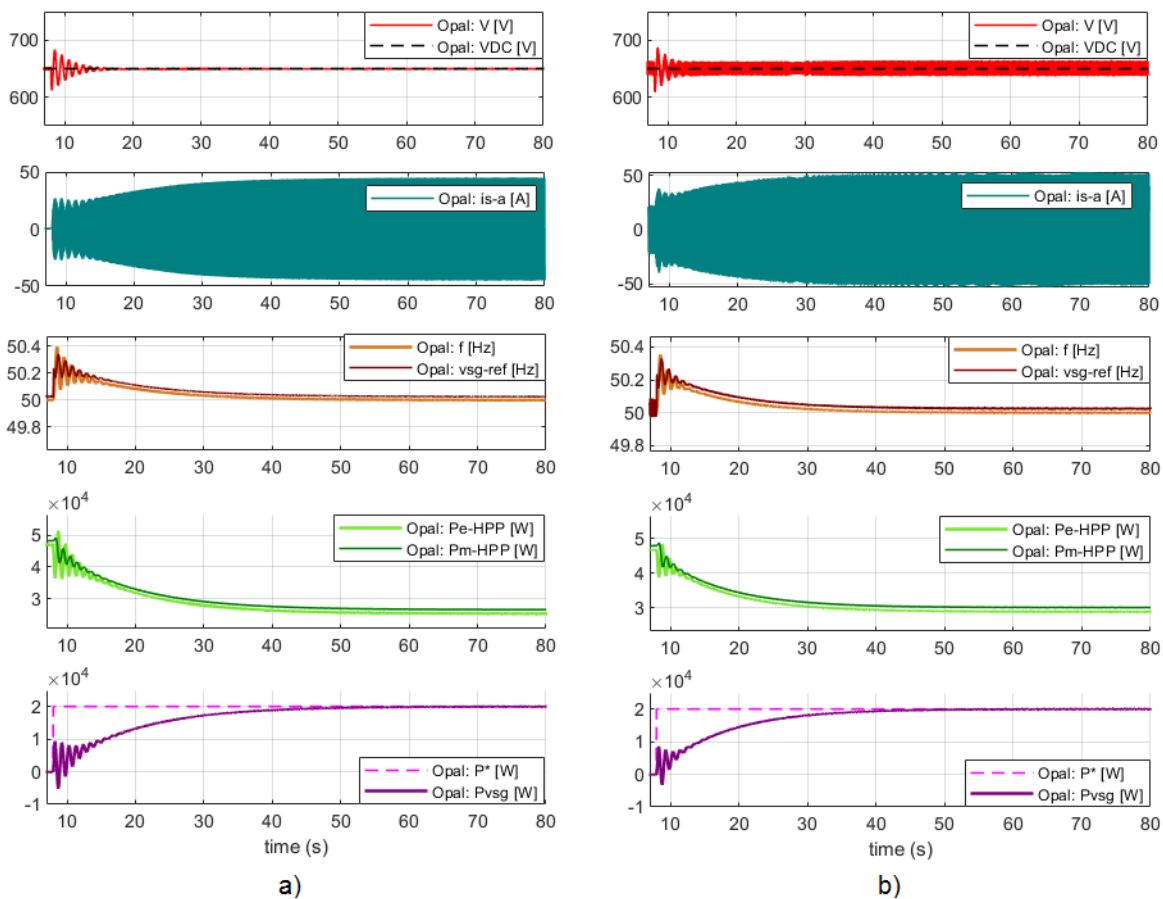


Fig. 135: OpalRT Test: a) PV mode power sharing with with $T_S = 2.5\mu s$; b) PV mode power sharing with with $T_S = 25\mu s$;

The DC-link voltage presented oscillations around the reference in the $25\mu s$ simulation. The phenomenon is due to the change of time step, as the battery controller's PI parameters were not changed. The controller still managed to maintain constant voltage on the DC side of the inverter,

but with reduced stability. Higher time steps were applied to the simulations, but the battery controller resulted to be not able of providing voltage regulation on the 650 V set-point. The step test was performed at $t = 85$ s by disconnecting the 9 kW *Test Load 2* from the microgrid. Results for tests with the $2.5\mu\text{s}$ time step and $25\mu\text{s}$ time step are shown in *Fig.136-a* and *Fig.136-b*. Both tests presents analogous behaviours for the frequency nadir, that reached 50.15 Hz during the load detachment. The synchronverter successfully covered the initial negative step by reducing production of approximately 10 kW and realigned again to the reference P^* afterwards. The HPP plant power droop control reduced the power production to the new set-point.

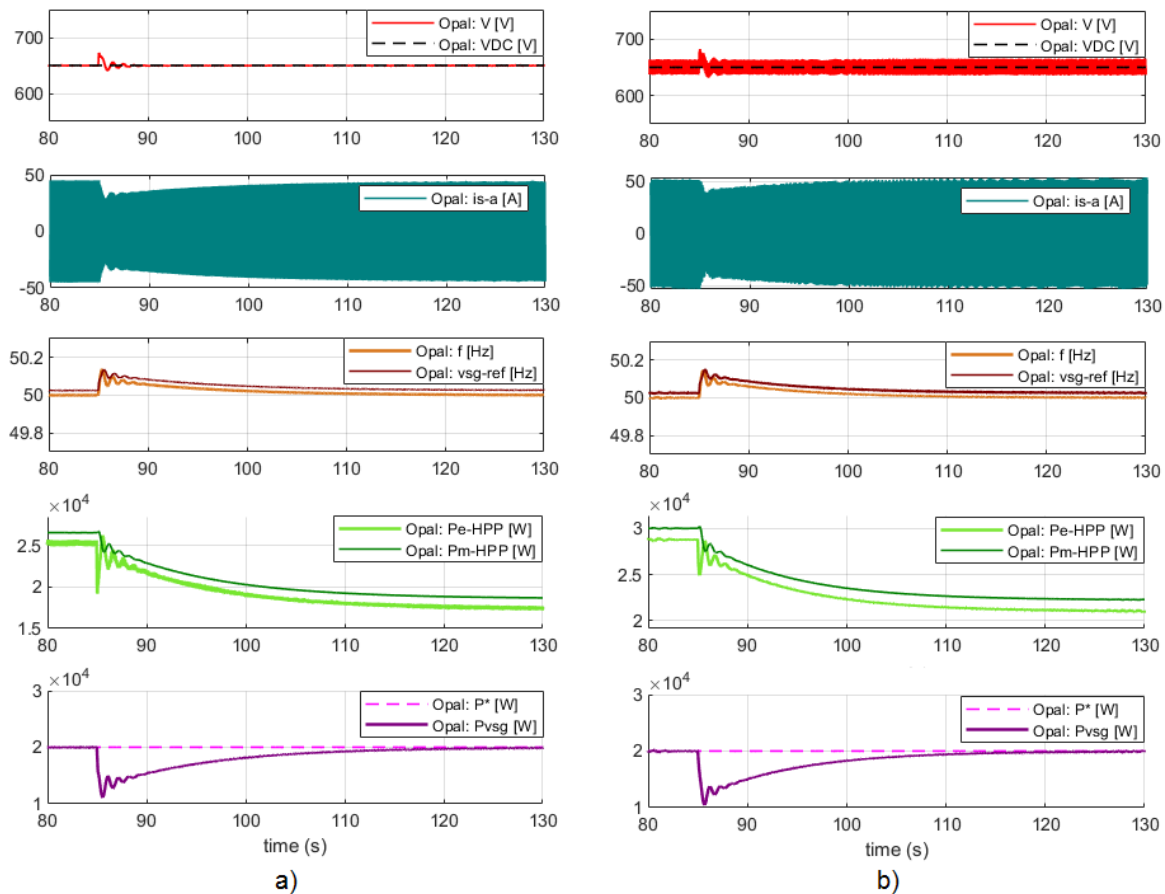


Fig. 136: OpalRT Test: a) negative 9 kW step @ $t = 85$ s with $T_S = 2.5\mu\text{s}$; b) negative 9 kW step @ $t = 85$ s with $T_S = 25\mu\text{s}$;

The DC voltage presented a small perturbation during the load disconnection and was successfully controlled back to constant value. The $25\mu\text{s}$ simulation still presented increased oscillations the around V_{DC} reference. The current i_S correctly recovered the step by the end of the transient and realigned to the synchronverter power injection.

The *Dynamic Load* was used to recover the previous step with a positive 9 kW ramp, starting from $t = 135$ s until $t = 160$ s. Results for tests with the $2.5\mu\text{s}$ time step and $25\mu\text{s}$ time step are shown in *Fig.137-a* and *Fig.137-b*. The ramp temporarily reduced the microgrid frequency, while the power droop controls of the HPP and VSG were working to restore the nominal value. The frequency was correctly restored to 50 Hz in both simulations.

The synchronverter reference $vsg-ref$ presented in both cases a small offset of 0.02 Hz as discussed in **section 7.3.1** and in the $25\mu s$ was slightly oscillating. The synchronverter increased the power injection to support the microgrid during the ramp and correctly returned the power to reference afterwards. The HPP plant slowly adapted the output power P_e with its droop control and returned to the same power levels observed before the 9 kW step by the end of the transient.

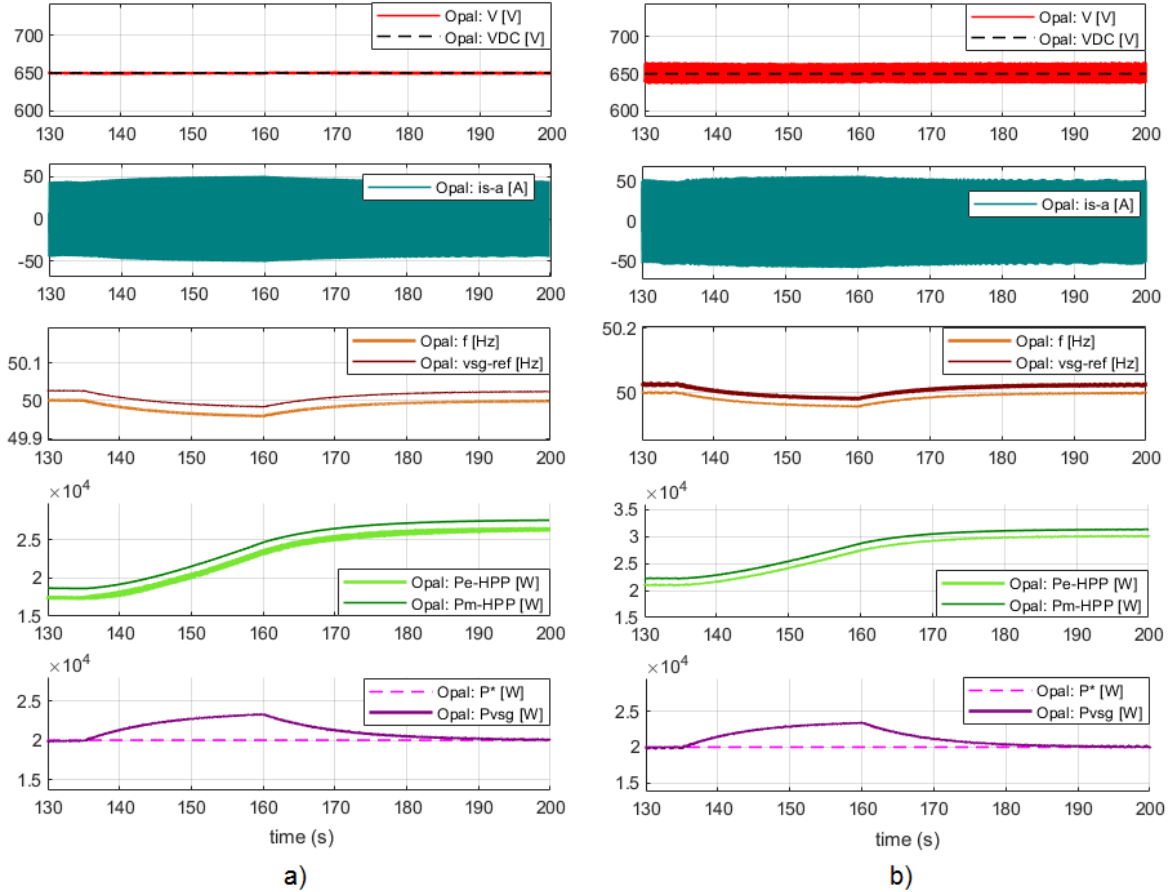


Fig. 137: OpalRT Test: a) positive 9 kW ramp @ $t = 135$ s with $T_S = 2.5\mu s$; b) positive 9 kW ramp @ $t = 135$ s with $T_S = 25\mu s$;

The full model implementation in OpalRT proved to be successful, as the model architecture is fully operative and running with the exception of the PI in the synchronverter’s frequency loop. The frequency behaviour confirmed the offline test results, displaying an improved response to contingency events in the microgrid and validating the efficiency of virtual synchronous generators in the grid.

The simulations with $T_S = 2.5\mu s$ confirmed optimal results, but with the presence of step overruns (due to a simulation burden greater than the target node possibilities) could not provide real-time simulation.

The execution of the model with $T_S = 25\mu s$ introduced additional oscillations and harmonic content in the synchronverter controller. The observed power and frequency variables followed the expected evolutions and some of them were filtered to remove high order noise from the displayed data. With a greater discrete time step the simulation speed was increased, but real-time execution was not achieved. The behaviours of the model were observed using the *OpMonitor Block* to extract the

computation time, the step time and the number of overruns. The simulation on the target node proved to have a variable performance. The computation time required by the cpu core to perform all the calculation in every step had a mean value of $34.39\mu s$, but multiple peaks where detected up to $160\mu s$. The step size was consequently variable based on the computation time, the execution time and the idle period. The mean step value was of $64.88\mu s$ with peaks over $270\mu s$, way above the expected fixed time step of $25\mu s$. As consequence, the number of step overruns was not negligible and the real-time execution was not achieved by the model.

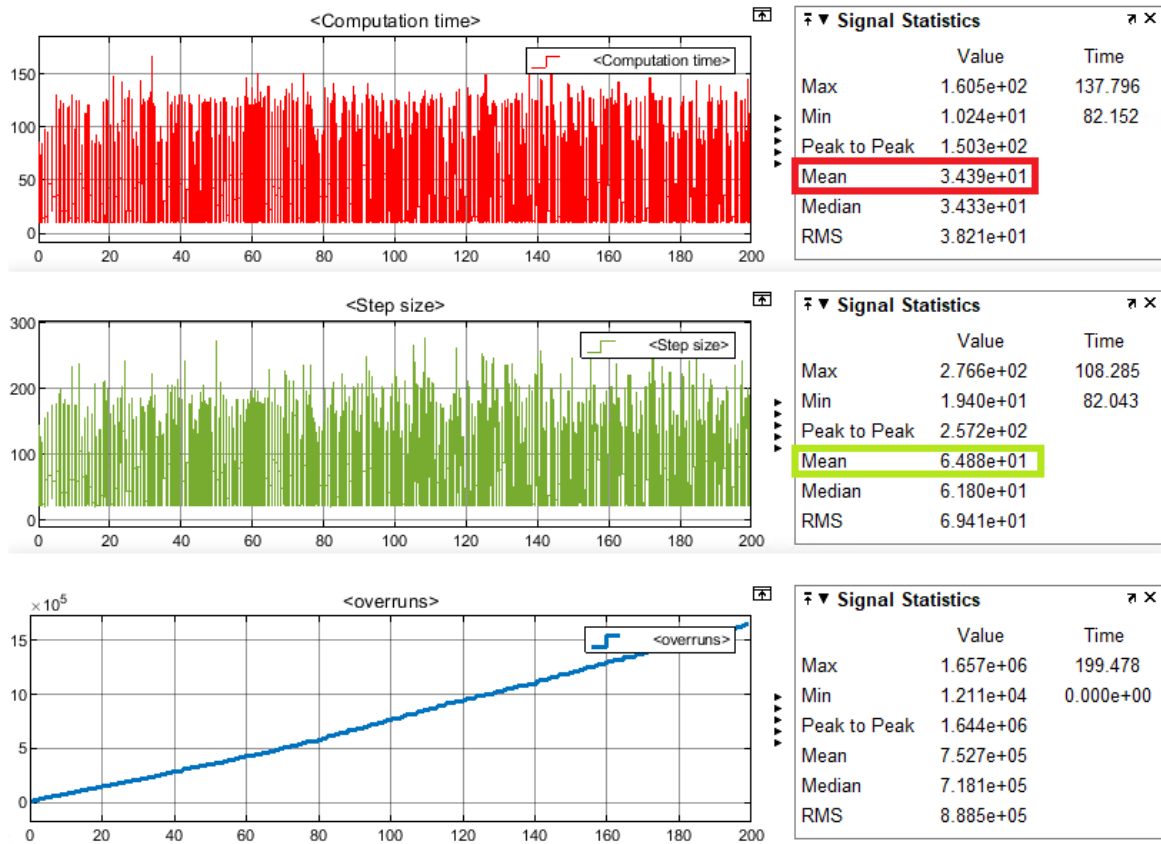


Fig. 138: Monitoring of the computation time and step size in tests with $T_S = 25\mu s$.

The variability and instability in the computation time was probably due to the complexity of the synchronverter model and the DC source, that added a heavy system of equation to the rest of the model. The slowed computation time negatively impacted on the step size and led to overruns. The model will require future development (for example the splitting of the model in more cores in OpalRT) and optimization to safely operate in PHIL with real hardware connection, starting from what has been already achieved in this thesis.

8 Conclusions

The focus of the thesis was to demonstrate the positive impact of synthetic inertia and virtual synchronous generators on a low inertia power system. An independent microgrid was used as a case study to represent a low inertia grid and to observe how the frequency stability is assessed both with and without the presence of a VSG.

A micro-hydro power plant was modelled on a real synchronous generator to represent a traditional generator unit, providing voltage and frequency reference to the microgrid. The stability simulation tests on the hydro plant were used to validate the efficiency of the turbine governor for load changes equal to 10% of the unit nominal power. The results were positive, presenting a frequency and power response aligned with the typical behaviour of hydro power plants. The test frequency variations were detected in the range of $[49.5 \div 50.5]$ Hz, complying with the *ISO Standards* for generator (± 1.5 Hz, $RoCoF = 0.6$ Hz/s). The results have been used as reference to prove the positive effects of synthetic inertia in the microgrid.

The *Self-Synchronized Synchronverter* control scheme [5] was successfully implemented from the literature to create the model of a virtual synchronous generator. The VSG power converter was supplied by a photovoltaic plant and a DC battery on the DC-link and was controlled to behave as a synchronous generator, with all the characteristic dynamic equations. The synchronverter architecture was successfully connected to the microgrid without the need of PLLs or synchronization units, confirming the advantages of the self-synchronization mechanism in the modelling. The DC source was sized to be 1/3 of the nominal hydro power, that in a low inertia normal scenario would have led to a reduction of the system inertia constant H from 4 seconds to 3 seconds.

The implementation of the VSG proved to be beneficial for the grid, increasing the inertia constant and reducing frequency variations. By applying load variations equal to 10% of the total nominal power the test frequency variations were detected in the range of $[49.85 \div 50.15]$ Hz and a maximum RoCoF of 0.15 Hz/s. The simulation results present a 20% reduction in the frequency variation, underlining the positive influence of virtual inertia on the grid. Additional benefits of synthetic inertia were also observed during frequency reductions, corresponding to microgrid power increases, where the synchronverter provided additional fast inertia support by using the DC battery storage. The long-term energy storage allowed to the VSG to cover the initial inertia requirements on the microgrid before the action of the slower control of the hydro governor, a feature that is not normally possible while operating a standard power converter. The operation of the VSG, alongside the traditional hydro synchronous generator, also validated the correct functioning of the droop controls of both generators. The VSG proved to be effective both as a grid-supporting unit and as a grid-forming unit, providing full power and voltage control at the point of connection.

The second objective of the thesis was to prepare the fully running model of the microgrid, comprehensive of the hydro plant and VSG, and make it available for real-time simulations. The aim of the conversion was to create a starting model to perform future PHIL tests, where the hydro plant model may be substituted by a real synchronous machine alongside other components for further testing. The original model was imported from *Matlab/Simulink* to *RT-Lab* and was successfully adapted to work on the target nodes of the OpalRT's *OP5600* and *OP5700* digital real-time simulators. The original model was executed with a discrete time step of $T_S = 2.5\mu s$, confirming all the results obtained by tests in the Simulink environment. The simulation presented however overruns and could not be executed in real-time due to an excessive computational burden on the OP target

node. An up-scaled version of the model was proposed with a discrete time step of $T_S = 25\mu s$, in the range of general electromagnetic transient simulation time constants. The model was correctly executed and presented the introduction of increased harmonic content on the current and voltage on the point of connection between the synchronverter and the microgrid. The real-time simulation was not achieved, due to the presence of an increased computation time of the model. The set of equations and control loops to be solved during every step prove to be excessive for the Opal target node and resulted in a variable step size around the value of $65\mu s$ (above the expected $25\mu s$). The variability in the step size led to multiple step overruns and the final loss of real-time performances. A possible solution to overcome the problem would be to split the full microgrid model in multiple subsystems, in order to assign the main microgrid to the principal target node (Master Subsystem) and spread the hydro plant, the synchronverter and the DC source on other computation secondary targets (Slave Subsystems). In this way different parts of the model would be managed by different cpu cores in parallel, speeding up the computation time of every subsystem until reaching real-time execution. The achievement of real-time simulation is considered essential to successfully perform PHIL studies.

Further development would be required to improve the harmonic content and overall stability of the synchronverter model, by studying an appropriate method to tune the controller's parameters (D_P , D_Q , K , J) and the LCL filter values according to the size and type of connection to different simulated power systems, for any discrete time-step condition in the typical range of electromagnetic applications.

References

- [1] POWER. *History of Power: The Evolution of the Electric Generation Industry*. 2020. URL: <https://www.powermag.com/history-of-power-the-evolution-of-the-electric-generation-industry/> (visited on 01/25/2021).
- [2] Federico Milano et al. “Foundations and challenges of low-inertia systems”. In: *2018 Power Systems Computation Conference (PSCC)*. IEEE. 2018, pp. 1–25.
- [3] Kamala Sarojini Ratnam, K Palanisamy, and Guangya Yang. “Future low-inertia power systems: Requirements, issues, and solutions-A review”. In: *Renewable and Sustainable Energy Reviews* 124 (2020), p. 109773.
- [4] Dolf Gielen et al. *Global energy transformation: a roadmap to 2050*. 2019.
- [5] Qing-Chang Zhong et al. “Self-synchronized synchronverters: Inverters without a dedicated synchronization unit”. In: *IEEE Transactions on power electronics* 29.2 (2013), pp. 617–630.
- [6] Enrico Carpaneto. *Appunti del Corso di Sistemi Elettrici di Potenza, Politecnico di Torino*. A.A. 2017/18.
- [7] Bálint Hartmann, István Vokony, and István Táci. “Effects of decreasing synchronous inertia on power system dynamics—Overview of recent experiences and marketisation of services”. In: *International Transactions on Electrical Energy Systems* 29.12 (2019), e12128.
- [8] Mikko Kuivaniemi et al. *Requirement for minimum inertia in the Nordic power system*. 2019.
- [9] Adolfo Anta. *On Low Inertia Grids*. 2017. URL: <http://www.incite-itn.eu/blog/on-low-inertia-grids/> (visited on 07/03/2020).
- [10] Mike Rycroft. *Synthetic inertia in grids with a high renewable energy content*. 2017.
- [11] Joan Rocabert et al. “Control of power converters in AC microgrids”. In: *IEEE transactions on power electronics* 27.11 (2012), pp. 4734–4749.
- [12] Ujjwol Tamrakar et al. “Virtual inertia: Current trends and future directions”. In: *Applied Sciences* 7.7 (2017), p. 654.
- [13] Lidong Zhang, Lennart Harnefors, and Hans-Peter Nee. “Power-synchronization control of grid-connected voltage-source converters”. In: *IEEE Transactions on Power systems* 25.2 (2009), pp. 809–820.
- [14] Qing-Chang Zhong and George Weiss. “Synchronverters: Inverters that mimic synchronous generators”. In: *IEEE transactions on industrial electronics* 58.4 (2010), pp. 1259–1267.
- [15] Yong Chen et al. “Improving the grid power quality using virtual synchronous machines”. In: *2011 International Conference on Power Engineering, Energy and Electrical Drives*. IEEE. 2011, pp. 1–6.
- [16] Mahdi Ashabani et al. “Inducverters: PLL-less converters with auto-synchronization and emulated inertia capability”. In: *IEEE Transactions on Smart Grid* 7.3 (2015), pp. 1660–1674.
- [17] Jaber Alipoor, Yushi Miura, and Toshifumi Ise. “Power system stabilization using virtual synchronous generator with alternating moment of inertia”. In: *IEEE journal of Emerging and selected topics in power electronics* 3.2 (2014), pp. 451–458.
- [18] Jia Liu, Yushi Miura, and Toshifumi Ise. “Dynamic characteristics and stability comparisons between virtual synchronous generator and droop control in inverter-based distributed generators”. In: *2014 International Power Electronics Conference (IPEC-Hiroshima 2014-ECCE ASIA)*. IEEE. 2014, pp. 1536–1543.

- [19] Daniel Remon et al. “Grid synchronization of renewable generation systems using synchronous power controllers”. In: *2017 IEEE 6th International Conference on Renewable Energy Research and Applications (ICRERA)*. IEEE. 2017, pp. 169–174.
- [20] Miguel Torres and Luiz AC Lopes. “Virtual synchronous generator: A control strategy to improve dynamic frequency control in autonomous power systems”. In: (2013).
- [21] Salvatore D’Arco and Jon Are Suul. “Equivalence of virtual synchronous machines and frequency-droops for converter-based microgrids”. In: *IEEE Transactions on Smart Grid* 5.1 (2013), pp. 394–395.
- [22] Joan Rocabert et al. “Control of energy storage system integrating electrochemical batteries and supercapacitors for grid-connected applications”. In: *IEEE Transactions on Industry Applications* 55.2 (2018), pp. 1853–1862.
- [23] AA Khodadoost Arani et al. “Review of Flywheel Energy Storage Systems structures and applications in power systems and microgrids”. In: *Renewable and Sustainable Energy Reviews* 69 (2017), pp. 9–18.
- [24] Jiale Yu, Jingyang Fang, and Yi Tang. “Inertia emulation by flywheel energy storage system for improved frequency regulation”. In: *2018 IEEE 4th Southern Power Electronics Conference (SPEC)*. IEEE. 2018, pp. 1–8.
- [25] Yang Liu et al. “Comparison of synchronous condenser and STATCOM for inertial response support”. In: *2014 IEEE Energy Conversion Congress and Exposition (ECCE)*. IEEE. 2014, pp. 2684–2690.
- [26] Ha Thi Nguyen et al. “Frequency stability improvement of low inertia systems using synchronous condensers”. In: *2016 IEEE International Conference on Smart Grid Communications (SmartGridComm)*. IEEE. 2016, pp. 650–655.
- [27] Andrew Blakers et al. “Pathway to 100% renewable electricity”. In: *IEEE Journal of Photovoltaics* 9.6 (2019), pp. 1828–1833.
- [28] Voith. *Pumped Storage Plants*. URL: <https://voith.com/uk-en/industry-solutions/hydropower/pumped-storage-plants.html> (visited on 07/14/2020).
- [29] Emilia Nobile, Gökhan Sari, and Alexander Schwery. “Variable speed hydro pumped storage as flexible enabler of intermittent renewable penetration”. In: *2018 IEEE Power & Energy Society General Meeting (PESGM)*. IEEE. 2018, pp. 1–5.
- [30] Laijun Chen et al. “Review and prospect of compressed air energy storage system”. In: *Journal of Modern Power Systems and Clean Energy* 4.4 (2016), pp. 529–541.
- [31] Wen Xian-kui et al. “Study on Primary Frequency Modulation Parameter Setting of Compressed Air Energy Storage”. In: *2018 2nd International Conference on Green Energy and Applications (ICGEA)*. IEEE. 2018, pp. 143–146.
- [32] RTDS Technologies. URL: <https://www.rtds.com/technology/> (visited on 08/26/2020).
- [33] RTDS Technologies. *Power Hardware In The Loop Simulations (PHIL)*. URL: <https://www.rtds.com/technology/> (visited on 08/26/2020).
- [34] Santi Insinga. “Design and Implementation of a Test Lab Setup to Perform Power Hardware-in-the-Loop Experiments”. PhD thesis. Politecnico di Torino, 2018.
- [35] Wei Ren, Michael Steurer, and Thomas L Baldwin. “Improve the stability and the accuracy of power hardware-in-the-loop simulation by selecting appropriate interface algorithms”. In: *IEEE Transactions on Industry Applications* 44.4 (2008), pp. 1286–1294.

- [36] Tomoyuki Hatakeyama, Antonino Riccobono, and Antonello Monti. “Stability and accuracy analysis of power hardware in the loop system with different interface algorithms”. In: *2016 IEEE 17th Workshop on Control and Modeling for Power Electronics (COMPEL)*. IEEE. 2016, pp. 1–8.
- [37] MD Omar Faruque et al. “Real-time simulation technologies for power systems design, testing, and analysis”. In: *IEEE Power and Energy Technology Systems Journal* 2.2 (2015), pp. 63–73.
- [38] Mayank Panwar et al. “An overview of real time hardware-in-the-loop capabilities in digital simulation for electric microgrids”. In: *2013 North American Power Symposium (NAPS)*. IEEE. 2013, pp. 1–6.
- [39] Xavier Guillaud et al. “Applications of real-time simulation technologies in power and energy systems”. In: *IEEE Power and Energy Technology Systems Journal* 2.3 (2015), pp. 103–115.
- [40] Chris S Edrington et al. “Role of power hardware in the loop in modeling and simulation for experimentation in power and energy systems”. In: *Proceedings of the IEEE* 103.12 (2015), pp. 2401–2409.
- [41] Michael Steurer et al. “A megawatt-scale power hardware-in-the-loop simulation setup for motor drives”. In: *IEEE Transactions on Industrial Electronics* 57.4 (2009), pp. 1254–1260.
- [42] James Langston et al. “Power hardware-in-the-loop testing of a 500 kW photovoltaic array inverter”. In: *IECON 2012-38th Annual Conference on IEEE Industrial Electronics Society*. IEEE. 2012, pp. 4797–4802.
- [43] Ha Thi Nguyen et al. “Combination of synchronous condenser and synthetic inertia for frequency stability enhancement in low-inertia systems”. In: *IEEE Transactions on Sustainable Energy* 10.3 (2018), pp. 997–1005.
- [44] Sergio Bruno et al. “A low-cost controller to enable synthetic inertia response of distributed energy resources”. In: *2020 IEEE International Conference on Environment and Electrical Engineering and 2020 IEEE Industrial and Commercial Power Systems Europe (EEEIC/I&CPS Europe)*. IEEE. 2020, pp. 1–6.
- [45] IEEE Power and Electric machinery Committee Energy Society. “IEEE Guide for Synchronous Generator Modeling Practices and Parameter Verification with Applications in Power System Stability Analyses”. In: *IEEE Std 1110-2019* (2019).
- [46] Electrical Academia. *How Hydropower Plants Work — Types of Hydropower Plants*. URL: <https://electricalacademia.com/renewable-energy/hydroelectric-power-plant-working-types-hydroelectric-power-plants/attachment/figure-1-17/> (visited on 11/10/2020).
- [47] RA Nanaware, SR Sawant, and BT Jadhav. “Modeling of hydraulic turbine and governor for dynamic studies of HPP”. In: *IJCA Proceedings on International Conference on Recent Trends in Information Technology and Computer Science*. 2012, pp. 6–11.
- [48] MathWorks. *Synchronous Machine - Simscape Library*. URL: <https://it.mathworks.com/help/physmod> (visited on 09/05/2020).
- [49] Working Group Prime Mover and Energy Supply. “Hydraulic turbine and turbine control models for system dynamic studies”. In: *IEEE Transactions on Power Systems* 7.1 (1992), pp. 167–179.
- [50] Prabha Kundur. “Power system stability”. In: *Power system stability and control* (2007), pp. 7–1.

- [51] Power IEEE and System Energy Society. “PES-TR1 technical Report: Dynamic Models for Turbine-Governors in Power System Studies”. In: *IEEE Institute of Electrical and Electronic Engineers* (2013).
- [52] Bahram Khodabakhchian, Gia T Vuong, and Sylvain Bastien. “On the comparison between a detailed turbine-generator EMTP simulation and corresponding field test results”. In: *International Journal of Electrical Power & Energy Systems* 19.4 (1997), pp. 263–268.
- [53] Wei Li. “Hydro turbine and governor modeling and scripting for small-signal and transient stability analysis of power systems”. In: *Master’s degree project, KTH Royal Institute of Technology, Stockholm, Sweden* (2011).
- [54] P.M.B. dos Santos. “Primary frequency control in isolated power grids”. Thesis for the Master of Science Degree in Electrical and Computer Engineering. técnico Lisboa, 2014.
- [55] *PID Control Schemes*. URL: <https://yilinmo.github.io/EE3011/Lec9.html>. (visited on 09/18/2020).
- [56] Pieter Tielens, Pierre Henneaux, and Stijn Cole. *Penetration of renewables and reduction of synchronous inertia in the European power system-Analysis and solutions*. 2018.
- [57] Prof. Dr. Atil Bulu. *HYDROELECTRIC POWER PLANTS - Lecture Notes*.
- [58] *Dimesionamento di massima di una Pelton*. URL: <https://fantasiaipsiam.files.wordpress.com/2015/04/pelton.pdf> (visited on 10/04/2020).
- [59] M. U. Leonorman. “Real-Time Modeling Of Power Grids With Hardware-in-the-loop Implementation”. Master Thesis in Electronic Engineering. Politecnico di Torino, 2017.
- [60] OPAL-RT Technology. *RT-LAB Quick Start Guide*. URL: https://blob.opal-rt.com/medias/L00161_0582.pdf (visited on 01/12/2021).
- [61] N. Pandiarajan. *A ResearchGate Flow chart of P & O MPPT algorithm*. URL: https://www.researchgate.net/figure/The-flowchart-of-P-and-O-MPPT-algorithm_fig2_258432277 (visited on 11/24/2020).
- [62] J. Green. *Perturb and Observe Maximum Power Point Tracking in Simulink*. URL: <https://www.you-tube.com/watch?v=VCDUw95p1ro> (visited on 11/27/2020).
- [63] Erdal Irmak et al. “A modified droop control method for PV systems in island mode DC microgrid”. In: *2019 8th International Conference on Renewable Energy Research and Applications (ICRERA)*. IEEE. 2019, pp. 1008–1013.
- [64] Krishnakumar R Vasudevan et al. “Synchronverter: A Comprehensive Review of Modifications, Stability Assessment, Applications and Future Perspectives”. In: *IEEE Access* 8 (2020), pp. 131565–131589.
- [65] Eitan Brown. “A study of the use of synchronverters for grid stabilization using simulations in SimPower”. In: *MSc thesis, Tel Aviv University* (2015).
- [66] Dongqi Liu et al. “Modeling and control of a V2G charging station based on synchronverter technology”. In: *CSEE Journal of Power and Energy Systems* 4.3 (2018), pp. 326–338.
- [67] Gianfranco Chicco. *Appunti del corso di Distribuzione e Utilizzazione dell’Energia Elettrica, Politecnico di Torino*. A.A. 2018/19.